CDF/PHYS/EXOTIC/CDFR/9863
July 27, 2009
Version 1.0

Updated Search for H $\rightarrow$ WW Production Using Likelihood-Based Electron Selection

Doug Benjamin, Mark Kruse

Duke University

Eric James, Sergo Jindariani, Britney Rutherford

Fermilab

Roman Lysak

IEP SAS, Slovakia

Dean Andrew Hidas

Rutgers University

Aidan Robson, Rick St. Denis, Peter Bussey

University of Glasgow

Matthew Herndon, Jason Nett, Jennifer Pursley

University of Wisconsin, Madison

Maria d'Errico, Simone Pagan Griso, Donatella Lucchesi

INFN and University of Padova

Abstract

We present a search for Standard Model (SM) Higgs to WW^* production in dilepton plus $\not\!\!E_T$ channels using approximately 4.8 fb^{-1} of integrated luminosity. The analysis described here relies on almost the same techniques described in CDF Note 9697. The primary difference in the two searches is an extended lepton identification implemented in this version of the analysis. We define a likelihood-based electron selection which improves acceptance while keeping the same electron fake rate as in previous versions of the analysis. We utilize multivariate discriminants separately optimized for events containing zero, one, and two or more jets in the final state. Also, in the optimized analyses for events with one and two or more jets, we take into account four possible Higgs boson production mechanisms: gluon fusion, associated production with a W boson, associated production with a Z boson, and vector boson fusion (in the case of zero jets only gluon fusion is considered). We also include an analysis of a same-sign dilepton event sample which can potentially contain additional signal events originating from the associated Higgs boson production mechanisms. Based on the dilepton opposite-sign selection criteria defined in CDF Note 9195 and a data sample of about 4.8 fb^{-1}, we observe (summing over all jet bins) a total of XXXX candidate events compared with an expectation of $XXXX \pm XXX$ background events and $XXX \pm XXX$ signal events for a Standard Model Higgs boson with a mass of 165 GeV/c^2. In our same-sign dilepton event candidate sample we additionally observe 81 candidate events compared with an expectation of 77.2 ± 12.9 background events and 1.9 ± 0.3 signal events for a Standard Model Higgs boson with a mass of 165 GeV/c^2. Based on these samples, we determine an observed 95% C.L. upper cross section limit of XXXX times the SM prediction at NNLL for a Higgs mass of 165 GeV/c^2 to be compared with the value for the median of the expected limit (XXXX). Results for thirteen other Higgs mass hypotheses ranging from 110 GeV/c^2 to 200 GeV/c^2 are also presented.

Contents

1 Introduction

In this note, we present a search for Standard Model $H \to WW^* \to l\nu l\nu$ production using approximately 4.8 fb^{-1} of integrated luminosity. This search builds on CDF Note 9697 [1], from which it inherits the most recent improvements of the analysis, most notably new data up to period 23 and an extended muon categorization which includes CMP and CMX MiniSkirt or Keystone trigger paths.

In this Note we present for the first time a likelihood-based electron selection to replace the tight central electron (TCE) selection used in previous versions of this analysis. Section 2 descibes the likelihood and improvements over selecting TCE electrons, along with the updated trigger efficiencies, fake rate measurements, and Drell-Yan cross section measurement divided into all possible dilepton types.

Another improvement implemented in this version of the analysis is the extension of the $t\bar{t}$ Monte Carlo sample to include modeling of the later run periods. Previously, the $t\bar{t}$ sample consisted of one fully run-dependent sample which went through period 13. We now use an additional Monte Carlo sample generated with a higher luminosity profile (based on a specific set of runs from periods 10 to 12) to model data collected from periods 14 onward (periods 14 to 23 for the case of 4.8 fb^{-1}). In order to avoid complications in data-to-Monte-Carlo comparisons, we treat periods 14 to 23 as a single data period with a unique set of scale factors, trigger efficiencies, etc. Monte Carlo events in the higher luminosity samples are each assigned to a specific run number contained within period 15 and a unique event number to ensure that events are not accidentally removed as duplicates. All of the signal samples and most of the other background samples were already updated this way in [1].

2 Updated Lepton Identification

The current Higgs searches are mainly statistically limited; for this reason it's important to maximize the acceptance of the analysis. Since we're looking at both Ws decaying leptonically, one of the key points in maximizing the acceptance is the lepton identification for electrons and muons[1].

Previous $H \to WW$ analyses rely on the lepton identification described in CDF Note 8538 [2], which aims to exploit every region of the CDF detector where an energy measurement can be made to define a set of unique (non-overlapping) categories for electron and muon identification. The muon selections were updated in the most recent $H \to WW$ analysis, described in CDF Note 9697 [1]. The analysis presented in 9697 used the following categories:

- Electrons: TCE, PHX
- Muons: CMUP, CMP, CMU, CMX, CMXMsKs, BMU, CMIOCES, CMIOPES, CrkTrk

The triggers used to collect the data sample for this analysis are based on leptons, and are deeply connected with the lepton definitions. Trigger paths exploited by the analysis in Note 9402 can be summarized in 4 categories (present in the CDF trigger tables in various versions):

- MUON_CMUP18
- MUON_CMP18_PHI_GAP
- MUON_CMX18
- ELECTRON_CENTRAL_18
- MET_PEM

The CMU muons triggered by the MUON_CMU18_ETA_GAP path will be included in a later version of the analysis, as this trigger has only been working properly since period 21 data-taking.

The aim of the study described in this CDF Note is to improve electron identification using a likelihood method. In Section 2.1 we describe in detail this likelihood method. Section 2.2 describes the calculation of the trigger efficiencies for the new likelihood-based electron category. Sections 2.3 and 2.4 describe the lepton ID scale factor and fake rate calculations for each of the categories. Finally, we perform the strongest check of the new electrons' behavior in Section 2.5, measuring the cross section of the Drell-Yan ($p\bar{p} \to Z/\gamma^\star \to l^+l^-$, $l = e, \mu$) process separately for each dilepton type.

[1] τ's are currently considered only if decaying to an electron or muon. Studies are ongoing to include hadronically decaying τ's in the same framework, but they will not be discussed in this note.

2.1 Likelihood Method for Lepton Identification

The standard methods for lepton identification use cuts on many different identification variables (see TCE definition in Tab. 1). Each cut decrease reconstruction efficiency. This way candidates which fail even one cut by small margin are removed from the sample. Catching each possible lepton candidate is extremely important in such low-statistic search as looking for the Higgs boson at Tevatron.

Therefore we developed method which tries to exploit the identification variables in better way. We will not cut on each individual variable, rather combine identification variables into one discriminant and cut only on the value of this final discriminant. It is expected that this should increase the efficiency of reconstruction (while keeping the same fake rate).

The method we use is the likelihood method which calculates the probability of the candidate to be real and "fake" lepton and computes the likelihood discriminant.

We apply the method on central electron candidates, so the newly identified central electrons (Likelihood based electrons – LBE) replace in our analysis the up to now used TCE.

2.1.1 Likelihood definition for central electrons

For our likelihood method, we choose most of the identification, non kinematic variables which were used in identification of TCE (for definition of TCE, see Tab. 1). Specifically, these are

- E_{HAD}/E_{EM} – the ratio of the hadronic calorimeter energy to the electromagnetic calorimeter energy associated with the candidate
- E/P – the ratio of the EM cluster transverse energy to the COT track transverse momentum
- $Lshr$ – the lateral shower profile in the transverse plane to the electron direction
- $CalIso$ – The energy E_T in a cone of radius $\Delta R = \sqrt{(\Delta\eta)^2 + (\Delta\phi)^2} \leq 0.4$ around the electron cluster excluding the electron cluster divided by the energy in the electron cluster:
$$CalIso = \frac{E_T^{cone} - E_T^{electron}}{E_T^{electron}}$$
- $TrkIso$ – the same variable as above $CalIso$ but measured using tracks instead of calorimeter
- $Q \times \Delta x_{CES}$ – The distance in the r-ϕ plane between the extrapolated, COT beam constrained track and the best matching CES cluster, times the charge Q of the track.

- Δz_{CES} – The distance in the r-z plane between the extrapolated, COT beam constrained track and the best matching CES cluster.
- $NCotHitsAx$ – number of COT hits on axial layers belonging to track associated to the candidate electron
- $NCotHitsSt$ – number of COT hits on stereo layers belonging to track associated to the candidate electron
- χ^2_{COT} – χ^2 associated with the COT hits belonging to track
- $NSvxHits$ – number of SVX hits belonging to track associated to the candidate electron

These variables are then used in calculation of the likelihood which has the following form:

$$\mathcal{L}(\vec{x}) = \frac{L_{sig}}{L_{sig} + L_{bckg}} = \frac{\prod_{i=1}^{N} P_i^{sig}(x_i)}{\prod_{i=1}^{N} P_i^{sig}(x_i) + \prod_{i=1}^{N} P_i^{bckg}(x_i)} \tag{1}$$

where

- x_i – means $i-th$ identification variable used in likelihood. These are all 11 variables described above.
- N - is the number of ID variables, in our case it is 11.
- $P_i^{sig}(x_i), P_i^{bckg}(x_i)$ - these are the functions which give probability to obtain a certain value x_i for i-th ID variable. These are obtained using signal and "background"("fakes") templates.

By definition, the value of $\mathcal{L}$ is restricted within range $(0.0, 1.0)$.

As can be seen the essential feature of this method is to obtain templates for ID variables for real electrons and "fakes".

2.1.2 Building of signal and background templates

We use data to build the signal and background templates. This is done by selecting the samples dominated by real high P_T electrons (Z boson candidates) for signal templates and dominated by fake electrons (dijet data) for background templates.

Building of the signal templates is done as follows. We select Z candidates (76 GeV < $M_{\ell\ell}$ < 106 GeV) from high P_T electron data (bhelbj dataset) where the one electron is fully identified central electron (TCE) while the second electron candidate must pass just basic central electron object criteria (must pass "CEM probe" criteria, see definition in Tab. 2. Such sample is completely dominated by Drell-Yan events. The ID variables of

	TCE
Region	central
Fiducial	track fiducial to CES
Track p_T	≥ 10 $(5 if E_T < 20)$
Track $\lvert z_0 \rvert$	≤ 60 cm
# Ax SL (5hits)	≥ 3
# St SL (5hits)	≥ 2
Conversion	$\neq 1$
E_{HAD}/E_{EM}	$\leq 0.055 + 0.00045 * E$
Iso/E_T	≤ 0.1
Lshr	≤ 0.2
E/P	$< 2.5 + 0.015 * E_T$
signed CES ΔX	$-3 \leq q * \Delta X \leq 1.5$ cm
CES $\lvert \Delta Z \rvert$	< 3 cm
Track	Beam constrained

Table 1: Definition of TCE.

Central electron probe
Track or SMX fiducial to CES
Track $p_T \geq 5$ GeV
Track $Z_0 \leq 60$ cm

Table 2: Definition of central electron probe object.

Central fakeable electron
Track fiducial to CES
$E_{HAD}/E_{EM} <= 0.125 + 0.00045 * E$
$CalIso < 0.3$
not a conversion

Table 3: Definition of central electron fakeable object.

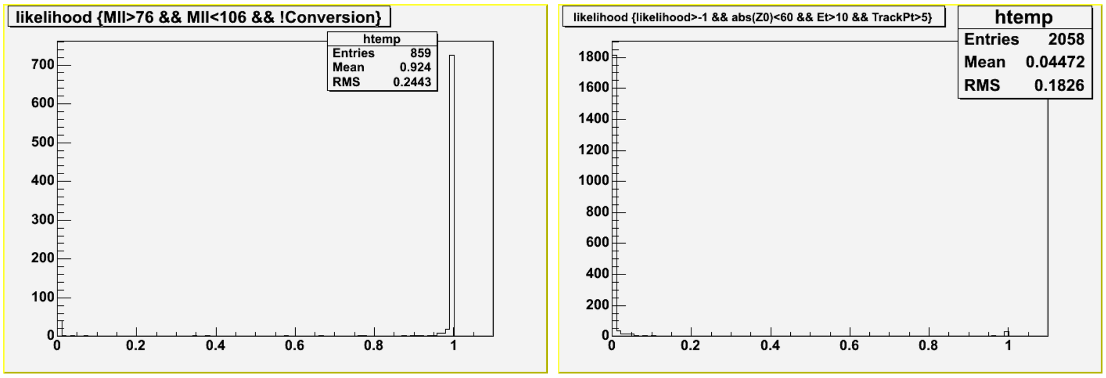

Figure 1: Likelihood distribution for signal probes (left) and fakeable objects (right).

these probes are used to make the signal templates. In case there are both legs identified as TCE, they are both used for template creation.

Building of the templates for "fakes" is done the following way. We select candidates from jet data (JET20 dataset - gjt1bk) where there is one identified jet and another fakeable abject ("CEM Fakeable" object,see definition in Tab. 3). We require that the combination of jet and fakeable object fall out of Z mass peak. We also make sure that fakeable electron is not in leading P_T jet in order to remove trigger bias.

Since we obtained our templates using data samples, our templates contain background events. In case of signal, this means "fake" electrons, in case of template for "fakes", this means real electrons. Therefore we perform background subtraction to the templates. The background subtraction is done the following way:

- for signal: We plot the distribution of likelihood variable for the probes. As can be seen in Fig. 1, the histogram have very sharp peak at 1.0 while having small bump at 0.0 (for the background case, this is opposite). We normalize the likelihood distribution for the "fakes" in such way that it has the same value in the first bin as the value in the 1st bin of signal likelihood distribution. By obtaining the integral over whole range (0.0,1.0), we get estimate of number of "fake" electrons in signal templates. This turns out to be small (3%). We then subtract such fraction of background templates from signal templates.

- for fakes: we estimate expected contribution of "signal" events (real electrons) in background templates using $W \to \ell\nu$ and$Z \to ee$ MC samples. This turns out to be event smaller effect (1%), but we anyway subtract the signal templates (appropriately scaled to 1%) from background templates.

The signal and background templates for all used electron ID variables are shown in Fig. **??**. Just for comparison, there are shown distributions of variables for data and MC ($Z \to ee$) in signal case and JET20 and JET100 samples in case of background templates. For signal, the data and MC distributions agree quite well for most of the variables. For background, JET20 and JET100 do not agree very well which is given by the fact that some of the variables are E_T dependent and the E_T spectrum of these two datasets is quite different. Since JET20 E_T distribution is more close to what we expect for our signal sample, we use templates obtained from JET20 sample.

2.1.3 Likelihood based electron (LBE)

We define a new central electron category – Likelihood based electron (LBE) which we will use instead of TCE electrons. We first apply basic identification and kinematic criteria on electron candidates and we make the cut on the likelihood value at the end. All the requirements used for LBEs are listed below:

- have CEM fiducial track
- $Z_0(track) < 60$ cm
- electron candidate is not a conversion
- $E_{HAD}/E_{EM} < 0.125$ in order to satisfy trigger requirement
- $CalIso < 0.3$ poor cut on calorimeter isolation to satisfy requirement on fakeable objects used in template building procedure
- $P_T(track) > 10$ GeV ($P_T(track) > 5$ GeV if $E_T < 20$ GeV)
- $\mathcal{L} > \mathcal{L}_{cut}$ - value of likelihood must be greater than a cut value, which we set for now to be $\mathcal{L}_{cut} = 0.99$.

The value of likelihood cut was not optimized. It was chosen this way (according preliminary studies) in order to have about the same fake rate as TCE. We will see later in 2.4 that this is really the case.

One assumption which we use for LBE is that it has the same trigger efficiency as TCE. We quickly checked this assumption by selecting $e - \mu$ events from our $Base0Jets$ region where we require that the μ fires a trigger. By checking how often TCE and LBE pass the trigger requirement, we obtained the following trigger efficiency for TCE ($78/83 = 0.94$) and for LBE ($84/88 = 0.95$). Within our limited statistics, we conclude that the trigger efficiency is the same for LBE and TCE. However, for the future we plan to make more detailed study.

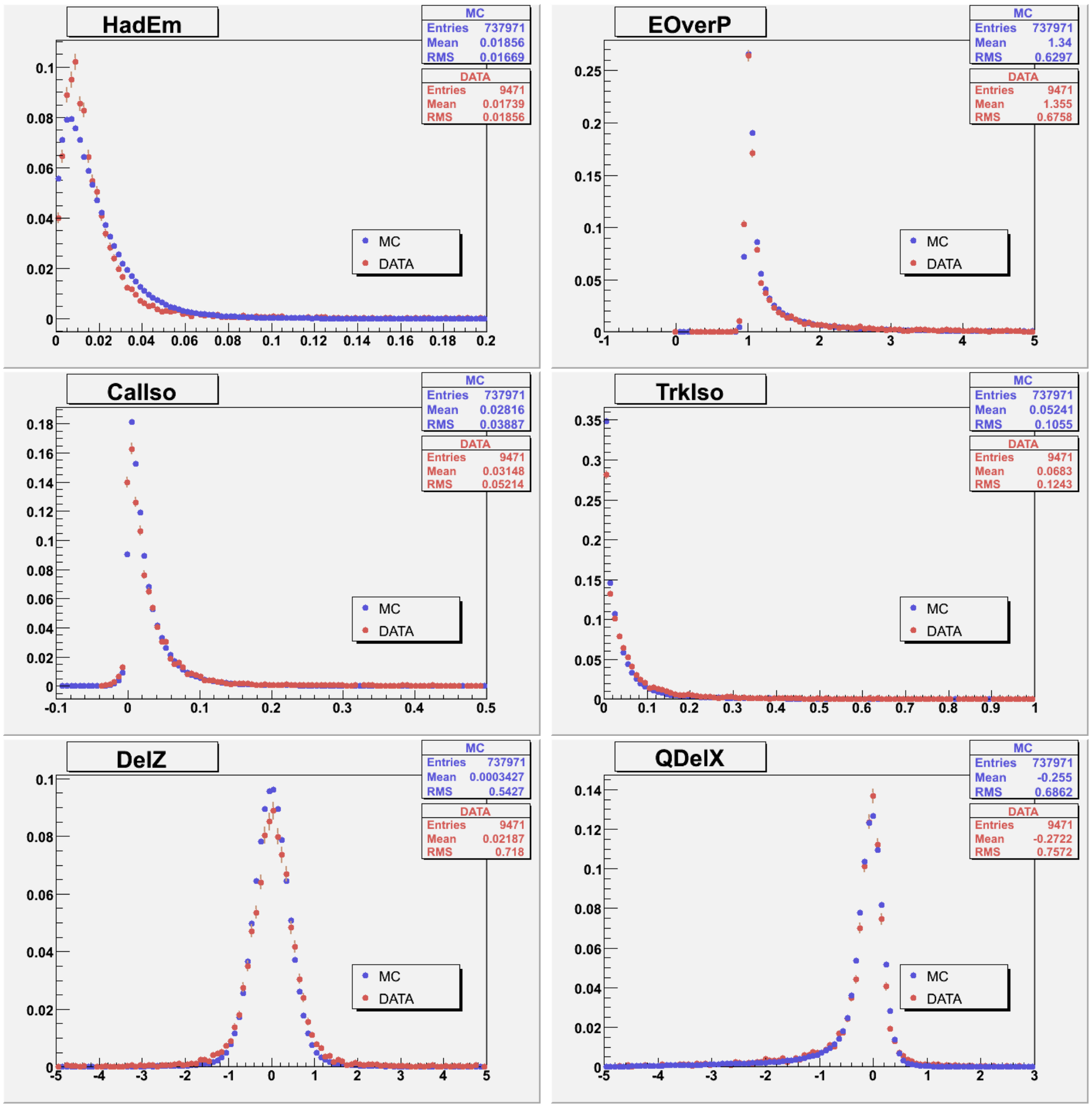

Figure 2: Signal templates for the likelihood method.

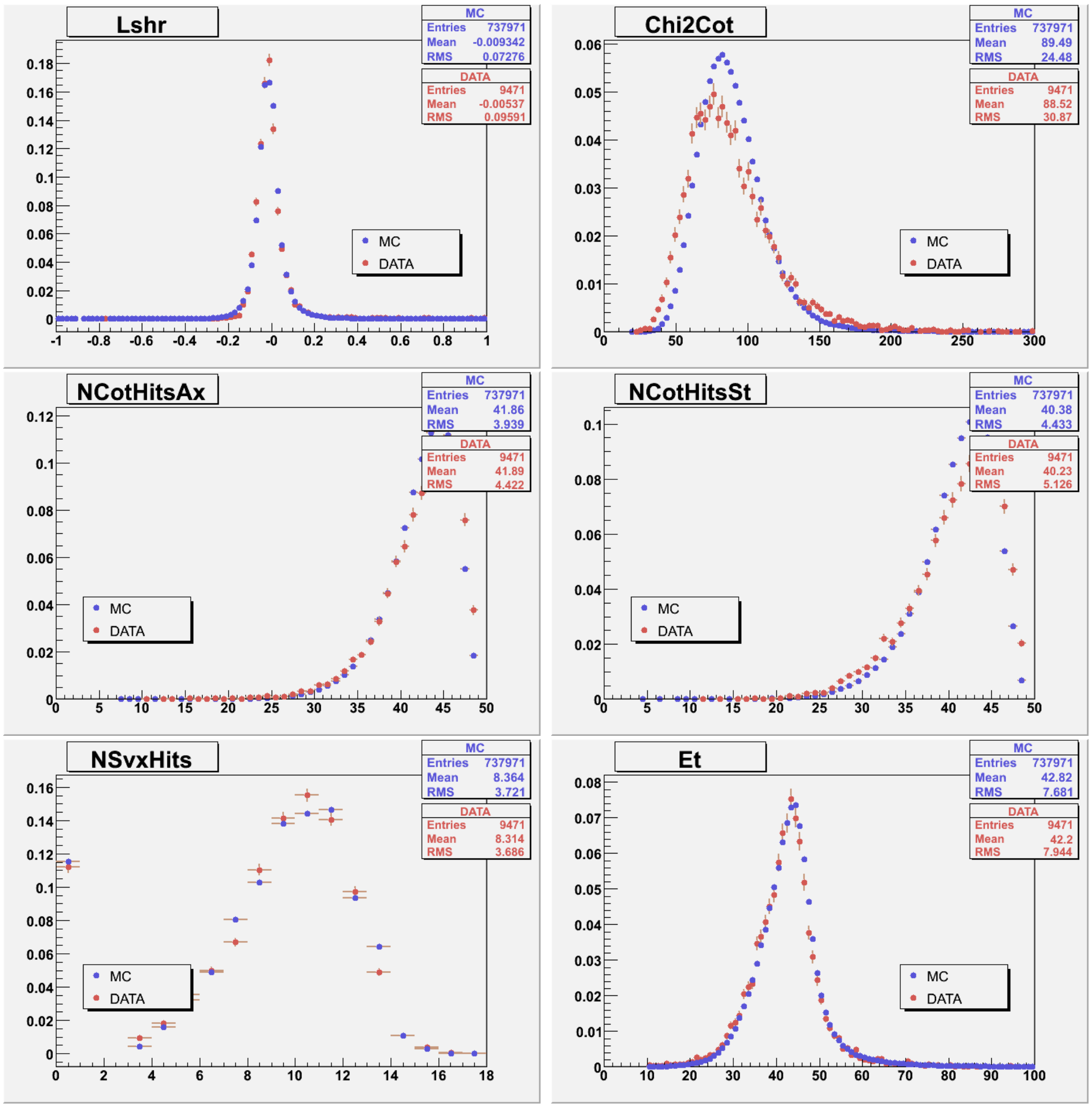

Figure 3: Signal templates for the likelihood method.

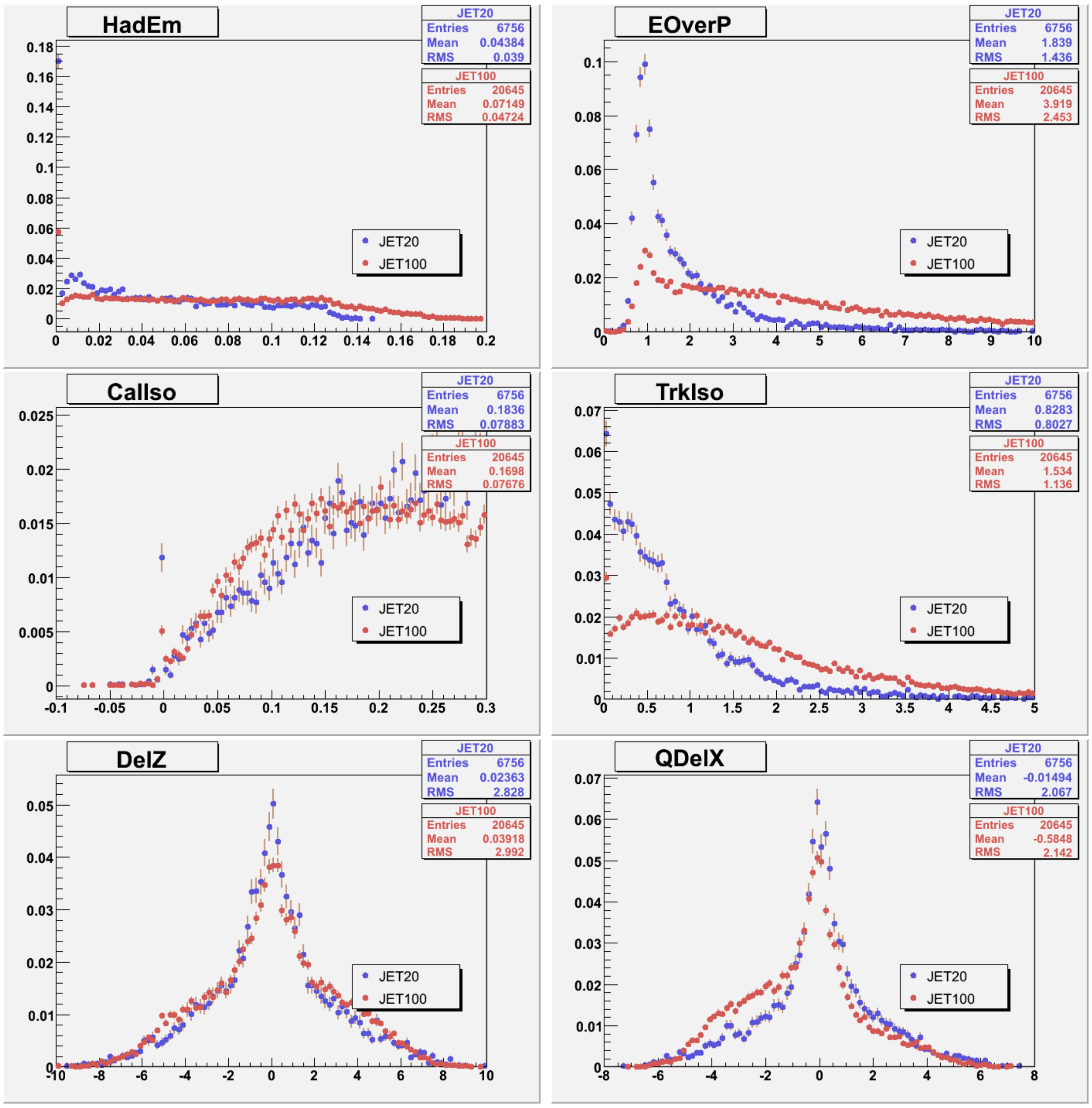

Figure 4: Background templates for the likelihood method.

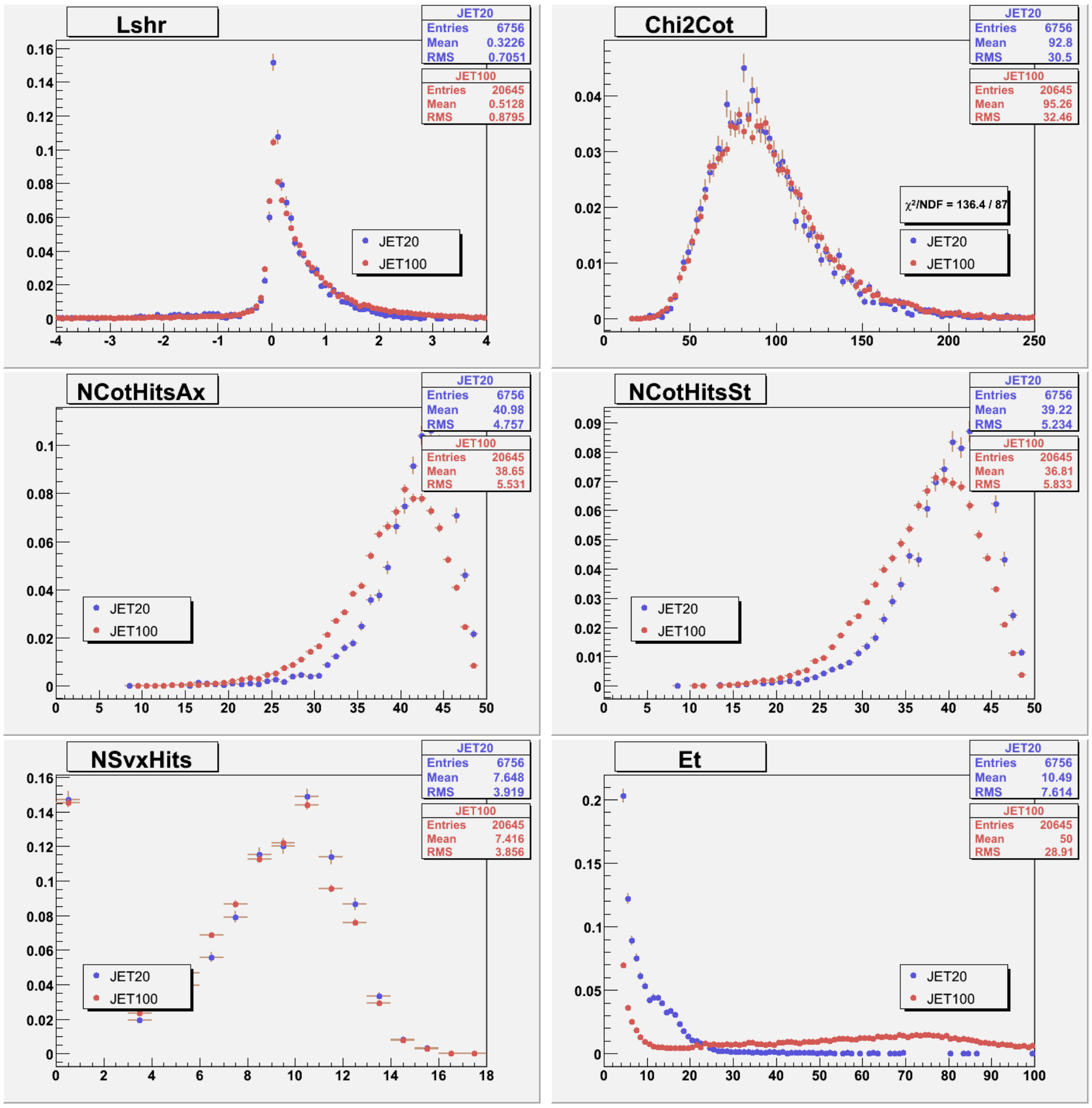

Figure 5: Background templates for the likelihood method.

2.2 Trigger Efficiencies

We define trigger categories as the identified muons that could have triggered the online event selection. Given the trigger paths used in this analysis, the following categories are considered as triggerable objects: CMUP, CMU, CMP, CMX, CMXMsKs. CMU will not be considered in the following since the trigger path associated with CMU has a bug, as pointed out in the previous section. We require these muons to have $p_T > 20$ GeV in order to be defined as triggerable objects, since trigger requirements usually apply a $p_T > 18$ GeV online cut to the XFT tracks.

To calculate trigger efficiencies for these muons, we select Z candidates in the $66 < m(ll) < 106$ GeV dilepton invariant mass window and use the *tag & probe* method. The basic idea is to consider all the events in which one muon is fiducial to a part of the detector and had triggered the event, and compare the cases in which the other muon let the trigger fire or not, dividing the calculation by the fiduciality of this second muon.

We divide the calculation for 2D and 3D triggers, based on the usage or not of the XFT 3D matching functionality (available after the trigger upgrade described in [3]) in the particular trigger path. Trigger efficiencies for 2D triggers are trivial, and below we list the formulas used in the calculations of CMUP 2D trigger paths:

$$\epsilon_{CMUP-2D} = \frac{\#(CMUP-2D \quad \text{AND} \quad CMX-2D)}{\#CMX-2D} \tag{2}$$

To calculate the efficiencies of 3D triggers we use two different methods. The first is to calculate it relative to the corresponding 2D trigger path, evaluating in this way just the efficiency of the 3D part of the requirements. The second method is analogous to the 2D method and evaluates directly the entire efficiency.

$$\epsilon^{\star}_{CMUP-3D}(I) = \frac{\#(CMX-2D \quad \text{AND} \quad CMUP-2D \quad \text{AND} \quad CMUP-3D)}{\#(CMX-2D \quad \text{AND} \quad CMUP-2D)} \tag{3}$$

$$\epsilon_{CMUP-3D}(I) = \epsilon_{CMUP-2D} \cdot \epsilon^{\star}_{CMUP-3D}(I) \tag{4}$$

$$\epsilon_{CMUP-3D}(II) = \frac{\#(CMUP-3D \quad \text{AND} \quad CMX-3D)}{\#CMX-3D} \tag{5}$$

The two methods agree very well and we use the second one when available, since it's should give a slightly more accurate estimation. Results can be found divided by run period in Table 4; we summed over periods 14 to 23 since the behaviour is pretty homogenous. The drop of efficiency in period 18 for CMUP-3D is a known problem. We do not have a clear motivation for the drop of efficiency after period 14-17 for CMP phi-gap trigger paths, but we're confident of the correctness of our results. Numbers were also compared to Joint Physics ones, where available, and they agree well.

Livetime corrections are also applied and listed in Table 4 to account for different prescales of the trigger paths. Trigger efficiencies and livetimes are then applied to MC simulations on a per-event basis, in order to model online triggering effects on the simulation samples.

Run Period	P8	P9	P10	P11	P12	P13	P14	P15	P16	P17	P14-17
Trigger ϵ											
CMUP 2-D	0.906	0.910	0.920	0.911	0.915	0.918	0.908	0.921	0.906	0.921	0.917
CMUP 3-D (I)				0.858	0.839	0.835	0.881	0.882	0.860	0.875	0.875
CMUP 3-D (II)				0.863	0.838	0.838	0.888	0.885	0.852	0.878	0.876
CMX ARCH 2-D	0.941	0.948	0.978	0.970	0.936	0.935	0.915	0.950	0.947	0.940	0.942
CMX ARCH 3-D (I)		(0.927)	0.927	0.930	0.889	0.894	0.892	0.928	0.929	0.905	0.916
CMX ARCH 3-D (II)				0.931	0.894	0.880	0.895	0.928	0.926	0.912	0.916
CMX MS/KS 2-D		(0.849)	0.849	0.814	0.773	0.750	0.847	0.861	0.889	0.816	0.849
CMX MS/KS 3-D (I)			0.835	0.784	0.745	0.737	0.847	0.834	0.879	0.800	0.831
CMX MS/KS 3-D (II)				0.780	0.758	0.766	0.849	0.807	0.864	0.791	0.814
CMP PHI-GAP			(0.948)	0.948	0.891	0.924	0.889	0.764	0.774	0.845	0.803

LiveTimes	P8	P9	P10	P11	P12	P13	P14	P15	P16	P17	P14-17
CMUP 2-D	1.000	1.000	1.000	0.959	0.933	0.936	0.945	0.939	0.924	0.923	0.930
CMUP 3-D	1.000	1.000	1.000	1.000	1.000	1.000	1.000	1.000	1.000	1.000	1.000
CMX 2-D	1.000	0.963	0.958	0.913	0.885	0.899	0.941	0.900	0.845	0.845	0.871
CMX 3-D	1.000	0.965	0.988	0.971	0.952	0.950	0.951	0.961	0.989	1.000	0.981
CMP PG	0.000	0.000	0.558	0.669	0.840	0.885	0.968	0.977	0.954	0.946	0.959

Run Period	P18	P19	P14-19	P20	P21	P22	P23	P14-23
Trigger ϵ								
CMUP 2-D	0.924	0.907	0.917	0.916	0.902	0.905	0.912	0.913
CMUP 3-D (I)	0.736	0.861	0.826	0.867	0.851	0.857	0.869	0.842
CMUP 3-D (II)	0.744	0.862	0.828	0.871	0.853	0.852	0.868	0.843
CMX ARCH 2-D	0.956	0.927	0.944	0.921	0.954	0.967	0.956	0.948
CMX ARCH 3-D (I)	0.922	0.901	0.916	0.898	0.919	0.937	0.899	0.916
CMX ARCH 3-D (II)	0.900	0.876	0.901	0.883	0.896	0.923	0.885	0.899
CMX MS/KS 2-D	0.813	0.785	0.828	0.802	0.826	0.774	0.863	0.822
CMX MS/KS 3-D (I)	0.792	0.768	0.810	0.783	0.813	0.752	0.811	0.801
CMX MS/KS 3-D (II	0.777	0.774	0.794	0.753	0.787	0.775	0.808	0.787
CMP PHI-GAP	0.758	0.693	0.769	0.794	0.802	0.797	0.838	0.787

LiveTimes	P18	P19	P14-19	P20	P21	P22	P23	P14-23
CMUP 2-D	0.851	0.803	0.876	0.830	0.776	0.800	0.813	0.837
CMUP 3-D	1.000	1.000	1.000	1.000	1.000	1.000	1.000	1.000
CMX 2-D	0.768	0.719	0.802	0.750	0.667	0.701	0.711	0.750
CMX 3-D	1.000	1.000	0.992	1.000	1.000	1.000	1.000	0.996
CMP PG	0.929	0.819	0.920	0.876	0.813	0.800	0.811	0.871

Table 4: Trigger efficiencies and livetimes divided by run periods. **To be updated.**

Period	SF
0-9	1.001
10-13	0.945
14-23	0.866

Table 5: Scale Factor evaluated for muons pointing to the bottom 90° of the detector.

2.3 Lepton ID Scale Factors

To measure lepton ID scale factors, we measure the lepton efficiencies in both data and MC simulation and divide the two result to apply a per-event SF to our MC simulations. We again use the *tag & probe* method, selecting Z candidates in the $66 < m(ll) < 106$ GeV dilepton invariant mass window, as described in the CDF Note 8538 [2]. As explained in detail in this reference, we use probe objects for which we assume MC simulation well describes the efficiency, and calculate the only the efficiency on top of these requirements. Generic probes are defined for Central and Forward muons and then used with the fiduciality requirement to define the actual probe to be used in the efficiency calculation. Background subtraction is also performed using data from the Z-mass sidebands.

Results are shown in Tables 6-19, grouped by run period ranges as defined in the official webpage [4]. The only exception is what we call period 0k, which groups also data acquired in the 0m dataset, since these data are pretty homogenous. Efficiencies, as well as scale factors, are calculated for both track isolated (which are the ones actually used in the analysis) and non-track isolated leptons. Track isolation (< 0.1) is required in a cone of 0.4 around the leptons. We also calculate the electron efficiencies that will be used in the analysis with exactly the same method described in [2]. As also in this reference, we calculate efficiencies for stubless categories as the difference of the one removing vetos and the veto efficiency, in order to properly account for stubbed muon SFs using the same formulas described in that note. For CMIOPES and BMU categories, we apply the PES tracking efficiency scale factor to account for forward tracking reconstruction scale factors between data and MC. This scale factor is evaluated using electrons, since that is the only way to measure it in data, but should also model well what happens for muons.

We observe an excess of central tracks in MC reconstructed near the bottom 90° of the COT. Figure 6 shows the ϕ distribution for central tracks with $\rho_{COT} > 140$ cm in Z events selected with a CMUP tag leg and requiring $86 < m(ll) < 106$ GeV for different run periods (p0-p9, p10-p13, and p14-p23). Data and Monte Carlo distributions are normalized in the region $0° < \phi < 225°$ and $315° < \phi < 360°$. Since the effect is clearly dependent on the run period, we apply a scale factor to all central muon types which point in the $225° < \phi < 315°$ region depending on the run period as in Table 5.

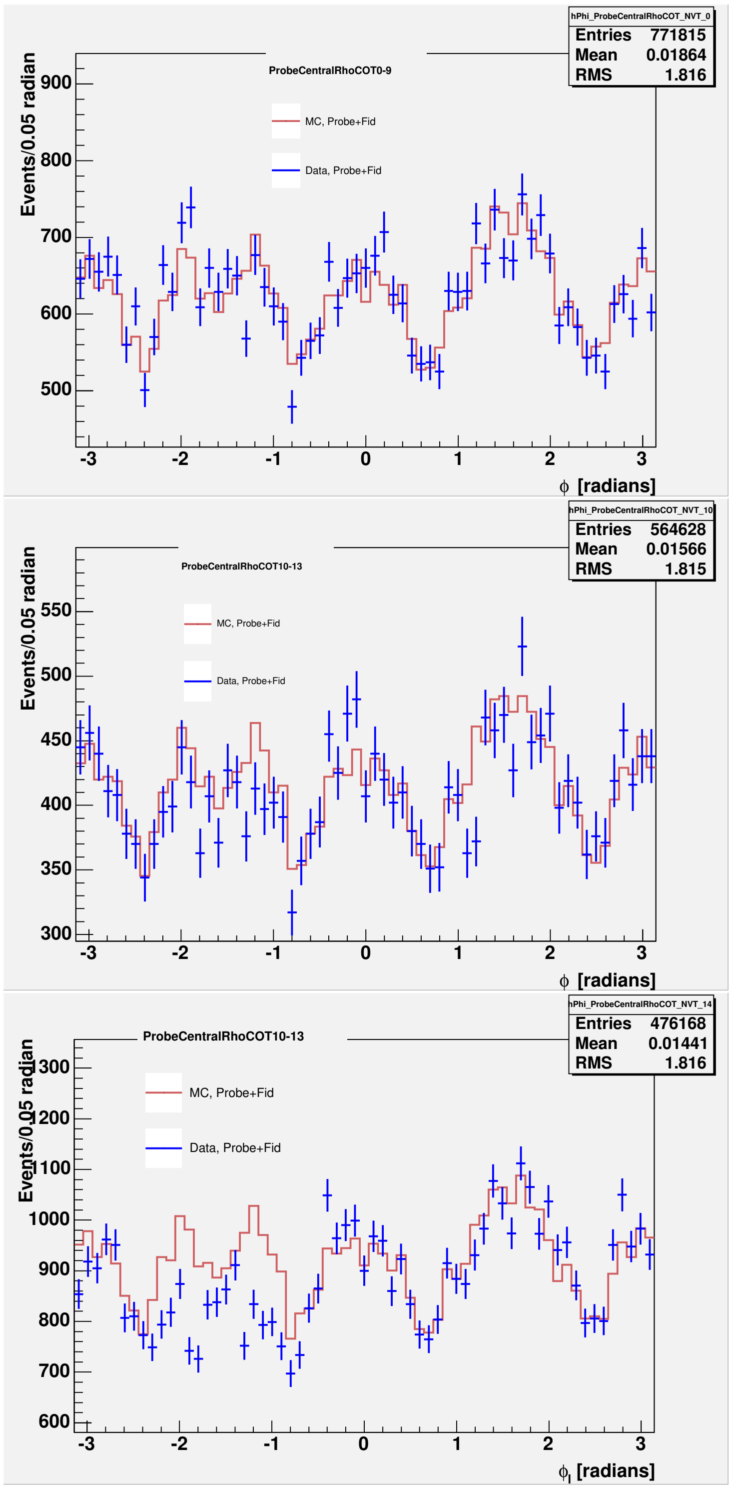

Figure 6: ϕ distribution for central tracks in Z events selected with a CMUP tag. Data periods 0 to 9 shown on top, periods 10 to 13 in the middle, and periods 14 to 23 on the bottom.

Run Range: 0d

	data	MC	Scale Fac
CMUP	0.878 ± 0.011	0.903 ± 0.001	0.972 ± 0.012
CMU	0.000 ± 1.000	0.000 ± 1.000	0.000 ± 1.000
CMP	0.000 ± 1.000	0.000 ± 1.000	0.000 ± 1.000
CMX	0.947 ± 0.014	0.922 ± 0.003	1.027 ± 0.016
CMXMsKs	0.000 ± 1.000	0.000 ± 1.000	0.000 ± 1.000
BMU	0.829 ± 0.024	0.733 ± 0.004	1.131 ± 0.033
CMIOCES	0.367 ± 0.006	0.350 ± 0.002	1.049 ± 0.019
CMIOPES	0.689 ± 0.012	0.689 ± 0.002	1.000 ± 0.018
CrkTrk μ	0.733 ± 0.011	0.765 ± 0.002	0.958 ± 0.015
CMUP Trk Iso	0.869 ± 0.011	0.896 ± 0.001	0.970 ± 0.012
CMU Trk Iso	0.000 ± 1.000	0.000 ± 1.000	0.000 ± 1.000
CMP Trk Iso	0.000 ± 1.000	0.000 ± 1.000	0.000 ± 1.000
CMX Trk Iso	0.927 ± 0.014	0.912 ± 0.003	1.016 ± 0.016
CMXMsKs Trk Iso	0.000 ± 1.000	0.000 ± 1.000	0.000 ± 1.000
BMU Trk Iso	0.818 ± 0.024	0.725 ± 0.004	1.128 ± 0.034
CMIOCES Trk Iso	0.364 ± 0.006	0.347 ± 0.002	1.049 ± 0.019
CMIOPES Trk Iso	0.668 ± 0.012	0.683 ± 0.002	0.978 ± 0.018
CrkTrk μ Trk Iso	0.719 ± 0.011	0.756 ± 0.002	0.951 ± 0.015

Table 6: Muon efficiencies for dataset 0d (period 0) with and without track isolation cut. **To be updated.**

Run Range: 0h

	data	MC	Scale Fac
CMUP	0.845 ± 0.009	0.903 ± 0.001	0.936 ± 0.010
CMU	0.000 ± 0.500	0.000 ± 0.500	0.000 ± 0.500
CMP	0.000 ± 0.500	0.000 ± 0.500	0.000 ± 0.500
CMX	0.937 ± 0.015	0.920 ± 0.002	1.020 ± 0.017
CMXMsKs	0.000 ± 0.500	0.000 ± 0.500	0.000 ± 0.500
BMU	0.796 ± 0.018	0.720 ± 0.003	1.106 ± 0.025
CMIOCES	0.364 ± 0.005	0.343 ± 0.001	1.060 ± 0.015
CMIOPES	0.609 ± 0.012	0.606 ± 0.002	1.006 ± 0.020
CrkTrk μ	0.777 ± 0.009	0.795 ± 0.002	0.978 ± 0.012
CMUP Trk Iso	0.832 ± 0.008	0.895 ± 0.001	0.930 ± 0.009
CMU Trk Iso	0.000 ± 0.500	0.000 ± 0.500	0.000 ± 0.500
CMP Trk Iso	0.000 ± 0.500	0.000 ± 0.500	0.000 ± 0.500
CMX Trk Iso	0.906 ± 0.016	0.908 ± 0.002	0.998 ± 0.018
CMXMsKs Trk Iso	0.000 ± 0.500	0.000 ± 0.500	0.000 ± 0.500
BMU Trk Iso	0.767 ± 0.018	0.714 ± 0.003	1.074 ± 0.026
CMIOCES Trk Iso	0.354 ± 0.005	0.340 ± 0.001	1.043 ± 0.015
CMIOPES Trk Iso	0.589 ± 0.012	0.601 ± 0.002	0.980 ± 0.020
CrkTrk μ Trk Iso	0.760 ± 0.009	0.786 ± 0.002	0.967 ± 0.012

Table 7: Muon efficiencies for dataset 0h (periods 1-4) with and without track isolation cut.

Run Range: 0i1

	data	MC	Scale Fac
CMUP	0.835 ± 0.011	0.902 ± 0.001	0.927 ± 0.013
CMU	0.000 ± 0.577	0.000 ± 0.577	0.000 ± 0.577
CMP	0.000 ± 0.577	0.000 ± 0.577	0.000 ± 0.577
CMX	0.943 ± 0.018	0.919 ± 0.003	1.026 ± 0.019
CMXMsKs	0.000 ± 0.577	0.000 ± 0.577	0.000 ± 0.577
BMU	0.779 ± 0.023	0.721 ± 0.004	1.080 ± 0.032
CMIOCES	0.370 ± 0.006	0.341 ± 0.002	1.085 ± 0.018
CMIOPES	0.619 ± 0.015	0.599 ± 0.003	1.032 ± 0.025
CrkTrk μ	0.774 ± 0.012	0.793 ± 0.002	0.976 ± 0.015
CMUP Trk Iso	0.826 ± 0.011	0.892 ± 0.001	0.926 ± 0.013
CMU Trk Iso	0.000 ± 0.577	0.000 ± 0.577	0.000 ± 0.577
CMP Trk Iso	0.000 ± 0.577	0.000 ± 0.577	0.000 ± 0.577
CMX Trk Iso	0.903 ± 0.018	0.905 ± 0.003	0.998 ± 0.020
CMXMsKs Trk Iso	0.000 ± 0.577	0.000 ± 0.577	0.000 ± 0.577
BMU Trk Iso	0.756 ± 0.023	0.715 ± 0.004	1.057 ± 0.032
CMIOCES Trk Iso	0.363 ± 0.006	0.336 ± 0.002	1.082 ± 0.017
CMIOPES Trk Iso	0.602 ± 0.015	0.594 ± 0.003	1.012 ± 0.025
CrkTrk μ Trk Iso	0.758 ± 0.012	0.783 ± 0.002	0.969 ± 0.015

Table 8: Muon efficiencies for dataset 0i1 (periods 5-7) with and without track isolation cut.

Run Range: 0i2

	data	MC	Scale Fac
CMUP	0.855 ± 0.008	0.897 ± 0.001	0.952 ± 0.009
CMU	0.000 ± 0.577	0.000 ± 0.577	0.000 ± 0.577
CMP	0.881 ± 0.028	0.919 ± 0.003	0.958 ± 0.031
CMX	0.920 ± 0.013	0.914 ± 0.002	1.007 ± 0.014
CMXMsKs	0.834 ± 0.031	0.907 ± 0.004	0.920 ± 0.035
BMU	0.798 ± 0.015	0.725 ± 0.003	1.099 ± 0.021
CMIOCES	0.332 ± 0.004	0.305 ± 0.001	1.086 ± 0.014
CMIOPES	0.583 ± 0.011	0.598 ± 0.002	0.977 ± 0.018
CrkTrk μ	0.708 ± 0.009	0.722 ± 0.001	0.973 ± 0.012
CMUP Trk Iso	0.835 ± 0.008	0.887 ± 0.001	0.941 ± 0.009
CMU Trk Iso	0.000 ± 0.577	0.000 ± 0.577	0.000 ± 0.577
CMP Trk Iso	0.845 ± 0.028	0.907 ± 0.003	0.931 ± 0.031
CMX Trk Iso	0.907 ± 0.013	0.900 ± 0.002	1.008 ± 0.014
CMXMsKs Trk Iso	0.787 ± 0.031	0.895 ± 0.004	0.880 ± 0.034
BMU Trk Iso	0.758 ± 0.016	0.719 ± 0.003	1.054 ± 0.022
CMIOCES Trk Iso	0.323 ± 0.004	0.301 ± 0.001	1.069 ± 0.014
CMIOPES Trk Iso	0.558 ± 0.011	0.592 ± 0.002	0.944 ± 0.018
CrkTrk μ Trk Iso	0.681 ± 0.008	0.711 ± 0.001	0.947 ± 0.012

Table 9: Muon efficiencies for dataset 0i2 (periods 8-10) with and without track isolation cut.

Run Range: 0j

	data	MC	Scale Fac
CMUP	0.826 ± 0.010	0.893 ± 0.001	0.924 ± 0.011
CMU	0.000 ± 0.707	0.000 ± 0.707	0.000 ± 0.707
CMP	0.819 ± 0.019	0.916 ± 0.002	0.894 ± 0.021
CMX	0.896 ± 0.016	0.915 ± 0.002	0.979 ± 0.018
CMXMsKs	0.853 ± 0.027	0.911 ± 0.003	0.937 ± 0.030
BMU	0.777 ± 0.020	0.727 ± 0.003	1.069 ± 0.028
CMIOCES	0.303 ± 0.004	0.252 ± 0.002	1.204 ± 0.019
CMIOPES	0.559 ± 0.013	0.586 ± 0.002	0.954 ± 0.023
CrkTrk μ	0.577 ± 0.012	0.583 ± 0.002	0.990 ± 0.020
CMUP Trk Iso	0.796 ± 0.010	0.882 ± 0.001	0.903 ± 0.011
CMU Trk Iso	0.000 ± 0.707	0.000 ± 0.707	0.000 ± 0.707
CMP Trk Iso	0.795 ± 0.019	0.903 ± 0.002	0.881 ± 0.021
CMX Trk Iso	0.866 ± 0.016	0.895 ± 0.002	0.967 ± 0.018
CMXMsKs Trk Iso	0.842 ± 0.026	0.896 ± 0.003	0.940 ± 0.030
BMU Trk Iso	0.748 ± 0.020	0.720 ± 0.004	1.038 ± 0.028
CMIOCES Trk Iso	0.286 ± 0.005	0.248 ± 0.002	1.152 ± 0.021
CMIOPES Trk Iso	0.529 ± 0.013	0.579 ± 0.002	0.914 ± 0.024
CrkTrk μ Trk Iso	0.549 ± 0.011	0.572 ± 0.002	0.961 ± 0.020

Table 10: Muon efficiencies for dataset 0j (period 11-12) with and without track isolation cut.

Run Range: 0j13

	data	MC	Scale Fac
CMUP	0.839 ± 0.010	0.895 ± 0.001	0.937 ± 0.011
CMU	0.000 ± 1.000	0.000 ± 1.000	0.000 ± 1.000
CMP	0.823 ± 0.019	0.913 ± 0.003	0.901 ± 0.021
CMX	0.897 ± 0.018	0.913 ± 0.003	0.982 ± 0.020
CMXMsKs	0.818 ± 0.030	0.916 ± 0.003	0.893 ± 0.033
BMU	0.803 ± 0.026	0.696 ± 0.004	1.154 ± 0.038
CMIOCES	0.300 ± 0.005	0.253 ± 0.002	1.186 ± 0.022
CMIOPES	0.522 ± 0.019	0.521 ± 0.003	1.002 ± 0.037
CrkTrk μ	0.560 ± 0.012	0.588 ± 0.002	0.952 ± 0.021
CMUP Trk Iso	0.814 ± 0.011	0.884 ± 0.001	0.921 ± 0.012
CMU Trk Iso	0.000 ± 1.000	0.000 ± 1.000	0.000 ± 1.000
CMP Trk Iso	0.805 ± 0.019	0.901 ± 0.003	0.893 ± 0.021
CMX Trk Iso	0.883 ± 0.018	0.898 ± 0.003	0.983 ± 0.020
CMXMsKs Trk Iso	0.800 ± 0.029	0.904 ± 0.003	0.885 ± 0.032
BMU Trk Iso	0.780 ± 0.025	0.692 ± 0.004	1.127 ± 0.037
CMIOCES Trk Iso	0.290 ± 0.005	0.249 ± 0.002	1.165 ± 0.022
CMIOPES Trk Iso	0.497 ± 0.018	0.517 ± 0.003	0.961 ± 0.035
CrkTrk μ Trk Iso	0.542 ± 0.012	0.578 ± 0.002	0.938 ± 0.021

Table 11: Muon efficiencies for dataset 0j13 (period 13) with and without track isolation cut.

Run Range: 0k

	data	MC	Scale Fac
CMUP	0.785 ± 0.004	0.889 ± 0.001	0.883 ± 0.005
CMU	0.000 ± 1.000	0.000 ± 1.000	0.000 ± 1.000
CMP	0.807 ± 0.008	0.911 ± 0.002	0.886 ± 0.009
CMX	0.891 ± 0.007	0.906 ± 0.002	0.984 ± 0.008
CMXMsKs	0.826 ± 0.011	0.907 ± 0.002	0.911 ± 0.012
BMU	0.783 ± 0.010	0.705 ± 0.003	1.110 ± 0.014
CMIOCES	0.298 ± 0.003	0.252 ± 0.001	1.184 ± 0.013
CMIOPES	0.568 ± 0.006	0.582 ± 0.002	0.975 ± 0.011
CrkTrk μ	0.564 ± 0.004	0.589 ± 0.001	0.957 ± 0.008
CMUP Trk Iso	0.763 ± 0.004	0.875 ± 0.001	0.872 ± 0.005
CMU Trk Iso	0.000 ± 1.000	0.000 ± 1.000	0.000 ± 1.000
CMP Trk Iso	0.784 ± 0.009	0.897 ± 0.002	0.874 ± 0.010
CMX Trk Iso	0.860 ± 0.007	0.887 ± 0.002	0.970 ± 0.008
CMXMsKs Trk Iso	0.795 ± 0.011	0.891 ± 0.002	0.892 ± 0.012
BMU Trk Iso	0.766 ± 0.010	0.696 ± 0.003	1.101 ± 0.015
CMIOCES Trk Iso	0.288 ± 0.003	0.248 ± 0.001	1.162 ± 0.013
CMIOPES Trk Iso	0.560 ± 0.006	0.574 ± 0.002	0.975 ± 0.011
CrkTrk μ Trk Iso	0.545 ± 0.004	0.577 ± 0.001	0.945 ± 0.008

Table 12: Muon efficiencies for dataset 0k (periods 14-23) with and without track isolation cut.

Run Range: 0d

	data	MC	Scale Fac
LBE ($L > 0.99$)	0.882 ± 0.003	0.869 ± 0.001	1.015 ± 0.004
TCE	0.877 ± 0.005	0.861 ± 0.002	1.019 ± 0.006
LCE	0.041 ± 0.003	0.045 ± 0.001	0.911 ± 0.078
PHXTrk	0.864 ± 0.004	0.865 ± 0.001	0.999 ± 0.005
PHXPEM	0.850 ± 0.005	0.894 ± 0.001	0.951 ± 0.006
PEM	0.808 ± 0.009	0.857 ± 0.001	0.943 ± 0.011
CrkTrk e	0.791 ± 0.013	0.834 ± 0.002	0.948 ± 0.016
PESTrk	0.371 ± 0.005	0.404 ± 0.001	0.918 ± 0.013
LBE ($L > 0.99$) Trk Iso	0.847 ± 0.004	0.842 ± 0.001	1.006 ± 0.005
TCE Trk Iso	0.821 ± 0.005	0.813 ± 0.002	1.010 ± 0.006
LCE Trk Iso	0.031 ± 0.002	0.036 ± 0.001	0.861 ± 0.063
CrkTrk e Trk Iso	0.766 ± 0.012	0.821 ± 0.002	0.933 ± 0.015
PESTrk Trk Iso	0.371 ± 0.005	0.404 ± 0.001	0.918 ± 0.013
PHXTrk Trk Iso	0.864 ± 0.004	0.865 ± 0.001	0.999 ± 0.005
PHXPEM Trk Iso	0.850 ± 0.005	0.894 ± 0.001	0.951 ± 0.006
PEM Trk Iso	0.808 ± 0.009	0.857 ± 0.001	0.943 ± 0.011

Table 13: Electron efficiencies for dataset 0d (period 0) with and without track isolation cut. No track isolation cut is applied to the PHX category.

Run Range: 0h

	data	MC	Scale Fac
LBE ($L > 0.99$)	0.871 ± 0.003	0.870 ± 0.001	1.001 ± 0.004
TCE	0.869 ± 0.004	0.862 ± 0.001	1.008 ± 0.004
LCE	0.039 ± 0.002	0.042 ± 0.001	0.934 ± 0.041
PHXTrk	0.881 ± 0.004	0.874 ± 0.001	1.008 ± 0.004
PHXPEM	0.840 ± 0.004	0.882 ± 0.001	0.953 ± 0.005
PEM	0.762 ± 0.008	0.832 ± 0.001	0.916 ± 0.010
CrkTrk e	0.850 ± 0.013	0.864 ± 0.002	0.983 ± 0.016
PESTrk	0.361 ± 0.005	0.379 ± 0.001	0.952 ± 0.013
LBE ($L > 0.99$) Trk Iso	0.831 ± 0.003	0.840 ± 0.001	0.990 ± 0.004
TCE Trk Iso	0.806 ± 0.004	0.811 ± 0.001	0.994 ± 0.005
LCE Trk Iso	0.029 ± 0.002	0.033 ± 0.001	0.864 ± 0.049
CrkTrk e Trk Iso	0.812 ± 0.011	0.847 ± 0.002	0.958 ± 0.014
PESTrk Trk Iso	0.361 ± 0.005	0.379 ± 0.001	0.952 ± 0.013
PHXTrk Trk Iso	0.881 ± 0.004	0.874 ± 0.001	1.008 ± 0.004
PHXPEM Trk Iso	0.840 ± 0.004	0.882 ± 0.001	0.953 ± 0.005
PEM Trk Iso	0.762 ± 0.008	0.832 ± 0.001	0.916 ± 0.010

Table 14: Electron efficiencies for dataset 0h (periods 1-4) with and without track isolation cut. No track isolation cut is applied to the PHX category.

Run Range: 0i1

	data	MC	Scale Fac
LBE ($L > 0.99$)	0.861 ± 0.004	0.866 ± 0.001	0.994 ± 0.005
TCE	0.861 ± 0.005	0.856 ± 0.001	1.006 ± 0.006
LCE	0.043 ± 0.002	0.043 ± 0.001	0.986 ± 0.052
PHXTrk	0.883 ± 0.004	0.869 ± 0.001	1.016 ± 0.005
PHXPEM	0.825 ± 0.005	0.876 ± 0.001	0.943 ± 0.006
PEM	0.743 ± 0.012	0.813 ± 0.002	0.913 ± 0.015
CrkTrk e	0.817 ± 0.016	0.858 ± 0.002	0.952 ± 0.019
PESTrk	0.362 ± 0.006	0.374 ± 0.001	0.967 ± 0.016
LBE ($L > 0.99$) Trk Iso	0.819 ± 0.004	0.834 ± 0.001	0.982 ± 0.005
TCE Trk Iso	0.794 ± 0.005	0.804 ± 0.001	0.987 ± 0.007
LCE Trk Iso	0.028 ± 0.002	0.033 ± 0.001	0.853 ± 0.080
CrkTrk e Trk Iso	0.784 ± 0.014	0.840 ± 0.003	0.932 ± 0.017
PESTrk Trk Iso	0.362 ± 0.006	0.374 ± 0.001	0.967 ± 0.016
PHXTrk Trk Iso	0.883 ± 0.004	0.869 ± 0.001	1.016 ± 0.005
PHXPEM Trk Iso	0.825 ± 0.005	0.876 ± 0.001	0.943 ± 0.006
PEM Trk Iso	0.743 ± 0.012	0.813 ± 0.002	0.913 ± 0.015

Table 15: Electron efficiencies for dataset 0i1 (periods 5-7) with and without track isolation cut. No track isolation cut is applied to the PHX category.

Run Range: 0i2

	data	MC	Scale Fac
LBE ($L > 0.99$)	0.852 ± 0.003	0.863 ± 0.001	0.987 ± 0.003
TCE	0.858 ± 0.003	0.857 ± 0.001	1.000 ± 0.004
LCE	0.042 ± 0.002	0.043 ± 0.001	0.974 ± 0.045
PHXTrk	0.876 ± 0.003	0.878 ± 0.001	0.998 ± 0.004
PHXPEM	0.812 ± 0.004	0.873 ± 0.001	0.931 ± 0.004
PEM	0.700 ± 0.007	0.799 ± 0.001	0.876 ± 0.009
CrkTrk e	0.812 ± 0.012	0.851 ± 0.001	0.952 ± 0.014
PESTrk	0.350 ± 0.004	0.370 ± 0.001	0.943 ± 0.011
LBE ($L > 0.99$) Trk Iso	0.802 ± 0.003	0.829 ± 0.001	0.967 ± 0.004
TCE Trk Iso	0.782 ± 0.004	0.803 ± 0.001	0.974 ± 0.005
LCE Trk Iso	0.028 ± 0.001	0.033 ± 0.001	0.845 ± 0.046
CrkTrk e Trk Iso	0.763 ± 0.010	0.836 ± 0.002	0.913 ± 0.013
PESTrk Trk Iso	0.350 ± 0.004	0.370 ± 0.001	0.943 ± 0.011
PHXTrk Trk Iso	0.876 ± 0.003	0.878 ± 0.001	0.998 ± 0.004
PHXPEM Trk Iso	0.812 ± 0.004	0.873 ± 0.001	0.931 ± 0.004
PEM Trk Iso	0.700 ± 0.007	0.799 ± 0.001	0.876 ± 0.009

Table 16: Electron efficiencies for dataset 0i2 (periods 8-10) with and without track isolation cut. No track isolation cut is applied to the PHX category.

Run Range: 0j

	data	MC	Scale Fac
LBE ($L > 0.99$)	0.838 ± 0.004	0.851 ± 0.001	0.986 ± 0.005
TCE	0.847 ± 0.004	0.851 ± 0.001	0.996 ± 0.005
LCE	0.046 ± 0.002	0.044 ± 0.001	1.051 ± 0.051
PHXTrk	0.875 ± 0.004	0.879 ± 0.001	0.995 ± 0.004
PHXPEM	0.803 ± 0.005	0.858 ± 0.001	0.937 ± 0.005
PEM	0.661 ± 0.009	0.759 ± 0.001	0.871 ± 0.012
CrkTrk e	0.848 ± 0.018	0.847 ± 0.002	1.002 ± 0.021
PESTrk	0.351 ± 0.005	0.362 ± 0.001	0.966 ± 0.015
LBE ($L > 0.99$) Trk Iso	0.782 ± 0.004	0.815 ± 0.001	0.961 ± 0.005
TCE Trk Iso	0.762 ± 0.005	0.792 ± 0.001	0.963 ± 0.006
LCE Trk Iso	0.030 ± 0.003	0.031 ± 0.001	0.951 ± 0.100
CrkTrk e Trk Iso	0.789 ± 0.014	0.827 ± 0.002	0.955 ± 0.017
PESTrk Trk Iso	0.351 ± 0.005	0.362 ± 0.001	0.966 ± 0.015
PHXTrk Trk Iso	0.875 ± 0.004	0.879 ± 0.001	0.995 ± 0.004
PHXPEM Trk Iso	0.803 ± 0.005	0.858 ± 0.001	0.937 ± 0.005
PEM Trk Iso	0.661 ± 0.009	0.759 ± 0.001	0.871 ± 0.012

Table 17: Electron efficiencies for dataset 0j (period 10-11) with and without track isolation cut. No track isolation cut is applied to the PHX category.

Run Range: 0j13

	data	MC	Scale Fac
LBE ($L > 0.99$)	0.849 ± 0.004	0.854 ± 0.001	0.994 ± 0.005
TCE	0.851 ± 0.005	0.855 ± 0.002	0.995 ± 0.006
LCE	0.047 ± 0.002	0.042 ± 0.001	1.119 ± 0.057
PHXTrk	0.855 ± 0.005	0.857 ± 0.001	0.998 ± 0.006
PHXPEM	0.806 ± 0.005	0.863 ± 0.001	0.934 ± 0.006
PEM	0.693 ± 0.009	0.790 ± 0.002	0.877 ± 0.012
CrkTrk e	0.816 ± 0.017	0.846 ± 0.002	0.965 ± 0.020
PESTrk	0.261 ± 0.005	0.283 ± 0.001	0.922 ± 0.018
LBE ($L > 0.99$) Trk Iso	0.800 ± 0.005	0.822 ± 0.001	0.973 ± 0.006
TCE Trk Iso	0.777 ± 0.005	0.799 ± 0.002	0.972 ± 0.007
LCE Trk Iso	0.033 ± 0.002	0.031 ± 0.001	1.065 ± 0.083
CrkTrk e Trk Iso	0.769 ± 0.015	0.830 ± 0.002	0.927 ± 0.018
PESTrk Trk Iso	0.261 ± 0.005	0.283 ± 0.001	0.922 ± 0.018
PHXTrk Trk Iso	0.855 ± 0.005	0.857 ± 0.001	0.998 ± 0.006
PHXPEM Trk Iso	0.806 ± 0.005	0.863 ± 0.001	0.934 ± 0.006
PEM Trk Iso	0.693 ± 0.009	0.790 ± 0.002	0.877 ± 0.012

Table 18: Electron efficiencies for dataset 0j13 (period 13) with and without track isolation cut. No track isolation cut is applied to the PHX category.

Run Range: 0k

	data	MC	Scale Fac
LBE ($L > 0.99$)	0.830 ± 0.002	0.842 ± 0.001	0.985 ± 0.002
TCE	0.846 ± 0.002	0.847 ± 0.002	0.998 ± 0.003
LCE	0.045 ± 0.001	0.043 ± 0.001	1.041 ± 0.047
PHXTrk	0.886 ± 0.002	0.866 ± 0.001	1.023 ± 0.002
PHXPEM	0.772 ± 0.002	0.847 ± 0.001	0.911 ± 0.002
PEM	0.618 ± 0.004	0.733 ± 0.001	0.844 ± 0.006
CrkTrk e	0.803 ± 0.006	0.834 ± 0.001	0.963 ± 0.008
PESTrk	0.325 ± 0.002	0.352 ± 0.001	0.922 ± 0.007
LBE ($L > 0.99$) Trk Iso	0.776 ± 0.002	0.806 ± 0.001	0.963 ± 0.003
TCE Trk Iso	0.761 ± 0.002	0.786 ± 0.002	0.969 ± 0.003
LCE Trk Iso	0.028 ± 0.001	0.031 ± 0.001	0.897 ± 0.056
CrkTrk e Trk Iso	0.762 ± 0.006	0.814 ± 0.002	0.936 ± 0.008
PESTrk Trk Iso	0.325 ± 0.002	0.352 ± 0.001	0.922 ± 0.007
PHXTrk Trk Iso	0.886 ± 0.002	0.866 ± 0.001	1.023 ± 0.002
PHXPEM Trk Iso	0.772 ± 0.002	0.847 ± 0.001	0.911 ± 0.002
PEM Trk Iso	0.618 ± 0.004	0.733 ± 0.001	0.844 ± 0.006

Table 19: Electron efficiencies for dataset 0k (periods 14-23) with and without track isolation cut. No track isolation cut is applied to the PHX category.

2.4 Fake Rate Measurements

The lepton fake rates (*ie.* the probability for jets to fake a lepton) are measured in the jet samples and corrected for the small contribution of real isolated leptons from electroweak processes, as described in detail in [2]. This probability is measured as a function of the p_T of the object and results are used to derive a data-driven modeling of the W+jets background as described in Section 4.3.

As a brief reminder we repeat here the master formula for the calculation of such fake rates for a generic category i:

$$f_i = \frac{N_i(\text{IdentifiedLeptons}) - \sum_{j \in \text{EWK}} N_{ij}(\text{IdentifiedLeptons})}{N_i(\text{DenominatorObjects}) - \sum_{j \in \text{EWK}} N_{ij}(\text{DenominatorObjects})} \tag{6}$$

As with the scale factor calculation, the procedure relies on generic Central/Forward muons *Denominator Objects* which are then made category specific by applying the fiduciality requirements. The new categories were designed to fit in the existing denominator definitions, so there is no need to define any new generic categories. In order to perform the electroweak subtraction we normalize the MC simulation to the data effectively analyzed in each of the jet 20, 50, 70 and 100 triggered samples. Table 20 reports the effective (*ie.* corrected for trigger prescale factors) luminosities of such samples.

Sample	Effective Luminosity (nb)
Jet 20	$3154 \cdot 1.019$
Jet 50	$69756 \cdot 1.019$
Jet 70	$592747 \cdot 1.019$
Jet 100	$4738208 \cdot 1.019$

Table 20: Effective luminosity for each of the samples after trigger prescale correction for em_nosi goodrun list. There are used for the electroweak subtraction.

Results of the fake rate calculations are shown in Figures 7 to 8. Fake rate calculations are averaged over all the data available to maximize the statistics available. We assign a systematic based on the scatter of the results between the jet samples: an uncorrelated systematic, α, is added to each jet sample measurement until all the points are consistent within 1σ of the new mean, where the mean and the σ from the mean are calculated using $\sqrt{\text{stat err} + \alpha}$ as the uncertainty on each point. This result is shown as a light gray band in the figures, while the dark band is the result of the statistical error only.

The new stubbed categories (which, as shown in Table **??**, consist of some promoted stubless muons) have a sensible reduction of the fake rate; the effect is particularly noticeable for CMP muons compared to CrkTrks.

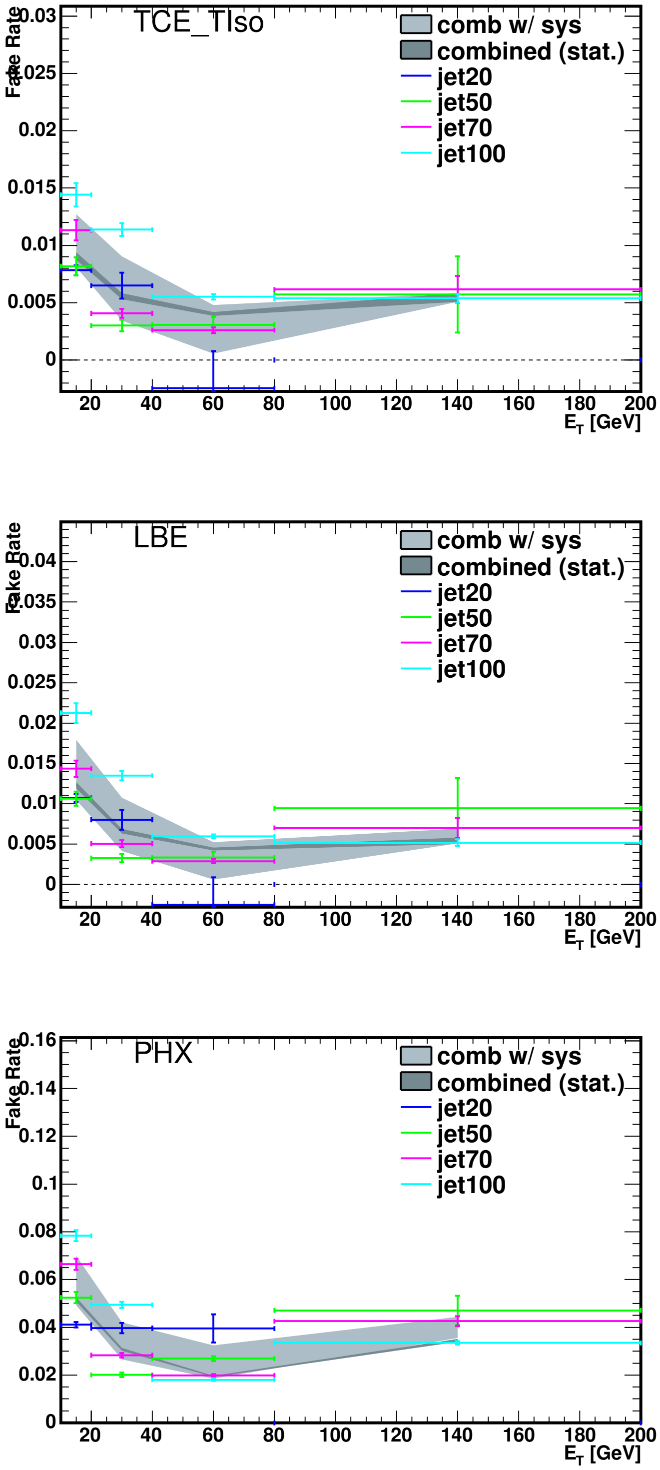

Figure 7: Fake rates for electrons. PHX and LBE have no track isolation requirement.

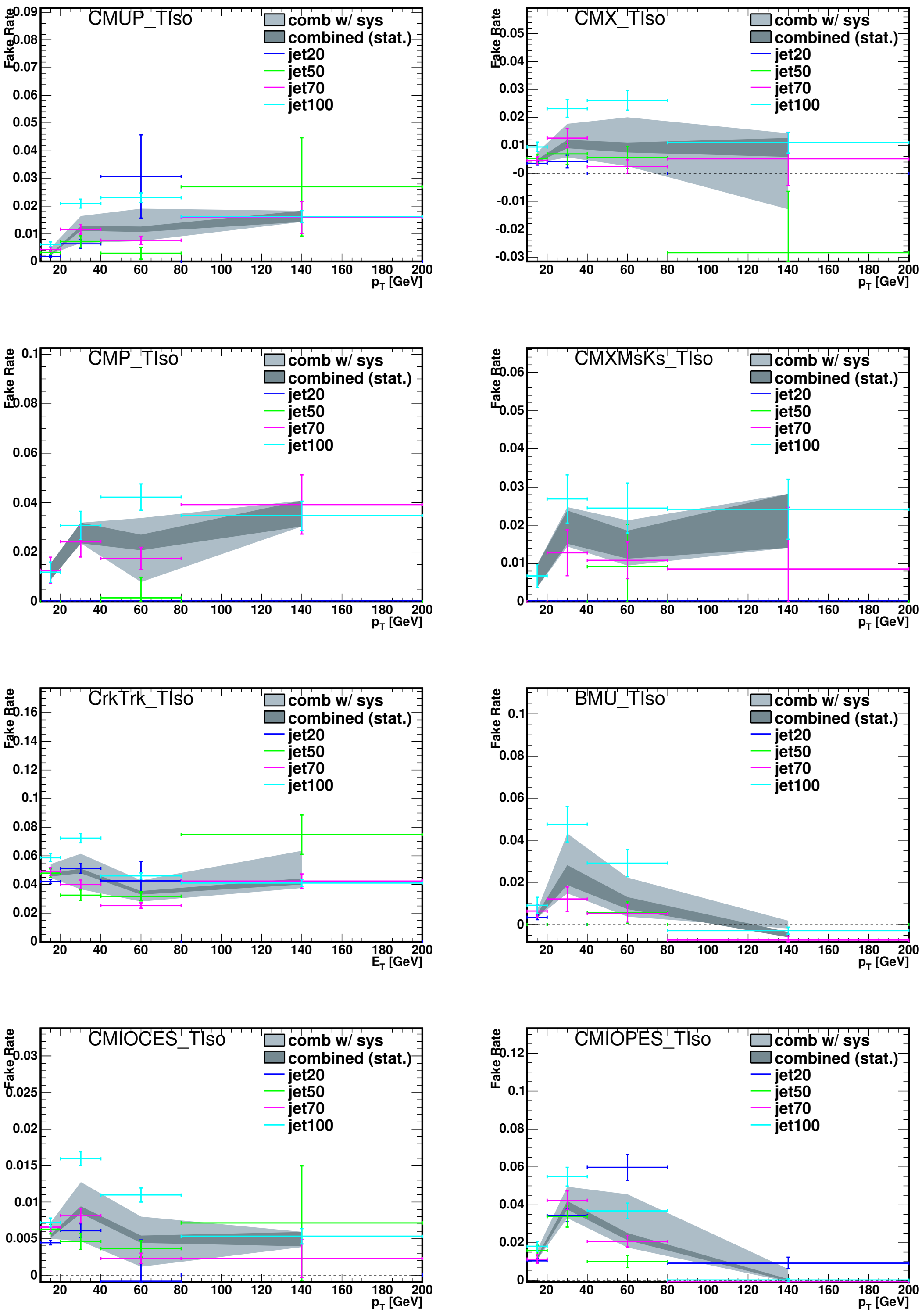

Figure 8: Fake rates for muons.

2.5 DY Cross Section Measurements

In this section we measure the DY cross-section by comparing reconstructed $p\bar{p} \to Z \to l^+l^-(l = e, \mu)$ events in data with Pythia MC simulations. This provides a sensible measurement of the luminosity of the data sample, and is also probably the strongest check of the definition of new categories. Agreement on the cross section value among different dilepton categories tells us that we're correctly modeling their behaviour in our simulation, and the average cross section value of all dilepton categories tells us if the observed yields are in agreement with the luminosity measurement. We select Z candidates requiring two opposite sign leptons (e or μ, belonging to the defined categories) with invariant mass $66 < m(ll) < 106$ GeV, and require $\not{E}_T < 15$ GeV for $e\mu$ events and $\not{E}_T < 25$ GeV for all other combinations. All base analysis requirements are also applied: good run list selection, $\Delta z_0(ll) < 4$ cm, cosmic veto, and requiring a trigger lepton coherent with trigger bits (for data).

In Table 21 we show the following results for each dilepton category: the number of events predicted and observed, their ratio, the resulting DY cross section with its statistical error, and the residual between the measured value and the weighted average of all the categories (systematic uncertainties are not accounted for).

Results from the previous tables show a reasonable agreement for all categories within few percent. The only visible shift is for CMXMsKs, for which the statistics are quite low and considering that systematic uncertainties are not accounted in these errors (like trigger efficiencies, SF errors) we think this effect is not worrisome. The PHX category is known to have a lower measurement (and for this reason it's excluded in the calculation of the weighted mean) since in this low $\not{E}_T$ region we do not model correctly the turn-on of the MET_PEM trigger (by which these events are triggered); this effect is not present in the signal region since the $\not{E}_T$ cut puts events in the plateau of the turn-on curve.

Category	DY MC	Data	Data/MC	DY x-sec (pb) $\pm$ stat.	Residual $[\sigma]$
LBE LBE	92731.9	90969	0.98	246.53 $\pm$ 0.85	0.7
LBE PHX	88948.6	87014	0.98	245.84 $\pm$ 0.86	-0.1
PHX PHX	2324.9	883	0.38	95.45 $\pm$ 3.22	-46.8
LBE CMUP	22.6	19	0.84	211.35 $\pm$ 49.83	-0.7
LBE CMP	2.8	3	1.08	271.86 $\pm$ 166.48	0.2
LBE CMX	10.4	19	1.83	459.38 $\pm$ 111.99	1.9
LBE CMXMsKs	2.2	1	0.45	112.78 $\pm$ 115.43	-1.2
LBE BMU	3.4	3	0.88	220.45 $\pm$ 130.96	-0.2
LBE CMIOCES	18.0	22	1.22	307.56 $\pm$ 68.44	0.9
LBE CMIOPES	8.7	10	1.15	288.20 $\pm$ 94.38	0.4
PHX CMUP	26.8	32	1.19	299.57 $\pm$ 54.85	1.0
PHX CMP	4.7	5	1.06	265.45 $\pm$ 123.90	0.2
PHX CMX	12.2	13	1.06	267.42 $\pm$ 76.64	0.3
PHX CMXMsKs	2.3	2	0.87	217.62 $\pm$ 158.10	-0.2
PHX BMU	3.6	6	1.68	421.40 $\pm$ 180.57	1.0
PHX CMIOCES	17.4	30	1.72	432.89 $\pm$ 83.25	2.2
PHX CMIOPES	7.9	6	0.76	189.78 $\pm$ 78.99	-0.7
CMUP CMUP	19835.5	19524	0.98	247.36 $\pm$ 1.82	0.8
CMUP CMP	5339.2	5446	1.02	256.33 $\pm$ 3.59	2.9
CMUP CMX	19650.1	19415	0.99	248.30 $\pm$ 1.84	1.3
CMUP CMXMsKs	3665.4	3402	0.93	233.25 $\pm$ 4.11	-3.1
CMUP BMU	6347.8	6172	0.97	244.34 $\pm$ 3.19	-0.5
CMUP CMIOCES	29147.6	29817	1.02	257.08 $\pm$ 1.54	7.3
CMUP CMIOPES	13075.3	12841	0.98	246.80 $\pm$ 2.23	0.4
CMX CMP	2694.7	2749	1.02	256.37 $\pm$ 5.07	2.1
CMX CMX	5666.5	5441	0.96	241.30 $\pm$ 3.38	-1.4
CMX CMXMsKs	1354.5	1231	0.91	228.40 $\pm$ 6.71	-2.6
CMX BMU	3230.9	2928	0.91	227.74 $\pm$ 4.33	-4.2
CMX CMIOCES	14972.3	14438	0.96	242.34 $\pm$ 2.09	-1.7
CMX CMIOPES	6447.4	6155	0.95	239.91 $\pm$ 3.14	-1.9
CMXMsKs CMP	797.0	730	0.92	230.17 $\pm$ 8.75	-1.8
CMXMsKs CMXMsKs	312.5	334	1.07	268.58 $\pm$ 15.18	1.5
CMXMsKs BMU	531.6	513	0.96	242.50 $\pm$ 10.97	-0.3
CMXMsKs CMIOCES	2041.7	2499	1.22	307.59 $\pm$ 6.40	9.6
CMXMsKs CMIOPES	839.9	872	1.04	260.92 $\pm$ 9.05	1.7
CMP CMP	615.5	649	1.05	264.98 $\pm$ 10.70	1.8
CMP BMU	660.9	674	1.02	256.27 $\pm$ 10.12	1.0
CMP CMIOCES	2883.6	3195	1.11	278.45 $\pm$ 5.10	6.4
CMP CMIOPES	1327.8	1388	1.05	262.71 $\pm$ 7.21	2.3
LBE CrkTrk	43584.4	41151	0.94	237.27 $\pm$ 1.21	-7.2
PHX CrkTrk	10079.0	8431	0.84	210.21 $\pm$ 2.32	-15.4
CMUP CrkTrk	24145.5	23219	0.96	241.66 $\pm$ 1.63	-2.6
CMP CrkTrk	2403.7	2574	1.07	269.11 $\pm$ 5.45	4.3
CMX CrkTrk	12238.0	11302	0.92	232.08 $\pm$ 2.25	-6.2
CMXMsKs CrkTrk	1726.3	1808	1.05	263.19 $\pm$ 6.37	2.7

Table 21: Drell-Yan cross section measurement for each dilepton category. See text for detailed explanation.

3 Event Selection

In this section, we describe our candidate selection. This includes the triggers, reconstruction of low-level objects, and our high-level cuts. The general strategy is to use cuts to supress the Drell-Yan background and then rely on matrix element calculations and neural networks to discriminate against the other backgrounds.

3.1 Datasets

We use the following trigger paths:

- ELECTRON_CENTRAL_18
- MUON_CMUP18
- MUON_CMX18
- MET_PEM
- MUON_CMP18_PHI_GAP

The corresponding datasets are bhel0d/0h/0i/0j/0k/0m (electrons), bhmu0d/0h/0i/0j/0k/0m (muons), and bpel0d/0h/0i/0j/0k/0m (MET+PEM). We use the following v29 good run lists slightly modified to recover portions of runs that contain bad beamline data (see CDF Note 9195):

- EM_NOSI
- EM_CMUP_NOSI
- EM_MU_NOSI_CMXIGNORED
- EM_SI
- EM_CMUP_SI
- EM_MU_SI_CMXIGNORED
- EM_MU_SI_BMU

The luminosity of each good run list is shown in Table 3.1.

Good run list	$\mathcal{L}$ (pb^{-1})
EM_NOSI	4828.8
EM_CMUP_NOSI	4772.5
EM_MU_NOSI_CMXIGNORED	4661.5
EM_SI	4549.4
EM_CMUP_SI	4499.5
EM_MU_SI_CMXIGNORED	4394.8
EM_MU_SI_BMU	4300.7

Table 22: Luminosity for each of the good run lists (v29) used in this analysis. These have been scaled by the factor of 1.019.

3.2 Low-level Objects

The muon categories introduced in the previous version of this analysis (CMP, CMU, CMXMsKs, and BMU) are described in CDF 9697 [1]. All previous lepton categories are identically defined as in CDF 8719, except for the changes mentioned in CDF 9697. For the CMIOPES category, there are also several additional requirements to those in CDF 8719, designed to veto events with a CMIOPES muon with poorly measured curvature. These cuts were also made in previous versions of the analysis (CDF 9685) and are as follows:

- Number of SVX hits > 3
- Curvature significance > 12 based on error from the covariance matrix

3.3 High-level Cuts

Except for the requirement on the dilepton invariant mass, m_{ll}, we use the same high-level cuts as in CDF 8719 to define a "base region". The m_{ll} cut was lowered from 25 GeV to 16 GeV as in CDF 8700.

4 Sample Modeling

In this section we describe how we model the selected sample. Section 4.1 describes the Monte Carlo samples used, Section 4.2 describes the data based corrections made to the Monte Carlo, and Section 4.3 describes the modeling of the W+jets background.

4.1 Monte Carlo Samples

The acceptance and several of the backgrounds are estimated using Monte Carlo samples. Table 23 lists all the samples used. Here we provide some brief notes on the samples.

WW

As WW is by far the dominant background to this analysis, we take special care using a NLO Monte Carlo generator, MC@NLO. Unfortunately, more recent versions of the MC generator have a bug which prevents us from generating NLO WW samples for run ranges subsequent to Period 8. As a temporary work-around, we use the NLO WW sample generated through period 7 in our analysis and apply a scale factor determined from the ratio of yields obtained in a region of interest for two Pythia WW samples: one covering all periods from 0 to 23 and another that spans only periods 0 to 7. The resulting scale factor is 0.943 for events with 0 jets in the final state, 0.988 for events with 1 jet in the final state and 1.026 for events with more than two jets in the final state. We assign an uncertainty of 2.2% in the 0-jet bin, 1.0% in the 1-jet bin and 1.4% in the jet bin with two or more jets to account for this scaling. In both the Pythia and MC@NLO samples both of the W bosons are required to decay into either an electron, muon, or tau.

Heavy dibosons: WZ, ZZ

The WZ and ZZ samples used are all Pythia based. The WZ samples are generated with a forced decay of the Z into a lepton pair (electrons, muons, or taus) while the W is allowed to decay inclusively. The events are filtered using the generator-level information, requiring two leptons with p_T greater than 1 GeV. The ZZ sample is generated having both Z's decay inclusively and then filtering for two leptons with p_T greater than 1 GeV. The ZZ Monte Carlo includes γ^* component with M_{ll} >15 GeV/c^2.

$W\gamma$

The $W\gamma$ Monte Carlo used for this analysis uses the Baur matrix element generator [5] which is passed to Pythia via the LesHouchesModule. Because of indecision over the proper settings for the Pythia QED radiation settings the Gen5 sample has the QED turned off and the Gen6 sample has it turned on. The two settings correspond to slightly over estimating the lepton id efficiency and double counting at order $\alpha_{\rm EM}$ the hard radiation, respectively. Neither of these effects should be significant for this analysis, relative to the conversion finding efficiency and K-factor uncertainties. It should also be noted that the $W\gamma$ cross-section has been measured at CDF [6] and DØ.

$t\bar{t}$

The $t\bar{t}$ sample is generated at a mass of 175 GeV, uses Gen5 for the full run range and has no minbias in the events. **Update to include new ttbar sample.**

$Z \to \tau\tau$

The $Z \to \tau\tau$ sample is generated with a 10 GeV/c^2 minimum dilepton mass, uses Gen5 for the full run range and has no minbias in the events.

$Z \to ee$ **and** $Z \to \mu\mu$

The $Z \to ee$ and $Z \to \mu\mu$ samples are generated with a 20 GeV/c^2 minimum dilepton mass. They use Gen5 for the 0d run range and Gen6 for the 0h/0i/0j/0k/0m run ranges. They have a full luminosity dependent addition of minbias in the events.

4.2 Corrections to the Monte Carlo

Luminosity scaling, data-base corrections, and measured trigger efficiencies are applied to the Monte Carlo samples separately for each of the lepton pair categories. The master formula used is:

$$\frac{\sigma \times \mathcal{B} \times \epsilon_{\rm filter} \times \epsilon_i^{\rm trg} \times s_i^{\rm lep} \times \epsilon_{\rm vtx} \times \mathcal{L}_i}{N_i^{\rm gen}(|Z_0| < 60 \text{ cm})} \tag{7}$$

where

σ	is the cross-section for the Monte Carlo process (as listed in Tables 23-27)
$\mathcal{B}$	is any branching fraction for the Monte Carlo process (as listed in Tables 23-27)
$\epsilon_{\rm filter}$	is the filter efficiency applied for any filter used in the generation process (as listed in Tables 23-27)
$\epsilon_i^{\rm trg}$	is the effective trigger efficiency for the category (see below)
$s_i^{\rm lep}$	is the effective lepton id scale factor (see below)
$\epsilon_{\rm vtx}$	is the run dependent efficiency of the z-vertex position requirement ($\|z_0\| < 60$ cm)
$\mathcal{L}_i$	is the luminosity of the dataset in good run list in which the lepton category falls (see Table 3.1)

mode	Period	Stntuple	$\sigma \times \mathcal{B}$ (pb)	K-factor[a]	Filter Eff
$W\gamma \to e\nu\gamma$	0-11	re0s68	13.6	1.36	1.0
$W\gamma \to \mu\nu\gamma$	0-11	re0s69	13.6	1.36	1.0
$W\gamma \to \tau\nu\gamma$	0-11	re0s6a	13.6	1.36	1.0
WW	0-23	we0s5d,we0sbd,we0sgd we0skd,we0snd,we0saf we0sgf	11.66×0.1027	1.0	1.0
$WW@NLO$	0-7	we0sfd,we0sed	11.66×0.1027	1.0	1.0
WZ	0-23	we0s6d,we0scd,we0shd we0sld,we0sod,we0sbf we0shf	3.46×0.101	1.0	0.754
ZZ	0-23	we0s7d,we0sdd,we0sid we0smd, we0spd,we0scf we0sif	1.511	1.0	0.233
$t\bar{t}$	0-11	te0s2z	7.9×0.1027	1.0	1.0
$Z \to ee$	0-23	ze1s6d[b],ze1sad,ze0scd ze0sdd,ze0sed,ze0see ze0seh, ze0sej,ze0sei	355[c]	1.38	1.0
$Z \to \mu\mu$	0-23	ze1s6m[b],ze1s9m,ze0sbm ze0scm,ze0sdm,ze0sem ze0sfm, ze0sgm,ze0sim	355[c]	1.38	1.0
$Z \to \tau\tau$	0-11	zx0set	1272[d]	1.38	0.00713
$Z \to ee$	0-11	zx0see	920[e]	1.38	0.0156
$Z \to \mu\mu$	0-11	zx0sem	920[e]	1.38	0.0156

[a] If cross section is NLO, then K-factor is one.
[b] Gen5 tarball for period 0.
[c] $m_{ll} > 20$.
[d] $m_{ll} > 10$.
[e] $10 < m_{ll} < 20$.

Table 23: Monte Carlo samples used in this analysis **Update to include new ttbar sample.**

$M_H(GeV^2)$	Period	Stntuple	σ (pb)	BR ($H \to WW$)	BR($WW \to \ell\nu\ell\nu$)
110	0-23	dhgs4a,dhgs6a	1.3320	0.0441	0.1027
120	0-23	dhgs4b,dhgs6b	1.0575	0.1320	0.1027
130	0-23	dhgs4c,dhgs6b	0.8478	0.2869	0.1027
140	0-23	dhgs4d,dhgs6b	0.6875	0.4833	0.1027
150	0-23	dhgs4e,dhgs6b	0.5634	0.6817	0.1027
160	0-23	dhgs4f,dhgs6b	0.4607	0.9011	0.1027
170	0-23	dhgs4g,dhgs6b	0.3677	0.9653	0.1027
180	0-23	dhgs4h,dhgs6b	0.3031	0.9345	0.1027
190	0-23	dhgs4i,dhgs6b	0.2478	0.7761	0.1027
200	0-23	dhgs4j,dhgs6b	0.2073	0.7347	0.1027
145	0-23	dhgs4o,dhgs6b	0.6217	0.5731	0.1027
155	0-23	dhgs4p,dhgs6b	0.5113	0.8007	0.1027
165	0-23	dhgs4q,dhgs6b	0.4096	0.9566	0.1027
175	0-23	dhgs4r,dhgs6b	0.3335	0.9505	0.1027

Table 24: Higgs production via gluon fusion. The production cross section is taken from a NNLL calculation.

$M_H(GeV^2)$	Period	Stntuple	σ (pb)	BR ($H \to WW$)	BR($WW \to \ell\nu\ell\nu$)
110	0-23	vhgs1a,vhgs3a,vhgs6a	0.0841	0.0441	0.1027
120	0-23	vhgs1b,vhgs3b,vhgs6b	0.0717	0.1320	0.1027
130	0-23	vhgs1c,vhgs3c,vhgs6c	0.0611	0.2869	0.1027
140	0-23	vhgs1d,vhgs3d,vhgs6d	0.0521	0.4833	0.1027
150	0-23	vhgs1e,vhgs3e,vhgs6e	0.0445	0.6817	0.1027
160	0-23	vhgs1f,vhgs3f,vhgs6f	0.0382	0.9011	0.1027
170	0-23	vhgs1g,vhgs3g,vhgs6g	0.0329	0.9653	0.1027
180	0-23	vhgs1h,vhgs3h,vhgs6h	0.0283	0.9345	0.1027
190	0-23	vhgs1i,vhgs3i,vhgs6i	0.0244	0.7761	0.1027
200	0-23	vhgs1j,vhgs3j,vhgs6j	0.0210	0.7347	0.1027
145	0-23	vhgs2o,vhgs3o,vhgs6o	0.0481	0.5731	0.1027
155	0-23	vhgs2p,vhgs3p,vhgs6p	0.0412	0.8007	0.1027
165	0-23	vhgs2q,vhgs3q,vhgs6q	0.0354	0.9566	0.1027
175	0-23	vhgs2r,vhgs3r,vhgs6r	0.0305	0.9505	0.1027

Table 25: Higgs production via vector boson fusion.

$M_H(GeV^2)$	Period	Stntuple	σ (pb)	BR ($H \rightarrow WW$)	Filter Efficiency
110	0-23	fhgs4a,fhgs6a	0.2075	0.0441	0.6880
120	0-23	fhgs4b,fhgs6b	0.1529	0.1320	0.6978
130	0-23	fhgs4c,fhgs6c	0.1141	0.2869	0.7032
140	0-23	fhgs4d,fhgs6d	0.0860	0.4833	0.7065
150	0-23	fhgs4e,fhgs6e	0.0654	0.6817	0.7085
160	0-23	fhgs4f,fhgs6f	0.0510	0.9011	0.7108
170	0-23	fhgs4g,fhgs6g	0.0389	0.9653	0.7125
180	0-23	fhgs4h,fhgs6h	0.0306	0.9345	0.7141
190	0-23	fhgs4i,fhgs6i	0.0243	0.7761	0.7151
200	0-23	fhgs4j,fhgs6j	0.0193	0.7347	0.7165
145	0-23	fhgs4o,fhgs6o	0.0749	0.5731	0.7075
155	0-23	fhgs4p,fhgs6p	0.0572	0.8007	0.7098
165	0-23	fhgs4q,fhgs6q	0.0441	0.9566	0.7114
175	0-23	fhgs4r,fhgs6r	0.0344	0.9505	0.7130

Table 26: Associated Higgs production with a W boson.

$M_H(GeV^2)$	Period	Stntuple	σ (pb)	BR ($H \rightarrow WW$)	Filter Efficiency
110	0-23	uhgs4a,uhgs6a	0.1236	0.0441	0.6930
120	0-23	uhgs4b,uhgs6b	0.0927	0.1320	0.7031
130	0-23	uhgs4c,uhgs6c	0.0705	0.2869	0.7087
140	0-23	uhgs4d,uhgs6d	0.0542	0.4833	0.7122
150	0-23	uhgs4e,uhgs6e	0.0421	0.6817	0.7151
160	0-23	uhgs4f,uhgs6f	0.0331	0.9011	0.7172
170	0-23	uhgs4g,uhgs6g	0.0261	0.9653	0.7184
180	0-23	uhgs4h,uhgs6h	0.0208	0.9345	0.7204
190	0-23	uhgs4i,uhgs6i	0.0166	0.7761	0.7220
200	0-23	uhgs4j,uhgs6j	0.0135	0.7347	0.7239
145	0-23	uhgs4o,uhgs6o	0.0477	0.5731	0.7135
155	0-23	uhgs4p,uhgs6p	0.0373	0.8007	0.7155
165	0-23	uhgs4q,uhgs6q	0.0294	0.9566	0.7183
175	0-23	uhgs4r,uhgs6r	0.0233	0.9505	0.7196

Table 27: Associated Higgs production with a Z boson.

The trigger efficiencies and livetimes were described in Section 2.2 and summarized in Table 4. The lepton ID scale factors for this analysis were described in Section 2.3 and summarized in Tables 6-19.

4.3 W+jets Background

We use a data-driven fake rate proceedure to estimate the backgrounds from fake leptons. The procedure for extracting the fake rates is described in CDF Note 8538. In the dilepton plus MET final state we use both calorimeter and track isolation in our selection criteria for leptons.

Fake rates determined from generic jet samples are applied to a sample of lepton plus denominator object events where the deminator object is treated in the exact same manner as a fully identified lepton. These events are scaled by the rate at which the denominator object "fakes" a specific lepton type (as measured from the generic jet data). For each data event only the highest E_T denominator object is considered, although multiple events can be created in cases where the denominator object has the ability to "fake" more than one lepton type. Both possibilities are considered separately and each generated event is scaled by the appropriate measured fake rate.

A further correction is applied for non-triggerable fake leptons. Such a correction is necessary because events with a single real lepton corresponding to any of our non-triggerable lepton types will not appear in the single lepton samples from which our fake events are generated. The non-triggerable fake rate correction is obtained from our inclusive W Monte Carlo samples. For each dilepton category, we determine a weighted ratio of $W \to \ell\nu$ events with a second lepton originating from a promoted denominator object. The ratio is the weighted number of events in which the triggerable lepton originates from the promoted denominator divided by the weighted number of events in which the real lepton from the W decay is in fact the triggerable lepton ($N^{MC}_{\text{nontrig}}/N^{MC}_{\text{triggerable}}$). The weight of each generated fake event is the simply scaled up by $1 + N^{MC}_{\text{nontrig}}/\ N^{MC}_{\text{triggerable}}$, so that

$$N^{data}_{\text{total}} = N^{data}_{\text{triggerable}} + N^{data}_{\text{triggerable}} \frac{N^{MC}_{\text{nontrig}}}{N^{MC}_{\text{triggerable}}}. \tag{8}$$

The measured ratios of W+jet events with nontriggerable versus triggerable leptons originating from the W decay are shown in Table 28 for each dilepton category. Dilepton categories with two trigger lepton types (e.g. CMUP-CMUP) can have a small non-triggerable correction factor due to the fact that one of the two leptons can have a E_T between 10 and 20 GeV/c and hence be non-triggerable by our definition. Non-triggerable fake rate corrections are now obtained separately for each of the different candidate samples.

	Opp-sign(0 jets)	Opp-sign(1 jet)	Opp-sign(2+ jets)	Same-sign(1+ jets)	Same-sign(0 jets)
e e:					
TCE TCE	0.034	0.041	0.060	0.000	0.000
TCE PHX	0.043	0.039	0.039	0.000	0.000
PHX PHX	0.037	0.017	0.049	0.000	0.000
e μ:					
TCE CMUP	0.043	0.061	0.055	0.000	0.000
TCE CMP	0.066	0.020	0.000	0.000	0.000
TCE CMX	0.047	0.063	0.120	0.000	0.000
TCE CMXMsKs	0.041	0.011	0.000	0.000	0.000
TCE BMU	0.000	0.000	0.000	0.000	0.000
TCE CMIOCES	0.263	0.359	0.362	0.714	0.653
TCE CMIOPES	0.105	0.106	0.117	0.156	0.188
PHX CMUP	0.049	0.050	0.028	0.000	0.000
PHX CMP	0.052	0.022	0.000	0.000	0.000
PHX CMX	0.030	0.064	0.116	0.000	0.000
PHX CMXMsKs	0.028	0.050	0.000	0.000	0.000
PHX BMU	0.000	0.000	0.000	0.000	0.000
PHX CMIOCES	0.624	1.653	1.931	0.000	0.000
PHX CMIOPES	0.250	0.484	0.282	0.000	0.000
μ μ:					
CMUP CMUP	0.066	0.083	0.140	0.000	0.000
CMUP CMP	0.106	0.074	0.000	0.000	0.000
CMUP CMX	0.057	0.061	0.094	0.000	0.000
CMUP CMXMsKs	0.080	0.000	0.000	0.000	0.000
CMUP BMU	3.686	6.113	0.000	5.262	5.177
CMUP CMIOCES	0.618	0.715	1.126	1.246	1.198
CMUP CMIOPES	0.328	0.284	0.948	0.444	0.596
CMX CMP	0.057	0.000	0.000	0.000	0.000
CMX CMX	0.055	0.095	0.000	0.000	0.000
CMX CMXMsKs	0.067	0.000	0.000	0.000	0.000
CMX BMU	2.240	2.305	0.000	4.251	2.107
CMX CMIOCES	0.448	0.717	0.944	0.833	0.980
CMX CMIOPES	0.242	0.167	0.785	0.310	0.397
CMXMsKs CMP	0.144	0.000	0.000	0.000	0.000
CMXMsKs CMXMsKs	0.000	0.000	0.000	0.000	0.000
CMXMsKs BMU	2.842	0.000	0.000	0.000	2.814
CMXMsKs CMIOCES	0.551	0.594	0.000	1.397	1.553
CMXMsKs CMIOPES	0.124	1.315	0.000	0.730	0.134
CMP CMP	0.000	0.000	0.000	0.000	0.000
CMP BMU	1.407	0.000	0.000	0.000	2.023
CMP CMIOCES	1.705	1.964	1.450	2.534	2.632
CMP CMIOPES	0.450	0.758	1.824	0.889	0.911
e Trk:					
TCE Trk	0.071	0.091	0.140	0.257	0.241
PHX Trk	0.193	0.358	0.703	0.000	0.000
μ Trk:					
CMUP Trk	0.233	0.243	0.473	0.692	0.632
CMP Trk	0.450	0.436	0.000	1.127	1.223
CMX Trk	0.150	0.183	0.092	0.615	0.524
CMXMsKs Trk	0.244	0.341	0.354	0.435	0.461

Table 28: Ratio of non-triggerable to triggerable fakes by dilepton category and signal region. Note that the ratio for dilepton categories with two trigger lepton types is expected to be zero in the same-sign region since both leptons are required to have $p_T > 20$ GeV/c. **Update to for LBE.**

5 Control Regions

In this section, we present the control regions in which we have tested our data model. Each control region attempts to isolate or enhance effects that must be modeled. Control regions are generally events obtained using the standard opposite-sign selection criteria from Section 3 but with the cuts on one particular selection requirement reversed. The control regions considered are:

- Events in the Drell-Yan (DY) control region are required to have low $\not\!\!E_T$ and a dilepton invariant mass in the Z mass region. This event sample tests our modeling of lepton ID scale factors and trigger efficiencies over all the different lepton categories as well as the luminosity accounting based on our good run lists.
- Events in the same-sign region satisfy an equivalent set of selection criteria to the opposite-sign events contained within our signal regions. These events test our modeling of contributions from photons and jets misidentified as leptons
- Events in the low $\not\!\!E_{T\mathrm{sig}}$ region test our modeling of tails in the missing E_T distribution for the Drell-Yan process in particular as well as the effect of mismeasured unclustered energy or combinations of leptons on $\not\!\!E_T$ modeling.
- Events in the Low $\not\!\!E_{Tspec}$, High $\not\!\!E_T$ region test the modeling of the effects of mismeasured individual leptons and jets on the missing E_T.

We choose two separate control regions to study $\not\!\!E_T$ mis-modeling because $\not\!\!E_T$ can arise from either mismeasurement of single objects (*ie.* a lepton or a jet) or from tails in the response function of the detector as a whole. More detail regarding each of the control regions is given below.

5.1 Dilepton Z-mass (DY) Control Region

Here we consider opposite-sign same-flavor dileptons in the Z mass region which is completely dominated by the Drell-Yan process. We require one trigger lepton and a second lepton with $E_T > 10$ GeV. We also require $\not\!\!E_T < 20$ GeV in this region, and include events with any number of jets.

Table 29 and Figures 9-11 show the agreement between the expected number of events and the observed yield for each dilepton catagory, and for lepton categories combined into ee and $\mu\mu$. We generally find good agreement in the shapes and normalizaton.

5.2 Base Same Sign Control Region

To check modeling of the W+jets and $W\gamma$ fake backgrounds, we look at events with zero or one jets that satisfy all signal selection criteria with the exception of the opposite sign

Category	WW	WZ	ZZ	$t\bar{t}$	DY	$W\gamma$	W+jets	Total	Data
e e	10.8	65.6	62.0	3.1	184005.4	3.1	1018.1	185168.0	178866.0
e μ	10.4	0.2	0.1	2.4	143.1	0.8	150.3	307.3	171.0
μ μ	10.0	52.1	51.8	2.7	141437.9	0.0	710.5	142265.0	140413.0
e trk	8.6	19.8	19.3	2.4	53663.4	1.0	812.9	54527.3	49582.0
μ trk	5.7	14.9	14.5	1.6	40513.6	0.1	544.5	41094.7	38903.0
Total:	45.5	152.5	147.7	12.1	419763.4	5.0	3236.2	423362.3	407935.0

Category	WW	WZ	ZZ	$t\bar{t}$	DY	$W\gamma$	W+jets	Total	Data
LBE LBE	6.2	37.0	37.5	2.1	92731.9	0.2	117.8	92932.7	90969.0
LBE PHX	4.2	27.0	23.1	0.9	88948.6	2.5	852.8	89859.1	87014.0
PHX PHX	0.4	1.6	1.3	0.0	2324.9	0.4	40.9	2369.6	883.0
LBE CMUP	2.9	0.1	0.0	0.8	22.6	0.0	14.0	40.4	19.0
LBE CMP	0.4	0.0	0.0	0.1	2.8	0.0	44.5	47.8	3.0
LBE CMX	1.2	0.0	0.0	0.3	10.4	0.0	9.3	21.3	19.0
LBE CMXMsKs	0.1	0.0	0.0	0.1	2.2	0.0	3.5	5.9	1.0
LBE BMU	0.3	0.0	0.0	0.1	3.4	0.0	0.0	3.8	3.0
LBE CMIOCES	2.3	0.0	0.0	0.5	18.0	0.0	5.0	25.9	22.0
LBE CMIOPES	0.6	0.0	0.0	0.1	8.7	0.0	8.8	18.3	10.0
PHX CMUP	1.0	0.0	0.0	0.2	26.8	0.3	6.8	35.2	32.0
PHX CMP	0.1	0.0	0.0	0.0	4.7	0.0	26.3	31.2	5.0
PHX CMX	0.4	0.0	0.0	0.1	12.2	0.1	4.9	17.7	13.0
PHX CMXMsKs	0.1	0.0	0.0	0.0	2.3	0.0	1.7	4.1	2.0
PHX BMU	0.1	0.0	0.0	0.0	3.6	0.0	0.0	3.7	6.0
PHX CMIOCES	0.7	0.0	0.0	0.1	17.4	0.2	5.2	23.6	30.0
PHX CMIOPES	0.2	0.0	0.0	0.0	7.9	0.0	1.5	9.6	6.0
CMUP CMUP	1.5	8.1	8.7	0.5	19835.5	0.0	61.7	19916.0	19524.0
CMUP CMP	0.4	2.2	2.4	0.1	5339.2	0.0	20.2	5364.5	5446.0
CMUP CMX	1.4	7.8	7.8	0.4	19650.1	0.0	54.1	19721.7	19415.0
CMUP CMXMsKs	0.1	1.3	1.3	0.1	3665.4	0.0	14.7	3683.0	3402.0
CMUP BMU	0.4	2.1	1.8	0.1	6347.8	0.0	143.7	6496.0	6172.0
CMUP CMIOCES	2.3	11.5	11.8	0.7	29147.6	0.0	56.5	29230.4	29817.0
CMUP CMIOPES	0.8	3.6	3.2	0.2	13075.3	0.0	227.3	13310.5	12841.0
CMX CMP	0.2	1.1	1.0	0.1	2694.7	0.0	10.1	2707.2	2749.0
CMX CMX	0.5	1.9	1.8	0.1	5666.5	0.0	15.5	5686.3	5441.0
CMX CMXMsKs	0.1	0.7	0.7	0.0	1354.5	0.0	5.8	1361.7	1231.0
CMX BMU	0.2	0.9	0.8	0.0	3230.9	0.0	13.7	3246.6	2928.0
CMX CMIOCES	1.1	5.5	5.4	0.3	14972.3	0.0	31.0	15015.6	14438.0
CMX CMIOPES	0.3	1.7	1.5	0.1	6447.4	0.0	107.3	6558.2	6155.0
CMXMsKs CMP	0.1	0.3	0.3	0.0	797.0	0.0	3.8	801.4	730.0
CMXMsKs CMXMsKs	0.0	0.1	0.1	0.0	312.5	0.0	2.2	314.8	334.0
CMXMsKs BMU	0.0	0.2	0.1	0.0	531.6	0.0	1.0	532.9	513.0
CMXMsKs CMIOCES	0.1	0.8	0.8	0.0	2041.7	0.0	2.9	2046.3	2499.0
CMXMsKs CMIOPES	0.0	0.2	0.2	0.0	839.9	0.0	14.6	854.9	872.0
CMP CMP	0.0	0.2	0.2	0.0	615.5	0.0	2.9	618.9	649.0
CMP BMU	0.1	0.2	0.2	0.0	660.9	0.0	1.1	662.5	674.0
CMP CMIOCES	0.3	1.2	1.2	0.1	2883.6	0.0	15.6	2901.9	3195.0
CMP CMIOPES	0.1	0.4	0.3	0.0	1327.8	0.0	39.5	1368.1	1388.0
LBE CrkTrk	6.8	16.5	16.4	2.1	43584.4	0.2	602.3	44228.7	41151.0
PHX CrkTrk	1.8	3.3	2.9	0.3	10079.0	0.8	199.9	10288.0	8431.0
CMUP CrkTrk	3.4	9.1	8.9	1.0	24145.5	0.1	316.9	24484.9	23219.0
CMP CrkTrk	0.4	0.9	0.9	0.1	2403.7	0.0	59.3	2465.2	2574.0
CMX CrkTrk	1.7	4.3	4.1	0.4	12238.0	0.0	154.7	12403.4	11302.0
CMXMsKs CrkTrk	0.1	0.6	0.6	0.1	1726.3	0.0	22.6	1750.3	1808.0
Total:	45.5	152.5	147.7	12.1	419763.4	5.0	3343.9	423470.0	407935.0

Table 29: Predicted and observed yields in the Drell-Yan Region.

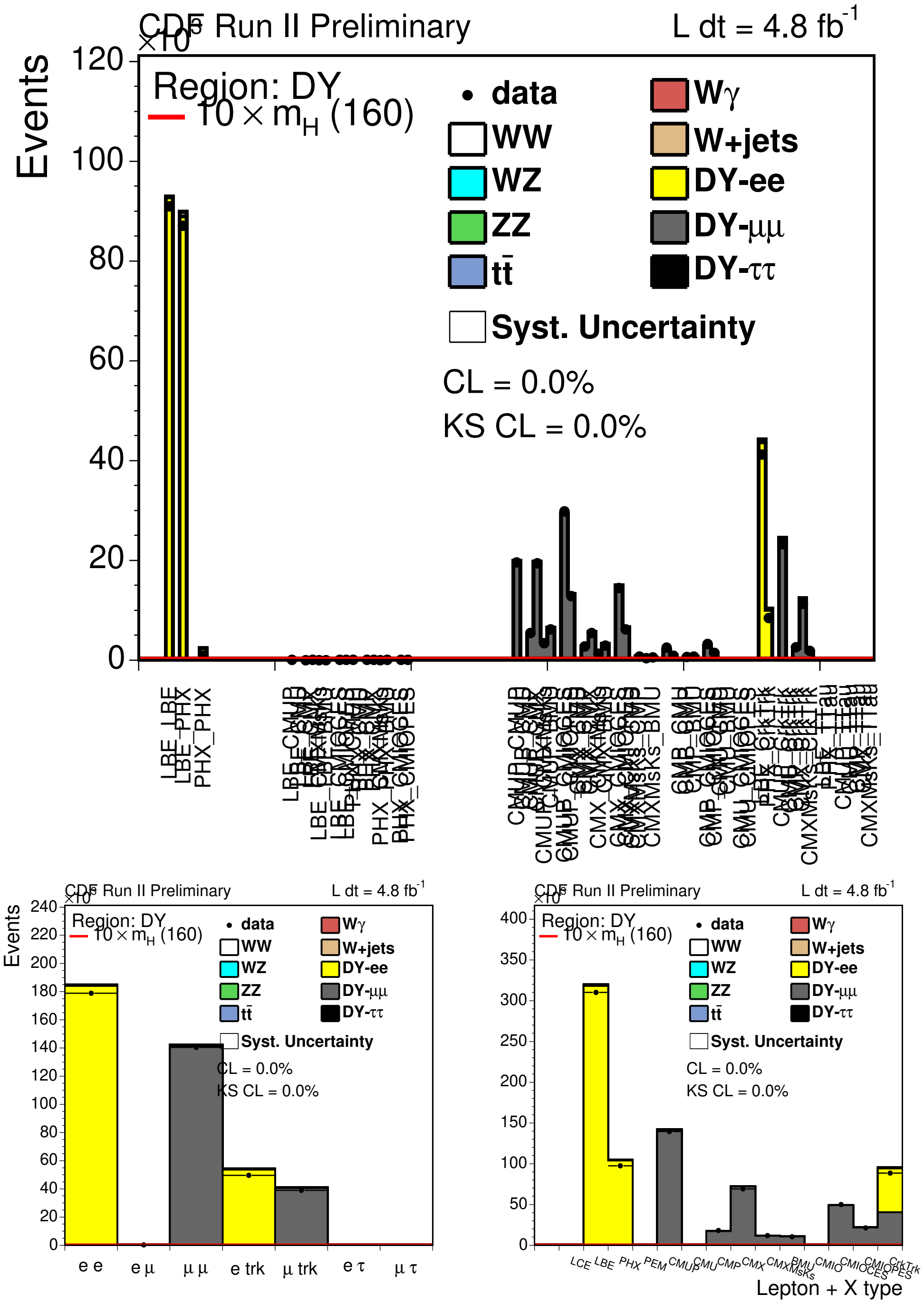

Figure 9: Drell-Yan ($Z \rightarrow l^+l^-$) control region.

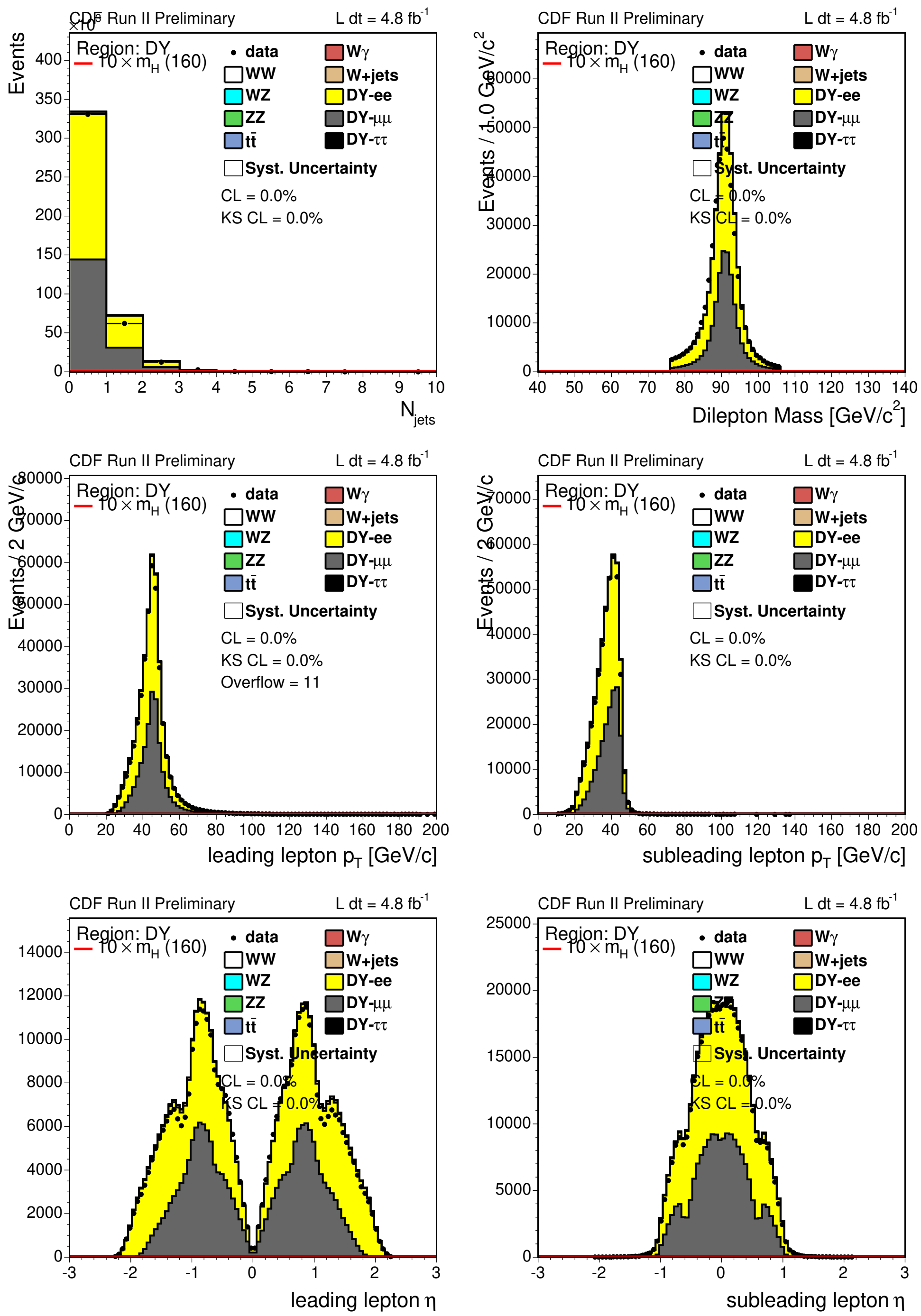

Figure 10: Drell-Yan ($Z \to l^+l^-$) control region.

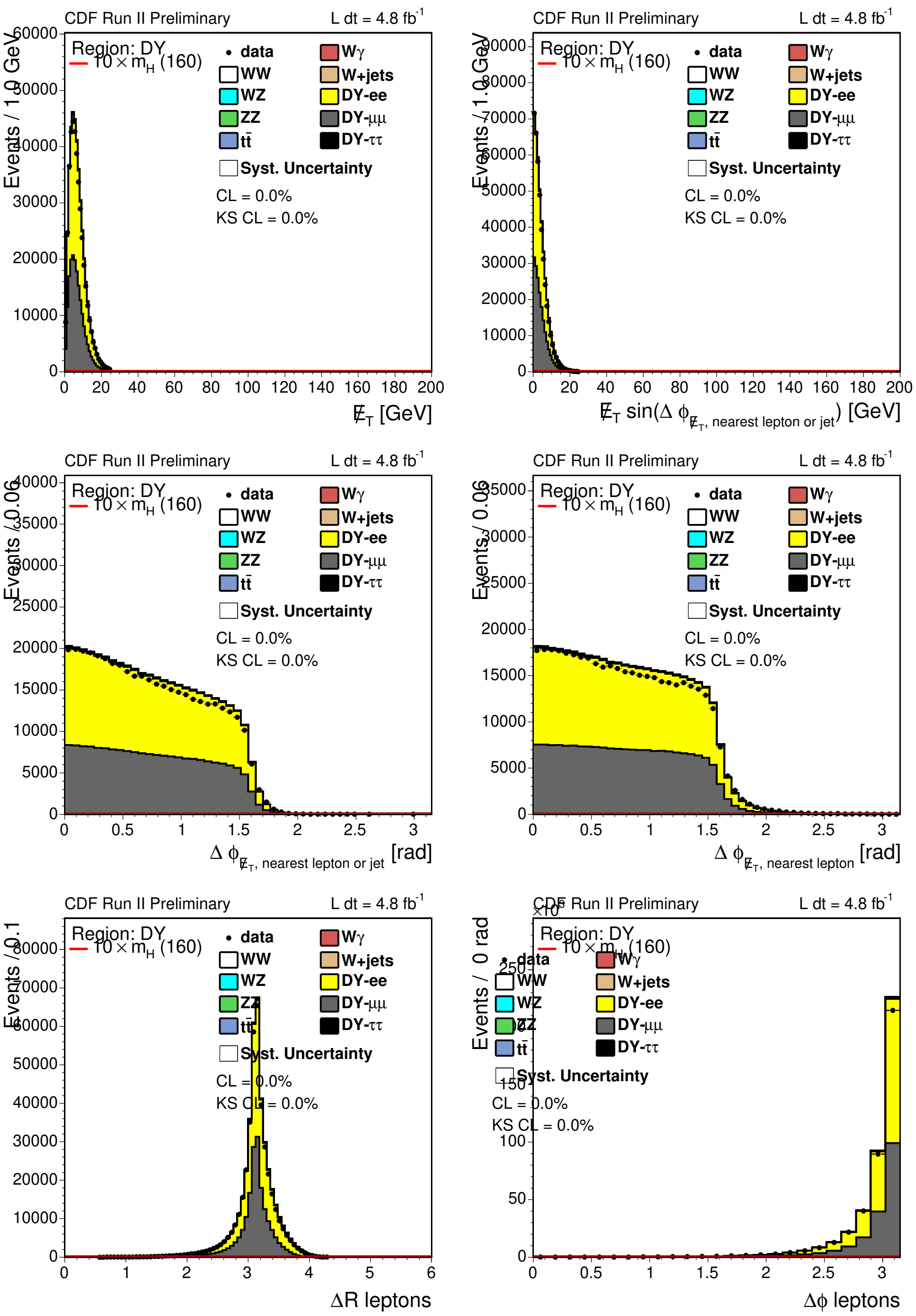

Figure 11: Drell-Yan ($Z \to l^+l^-$) control region.

requirement which is reversed. This region is dominated by fake leptons originating either from jets or photons. The PHX categories also have significant contributions from charge mis-identification. The results are shown in Table 30. In this region we observe excellent agreement in the observed and predicted numbers of events as well as in the predicted and observed kinematic distributions as shown in Figures 12-14.

5.3 Low $\not\!\!E_{T\mathrm{sig}}$ Control Region

As a cross check of the $\not\!\!E_T$ simulation and in order to assess a systematic on the Drell-Yan background, we create a control sample using the standard opposite-sign dilepton selection criteria along with an additional requirement of $\not\!\!E_{T\mathrm{sig}} \equiv \not\!\!E_T/\sqrt{\sum E_T} < 2.5\ \mathrm{GeV}^{\frac{1}{2}}$. The resulting contol sample is populated primarily by Drell-Yan events with large $\not\!\!E_T$ that results from mismeasurement of the unclustered energy or a combination of leptons and jets. Drell-Yan events with $\not\!\!E_T$ due to lost energy from a single lepton or jet are removed by the standard $\not\!\!E_{Tspec}$ cut. In this region , we also find good agreement between the data and our model as illustrated in Table 31 and Figures 15-17.

5.4 Low $\not\!\!E_{Tspec}$ High $\not\!\!E_T$ Control Region

As a secondary check of the $\not\!\!E_T$ modeling, we look in the region of $\not\!\!E_{Tspec}$ between 15 GeV (10 GeV $e\mu$) and the signal region lower requirement of 25 GeV (15 GeV $e\mu$) and also require high $\not\!\!E_T$. The events in this region are dominated by Drell-Yan with $\not\!\!E_T$ due to mismeasured single leptons or jets. In this region, the predicted and observed numbers of events agree at about the one sigma level as shown in Table 32. However, there are several significant disagreements between the observed and predicted kinematic distributions (in particular an excess of data events above the Z-peak in the dilepton invariant mass distribution) as illustrated in Figures 18-20. We suspect that some of these events might be originating from non-collision sources such as cosmic rays but understanding this tail will require additional studies. In the meantime, we already take a large systematic uncertainty on our modeling of the missing E_T tail in Drell-Yan events and believe that this is sufficient to cover the level of disagreement observed in these distributions.

Category	WW	WZ	ZZ	$t\bar{t}$	DY	$W\gamma$	W+jets	Total	Data
e e	6.2	3.6	1.1	0.4	7.1	70.2	67.7	156.3	141.0
e μ	7.4	7.4	0.6	0.4	17.5	61.9	70.6	165.8	153.0
μ μ	0.0	2.6	0.3	0.0	0.2	0.0	6.0	9.1	7.0
e trk	2.1	2.2	0.3	0.2	2.4	15.1	13.0	35.2	40.0
μ trk	0.0	1.3	0.1	0.0	0.5	3.0	6.2	11.1	10.0
Total:	15.7	17.0	2.3	1.0	27.7	150.1	163.6	377.4	351.0

Category	WW	WZ	ZZ	$t\bar{t}$	DY	$W\gamma$	W+jets	Total	Data
LBE LBE	0.0	1.4	0.0	0.0	0.2	15.8	8.2	25.7	12.0
LBE PHX	4.6	1.8	0.8	0.3	5.0	37.2	41.4	91.0	87.0
PHX PHX	1.6	0.4	0.3	0.1	1.9	17.3	18.1	39.6	42.0
LBE CMUP	0.0	1.8	0.2	0.0	1.6	9.4	8.4	21.4	12.0
LBE CMP	0.0	0.2	0.0	0.0	0.0	0.9	1.1	2.3	1.0
LBE CMX	0.0	0.9	0.1	0.0	1.0	4.6	4.3	10.9	11.0
LBE CMXMsKs	0.0	0.2	0.0	0.0	0.2	0.4	1.0	1.7	0.0
LBE BMU	0.0	0.2	0.0	0.0	0.0	0.5	0.0	0.8	0.0
LBE CMIOCES	-0.0	1.3	0.1	0.0	0.4	3.3	1.5	6.6	6.0
LBE CMIOPES	0.0	0.4	0.0	0.0	0.1	1.5	4.5	6.6	10.0
PHX CMUP	2.6	0.9	0.1	0.2	5.4	16.7	21.6	47.4	47.0
PHX CMP	0.4	0.1	0.0	0.0	0.4	2.0	3.0	6.0	4.0
PHX CMX	1.2	0.4	0.0	0.1	3.1	10.4	11.8	27.0	20.0
PHX CMXMsKs	0.2	0.1	0.0	0.0	0.8	1.3	1.7	4.2	4.0
PHX BMU	0.4	0.1	0.0	0.0	0.7	1.5	0.0	2.7	3.0
PHX CMIOCES	1.9	0.5	0.0	0.1	2.4	6.1	1.9	12.9	27.0
PHX CMIOPES	0.7	0.2	0.0	0.0	1.4	3.2	4.1	9.6	8.0
CMUP CMUP	0.0	0.4	0.0	0.0	0.0	0.0	0.7	1.2	0.0
CMUP CMP	0.0	0.1	0.0	0.0	0.0	0.0	0.2	0.3	1.0
CMUP CMX	0.0	0.4	0.0	0.0	0.0	0.0	0.5	1.0	0.0
CMUP CMXMsKs	0.0	0.1	0.0	0.0	0.0	0.0	0.1	0.2	0.0
CMUP BMU	0.0	0.1	0.0	0.0	0.0	0.0	0.2	0.3	0.0
CMUP CMIOCES	0.0	0.5	0.1	0.0	0.0	0.0	0.7	1.3	3.0
CMUP CMIOPES	0.0	0.2	0.0	0.0	0.1	0.0	1.5	1.8	1.0
CMX CMP	0.0	0.1	0.0	0.0	0.0	0.0	0.1	0.2	0.0
CMX CMX	0.0	0.1	0.0	0.0	0.0	0.0	0.1	0.2	1.0
CMX CMXMsKs	0.0	0.0	0.0	0.0	0.0	0.0	0.0	0.1	0.0
CMX BMU	0.0	0.1	0.0	0.0	0.0	0.0	0.0	0.1	0.0
CMX CMIOCES	0.0	0.3	0.0	0.0	0.0	0.0	0.4	0.7	1.0
CMX CMIOPES	0.0	0.1	0.0	0.0	0.0	0.0	0.8	0.9	0.0
CMXMsKs CMP	0.0	0.0	0.0	0.0	0.0	0.0	0.0	0.0	0.0
CMXMsKs CMXMsKs	0.0	0.0	0.0	0.0	0.0	0.0	0.0	0.0	0.0
CMXMsKs BMU	0.0	0.0	0.0	0.0	0.0	0.0	0.0	0.0	0.0
CMXMsKs CMIOCES	0.0	0.0	0.0	0.0	0.0	0.0	0.1	0.1	0.0
CMXMsKs CMIOPES	0.0	0.0	0.0	0.0	0.0	0.0	0.2	0.3	0.0
CMP CMP	0.0	0.0	0.0	0.0	0.0	0.0	0.0	0.0	0.0
CMP BMU	0.0	0.0	0.0	0.0	0.0	0.0	0.0	0.0	0.0
CMP CMIOCES	0.0	0.1	0.0	0.0	0.0	0.0	0.1	0.2	0.0
CMP CMIOPES	0.0	0.0	0.0	0.0	0.0	0.0	0.4	0.4	0.0
LBE CrkTrk	0.0	1.5	0.1	0.0	0.5	6.8	6.2	15.1	12.0
PHX CrkTrk	2.1	0.7	0.2	0.1	1.9	8.2	7.0	20.3	28.0
CMUP CrkTrk	0.0	0.8	0.1	0.0	0.2	1.9	4.0	7.0	2.0
CMP CrkTrk	0.0	0.1	0.0	0.0	0.0	0.2	0.3	0.7	0.0
CMX CrkTrk	0.0	0.4	0.0	0.0	0.2	0.7	1.7	3.0	8.0
CMXMsKs CrkTrk	0.0	0.1	0.0	0.0	0.0	0.1	0.2	0.4	0.0
Total:	15.7	17.0	2.3	1.0	27.7	150.1	158.1	371.9	351.0

Table 30: Expected and observed yields in the Same-Sign region.

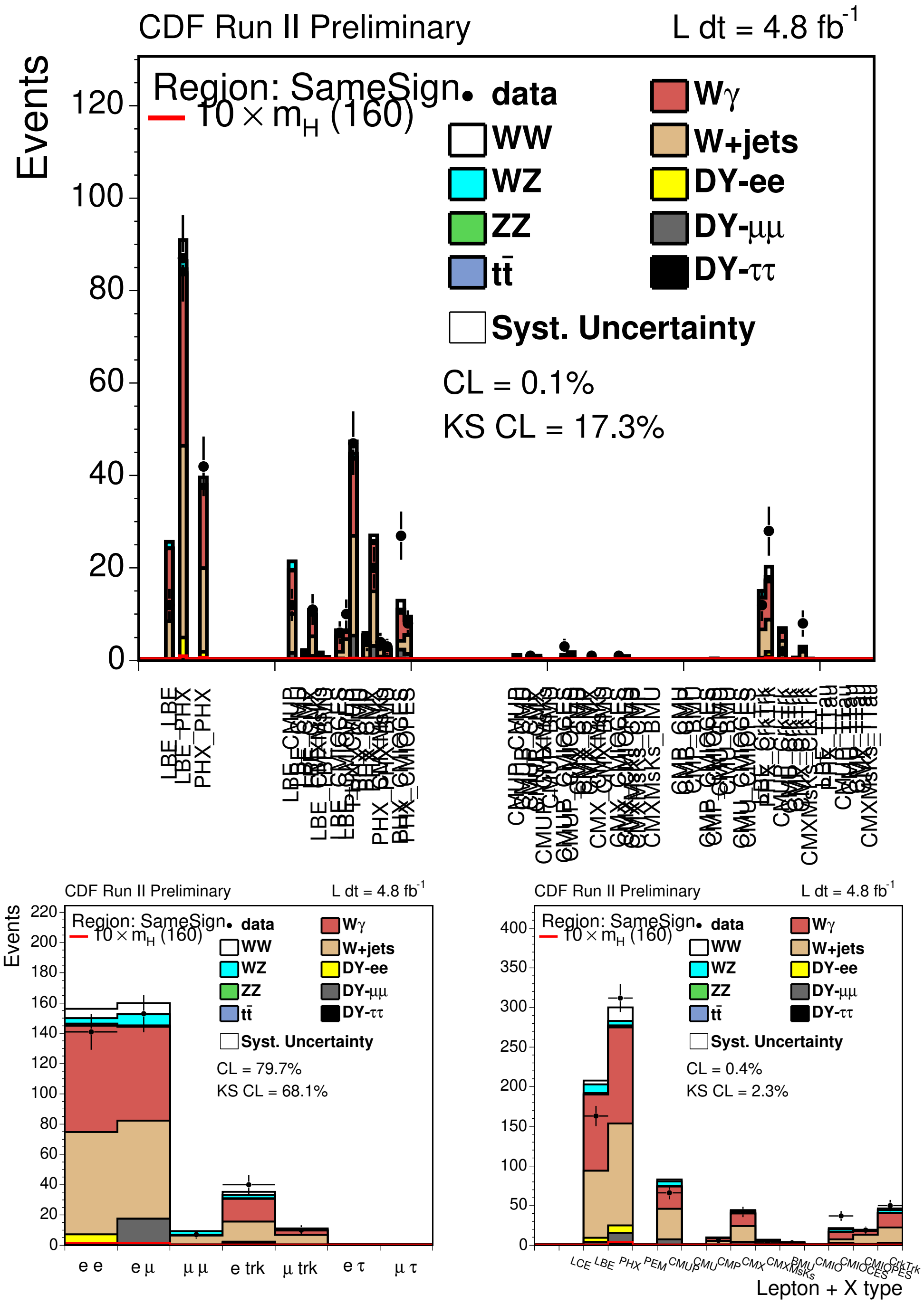

Figure 12: Base Same Sign control region.

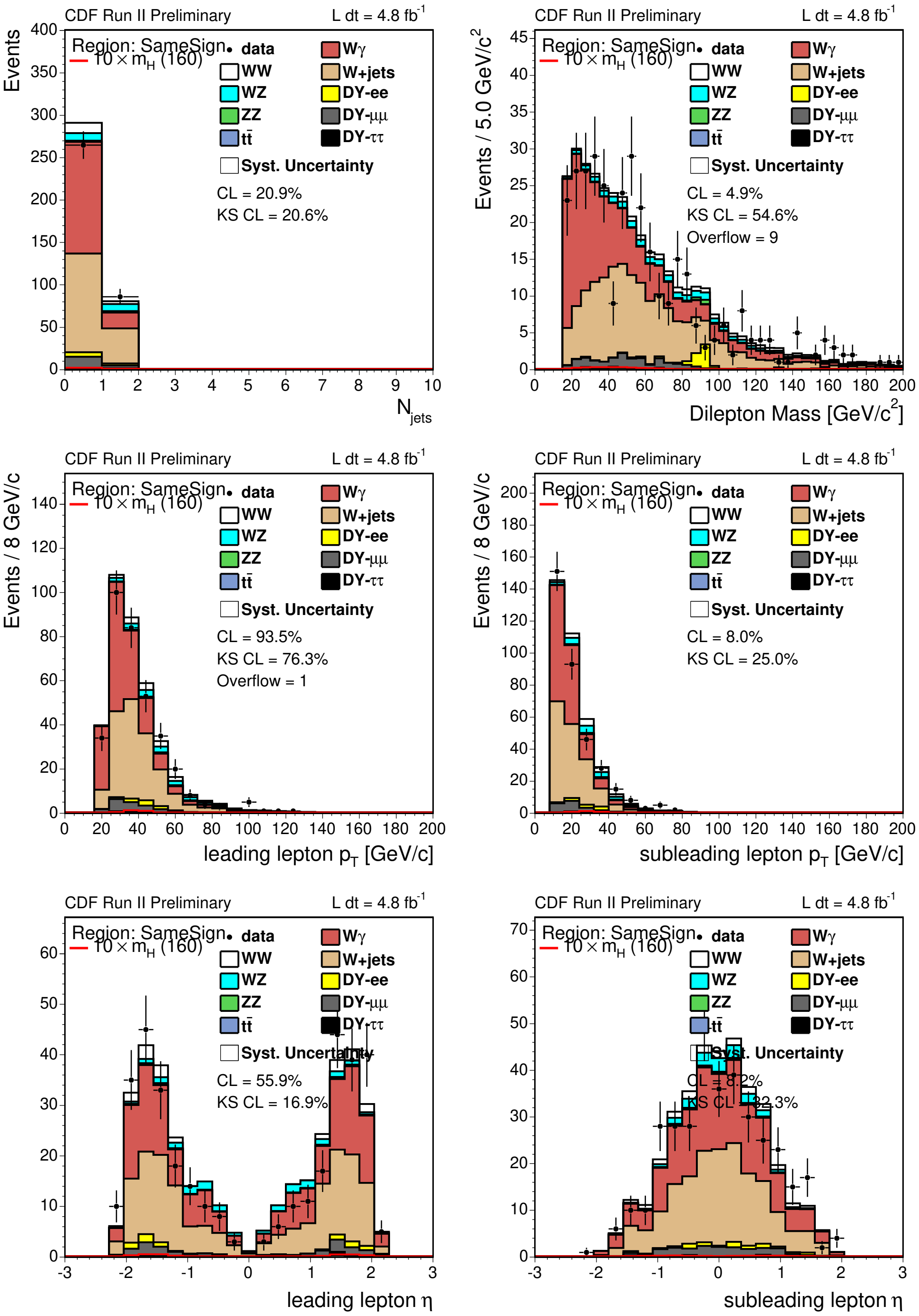

Figure 13: Base Same Sign control region.

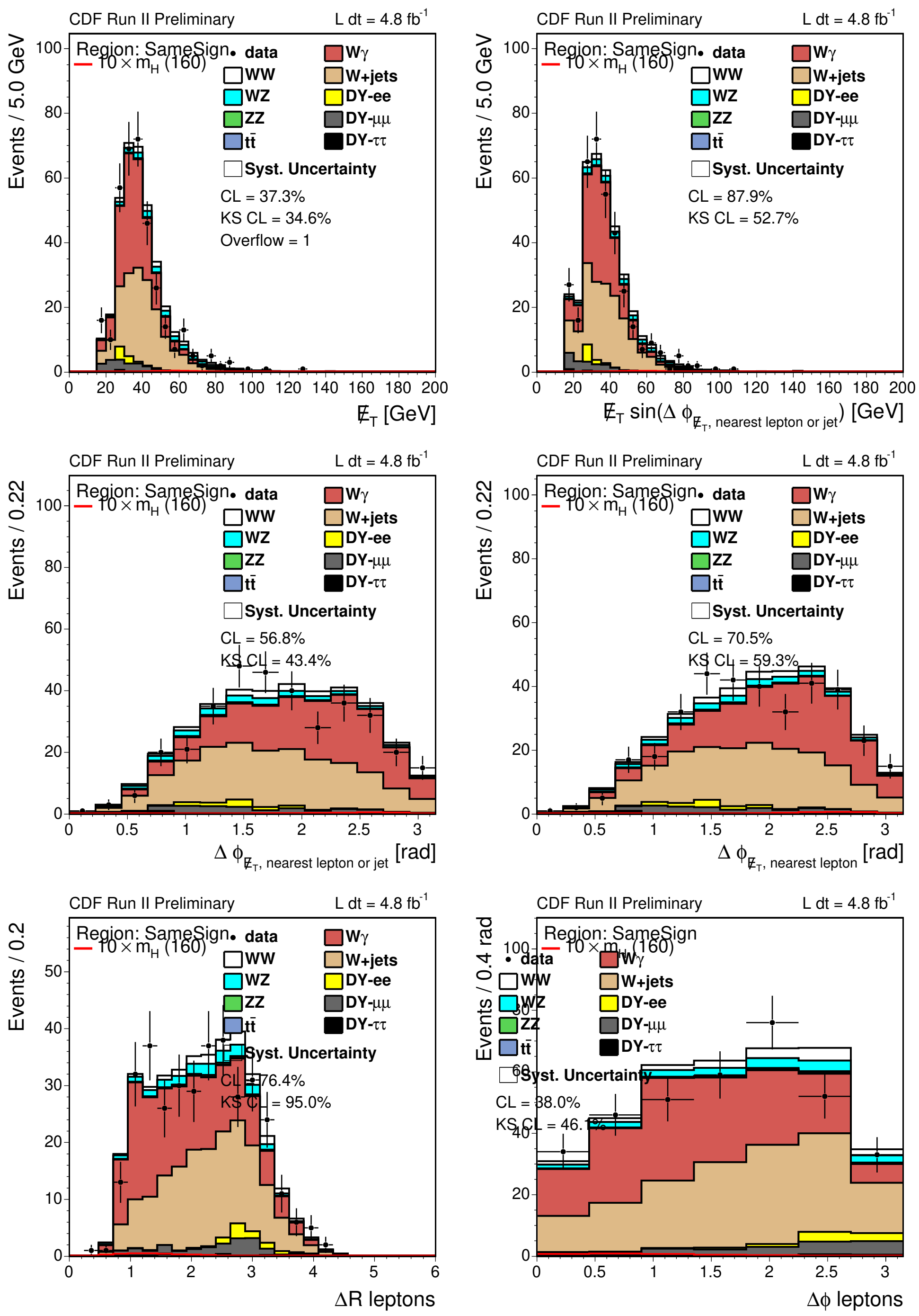

Figure 14: Base Same Sign control region.

Category	WW	WZ	ZZ	$t\bar{t}$	DY	$W\gamma$	W+jets	Total	Data
e e	6.8	1.6	1.3	0.9	65.5	6.5	17.7	100.2	132.0
e μ	0.0	0.0	0.0	0.0	0.0	0.0	0.0	0.0	0.0
μ μ	5.4	1.2	1.1	0.8	45.0	0.0	2.9	56.4	73.0
e trk	5.0	0.7	0.5	0.7	25.6	1.4	4.6	38.5	40.0
μ trk	2.9	0.4	0.3	0.4	11.3	0.2	2.4	17.8	18.0
Total:	20.1	3.8	3.2	2.8	147.3	8.1	27.6	212.9	263.0

Category	WW	WZ	ZZ	$t\bar{t}$	DY	$W\gamma$	W+jets	Total	Data
LBE LBE	4.0	0.8	0.8	0.6	34.3	1.1	2.8	44.6	63.0
LBE PHX	2.3	0.6	0.4	0.2	24.5	3.6	10.6	42.3	55.0
PHX PHX	0.4	0.1	0.1	0.0	6.6	1.7	4.3	13.3	14.0
LBE CMUP	0.0	0.0	0.0	0.0	0.0	0.0	0.0	0.0	0.0
LBE CMP	0.0	0.0	0.0	0.0	0.0	0.0	0.0	0.0	0.0
LBE CMX	0.0	0.0	0.0	0.0	0.0	0.0	0.0	0.0	0.0
LBE CMXMsKs	0.0	0.0	0.0	0.0	0.0	0.0	0.0	0.0	0.0
LBE BMU	0.0	0.0	0.0	0.0	0.0	0.0	0.0	0.0	0.0
LBE CMIOCES	0.0	0.0	0.0	0.0	0.0	0.0	0.0	0.0	0.0
LBE CMIOPES	0.0	0.0	0.0	0.0	0.0	0.0	0.0	0.0	0.0
PHX CMUP	0.0	0.0	0.0	0.0	0.0	0.0	0.0	0.0	0.0
PHX CMP	0.0	0.0	0.0	0.0	0.0	0.0	0.0	0.0	0.0
PHX CMX	0.0	0.0	0.0	0.0	0.0	0.0	0.0	0.0	0.0
PHX CMXMsKs	0.0	0.0	0.0	0.0	0.0	0.0	0.0	0.0	0.0
PHX BMU	0.0	0.0	0.0	0.0	0.0	0.0	0.0	0.0	0.0
PHX CMIOCES	0.0	0.0	0.0	0.0	0.0	0.0	0.0	0.0	0.0
PHX CMIOPES	0.0	0.0	0.0	0.0	0.0	0.0	0.0	0.0	0.0
CMUP CMUP	1.0	0.2	0.2	0.1	5.7	0.0	0.4	7.6	12.0
CMUP CMP	0.3	0.1	0.1	0.0	1.7	0.0	0.2	2.4	1.0
CMUP CMX	0.8	0.2	0.2	0.1	6.3	0.0	0.3	7.8	5.0
CMUP CMXMsKs	0.1	0.0	0.0	0.0	1.0	0.0	0.1	1.3	3.0
CMUP BMU	0.2	0.0	0.0	0.0	2.1	0.0	0.0	2.4	2.0
CMUP CMIOCES	1.3	0.3	0.3	0.2	7.8	0.0	0.4	10.2	16.0
CMUP CMIOPES	0.3	0.1	0.1	0.0	4.2	0.0	0.7	5.3	10.0
CMX CMP	0.1	0.0	0.0	0.0	1.1	0.0	0.0	1.3	1.0
CMX CMX	0.2	0.0	0.0	0.0	1.6	0.0	0.1	2.0	4.0
CMX CMXMsKs	0.1	0.0	0.0	0.0	0.6	0.0	0.0	0.7	0.0
CMX BMU	0.1	0.0	0.0	0.0	1.1	0.0	0.0	1.2	4.0
CMX CMIOCES	0.6	0.1	0.1	0.1	5.0	0.0	0.2	6.0	6.0
CMX CMIOPES	0.1	0.0	0.0	0.0	1.8	0.0	0.2	2.2	4.0
CMXMsKs CMP	0.0	0.0	0.0	0.0	0.7	0.0	0.0	0.7	0.0
CMXMsKs CMXMsKs	0.0	0.0	0.0	0.0	0.3	0.0	0.0	0.3	0.0
CMXMsKs BMU	0.0	0.0	0.0	0.0	0.5	0.0	0.0	0.5	0.0
CMXMsKs CMIOCES	0.0	0.0	0.0	0.0	1.1	0.0	0.0	1.2	2.0
CMXMsKs CMIOPES	-0.0	0.0	0.0	0.0	0.8	0.0	0.2	1.0	0.0
CMP CMP	0.0	0.0	0.0	0.0	0.2	0.0	0.0	0.2	1.0
CMP BMU	0.0	0.0	0.0	0.0	0.2	0.0	0.0	0.2	0.0
CMP CMIOCES	0.2	0.0	0.0	0.0	1.0	0.0	0.0	1.2	2.0
CMP CMIOPES	0.0	0.0	0.0	0.0	0.3	0.0	0.2	0.6	0.0
LBE CrkTrk	3.9	0.5	0.4	0.6	18.5	0.5	2.8	27.2	29.0
PHX CrkTrk	1.1	0.2	0.1	0.1	7.1	0.9	1.8	11.3	11.0
CMUP CrkTrk	1.8	0.2	0.2	0.3	6.9	0.1	1.1	10.5	13.0
CMP CrkTrk	0.2	0.0	0.0	0.0	0.8	0.0	0.5	1.6	0.0
CMX CrkTrk	0.8	0.1	0.1	0.1	3.0	0.1	0.8	5.0	3.0
CMXMsKs CrkTrk	0.1	0.0	0.0	0.0	0.6	0.0	0.1	0.8	2.0
Total:	20.1	3.8	3.2	2.8	147.3	8.1	27.7	213.0	263.0

Table 31: Expected and observed yields in the Low $\not\!\!E_{T\,\mathrm{sig}}$ region.

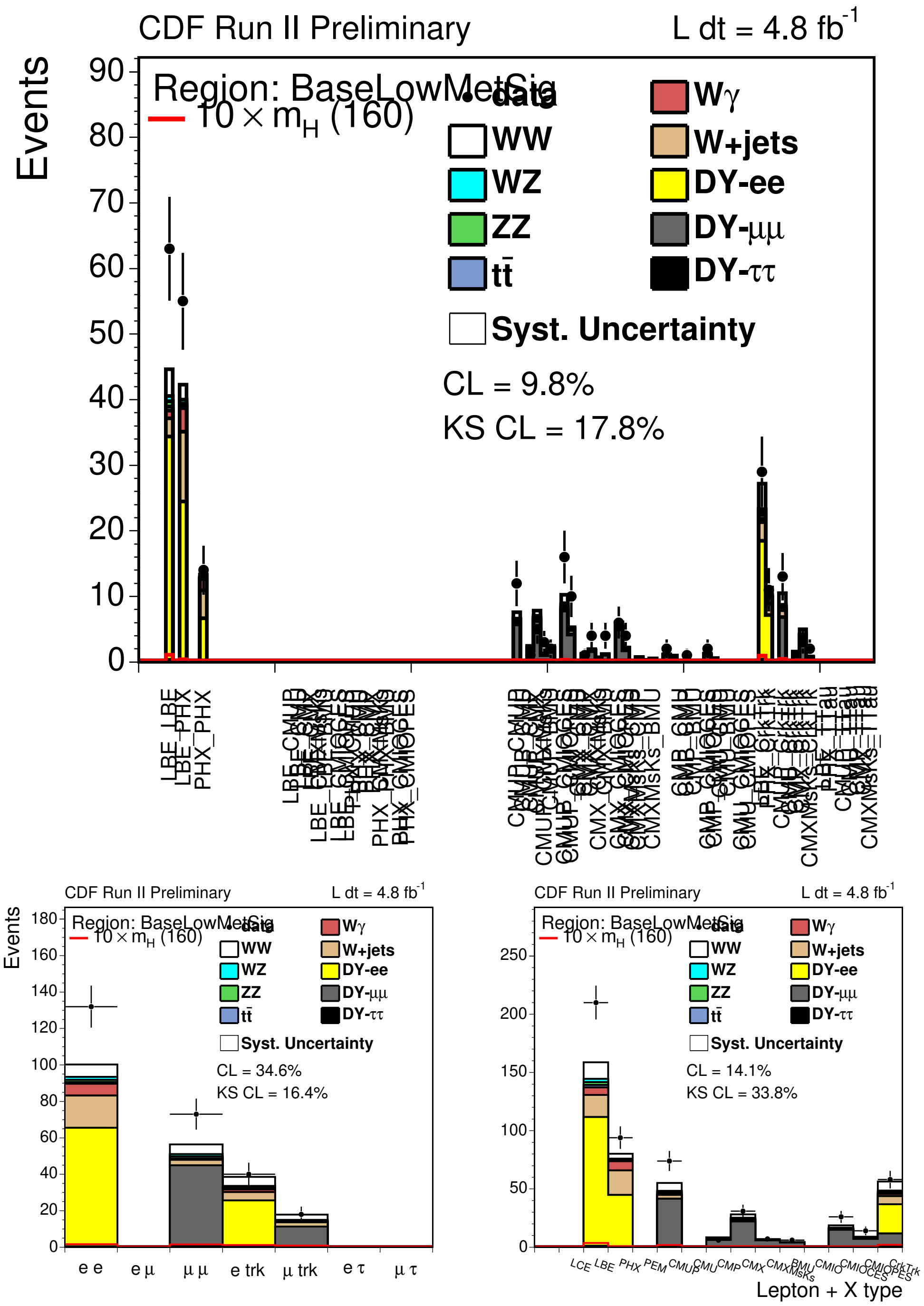

Figure 15: Base Low $\not\!\!E_{T\,\mathrm{sig}}$ control region.

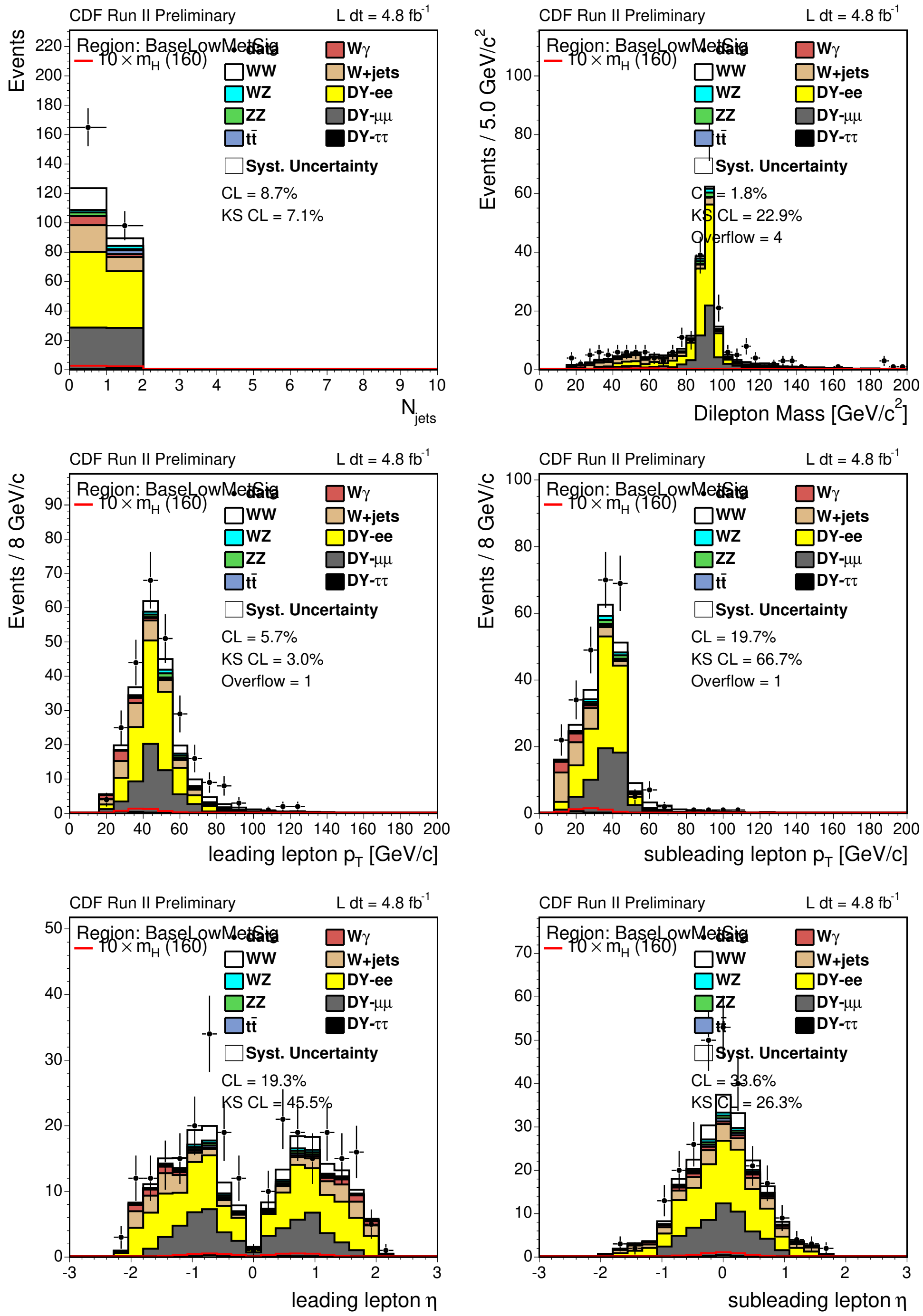

Figure 16: Base Low $\not\!\!E_{T\,\mathrm{sig}}$ control region.

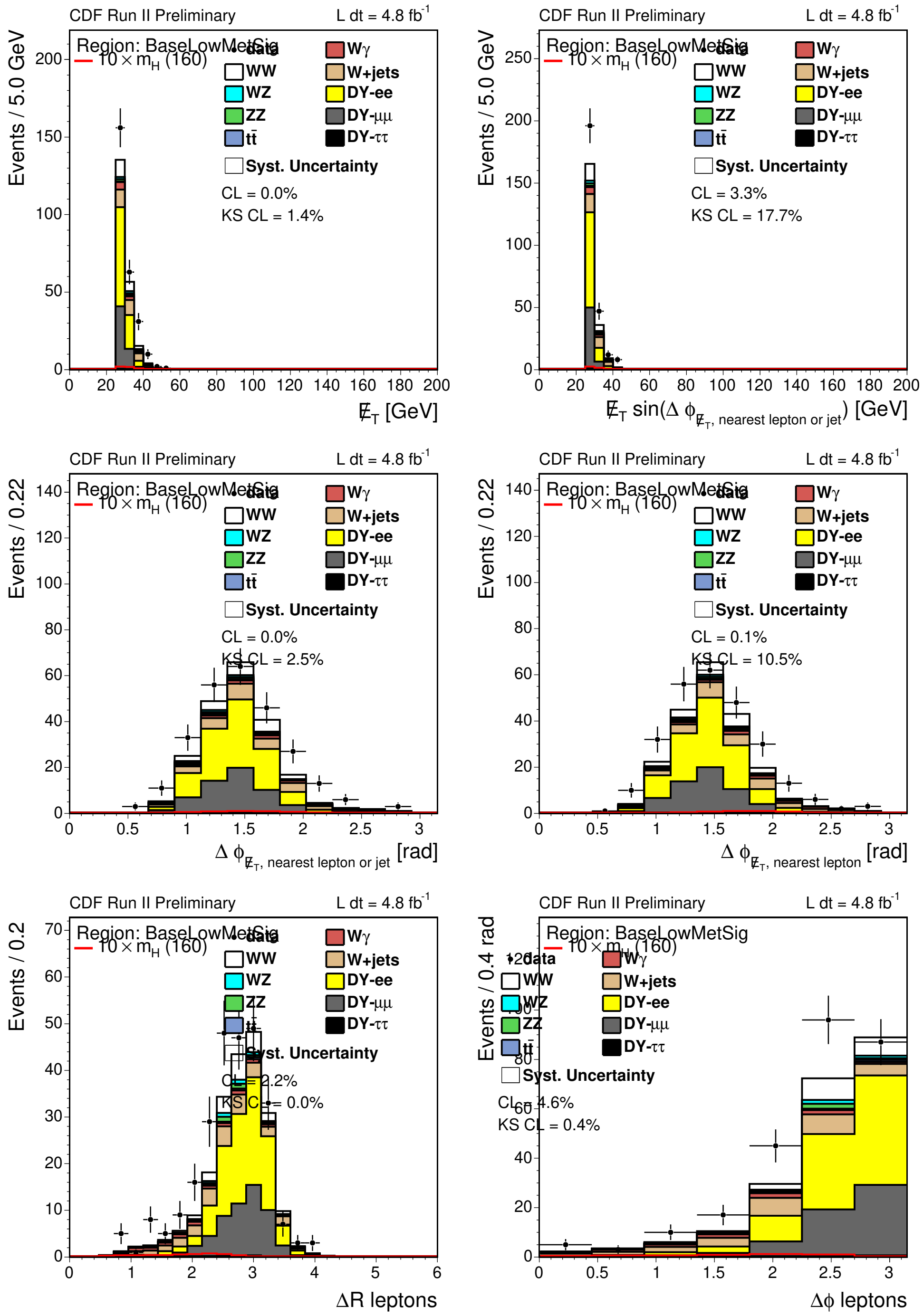

Figure 17: Base Low $\not{E}_{T\,\mathrm{sig}}$ control region.

Category	WW	WZ	ZZ	$t\bar{t}$	DY	$W\gamma$	W+jets	Total	Data
e e	9.0	2.4	2.0	1.2	120.8	6.1	15.6	157.1	142.0
e μ	14.1	0.6	0.2	1.6	85.9	3.9	15.6	121.8	81.0
μ μ	6.8	1.6	1.6	1.1	96.1	0.0	4.4	111.5	152.0
e trk	6.4	1.0	0.8	1.0	104.6	1.4	6.3	121.5	108.0
μ trk	3.9	0.5	0.4	0.6	19.7	0.2	4.0	29.3	38.0
Total:	40.2	6.1	5.0	5.5	427.1	11.6	45.9	541.3	521.0

Category	WW	WZ	ZZ	$t\bar{t}$	DY	$W\gamma$	W+jets	Total	Data
LBE LBE	5.4	1.3	1.2	0.9	62.0	1.0	2.7	74.5	74.0
LBE PHX	3.1	0.9	0.7	0.3	47.7	3.9	8.4	65.1	55.0
PHX PHX	0.4	0.2	0.1	0.0	11.1	1.2	4.5	17.6	13.0
LBE CMUP	4.0	0.2	0.0	0.5	27.0	0.6	2.5	34.8	24.0
LBE CMP	0.6	0.0	0.0	0.1	3.1	0.1	2.2	6.0	2.0
LBE CMX	1.8	0.1	0.0	0.2	10.9	0.1	1.3	14.6	10.0
LBE CMXMsKs	0.3	0.0	0.0	0.0	1.9	0.0	0.3	2.5	3.0
LBE BMU	0.5	0.0	0.0	0.0	2.5	0.1	0.0	3.1	0.0
LBE CMIOCES	2.8	0.1	0.0	0.3	11.4	0.2	0.5	15.4	13.0
LBE CMIOPES	0.9	0.0	0.0	0.1	4.7	0.1	0.7	6.6	1.0
PHX CMUP	1.2	0.1	0.0	0.1	8.5	1.2	3.9	15.0	9.0
PHX CMP	0.2	0.0	0.0	0.0	0.8	0.1	1.0	2.1	2.0
PHX CMX	0.5	0.0	0.0	0.0	6.4	0.6	0.9	8.6	6.0
PHX CMXMsKs	0.1	0.0	0.0	0.0	0.7	0.1	0.3	1.2	0.0
PHX BMU	0.2	0.0	0.0	0.0	1.7	0.1	0.0	2.0	1.0
PHX CMIOCES	0.8	0.0	0.0	0.1	2.8	0.4	0.5	4.6	9.0
PHX CMIOPES	0.3	0.0	0.0	0.0	3.5	0.2	0.5	4.5	1.0
CMUP CMUP	1.2	0.3	0.3	0.2	10.6	0.0	0.3	12.8	20.0
CMUP CMP	0.3	0.1	0.1	0.1	3.2	0.0	0.1	3.9	2.0
CMUP CMX	1.2	0.2	0.2	0.2	9.9	0.0	0.4	12.1	12.0
CMUP CMXMsKs	0.1	0.0	0.0	0.0	1.8	0.0	0.1	2.1	5.0
CMUP BMU	0.3	0.1	0.1	0.0	9.8	0.0	0.1	10.3	18.0
CMUP CMIOCES	1.4	0.4	0.4	0.3	13.1	0.0	0.3	15.9	31.0
CMUP CMIOPES	0.4	0.1	0.1	0.1	13.0	0.0	1.3	14.9	19.0
CMX CMP	0.2	0.0	0.0	0.0	2.9	0.0	0.1	3.2	3.0
CMX CMX	0.2	0.1	0.1	0.0	2.9	0.0	0.1	3.3	5.0
CMX CMXMsKs	0.1	0.0	0.0	0.0	1.3	0.0	0.0	1.4	2.0
CMX BMU	0.1	0.0	0.0	0.0	4.1	0.0	0.1	4.4	4.0
CMX CMIOCES	0.7	0.2	0.2	0.1	7.1	0.0	0.1	8.3	7.0
CMX CMIOPES	0.2	0.1	0.0	0.0	7.1	0.0	0.7	8.1	7.0
CMXMsKs CMP	0.0	0.0	0.0	0.0	0.5	0.0	0.1	0.6	0.0
CMXMsKs CMXMsKs	0.0	0.0	0.0	0.0	0.4	0.0	0.0	0.4	1.0
CMXMsKs BMU	0.0	0.0	0.0	0.0	0.9	0.0	0.0	1.0	0.0
CMXMsKs CMIOCES	0.1	0.0	0.0	0.0	1.0	0.0	0.0	1.2	4.0
CMXMsKs CMIOPES	0.0	0.0	0.0	0.0	1.1	0.0	0.2	1.3	1.0
CMP CMP	0.0	0.0	0.0	0.0	0.5	0.0	0.0	0.6	0.0
CMP BMU	0.1	0.0	0.0	0.0	1.0	0.0	0.0	1.0	3.0
CMP CMIOCES	0.2	0.0	0.0	0.0	2.2	0.0	0.0	2.5	5.0
CMP CMIOPES	0.0	0.0	0.0	0.0	1.9	0.0	0.1	2.0	3.0
LBE CrkTrk	5.2	0.8	0.6	0.8	80.7	0.6	3.9	92.7	81.0
PHX CrkTrk	1.2	0.3	0.2	0.1	23.9	0.8	2.4	28.9	27.0
CMUP CrkTrk	2.5	0.3	0.3	0.4	10.6	0.1	2.5	16.6	27.0
CMP CrkTrk	0.3	0.0	0.0	0.0	1.1	0.0	0.4	1.8	2.0
CMX CrkTrk	1.0	0.2	0.1	0.2	7.4	0.1	0.9	9.9	8.0
CMXMsKs CrkTrk	0.1	0.0	0.0	0.0	0.6	0.0	0.3	1.1	1.0
Total:	40.2	6.1	5.0	5.5	427.1	11.6	44.7	540.2	521.0

Table 32: Expected and observed yields in the Base Low $\not\!\!E_{T spec}$ High $\not\!\!E_T$ region.

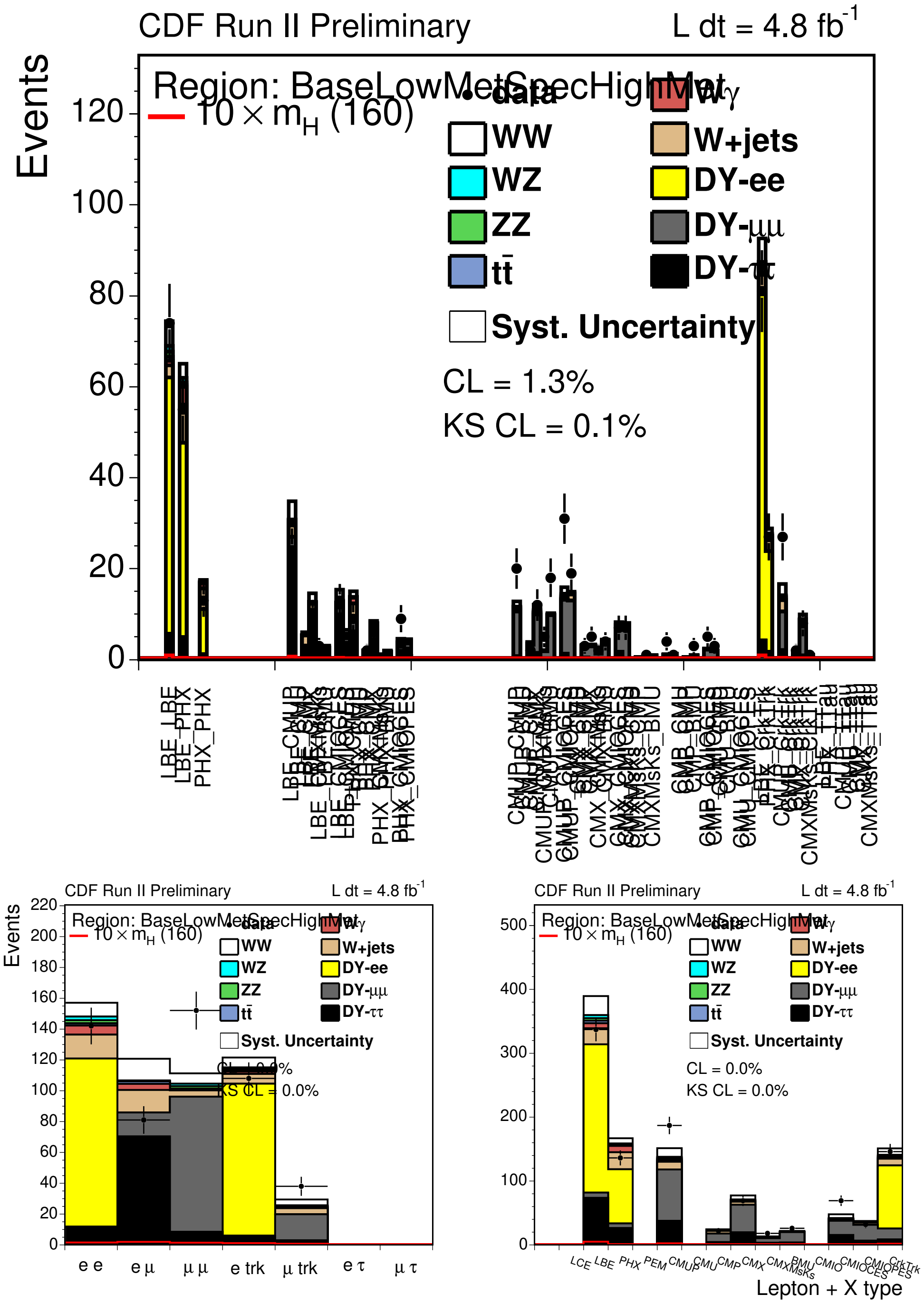

Figure 18: Base Low $\not{E}_{T spec}$ High $\not{E}_T$ control region.

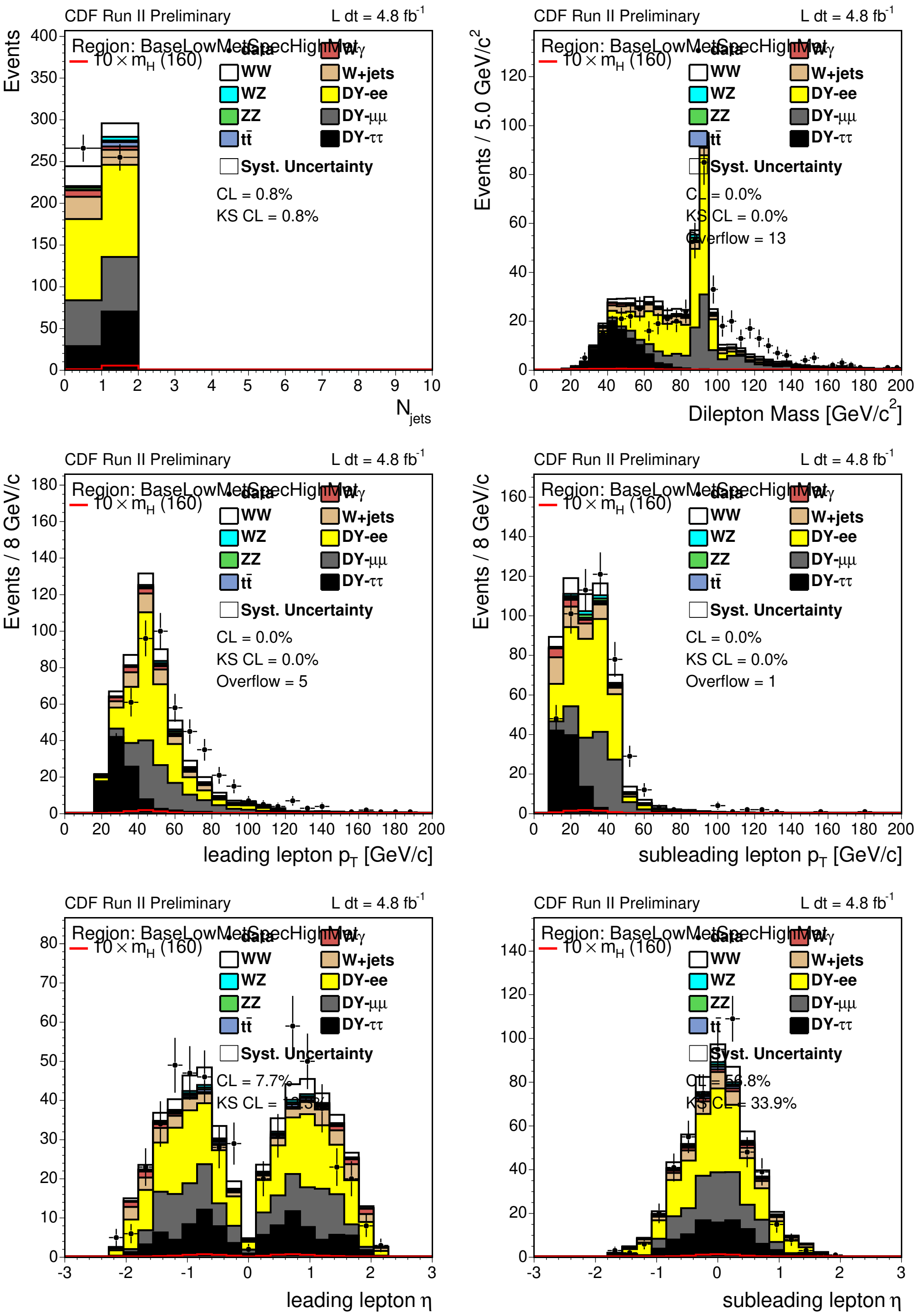

Figure 19: Base Low $\not\!\!E_{T spec}$ High $\not\!\!E_T$ control region.

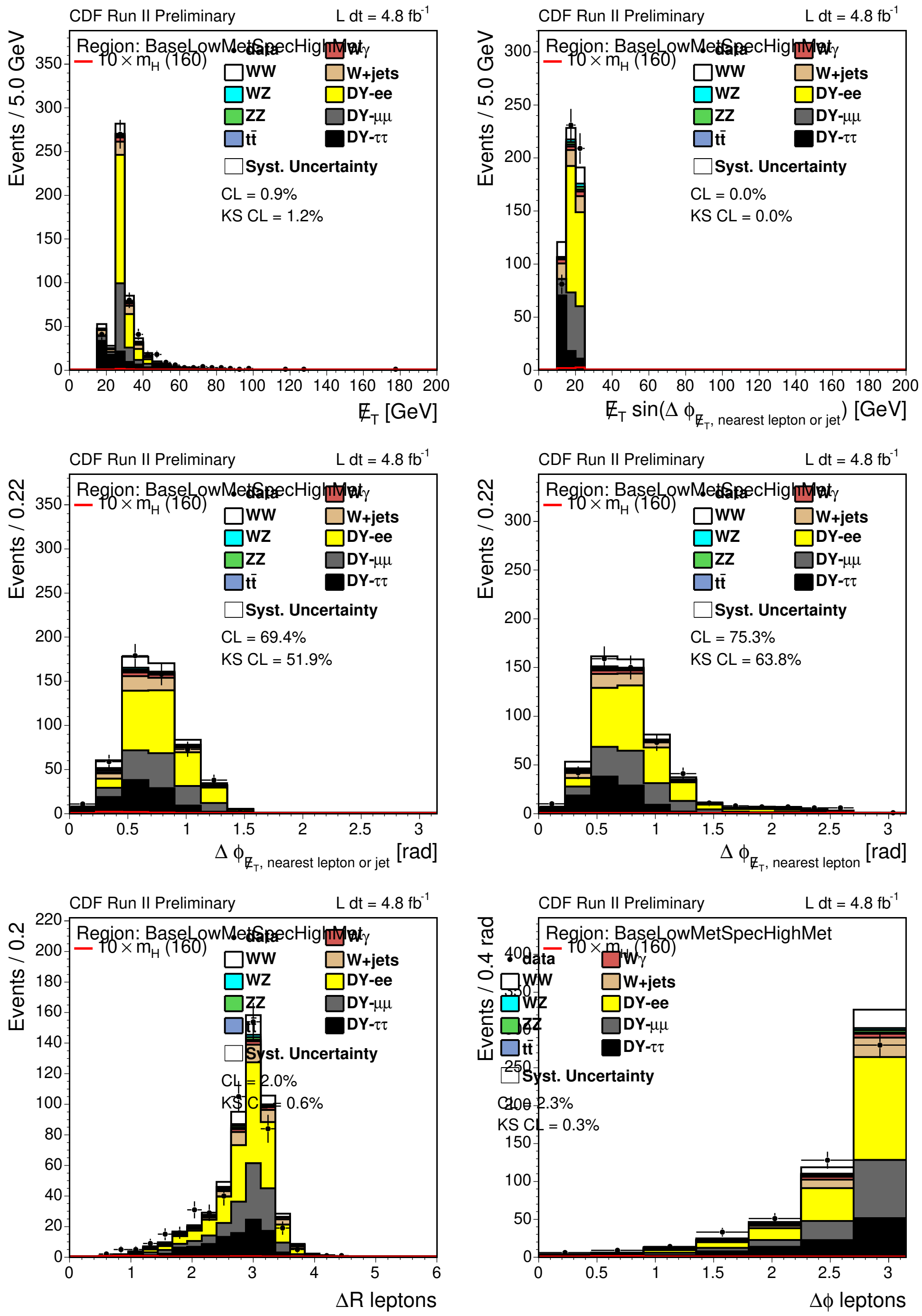

Figure 20: Base Low $\not{E}_{Tspec}$ High $\not{E}_T$ control region.

6 Systematics

Sources of systematic uncertainty for this analysis are the same as those for the previous analysis using 4.8 fb^{-1} [1]. There are no new systematic uncertainties associated with the likelihood based electrons. For convenience, some of the systematic studies which are new since the analysis detailed in [7] are repeated here.

Systematic uncertainties may effect both the normalization (or "rate") and the shape of the templates used in the limit calculation. As propagating the effects of shape uncertainties is CPU intensive, we only consider shape uncertainties for those expected to be significant. At this time the shape uncertainties considered in order of expected significance are the jet energy scale (JES) and initial state radiation (ISR). These studies are described below in Section 6.6. After evaluating the shapes, we decided to not apply any shape uncertainties at this point.

The rate systematics are determined separately for each opposite-sign jet channel and separately for the same-sign channel. Systematics relating only to the same-sign channel are discussed below in Section 6.5. The summary of all systematics are presented in Tables 41-42 for the 0 jet channel, Tables 47-48 for the 1 jet channel, Tables 53-54 for the 2 or more jets channel, and Tables 62-63 for the same-sign channel.

6.1 Cross Section Systematics

For the background processes, we take the theoretical uncertainties on the cross sections, which are calculated to either next-to-next-to-leading order ($t\bar{t}$ with $m_{top} = 172.4$ GeV [8]), next-to-leading order (WW [9], WZ and ZZ [10]), or leading order with estimated higher order corrections ($W\gamma$ [11] and Drell-Yan). Of the signal processes, VH and VBF are electroweak processes. VH are known to NNLO, so the theoretical uncertainty on these cross sections is small, less than 5% [12]. VBF is known only to NLO, so the residual theoretical uncertainty is estimated to be less than 10% [12].

Gluon fusion is a QCD process, so even though it is known to NNLO, the theoretical uncertainty is larger. Also important, since we divide our events by jet multiplicity, the theoretical uncertainty on the higher multiplicity jet bins is larger than the uncertainty on the inclusive cross section calculation. There exist several programs which compute the theoretical cross section for $gg \to H$ production at the Tevatron to NNLO. The previous zero and one jets version of this analysis used the FEHiP program [13]. For these studies we use the HNNLO program [14, 15, 16], which has the advantage that it makes user-specified histograms of kinematic variables. HNNLO also allows the user to define analysis selection cuts, but for these studies we do not use any selection cuts in HNNLO. Because the Higgs is a pseudo-scalar, we expect the effects on its kinematic variables to be limited to p_{T} and rapidity.

There are two main independent sources of theoretical uncertainty; other sources were found to be negligible [17]. These are the following: uncalculated higher-order QCD radiative corrections, and knowledge of the parton distributions. To estimate the size of the QCD corrections, we use a method commonly used in perturbative QCD calculations, which is to vary the renormalization and factorization scales (μ_R and μ_F respectively). Comparing NNLO calculations from FEHiP to recent N^{3}LO calculations [18, 19] shows the best value for NNLO predictions is to set $\mu_R = M_H/2$. Another reasonable choice is to set the factorization and normalization scales to be equal. For these studies, our default scale setting is $\mu_R = \mu_F = M_H/2$. We also use the MRST2004 PDFs as our default [20, 21].

To determine the uncertainty on the $gg \to H$ cross section due to higher order QCD corrections, we used $M_H = 160$ and varied the scale from the default setting of $M_H/2 = 80$ down to $M_H/4 = 40$ and up to $M_H = 160$. The resulting change in the NNLO Higgs p_{T} and η distributions are shown in Fig. 21 and the change in the total cross section is given in Tab. 33 (top). We see the calculated cross section changes by $\sim 11.6\%$ in going from $\mu_R = \mu_F = M_H/2$ to $\mu_R = \mu_F = M_H/4$, and by $\sim 10.2\%$ in going from $\mu_R = \mu_F = M_H/2$ to $\mu_R = \mu_F = M_H$. Thus we take the average change of 10.9% as the uncertainty on the $gg \to H$ cross section due to scale variations, or higher order QCD corrections. This is consistent with the theoretical uncertainty expected by theorists.

The second uncertainty on the cross section is due to our knowledge of the parton distributions. For $gg \to H$ production, we are specifically interested in the gluon luminosities. To determine this uncertainty, we calculate the Higgs cross section using PDFs with different gluon luminosities. Unfortunately these do not exist at NNLO, but only at NLO. In the HNNLO program, we have available the NLO MRST99 PDFs with central gg luminosity, higher gg luminosity, and lower gg luminosity [22, 21]. The changes in the NLO Higgs p_{T} and η distributions are shown in Fig. 22 and the change in the total cross section is given in Tab. 33 (bottom). We see the calculated cross section changes by $\sim 4.8\%$ in going from central to lower gluon luminosity, and $\sim 5.4\%$ in going from central to higher gluon luminosity. Thus we take the average change of 5.1% as the uncertainty on the cross section due to knowledge of the parton distributions.

The total $gg \to H$ cross section uncertainty is the addition in quadrature of these two independent uncertainties, or 12.0%. This systematic uncertainty is independent of the number of jets in the final state.

6.2 Acceptance Systematics

As previously, the lepton ID and trigger efficiencies are varied coherently up and down to determine their affect on the acceptance. Both uncertainties have a small effect, for the most part around 2%, on the signal and background processes. Lepton ID systematics are determined separately for each jet channel, while the trigger efficiencies are determined inclusively. Except for the $gg \to H$ signal process, as explained in Section 6.3, the PDF model uncertainties are determined using the standard CTEQ6M uncertainties and are the same across different channels. The PDF model systematics on VH and VBF production

Scale variations			
$\mu_R = \mu_F =$	40	80	160
NNLO cross section (fb)	4.895 ± 0.103	4.385 ± 0.058	3.936 ± 0.035
Gluon luminosity variations			
	lower gg	central gg	higher gg
NLO cross section (fb)	3.074 ± 0.006	3.228 ± 0.006	3.403 ± 0.007

Table 33: Changes in the value of the cross section calculated by HNNLO due to theoretical uncertainties. The top rows show the change in the NNLO calculation due to different values of the renormalization and factorization scales. The bottom rows show the change in the NLO calculation due to different gluon luminosities.

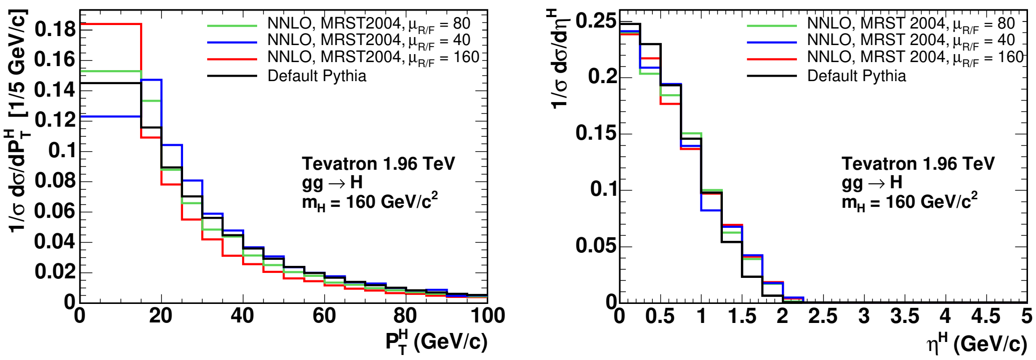

Figure 21: Changes calculated by the HNNLO program when the scales μ_R and μ_F are varied from $M_H/2$ to $M_H/4$ and M_H. On the left is the NNLO Higgs $p_{\rm T}$ distribution, while on the right is the Higgs rapidity distribution. The black lines show the distributions in default $gg \to H$ Pythia with $M_H = 160$.

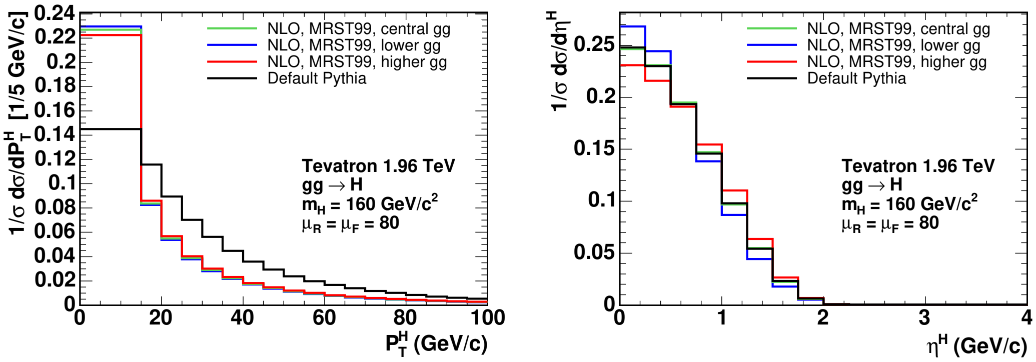

Figure 22: Changes calculated by the HNNLO program for different values of the gluon luminosity. On the left is the NLO Higgs p_{T} distribution, while on the right is the Higgs rapidity distribution. The black lines show the distributions in default $gg \to H$ Pythia with $M_H = 160$.

modes are taken from the studies done for the $H \to \tau\tau$ analysis, CDF Note 9179 [23].

We also consider the effect of the differences between LO and higher order calculations on the acceptance. We determine the size of higher order effects by comparing a LO Pythia WW sample to the WW MC@NLO sample. We take half of this difference (5%) as a systematic on the WW process, but assign the full difference (10%) to the processes simulated only by LO Pythia. For those MC samples with a restricted run range (the WW MC@NLO, $t\bar{t}$, and $W\gamma$ samples) we assign an additional uncertainty which is determined as described in the WW paragraph of Section 4.1. The $W\gamma$ process has an additional 20% systematic uncertainty on the MC modeling of conversions, based upon the studies in CDF Note 8073 [24].

The uncertainties on the modeling of $\not\!\!E_T$ has been shown in previous versions of this analysis to be very small for processes with real $\not\!\!E_T$. However, for the DY process which has no real $\not\!\!E_T$, we look in the DY control region described in Section 5.1 to estimate how well the MC models jets and $\not\!\!E_T$ for a process with no jets at LO. Based on the rate discrepancies seen in this control region, we assign a DY $\not\!\!E_T$ and jet modeling systematic of between 21-32% for each jet channel. For other processes modeled by MC which have no jets at LO (WW and $W\gamma$), we assume a systematic uncertainty of 20% in the 2 or more jets channel and evaluate the number of events moving between all three jet bins.

The only uncertainty on the W+jets process, which is determined from data, is the uncertainty on the fake rate of the jets. We estimate this uncertainty by varying the fake rates with their assigned uncertainties (shown by the solid light grey bands in Figures 7-8). These variations have different effects in the high S/B and low S/B categories due primarily to the smaller sample size of the high S/B categories. The standard luminosity uncertainty of 5.9% is assigned to all processes except for W+jets.

6.3 $gg \to H$ Acceptance Systematics

The $gg \to H$ acceptance also depends on the cross section. In the previous zero and one jet analysis, the Higgs acceptance systematic was estimated by reweighting the Higgs p_{T} spectrum in Pythia to match an NLO calculation from FEHiP, with $\mu_R = \mu_F = 82.5$. This reweighting led to acceptance changes of less than 10%. With this analysis, we again use the Higgs p_{T} spectrum from Pythia as the default and estimate the acceptance systematic by reweighting Pythia to match the calculations from HNNLO. This time, we reweight in the Higgs p_{T} and also, separately, the Higgs η distribution.

The effect of the Higgs p_{T} reweighting depends on how many jets are in the final state. By reweighting the Higgs p_{T} spectrum, we are reweighting the vector sum of the p_{T} of the two jets which are recoiling against the Higgs. The Pythia Higgs p_{T} spectrum is harder than that generated by HNNLO, so when we reweight Pythia to match HNNLO, events which previously had one or more jets passing selection cuts will move into a lower jet bin. There is more signal in the 0 and 1 jet bins, so the fractional percentage change there is smaller than in the 2+ jet bin. Because this reweighting is effectively moving events back and forth between the 0, 1, and 2+ jet bins, these acceptance systematics (referred to as "Scale (jets)" and "PDF Model (jets)" in the systematics tables) are anticorrelated between the jet bins.

The effect of the Higgs η distribution reweighting also depends on jet bin, again because the fractional percentage change is larger in the 2+ jets bin where there are fewer signal events to begin with. However, this reweighting does not appear to move events between different jet bins. The Higgs η distribution in Pythia is more central than the one generated by HNNLO, so when we reweight Pythia to match HNNLO, we move some of the leptons outside of our forward acceptance. These acceptance systematics, referred to as "Scale (leptons)" and "PDF Model (leptons)" in the systematics tables, are correlated among the jet bins.

For the acceptance systematic from the choice of scale, we use our default NNLO calculation with MRST2004 PDFs and $\mu_R = \mu_F = 80$. We divide the Higgs p_{T} and η distributions from HNNLO by the same distributions from our default $gg \to H$ Pythia sample, at $M_H = 160$. We then reweight the Pythia sample using this ratio histogram. The ratio histograms for the MRST2004 HNNLO sample are shown in Fig. 23. The changes in acceptance after reweighting are given in Tab. 34 (top). As expected, reweighting in η moves events out of our acceptance range, resulting in a decrease of events in all jet bins.

We also use HNNLO to calculate a systematic on the Higgs acceptance due to gluon luminosity/PDF model. This time we use the NLO MRST99 PDFs with $\mu_R = \mu_F = 80$. Again we divide the HNNLO distributions by Pythia and use the ratio histograms to reweight the Pythia. This is an older NLO calculation, so we do not look at the acceptance change from the default Pythia to each of the three gg luminosity models. Instead, we reweight Pythia to match the central gg model and take that as our default for these studies. Then we reweight Pythia to match the higer and lower gg models, and look at the acceptance change from the central gg model. The ratio histograms for all three HNNLO samples are shown in Fig. 24. The changes in acceptance after reweighting are given in Tab. 34. As expected, the total uncertainty is similar for reweighting the gg luminosity up or down. As the final $gg \to H$ acceptance systematic due to the PDF model, we use the average of the absolute value of the changes with higher and lower gluon luminosities.

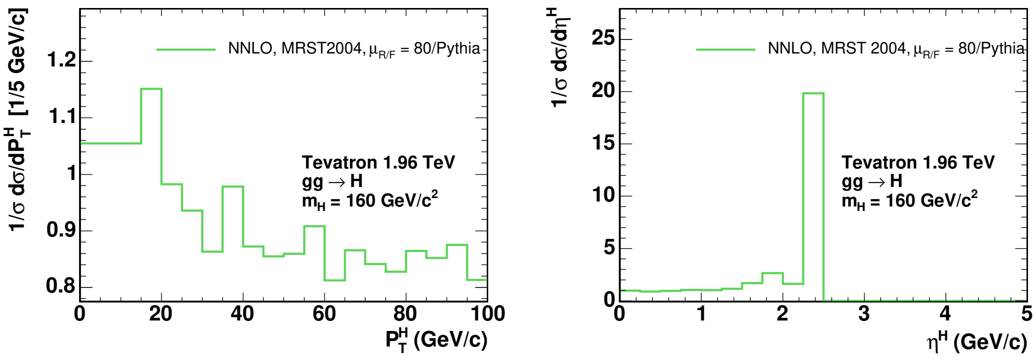

Figure 23: Ratio between default $gg \to H$ Pythia and the calculations of the HNNLO program using the NNLO MRST2004 PDFs with $M_H = 160$ and the scales $\mu_R = \mu_F = 80$. On the left is the ratio used to reweight the Higgs p_{T} distribution, while on the right is the ratio used to reweight the Higgs rapidity distribution.

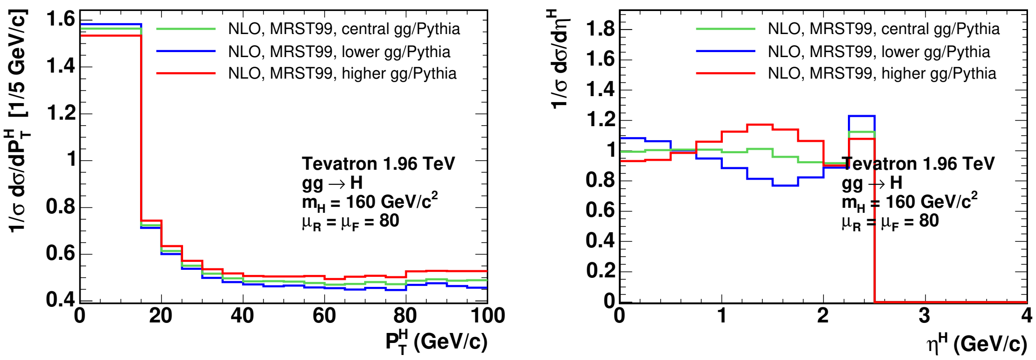

Figure 24: Ratio between default $gg \to H$ Pythia and the calculations of the HNNLO program using the NLO MRST99 PDFs with different gluon luminosities. On the left are the ratios used to reweight the Higgs p_{T} distribution, while on the right are the ratios used to reweight the Higgs rapidity distribution.

Choice of scale		
	Fractional (%) acceptance change	
Jet bin	Reweight p_{T}	Reweight η
0 jet	$+4.60\%$	-2.46%
1 jet	-5.07%	-2.78%
2+ jets	-8.74%	-3.05%
Gluon luminosity variations		
	Fractional (%) acceptance change	
Lower gg	Reweight p_{T}	Reweight η
0 jet	$+0.76\%$	$+1.57\%$
1 jet	-1.56%	$+1.75\%$
2+ jets	-2.32%	$+2.06\%$
Higher gg	Reweight p_{T}	Reweight η
0 jet	-1.09%	-1.49%
1 jet	$+2.19\%$	-1.65%
2+ jets	$+3.18\%$	-1.90%
Average Change	Reweight p_{T}	Reweight η
0 jet	0.93%	1.53%
1 jet	1.88%	1.70%
2+ jets	2.75%	1.98%

Table 34: Fractional (%) change in the $gg \to H$ acceptance in different jet bins due to the cross section. The top rows show the change in the acceptance after reweighting the Pythia Higgs p_T and η spectra to match the spectra from HNNLO, using the MRST2004 PDFs and $\mu_R = \mu_F = 80$ for $M_H = 160$. The bottom rows show the change in the acceptance after reweighting the Pythia Higgs p_T spectrum to PDFs with higher or lower gluon luminosities. The **Average Change** is the average of the absolute value of the changes with higher and lower gluon luminosities. The average changes are used for the gluon PDF systematics.

Region	$m_t = 175$	$m_t = 172.4$
0 Jets	1.35 ± 0.05	1.54 ± 0.17
1 Jets	34.87 ± 0.23	34.67 ± 0.84
2+ Jets	229.5 ± 0.6	222.2 ± 2.1

Table 35: Summary of $t\bar{t}$ events in the three opposite-sign signal regions for two $t\bar{t}$ Pythia samples: one generated with a top mass of 175 GeV, and one generated with a top mass of 172.4 GeV. The sample with $m_t = 172.4$ has much smaller statistics, so the statistical uncertainty on the number of events is much higher.

6.4 2 or More Jets Systematics

As explained in Section 9, the signal region with two or more reconstructed jets employs b-tagging to reduce $t\bar{t}$ background. When we apply b-tagging to our $t\bar{t}$ background model, we use the standard Data/MC efficiency scale factor correction for b-tagging which we take to be 0.94 ± 0.07. Half of this uncertainty is taken as an additional systematic, under the heading b-tag Veto as shown in Table 53.

An additional uncertainty comes from the new $t\bar{t}$ cross section prediction, which is calculated using a recent world average value for the top quark mass of 172.4 GeV [25]. Our $t\bar{t}$ MC sample was generated with a top quark mass of 175 GeV. To check how much of an effect the top quark mass has on the acceptance, we generated a small run independent $t\bar{t}$ sample with a top mass of 172.4 GeV. The resulting number of events in each of our signal regions are given in Table 35. The effect is negligible for events with zero or 1 jets. For events with 2 or more jets, we apply a scale factor of $222.2/229.5 = 0.968$ and assign a systematic uncertainty of 1.5% to be added in quadrature with the b-tag Veto uncertainty.

There is another systematic uncertainty to consider. We do not require data events to be in the silicon good run list. The only issue with this that could arise is that our Data/MC scale factor may not be properly scaling for events which fail b-tag requirements because they do not have silicon hits; the MC assumes there is always good silicon. To account for this, we look at the number of events in the data sample which come in on each good run list, as shown in Table 36. There are only 3 events not in the silicon good run list which have a b-tagged jet as found by SecVtx.

We then look only at the events in the silicon good run list. In this sample, the ratio of anti-b-tagged events to b-tagged events is 204:156. If the same ratio held true for events not in the silicon good run list (as the MC scale factor assumes it does), we would expect of the 23 events not in the silicon good run list that the ratio of anti-b-tagged events to b-tagged events should be 13:10. The observed ratio is actually 20:3, as shown in Table 36. Continuing with the thought, if we had only good Si runs we would expect $204 + 13 = 217$ events in the anti-b-tagged region, while our data show 224 events. In the same way, we expect $156 + 10 = 166$ events in the b-tagged region but see only 159 events.

2+ Jets Region	Number of Events
Total	383
Total b-tagged	159
Total anti-b-tagged	224
Total not in EM_SI	23
Total b-tagged not in EM_SI	3
Total anti-b-tagged not in EM_SI	20

Table 36: Summary of events with and without a b-tagged jet in the 2 or more jets signal region and which good run list they are selected in.

We therefore correct our MC prediction in the 2 or more jets signal region by scaling it up by the ratio $224/217 = 1.0323$, and in the b-tagged $t\bar{t}$ control region by scaling it down by $159/166 = 0.9578$. We take about half of the change in the signal region as an additional systematic to be added in quadrature with the b-tag Veto uncertainty.

6.5 Same-Sign Systematics

Most of the systematics for the same-sign channel are the same as those in the opposite sign channels. Because we do not make a $\not\!\!E_{\mathrm{T}}$ cut, we do not have a systematic due to $\not\!\!E_{\mathrm{T}}$ modeling. We have one extra systematic based on the ability of Monte Carlo to model charge mismeasurement, as described below.

WW, Drell-Yan, and $t\bar{t}$ contribute to the same-sign analysis only when the charge of a lepton is mismeasured[2]. These backgrounds are estimated using Monte Carlo samples; this assumes that the MC accurately models how often lepton charges are mismeasured in the data.

To test this assumption, we attempt to measure a charge fake rate from the data. We select events in the Drell-Yan control region, described in Sec. 5.1, which should have minimal contamination from other backgrounds such as W+jets, where same-sign events come from QCD rather than charge mismeasurement. We then repeat the procecure of counting the number of opposite-sign events and same-sign events, resulting in charge fake rates taken directly from the data. These CFR are shown in Table 37. Unfortunately the statistics are not large enough to reliably measure a CFR in the muon channels or for PHX electrons.

To determine the uncertainty on MC modeling of the charge fake rate, we compare the LBE-LBE and LBE-CrkTrk charge fake rates measured in data to those measured in MC. We subtract the MC CFR from the data CFR, and take half of that difference as the systematic. For LBE-LBE, this gives a systematic uncertainty of 16.2%, while for

[2]The case of $t\bar{t}$ where one lepton is missed and one of the b-jets fakes a lepton is included in the W+jets background.

Dilepton type	Opposite-sign events	Same-sign events	Charge fake rate
LBE-LBE	90969	68	7.48e-4
LBE-Central μ	64	4	0.0625
LBE-Forward μ	13	1	0.0769
LBE-CrkTrk	41151	17	4.13e-4
Central μ-Central μ	108870	0	–
Central μ-Forward μ	31543	5	1.59e-4
Central μ-CrkTrk	38903	2	5.14e-5
PHX-PHX	883	270	0.306
PHX-Central μ	82	54	0.659
PHX-Forward μ	12	11	0.917
PHX-CrkTrk	8431	1153	0.137
LBE-PHX	87014	10814	0.124

Table 37: Calculated charge fake rates (CFR) for all dilepton types in data, using the Drell-Yan control region. The lepton selection is described in the text. "Central μ" includes CMUP, CMP, CMX, CMXMsKs, CMIOCES, and CMP muons, while "Forward μ" includes CMIOPES and BMU muons.

LBE-CrkTrk the systematic uncertainty would be 1.6%. We take an uncertainty of 16.5% and apply it to the WW, $t\bar{t}$, and Drell-Yan backgrounds as shown in Table 62.

6.6 Shape Systematics

We consider two possible sources of systematics which would change the shape of the output NN distribution: jet energy scale (JES) and initial state radiation (ISR) or scale variations.

The jet energy scale is the correction factor applied to a measured jet to scale it back to the energy of the original parton [26]. We use the correction factors from the JetCorr15 package for L5 jets. To evaluate a systematic, we apply the $\pm 1\ \sigma$ variations given in this package, which increase or decrease the energy of the jets. The effect on the $gg \to H$ Pythia sample for $M_H = 160$ is shown in Fig. 25 for events with two or more jets in the final state. There is very little systematic change in the shape, and we do not take this as a shape systematic.

We use Pythia Tune A as our default for initial and final state radiation (for the process $gg \to H$, there is only ISR). To evaluate a systematic, we use Pythia $gg \to H$ samples at a Higgs mass of 160 with the ISR either increased or decreased from the default. For the zero or one jet case, where WW is the dominant background, we also study the effect of ISR on the WW shape. Although we use MC@NLO for WW in the analysis, for the purpose of looking at this systematic we use Pythia WW samples. The effect of increasing or decreasing ISR on the WW neural network output is shown in Fig. 26.

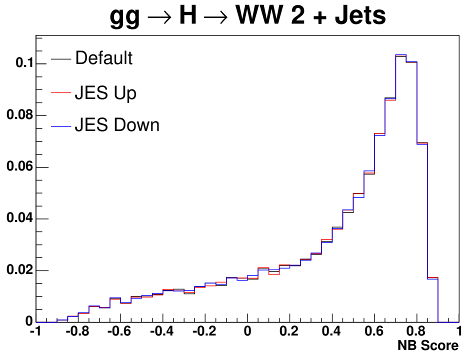

Figure 25: Effect of $\pm 1\ \sigma$ variations in the jet energy scale on the $gg \to H$ Pythia sample on the 2+ jets neural network output. The default shape is shown in black, while the higher JES is shown in red and the lower JES in blue.

The shape change is small, and has no effect on the limit at $M_H = 160$. The effect of increasing or decreasing ISR on the $gg \to H$ neural network output at $M_H = 160$ is shown in Fig. 27. Again the shape change is very small and has no effect on the limit.

Varying the scale of the renormalization and factorization scales is equivalent to varying the ISR in Pythia, and may be more reliable than the ISR for Higgs events in Pythia since the ISR was tuned on Z events in data. For events with two or more jets, we use the scale variations to check for a shape systematic in $gg \to H$. The shape variation for different scales is shown in Fig. 28. Again the shape variation is small and we do not expect it to affect the limits.

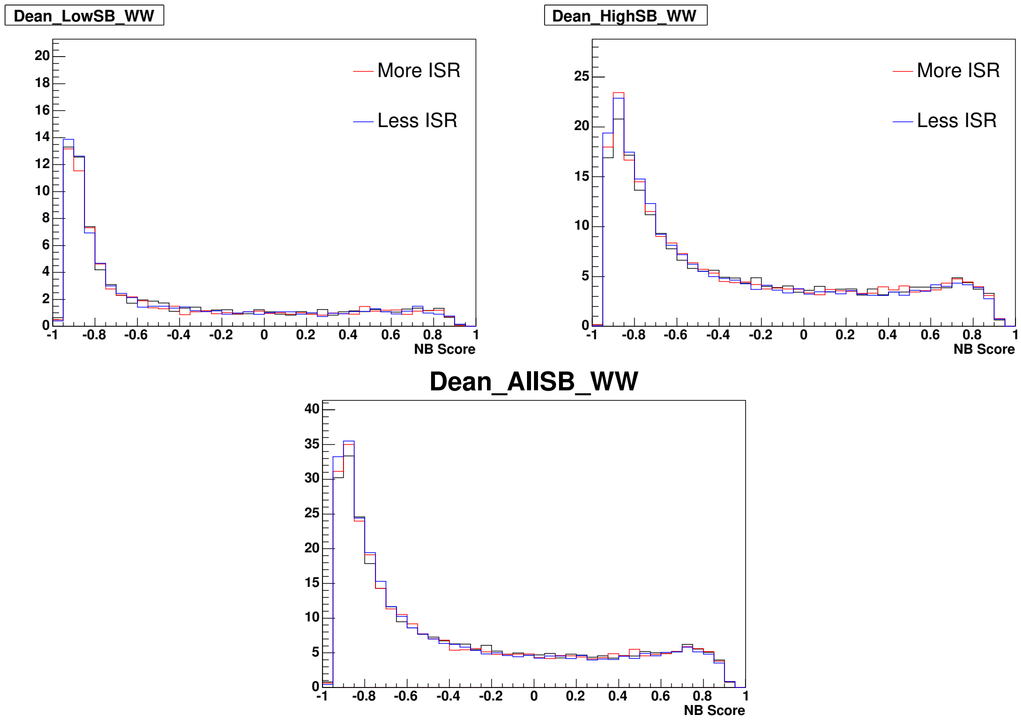

Figure 26: Effect of increasing or decreasing ISR in the WW Pythia sample on the zero or one jets neural network output for WW background. The default shape is shown in black, while more ISR is shown in red and less ISR in blue. The first plot shows the effect in the low SB region, the second plot shows the high SB region, and the third plot shows both regions combined.

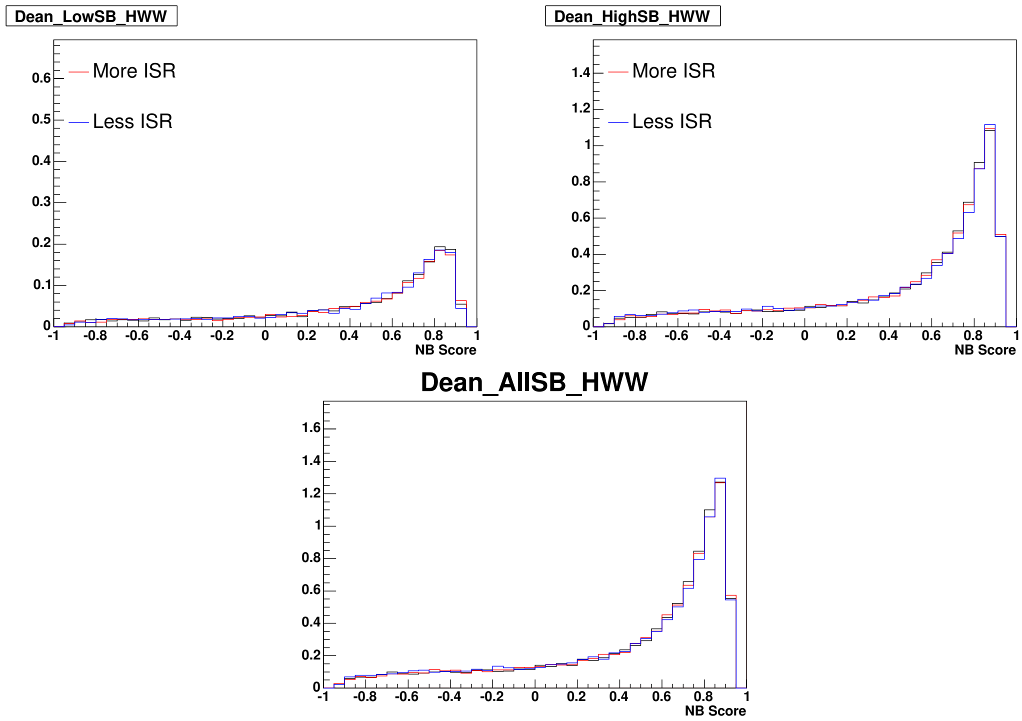

Figure 27: Effect of increasing or decreasing ISR in the $gg \to H$ Pythia sample on the zero or one jets neural network output for $gg \to H$ signal. The default shape is shown in black, while more ISR is shown in red and less ISR in blue. The first plot shows the effect in the low SB region, the second plot shows the high SB region, and the third plot shows both regions combined.

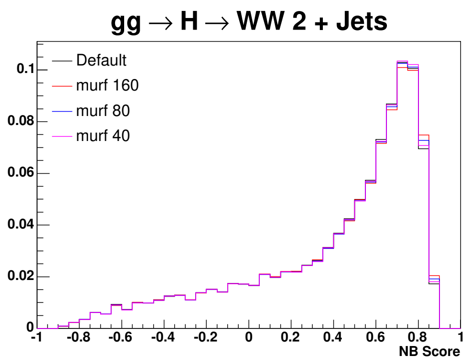

Figure 28: Effect of varying the scale of NNLO calculations on $gg \to H$ production. In black is the default Pythia shape for $M_H = 160$ for events with 2+ jets. The shape in blue is after the Pythia has been reweighted to match the default NNLO calculation with $\mu_R = \mu_F = 80$. The shape in red is after reweighting to match an NNLO calculation with $\mu_R = \mu_F = 160$, and the shape in magenta is after reweighting to $\mu_R = \mu_F = 40$.

7 Opposite-sign Dilepton Signal Region with 0 Jets

The background expectation and observed yield for the opposite-sign dilepton signal region for events containing no reconstructed jets with $E_T > 15$ GeV are shown in Table 38. The expected and observed kinematic distributions for these events are shown in Figures 29-31. We stack the backgrounds on top of each other, and then for comparison we overlay the contribution from a 160 GeV/c^2 Higgs boson with yields scaled up by a factor of 10. In addition, we calculate a confidence level for data versus background expectations on each plot. The confidence levels shown are for Poisson fluctuations and the KS test.

In CDF Note 9163 it was shown that using Matrix Element (ME) calculations as additional inputs to a NeuroBayes® (NB) neural network improved the overall sensitivity of the analysis. Since the ME calculations provide a model for each process based on the Leading Order (LO) behavior of the differential cross section, we expect that using this information in the neural network works well in cases where the events are LO-like, i.e. when no additional jets are present. We therefore use, for events with 0 jets (0J), ME-based Likelihood Ratios as inputs for a NB neural network in analogy of what has been done previously and described in detail in CDF Note 9163. We also incorporate inputs from additional kinematic variables to further improve the sensitivity.

To optimize the choice of variables to be used as input to the neural network we begin from a large set of what we think can be discriminant variables; we then evaluate a *ranking* associated to each of them using a NB pre-training functionality [27], which gives an estimation of the discrimination power between signal and background that this variable carries. We then train a set of neural networks starting from the full list of input variables and removing one variable at time, starting from the less significant. We calculate the expected limits for each output template obtained by these networks and finally choose the set of variables which minimize the expected limit; for this study a signal with $m_H = 160$ GeV was used.

The training method used for the neural network is mostly the same as described in CDF Note 9136. We train the net to distinguish the Higgs MC sample from an admixture of each background (both MC-derived and data-driven backgrounds); each background event has a weight according to its relative expectation, which is a function of the cross section, multiple scale factors, trigger efficiencies, and MC statistics. Only for the training, we then reweight all events so that the sum of the weights is equal to the number of signal events. The only significant differences with respect to the previous trainings is the use of a newer version of the NB package (v2.1) and the use of the BFGS algorithm in the minimization. The input variables used for the 0-jet NN are shown in Table 7 along with a brief explanation of their meaning; for the 0J net we use 5 input nodes, 7 hidden nodes and 1 output node. The observed distributions of each 0J neural network input parameter compared with the distributions predicted by our background model are shown in Figure 32. For reference, we also include a hypothetical signal component for a Higgs boson with $m_H = 160$ GeV.

Category	WW	WZ	ZZ	$t\bar{t}$	DY	$W\gamma$	W+jets	Total	Data
e e	85.7	5.9	12.5	0.4	52.5	61.9	57.0	275.8	293.0
e μ	199.8	3.8	0.4	0.8	19.4	52.8	64.5	341.5	334.0
μ μ	67.0	5.5	9.8	0.3	30.7	0.0	9.8	123.1	119.0
e trk	60.2	2.7	4.6	0.3	18.3	13.2	18.3	117.6	134.0
μ trk	34.2	1.9	2.7	0.2	7.6	2.6	12.0	61.1	70.0
Total:	446.9	19.7	29.9	2.0	128.5	130.5	161.5	919.0	950.0

Category	WW	WZ	ZZ	$t\bar{t}$	DY	$W\gamma$	W+jets	Total	Data
LBE LBE	49.2	3.1	7.4	0.3	27.4	14.1	9.3	110.7	120.0
LBE PHX	30.8	2.4	4.4	0.1	20.5	32.5	34.7	125.5	137.0
PHX PHX	5.7	0.4	0.7	0.0	4.7	15.2	13.0	39.7	36.0
LBE CMUP	57.0	1.0	0.1	0.3	4.1	8.0	10.7	81.1	76.0
LBE CMP	7.8	0.1	0.0	0.0	0.5	0.9	2.3	11.7	10.0
LBE CMX	25.0	0.5	0.1	0.1	1.5	3.5	5.3	35.9	25.0
LBE CMXMsKs	3.1	0.1	0.0	0.0	0.6	0.4	0.8	5.1	3.0
LBE BMU	6.5	0.1	0.0	0.0	0.3	0.5	0.0	7.5	9.0
LBE CMIOCES	40.5	0.7	0.1	0.2	1.8	3.0	2.4	48.7	39.0
LBE CMIOPES	12.3	0.2	0.0	0.0	0.8	0.9	5.2	19.5	15.0
PHX CMUP	17.6	0.5	0.0	0.1	3.4	14.3	17.5	53.4	65.0
PHX CMP	2.5	0.1	0.0	0.0	0.7	1.7	2.4	7.4	5.0
PHX CMX	8.5	0.2	0.0	0.0	3.3	9.1	8.8	30.0	36.0
PHX CMXMsKs	1.0	0.0	0.0	0.0	0.2	1.2	1.8	4.2	4.0
PHX BMU	2.3	0.0	0.0	0.0	0.5	1.6	0.0	4.5	9.0
PHX CMIOCES	11.5	0.3	0.0	0.0	1.3	5.1	1.6	19.8	25.0
PHX CMIOPES	4.2	0.1	0.0	0.0	0.2	2.7	2.5	9.7	13.0
CMUP CMUP	10.7	0.8	1.7	0.1	3.8	0.0	1.2	18.2	19.0
CMUP CMP	3.0	0.2	0.5	0.0	1.1	0.0	0.3	5.1	4.0
CMUP CMX	10.8	0.8	1.5	0.0	3.4	0.0	1.3	17.8	13.0
CMUP CMXMsKs	1.1	0.1	0.2	0.0	0.7	0.0	0.2	2.3	4.0
CMUP BMU	2.7	0.2	0.4	0.0	2.0	0.0	0.3	5.7	8.0
CMUP CMIOCES	15.5	1.2	2.2	0.1	5.7	0.0	1.3	26.0	27.0
CMUP CMIOPES	4.6	0.4	0.6	0.0	3.5	0.0	2.5	11.6	10.0
CMX CMP	1.4	0.1	0.2	0.0	1.0	0.0	0.1	2.7	4.0
CMX CMX	2.1	0.2	0.3	0.0	1.3	0.0	0.2	4.1	2.0
CMX CMXMsKs	0.6	0.1	0.1	0.0	0.2	0.0	0.1	1.1	1.0
CMX BMU	1.0	0.1	0.1	0.0	0.7	0.0	0.0	2.0	2.0
CMX CMIOCES	6.9	0.6	1.0	0.0	3.3	0.0	0.6	12.5	11.0
CMX CMIOPES	2.3	0.2	0.3	0.0	1.3	0.0	1.1	5.1	5.0
CMXMsKs CMP	0.2	0.0	0.1	0.0	0.3	0.0	0.0	0.6	1.0
CMXMsKs CMXMsKs	0.0	0.0	0.0	0.0	0.0	0.0	0.0	0.0	0.0
CMXMsKs BMU	0.2	0.0	0.0	0.0	0.4	0.0	0.0	0.6	0.0
CMXMsKs CMIOCES	0.6	0.1	0.1	0.0	0.6	0.0	0.1	1.6	2.0
CMXMsKs CMIOPES	0.2	0.0	0.0	0.0	0.4	0.0	0.1	0.7	0.0
CMP CMP	0.3	0.0	0.0	0.0	0.2	0.0	0.0	0.6	1.0
CMP BMU	0.3	0.0	0.0	0.0	0.2	0.0	0.0	0.6	2.0
CMP CMIOCES	1.8	0.1	0.2	0.0	0.5	0.0	0.1	2.8	3.0
CMP CMIOPES	0.6	0.0	0.1	0.0	0.2	0.0	0.3	1.2	0.0
LBE CrkTrk	46.5	2.0	3.6	0.3	13.0	6.0	11.3	82.7	97.0
PHX CrkTrk	13.7	0.7	1.0	0.0	5.3	7.2	7.0	34.8	37.0
CMUP CrkTrk	21.2	1.1	1.7	0.1	4.5	1.6	7.8	37.9	52.0
CMP CrkTrk	2.2	0.1	0.2	0.0	0.6	0.1	0.9	4.0	4.0
CMX CrkTrk	9.9	0.5	0.8	0.1	2.3	0.8	3.0	17.2	10.0
CMXMsKs CrkTrk	1.0	0.1	0.1	0.0	0.3	0.1	0.4	2.0	4.0
Total:	446.9	19.7	29.9	2.0	128.5	130.5	158.6	916.1	950.0

Table 38: Yields in opposite-sign dilepton signal region for events with zero jets.

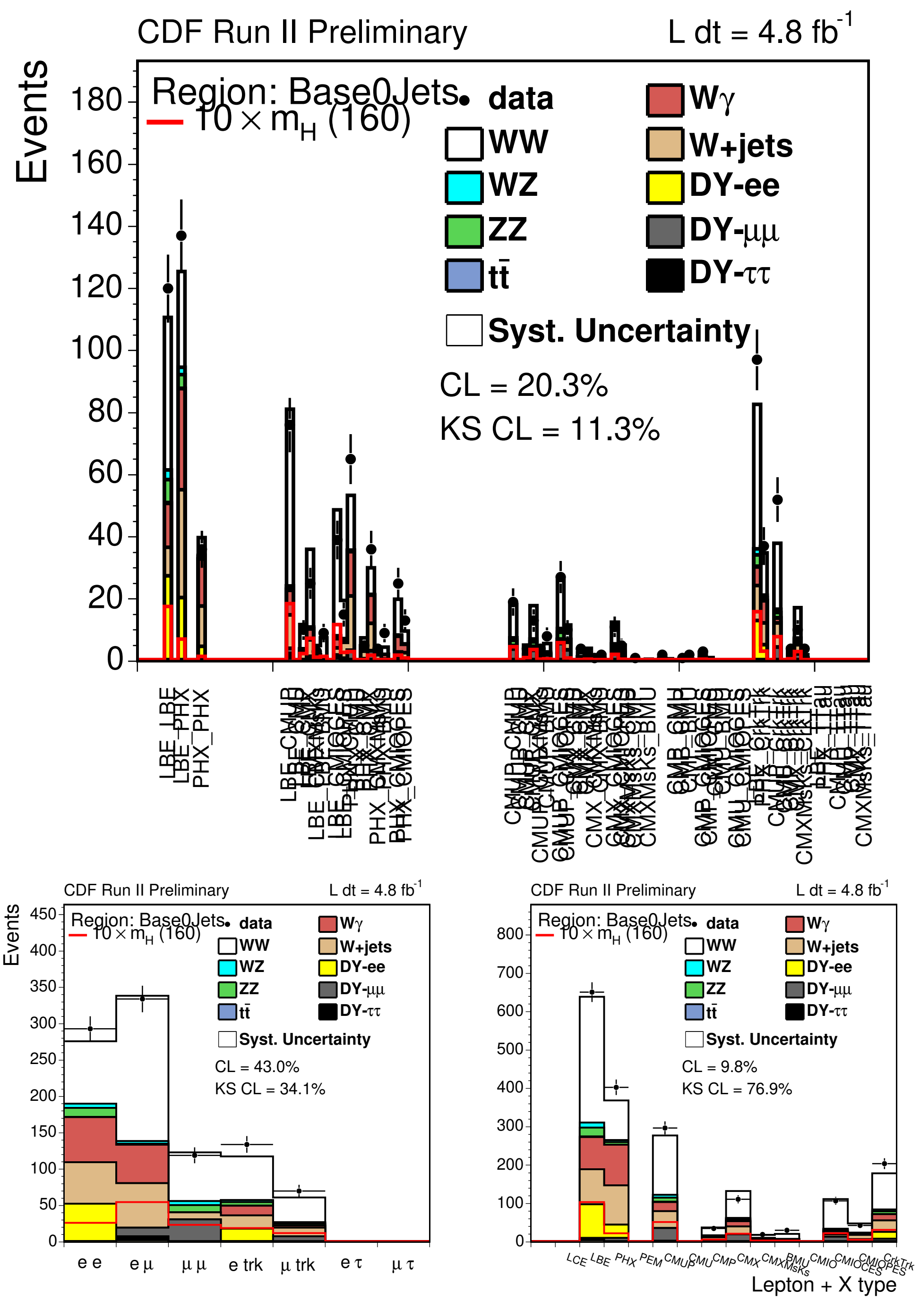

Figure 29: Signal and background in the opposite-sign signal region for events containing no reconstructed jets with $E_T > 15$ GeV.

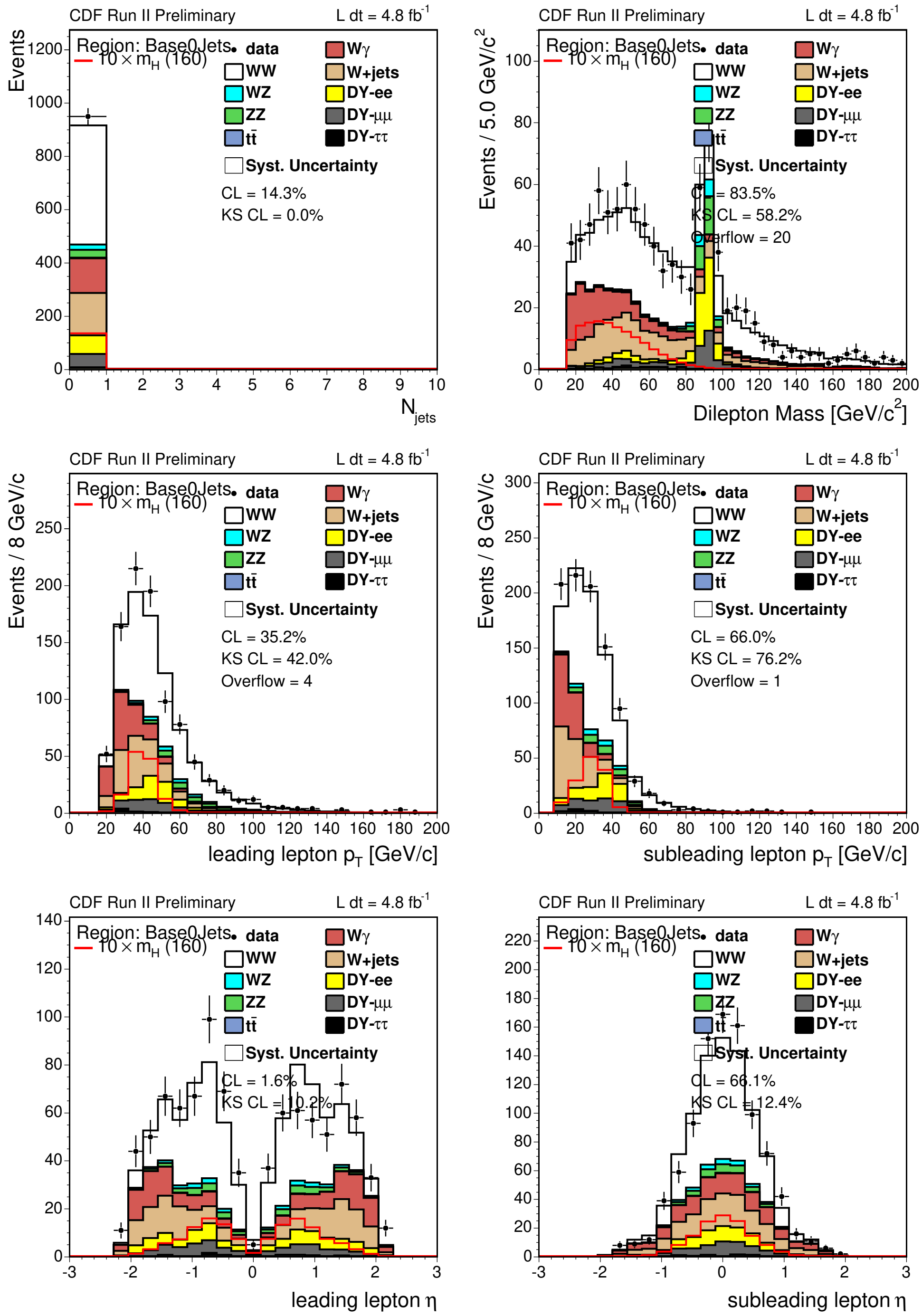

Figure 30: Signal and background in the opposite-sign signal region for events containing no reconstructed jets with $E_T > 15$ GeV.

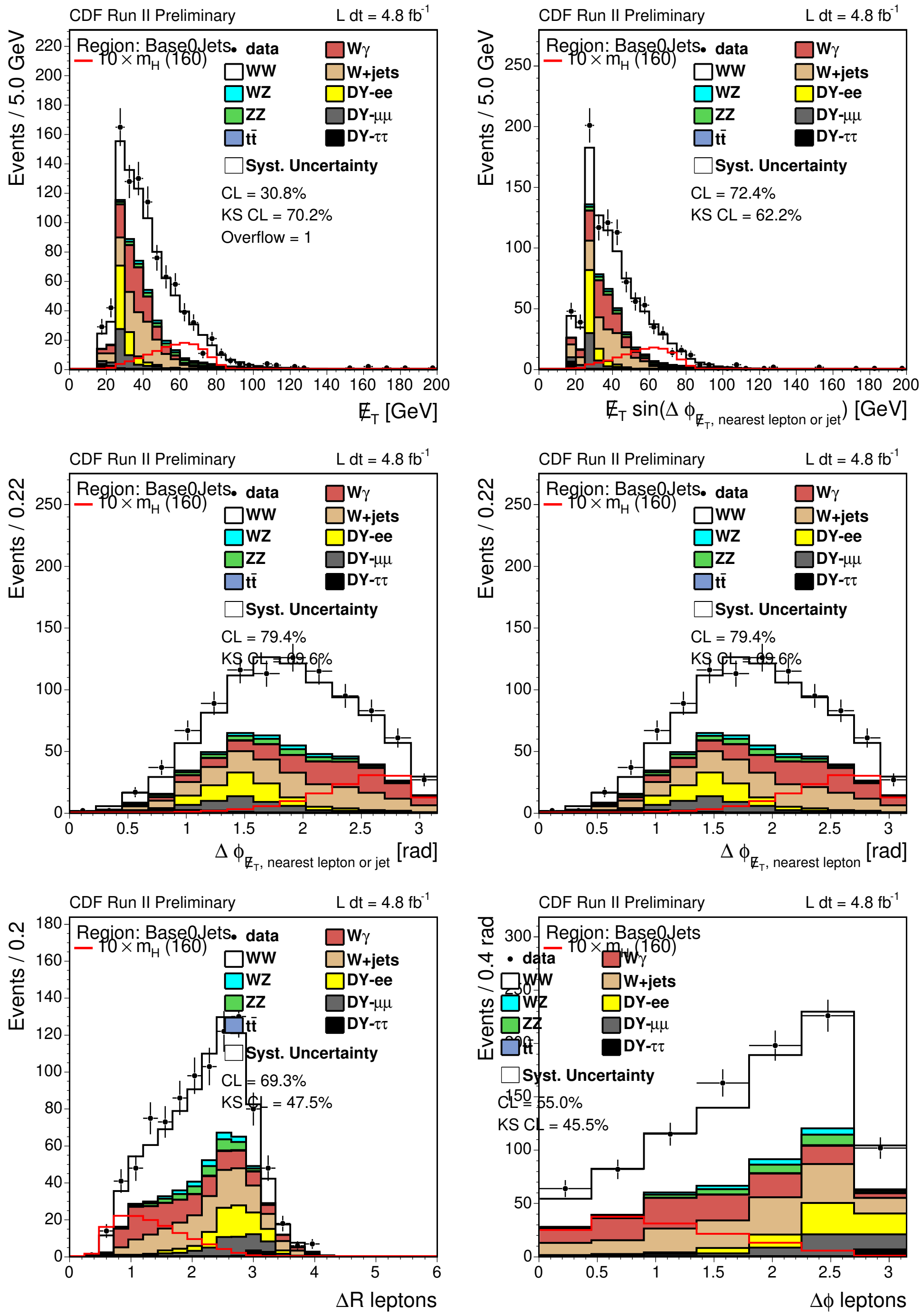

Figure 31: Signal and background in the opposite-sign signal region for events containing no reconstructed jets with $E_T > 15$ GeV.

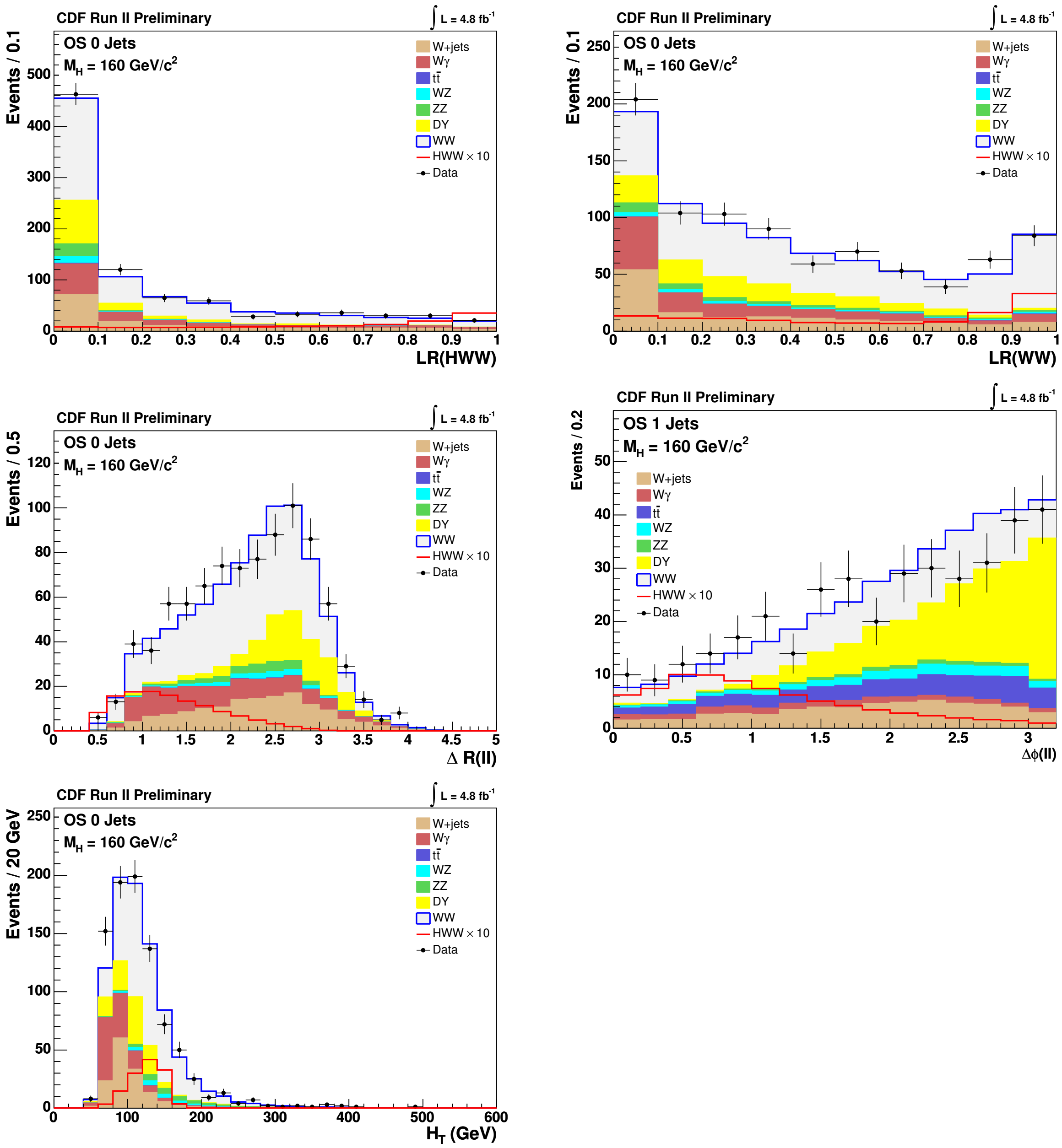

Figure 32: Neural Network input variables for 0J NN (signal for $M_H = 160$ GeV/c^2). **To be updated.**

Variable	Meaning
	0J Neural Network
LRHWW	Likelihood ratio - $H \rightarrow WW$
dRLeptons	ΔR between the leptons
LRWW	Likelihood ratio - WW production
dPhiLeptons	$\Delta\phi$ between the leptons
Ht	Scalar sum of leptons E_T and $\not{E}_T$ (no jets in the event)

Table 39: Summary of inputs to 0J neural networks.

Templates are created for each neural network and used for calculating 95% CL limits with the MCLimit program [28]. Events are separated into Low S/B and High S/B channels based on the dilepton types and a separate set of templates is created for each of the channels. MCLimit combines the two channels to produce a single set of limits for the 0J region. Output templates for the trained 0J neural network, divided into Low S/B and High S/B, are shown in Figures 33−36.

In the 0J region we consider only potential signal contributions from the gluon fusion production of a Higgs boson: $gg \rightarrow H \rightarrow WW \rightarrow ll\nu\nu$. The potential contribution from other production channels, Vector Boson Fusion (VBF) and associated production VH ($q\bar{q} \rightarrow ZH \rightarrow ZWW$ and $q\bar{q} \rightarrow WH \rightarrow WWW$), is negligible in this region. We start by evaluating the number of events expected from Higgs gluon fusion production as a function of the mass of the Higgs. These numbers are shown in Table 40.

In calculating the final limits, we take into account systematic uncertainties on both the signal and background models we use to train our neural networks. Systematic uncertainties for the 0J region are summarized in Tables 41 and 42.

Table 43 and Figure 37 show the expected (based on 10000 pseudo-experiments) and observed limits obtained from the 0J region, incorporating the systematic uncertainties listed in Tables 41 and 42.

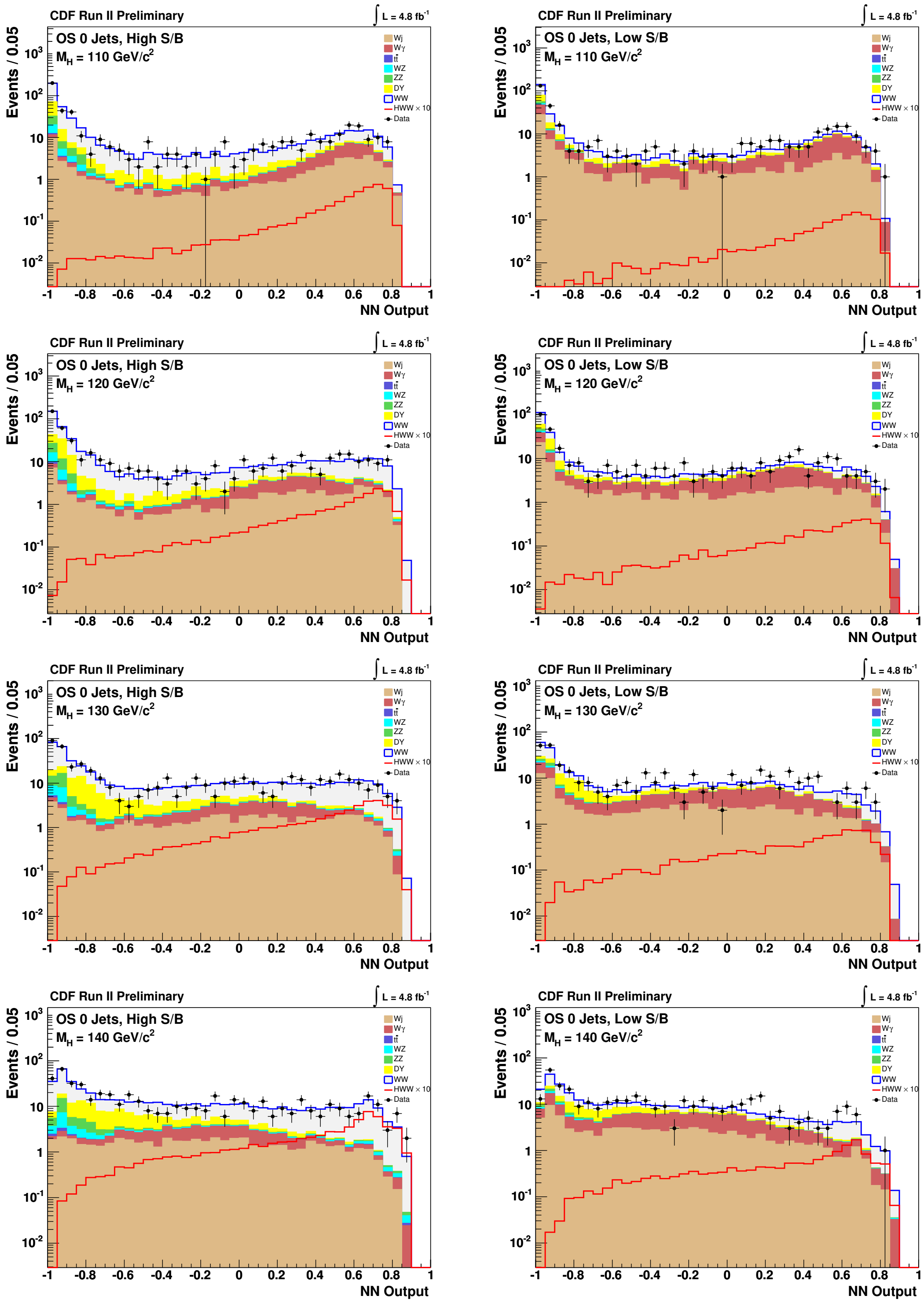

Figure 33: 0J Neural Network output templates for several Higgs masses. On the left for High S/B events and on the right for Low S/B. From the top to bottom: 110 GeV, 120 GeV, 130 GeV, and 140 GeV. **To be updated.**

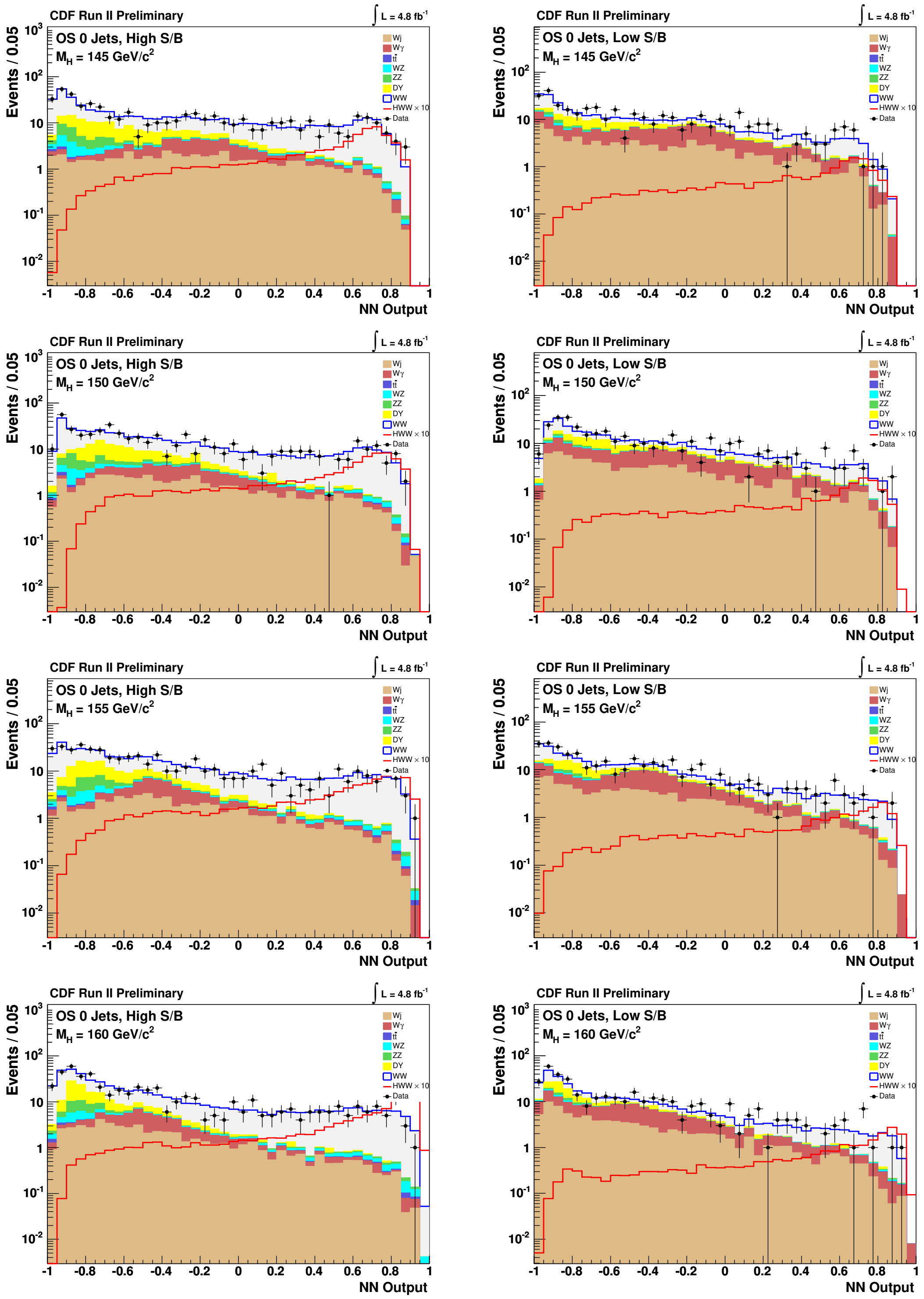

Figure 34: 0J Neural Network output templates for several Higgs masses. On the left for High S/B events and on the right for Low S/B. From the top to bottom: 145 GeV, 150 GeV, 155 GeV, and 160 GeV. **To be updated.**

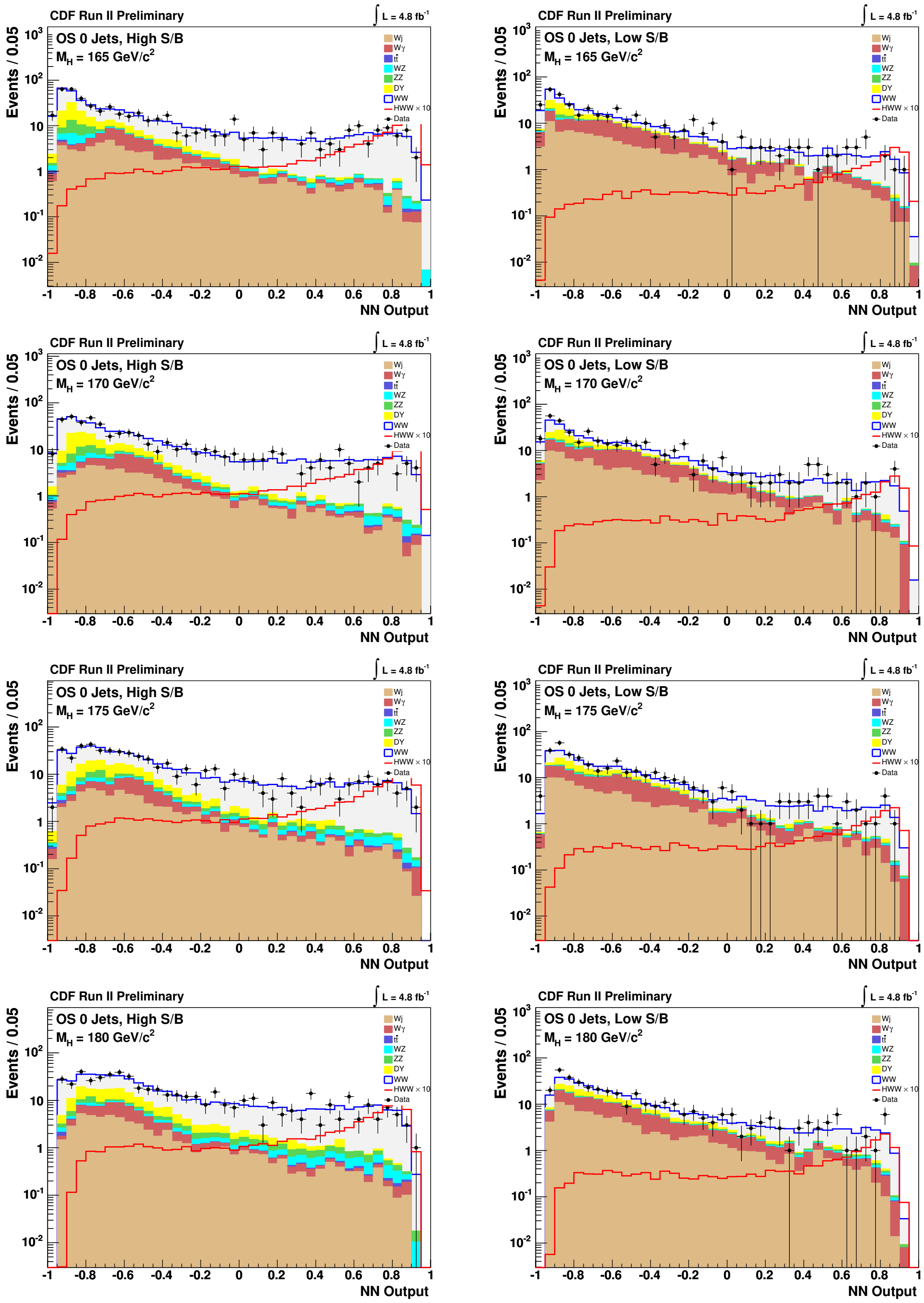

Figure 35: 0J Neural Network output templates for several Higgs masses. On the left for High S/B events and on the right for Low S/B. From the top to bottom: 165 GeV, 170 GeV, 175 GeV, 180 GeV. **To be updated.**

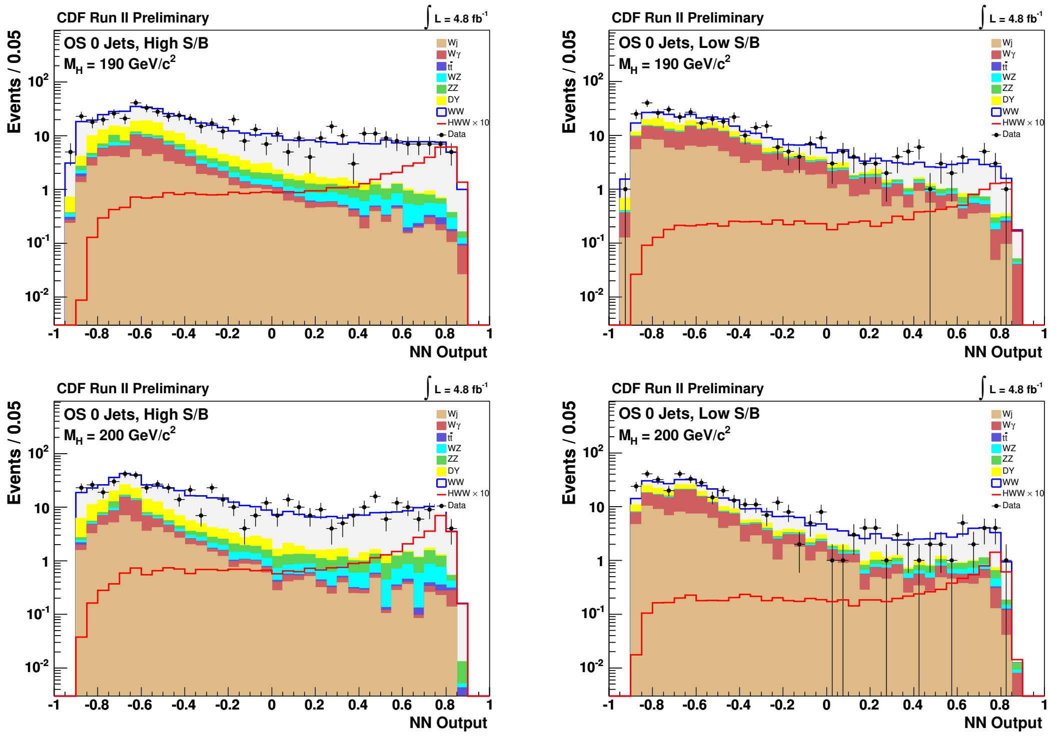

Figure 36: 0J Neural Network output templates for several Higgs masses. On the left for High S/B events and on the right for Low S/B. From the top to bottom: 190 GeV and 200 GeV. **To be updated.**

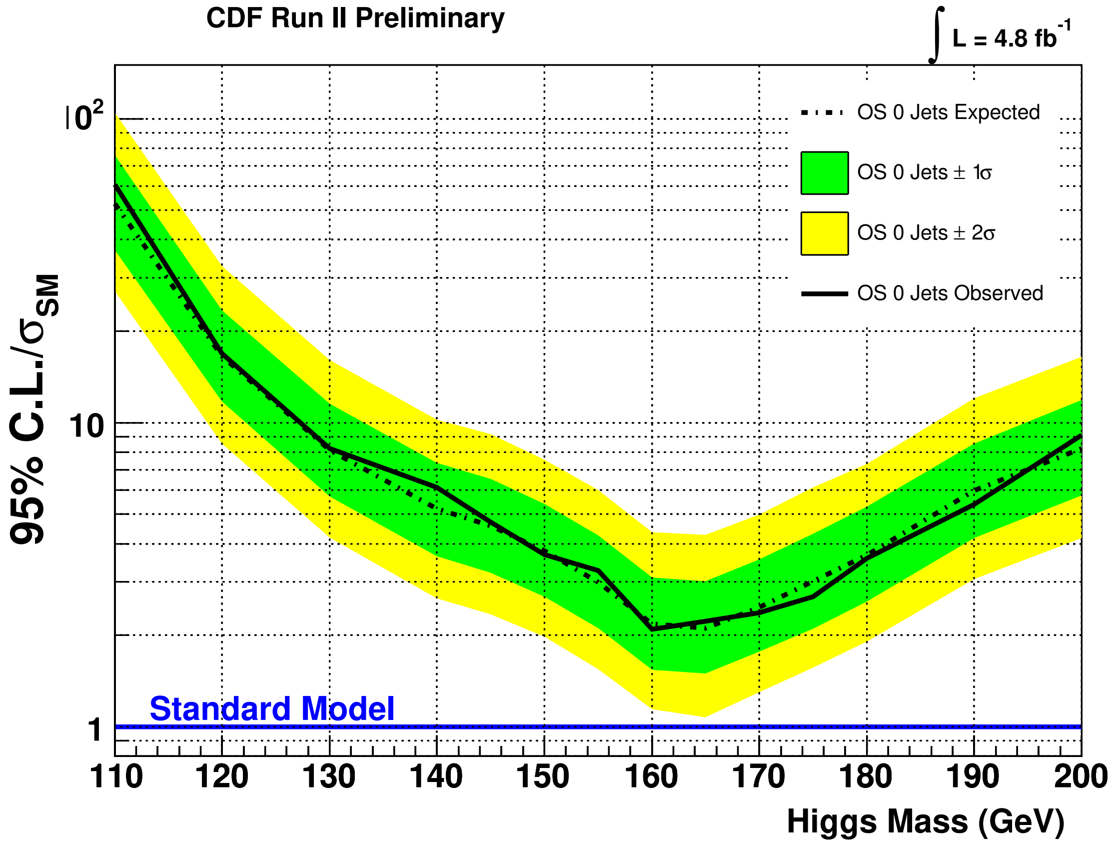

Figure 37: $H \rightarrow WW$ sensitivity normalized to NNLL σ_{SM} calculation from the combination of the High S/B and Low S/B channels in the 0J region. In this region we only consider a potential signal contribution from $gg \rightarrow H$. **To be updated.**

Mass (GeV/c^2)	gg→H	WH	ZH	VBF
110	0.634 (0.506/0.128)	-	-	-
120	2.16 (1.74/0.427)	-	-	-
130	4.79 (3.86/0.927)	-	-	-
140	7.7 (6.18/1.52)	-	-	-
145	8.76 (7.05/1.71)	-	-	-
150	9.96 (8.05/1.92)	-	-	-
155	11.2 (9.07/2.13)	-	-	-
160	12.1 (9.8/2.26)	-	-	-
165	11.8 (9.59/2.19)	-	-	-
170	10.8 (8.75/2.02)	-	-	-
175	9.57 (7.76/1.81)	-	-	-
180	8.55 (6.89/1.67)	-	-	-
190	5.82 (4.67/1.15)	-	-	-
200	4.56 (3.67/0.893)	-	-	-

Table 40: Expected Higgs Signal yields as a function of the Higgs boson mass in the 0J region for each of the contributing production processes. The numbers inside the parentheses are the expected relative contributions in the High S/B and Low S/B regions. **To be updated.**

Uncertainty Source	WW	WZ	ZZ	$t\bar{t}$	DY	$W\gamma$	W+jet
Cross Section							
Scale							
PDF Model							
Total	*6.0%*	*6.0%*	*6.0%*	10.0%	5.0%	10.0%	
Acceptance							
Scale							
PDF Model	*1.9%*	*2.7%*	*2.7%*	*2.1%*	*4.1%*	*2.2%*	
Higher-order Diagrams	*5.0%*	*10.0%*	*10.0%*	10.0%		*10.0%*	
Jet Modeling	-1.0%				21.0%	-4.0%	
Conversion Modeling						20.0%	
Jet Fake Rates							
(Low S/B)							21.5%
(High S/B)							27.7%
MC Run Dependence	*2.2%*			*1.0%*		*5.0%*	
Lepton ID Efficiencies	*2.0%*	*1.7%*	*2.0%*	*2.0%*	*1.9%*	*1.4%*	
Trigger Efficiencies	*2.1%*	*2.1%*	*2.1%*	*2.0%*	*3.4%*	*7.0%*	
Luminosity	*5.9%*	*5.9%*	*5.9%*	*5.9%*	*5.9%*	*5.9%*	

Table 41: Systematics table for 0J analysis background processes. Cross section systematics are correlated for the diboson processes (shown in italic font) but uncorrelated between all other processes. Higher-order diagram systematics shown in bold font are correlated among each other but uncorrelated across the 0, 1, and 2+ jet bins.

Uncertainty Source	$gg \to H$	WH	ZH	VBF
Cross Section				
Scale	10.9%			
PDF Model	5.1%			
Total	12.0%			
Acceptance				
Scale (leptons)	2.5%			
Scale (jets)	4.6%			
PDF Model (leptons)	*1.5%*			
PDF Model (jets)	0.9%			
Lepton ID Efficiencies	*1.9%*			
Trigger Efficiencies	*3.3%*			
Luminosity	*5.9%*			

Table 42: Systematics table for 0J analysis signal processes. For the 0 jet analysis, we only use $gg \to H$. The Scale (jets) and PDF Model (jets) systematics for $gg \to H$ are anticorrelated between the 0, 1, and 2+ jet bins, as these systematics cause events to fluctuate between jet bins.

OS 0 Jets	110	120	130	140	145	150	155
$-2\sigma/\sigma_{SM}$	27.07	8.53	4.18	2.64	2.35	1.98	1.55
$-1\sigma/\sigma_{SM}$	37.01	11.72	5.71	3.64	3.21	2.68	2.11
Median/$\sigma_{\mathbf{SM}}$	**52.51**	**16.52**	**8.14**	**5.20**	**4.58**	**3.79**	**2.98**
$+1\sigma/\sigma_{SM}$	75.84	23.42	11.56	7.37	6.55	5.41	4.27
$+2\sigma/\sigma_{SM}$	104.92	32.77	16.11	10.25	9.19	7.57	6.01
Observed/$\sigma_{\mathbf{SM}}$	**60.68**	**16.89**	**8.21**	**6.12**	**4.72**	**3.68**	**3.26**
	160	165	170	175	180	190	200
$-2\sigma/\sigma_{SM}$	1.14	1.08	1.30	1.56	1.91	3.06	4.17
$-1\sigma/\sigma_{SM}$	1.54	1.50	1.76	2.10	2.58	4.18	5.77
Median/$\sigma_{\mathbf{SM}}$	**2.18**	**2.11**	**2.47**	**3.02**	**3.66**	**5.99**	**8.24**
$+1\sigma/\sigma_{SM}$	3.09	3.01	3.55	4.32	5.29	8.54	11.86
$+2\sigma/\sigma_{SM}$	4.37	4.27	4.98	6.12	7.32	12.01	16.46
Observed/$\sigma_{\mathbf{SM}}$	**2.09**	**2.22**	**2.37**	**2.68**	**3.58**	**5.38**	**9.08**

Table 43: $H \to WW$ sensitivity normalized to NNLL σ_{SM} calculation from the combination of the High S/B and Low S/B channels for the 0J region. In this region we only consider a potential signal contribution from $gg \to H$. **To be updated.**

8 Opposite-sign Dilepton Signal Region with 1 Jet

The background expectation and observed yield for the opposite-sign dilepton signal region for events containing one reconstructed jet with $E_T > 15$ GeV are shown in Table 44. The expected and observed kinematic distributions for these events are shown in Figures 38-40. We stack the backgrounds on top of each other, and then for comparison we overlay the contribution from a 160 GeV/c^2 Higgs boson with yields scaled up by a factor of 10. In addition, we calculate a confidence level for data versus background expectations on each plot. The confidence levels shown are for Poisson fluctuations and the KS test.

For events with one jet (1J) we train a separate set of NB neural networks, one for each Higgs mass, and do not incorporate any inputs based on the Matrix Element calculations. As discussed previously, the ME calculations are done at LO and therefore are not as reliable for events with an extra jet which presumably originates from an extra quark or gluon radiated within the hard scattering process. Optimization and training of the neural network are done in the same manner as for the 0J case described in Section 7. For the 1J region our neural network uses 8 inputs, 10 hidden nodes and 1 output node. The input variables used for the 1J NN are shown in Table 8. The observed distributions of each 1J neural network input parameter compared with the distributions predicted by our background model are shown in Figures 41 and 42. For reference, we also include a hypothetical signal component for a Higgs boson with $m_H = 160$ GeV/c^2.

Templates are created for each neural network and used for calculating 95% CL limits with the MCLimit program [28]. Events are separated into Low S/B and High S/B channels based on the dilepton types and a separate set of templates is created for each of the channels. MCLimit combines the two channels to produce a single set of limits for the 1J region. Output templates for the trained 1J neural network, divided into Low S/B and High S/B, are shown in Figures 43−46.

In the 1J region we consider potential signal contributions from all four Higgs production processes that contribute significantly at high masses: gluon fusion ($gg \to H \to WW \to ll\nu\nu$), Vector Boson Fusion (VBF), and associated production VH ($q\bar{q} \to ZH \to ZWW$ and $q\bar{q} \to WH \to WWW$). The additional processes contribute significantly to the event regions with one or more jets and incorporating their contributions is fairly straight-forward since we do not attempt to use neural network inputs based on Matrix Element calculations in these regions. We evaluate the number of events expected from each production process as a function of the mass of the Higgs. These numbers are shown in Table 46.

In calculating the final limits, we take into account systematic uncertainties on both the signal and background models we use to train our neural networks. Systematic uncertainties for the 1J region are summarized in Tables 47 and 48.

Tables 49 and Figure 47 show the expected (based on 10000 pseudo-experiments) and observed limits obtained from the 1J region, incorporating the systematic uncertainties listed in Tables 47 and 48.

Category	WW	WZ	ZZ	$t\bar{t}$	DY	$W\gamma$	W+jets	Total	Data
$e\ e$	23.2	7.4	3.1	8.9	35.3	8.7	21.1	107.9	101.0
$e\ \mu$	54.1	3.6	0.5	20.8	45.1	7.9	28.0	160.0	137.0
$\mu\ \mu$	18.5	4.4	2.4	7.8	29.8	0.0	3.3	66.2	72.0
e trk	16.3	3.1	1.2	6.7	15.3	1.8	4.9	49.3	52.0
μ trk	9.2	1.5	0.7	4.2	7.3	0.3	4.0	27.2	32.0
Total:	121.3	20.0	8.0	48.4	132.8	18.8	61.2	410.6	394.0

Category	WW	WZ	ZZ	$t\bar{t}$	DY	$W\gamma$	W+jets	Total	Data
LBE LBE	13.6	3.9	1.9	6.1	18.0	1.8	3.1	48.4	51.0
LBE PHX	8.2	3.0	1.1	2.5	13.1	5.0	12.5	45.3	44.0
PHX PHX	1.5	0.5	0.2	0.2	4.2	1.9	5.5	14.1	6.0
LBE CMUP	16.7	0.9	0.2	7.2	13.7	1.0	4.3	43.9	41.0
LBE CMP	2.2	0.1	0.0	0.9	2.6	0.1	1.1	7.0	2.0
LBE CMX	7.0	0.5	0.1	2.9	5.6	0.4	1.9	18.3	17.0
LBE CMXMsKs	0.9	0.1	0.0	0.5	1.0	0.1	0.5	3.0	1.0
LBE BMU	1.7	0.1	0.0	0.5	0.6	0.1	0.0	3.0	2.0
LBE CMIOCES	10.9	0.7	0.1	4.7	8.2	0.4	0.7	25.7	24.0
LBE CMIOPES	3.0	0.2	0.0	0.9	2.9	0.2	1.8	9.1	7.0
PHX CMUP	4.6	0.4	0.0	1.4	3.2	2.3	7.2	19.1	18.0
PHX CMP	0.6	0.0	0.0	0.2	0.4	0.3	1.0	2.6	5.0
PHX CMX	1.9	0.2	0.0	0.6	1.6	1.4	4.6	10.3	7.0
PHX CMXMsKs	0.3	0.0	0.0	0.1	0.6	0.1	0.4	1.6	2.0
PHX BMU	0.5	0.0	0.0	0.1	0.8	0.2	0.0	1.6	1.0
PHX CMIOCES	2.9	0.2	0.0	0.8	2.3	1.0	1.0	8.3	6.0
PHX CMIOPES	0.9	0.1	0.0	0.2	1.3	0.4	1.6	4.5	4.0
CMUP CMUP	3.3	0.7	0.4	1.6	4.0	0.0	0.3	10.3	13.0
CMUP CMP	0.8	0.2	0.1	0.4	1.1	0.0	0.2	2.9	0.0
CMUP CMX	2.6	0.7	0.4	1.3	3.9	0.0	0.4	9.2	8.0
CMUP CMXMsKs	0.4	0.1	0.1	0.2	0.8	0.0	0.1	1.7	2.0
CMUP BMU	0.7	0.2	0.1	0.2	2.2	0.0	0.2	3.7	2.0
CMUP CMIOCES	4.3	1.0	0.6	1.9	4.5	0.0	0.5	12.7	17.0
CMUP CMIOPES	1.2	0.3	0.1	0.3	2.6	0.0	0.7	5.3	5.0
CMX CMP	0.4	0.1	0.1	0.2	0.3	0.0	0.1	1.1	0.0
CMX CMX	0.7	0.2	0.1	0.2	0.8	0.0	0.1	2.0	2.0
CMX CMXMsKs	0.2	0.1	0.0	0.1	0.4	0.0	0.0	0.7	1.0
CMX BMU	0.2	0.1	0.0	0.1	1.1	0.0	0.0	1.6	3.0
CMX CMIOCES	1.9	0.5	0.2	0.7	3.4	0.0	0.2	6.9	8.0
CMX CMIOPES	0.5	0.1	0.1	0.1	1.6	0.0	0.2	2.7	2.0
CMXMsKs CMP	0.1	0.0	0.0	0.0	0.4	0.0	0.0	0.6	0.0
CMXMsKs CMXMsKs	0.0	0.0	0.0	0.0	0.3	0.0	0.0	0.3	0.0
CMXMsKs BMU	0.0	0.0	0.0	0.0	0.2	0.0	0.0	0.3	1.0
CMXMsKs CMIOCES	0.2	0.1	0.0	0.1	0.6	0.0	0.0	1.0	3.0
CMXMsKs CMIOPES	0.1	0.0	0.0	0.0	0.4	0.0	0.3	0.8	0.0
CMP CMP	0.1	0.0	0.0	0.0	0.1	0.0	0.0	0.2	1.0
CMP BMU	0.1	0.0	0.0	0.0	0.2	0.0	0.0	0.3	2.0
CMP CMIOCES	0.5	0.1	0.1	0.2	0.5	0.0	0.1	1.5	2.0
CMP CMIOPES	0.1	0.0	0.0	0.0	0.3	0.0	0.0	0.6	0.0
LBE CrkTrk	13.1	2.3	0.9	5.7	11.1	0.8	3.1	37.0	33.0
PHX CrkTrk	3.2	0.8	0.2	1.0	4.3	1.0	1.8	12.3	19.0
CMUP CrkTrk	5.7	0.9	0.4	2.7	4.3	0.2	2.3	16.5	21.0
CMP CrkTrk	0.6	0.1	0.0	0.3	0.7	0.0	0.5	2.2	2.0
CMX CrkTrk	2.6	0.4	0.2	1.1	1.9	0.2	1.2	7.6	8.0
CMXMsKs CrkTrk	0.3	0.1	0.0	0.1	0.5	0.0	0.1	1.1	1.0
Total:	121.3	20.0	8.0	48.4	132.8	18.8	59.4	408.8	394.0

Table 44: Yields in opposite-sign dilepton signal region for events with one jet.

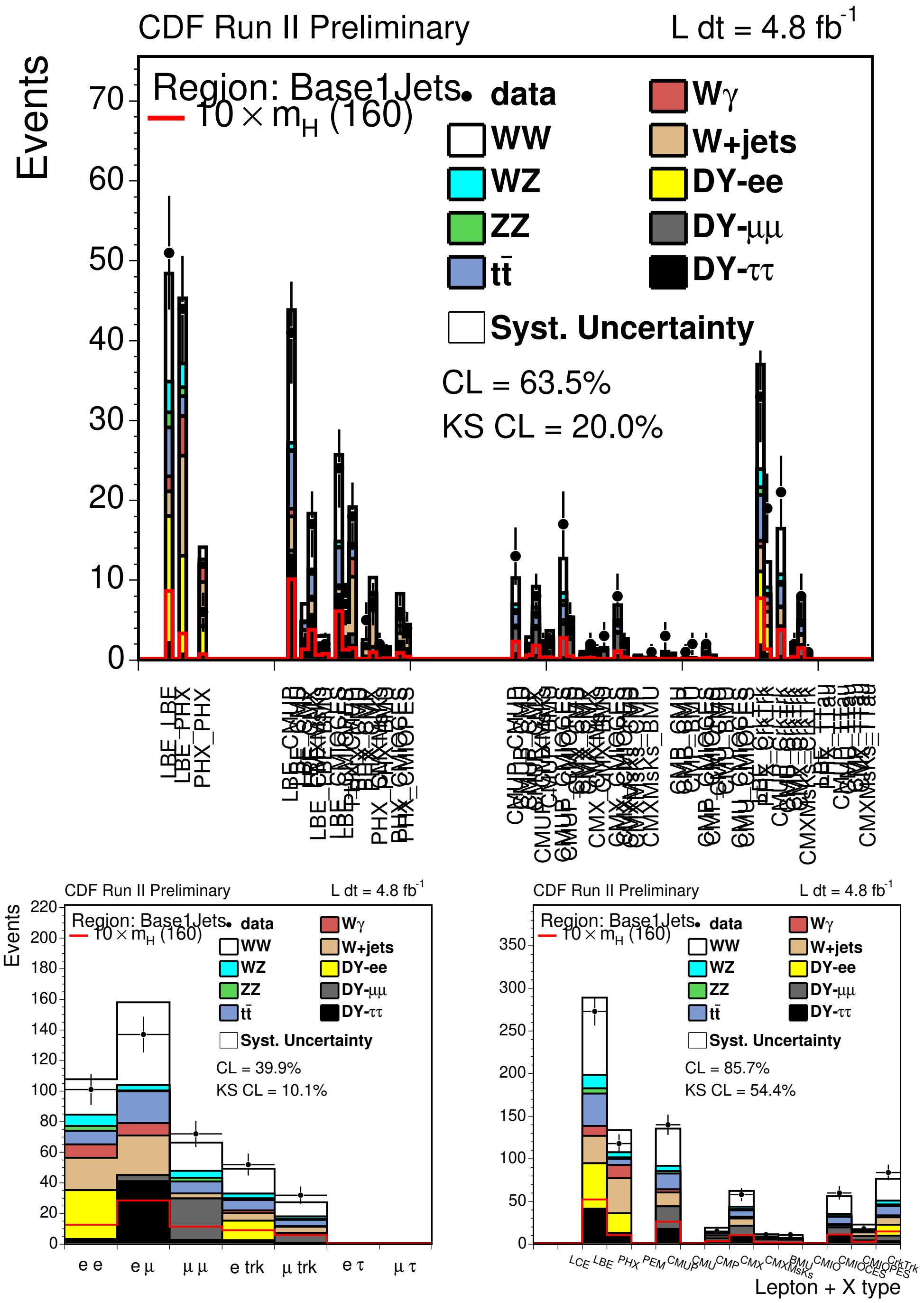

Figure 38: Signal and background in the opposite-sign signal region for events containing one reconstructed jet with $E_T > 15$ GeV.

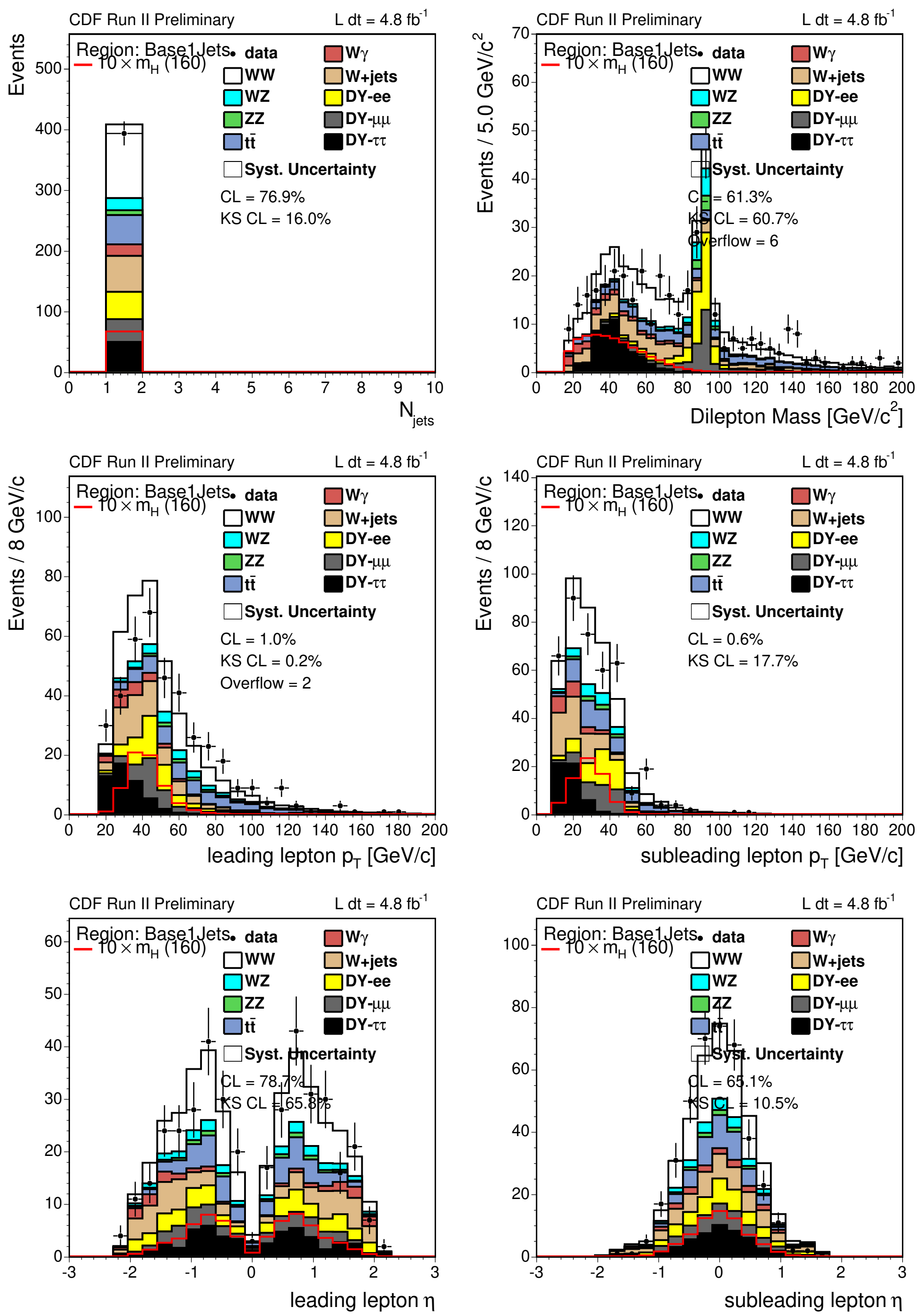

Figure 39: Signal and background in the opposite-sign signal region for events containing one reconstructed jet with $E_T > 15$ GeV.

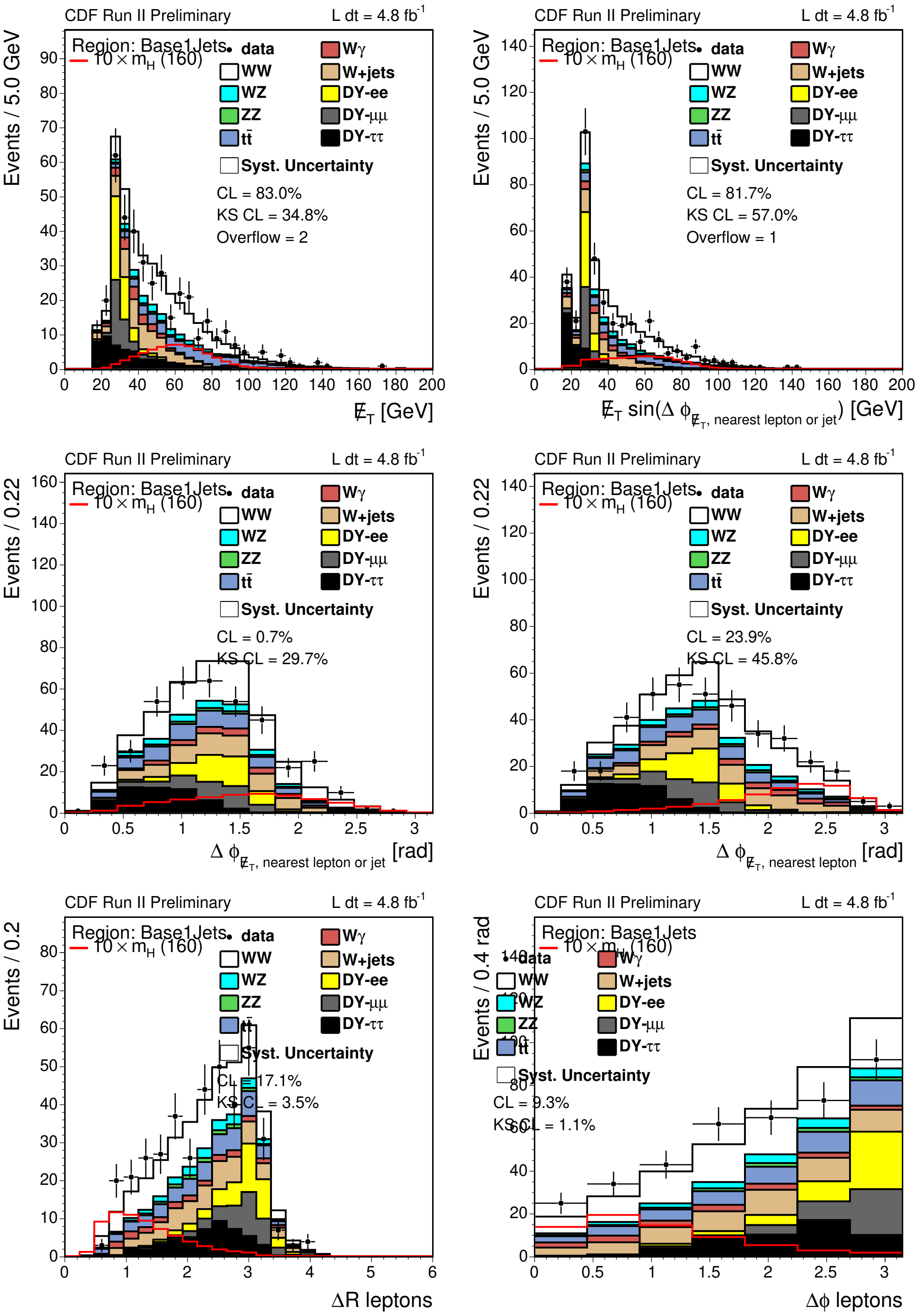

Figure 40: Signal and background in the opposite-sign signal region for events containing one reconstructed jet with $E_T > 15$ GeV.

Variable	Meaning
	1J neural networks
dRLeptons	ΔR between the leptons
Mt_H	Transverse mass of the sum of lepton's 4-momenta and ($\not\!\!E_T$, MetX, MetY, 0) where MetX/Y are the X/Y components of the $\vec{\not\!\!E}_T$
dimass	Dilepton invariant mass
MetSpec	$\not\!\!E_{Tspec} = \not\!\!E_T$ if $\Delta\phi$ ($\vec{\not\!\!E}_T$, l or j) $> \frac{\pi}{2}$ $\not\!\!E_{Tspec} = \not\!\!E_T$ $\sin(\Delta\phi$ ($\vec{\not\!\!E}_T$, l or j)) if $\Delta\phi$ ($\vec{\not\!\!E}_T$, l or j) $< \frac{\pi}{2}$
lep1_E	Energy of the leading (most energetic) lepton (for muons this is the lepton 3-momentum module)
lep1_Pt	Transverse momentum of the first lepton
lep2_Pt	Transverse momentum of the second lepton
Ht	Scalar sum of Leptons E_T, Jet E_T and $\not\!\!E_T$

Table 45: Summary of inputs to 1J neural networks.

Mass (GeV/c^2)	gg→H	WH	ZH	VBF
110	0.265 (0.217/0.0479)	0.129 (0.103/0.0261)	0.0441 (0.0346/0.00952)	0.0188 (0.0156/0.00312)
120	0.92 (0.75/0.17)	0.336 (0.268/0.0686)	0.108 (0.0858/0.0223)	0.0671 (0.056/0.0112)
130	2.12 (1.73/0.393)	0.595 (0.477/0.119)	0.2 (0.161/0.0393)	0.159 (0.132/0.027)
140	3.51 (2.87/0.635)	0.79 (0.638/0.152)	0.268 (0.217/0.0507)	0.275 (0.229/0.0461)
145	4.07 (3.32/0.75)	0.836 (0.676/0.16)	0.289 (0.235/0.054)	0.327 (0.271/0.0556)
150	4.76 (3.9/0.86)	0.866 (0.698/0.168)	0.308 (0.25/0.0586)	0.388 (0.322/0.0655)
155	5.44 (4.46/0.977)	0.892 (0.725/0.167)	0.325 (0.265/0.0602)	0.453 (0.376/0.0761)
160	5.99 (4.94/1.06)	0.883 (0.72/0.163)	0.329 (0.269/0.0602)	0.509 (0.425/0.0831)
165	5.96 (4.92/1.04)	0.821 (0.672/0.149)	0.317 (0.262/0.0553)	0.528 (0.442/0.0858)
170	5.6 (4.61/0.992)	0.746 (0.613/0.133)	0.287 (0.236/0.0507)	0.509 (0.425/0.0841)
175	5.02 (4.13/0.899)	0.663 (0.542/0.122)	0.256 (0.212/0.0447)	0.477 (0.397/0.0797)
180	4.59 (3.74/0.847)	0.591 (0.482/0.108)	0.228 (0.189/0.039)	0.442 (0.367/0.0751)
190	3.22 (2.62/0.6)	0.4 (0.328/0.0726)	0.153 (0.127/0.0267)	0.328 (0.27/0.0574)
200	2.6 (2.11/0.492)	0.306 (0.251/0.0545)	0.119 (0.0974/0.0216)	0.273 (0.224/0.0489)

Table 46: Expected Higgs Signal yields as a function of the Higgs boson mass in the 1J region for each of the contributing production processes. The numbers inside the parentheses are the expected relative contributions in the High S/B and Low S/B regions. **To be updated.**

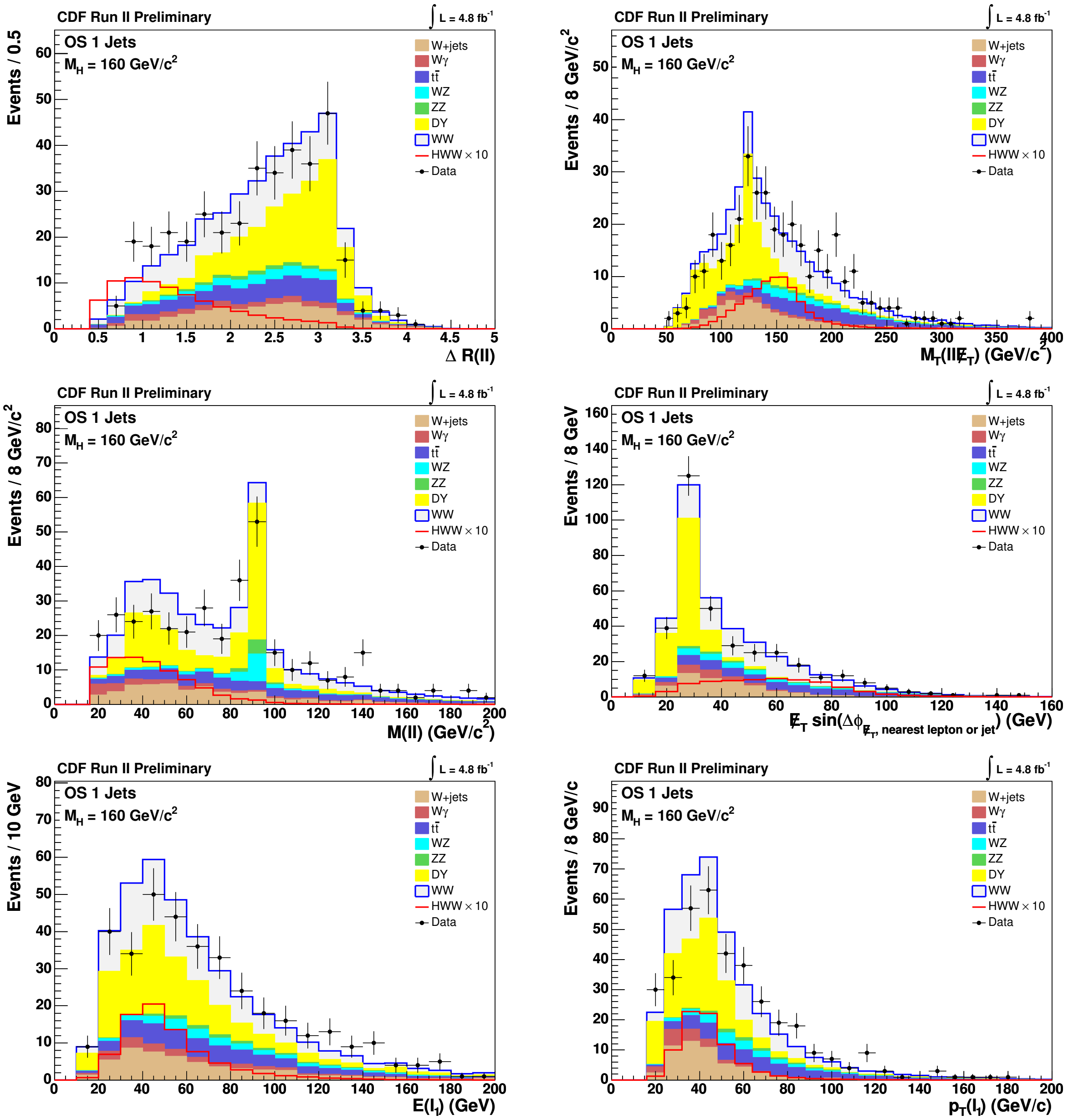

Figure 41: Neural Network input variables for 1J NN (signal for $M_H = 160$ GeV$/c^2$). **To be updated.**

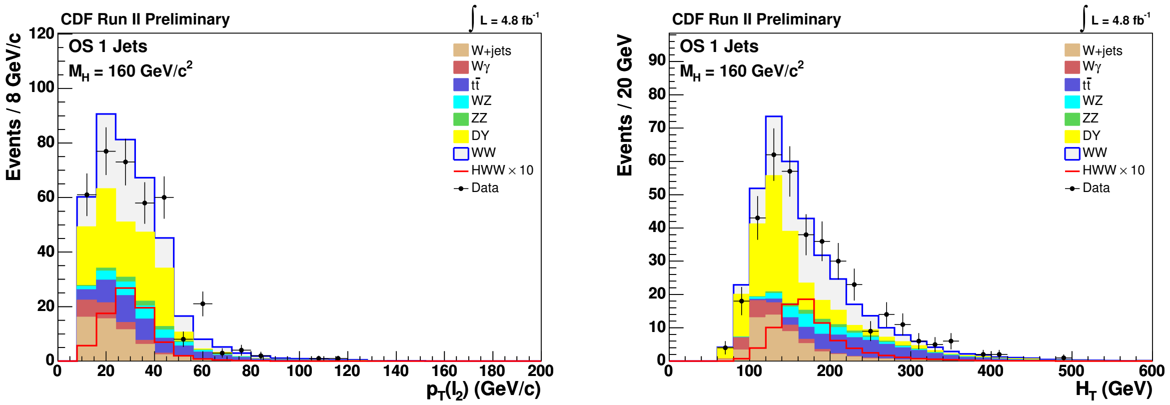

Figure 42: Neural Network input variables for 1J NN (signal for $M_H = 160$ GeV/c^2). **To be updated.**

Uncertainty Source	WW	WZ	ZZ	$t\bar{t}$	DY	$W\gamma$	W+jet
Cross Section							
Scale							
PDF Model							
Total	*6.0%*	*6.0%*	*6.0%*	10.0%	5.0%	10.0%	
Acceptance							
Scale							
PDF Model	*1.9%*	*2.7%*	*2.7%*	*2.1%*	*4.1%*	*2.2%*	
Higher-order Diagrams	*5.0%*	*10.0%*	*10.0%*	10.0%		*10.0%*	
Jet Modeling	-1.0%				30.0%	15.0%	
Conversion Modeling						20.0%	
Jet Fake Rates							
(Low S/B)							22.2%
(High S/B)							31.5%
MC Run Dependence	*1.0%*			*1.0%*		*2.4%*	
Lepton ID Efficiencies	*2.0%*	*2.0%*	*2.2%*	*1.8%*	*2.0%*	*2.0%*	
Trigger Efficiencies	*2.1%*	*2.1%*	*2.1%*	*2.0%*	*3.4%*	*7.0%*	
Luminosity	*5.9%*	*5.9%*	*5.9%*	*5.9%*	*5.9%*	*5.9%*	

Table 47: Systematics table for 1J analysis background processes. Cross section systematics are correlated for the diboson processes (shown in italic font) but uncorrelated between all other processes. Higher-order diagram systematics shown in bold font are correlated among each other but uncorrelated across the 0, 1, and 2+ jet bins.

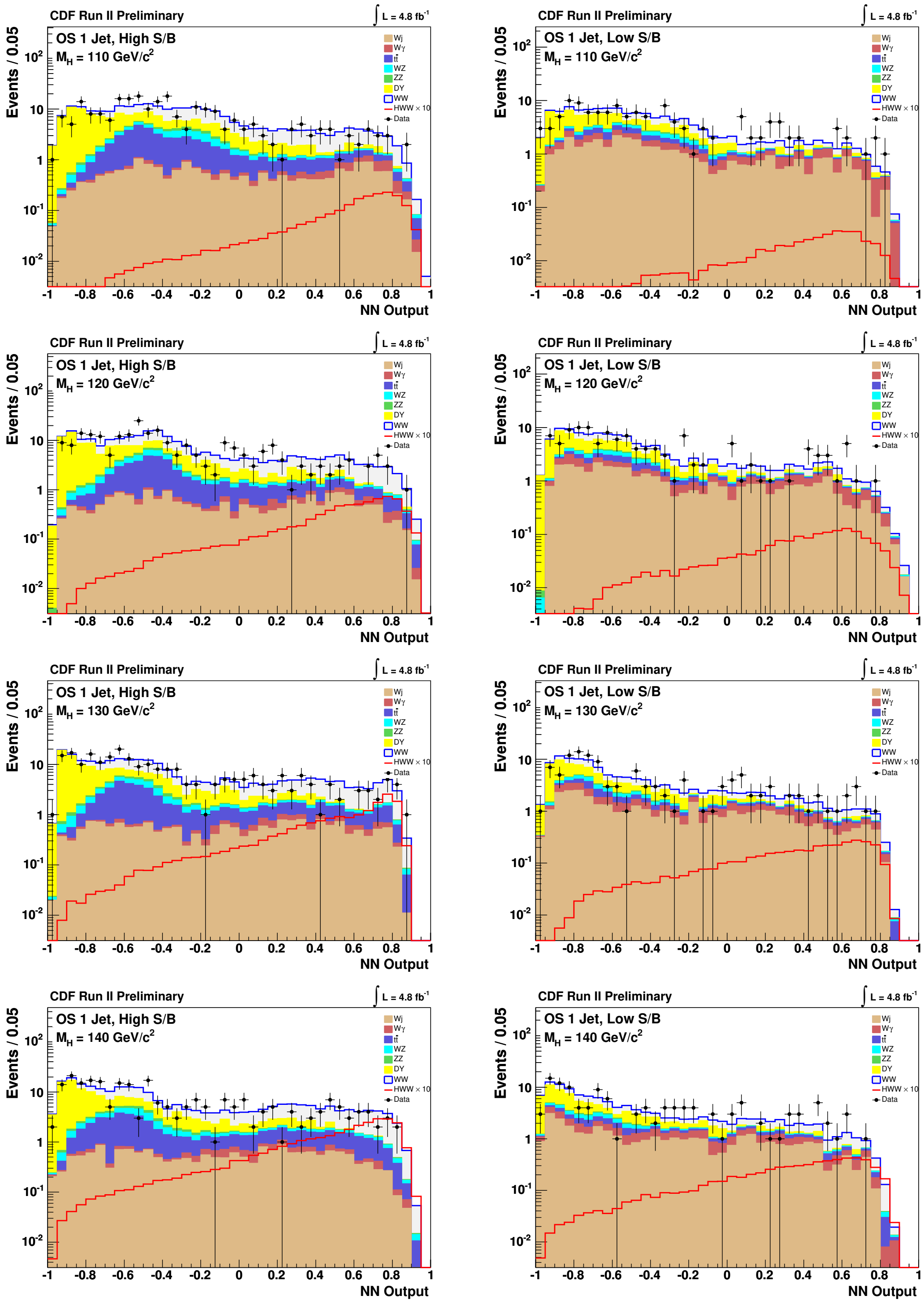

Figure 43: 1J Neural Network output templates for several Higgs masses. On the left for High S/B events and on the right for Low S/B. From the top to bottom: 110 GeV, 120 GeV, 130 GeV, and 140 GeV. **To be updated.**

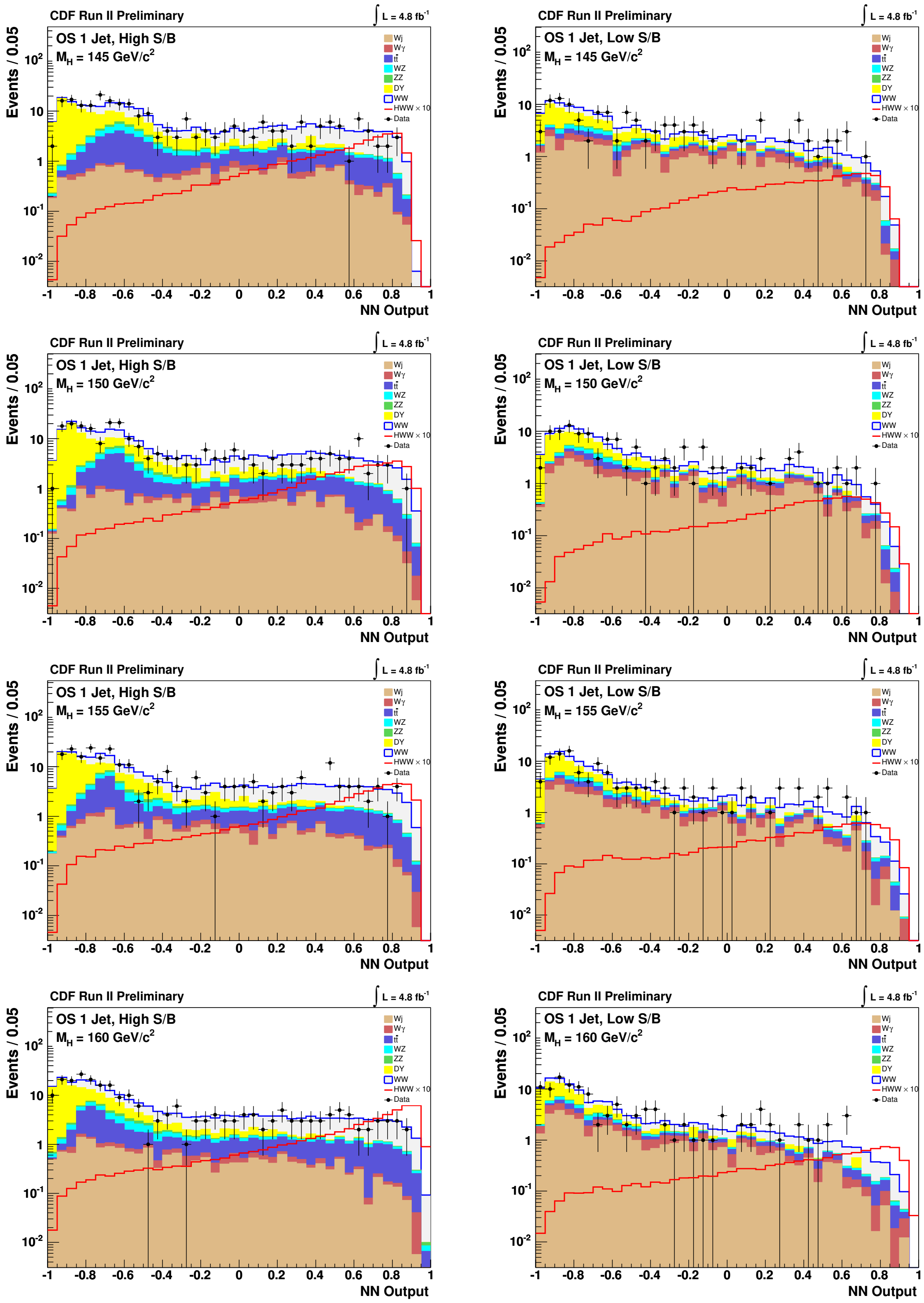

Figure 44: 1J Neural Network output templates for several Higgs masses. On the left for High S/B events and on the right for Low S/B. From the top to bottom: 145 GeV, 150 GeV, 155 GeV, and 160 GeV. **To be updated.**

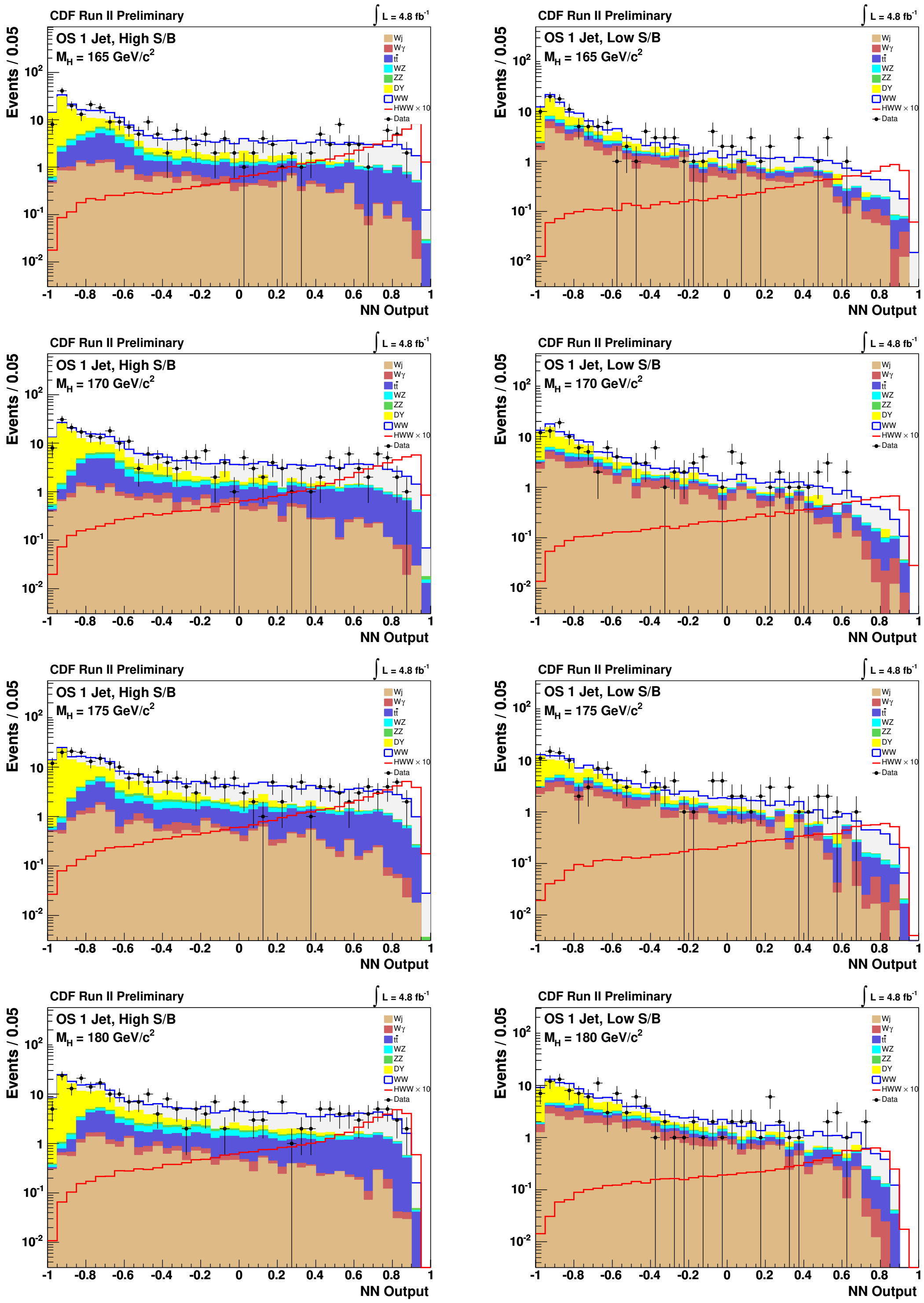

Figure 45: 1J Neural Network output templates for several Higgs masses. On the left for High S/B events and on the right for Low S/B. From the top to bottom: 165 GeV, 170 GeV, 175 GeV, 180 GeV. **To be updated.**

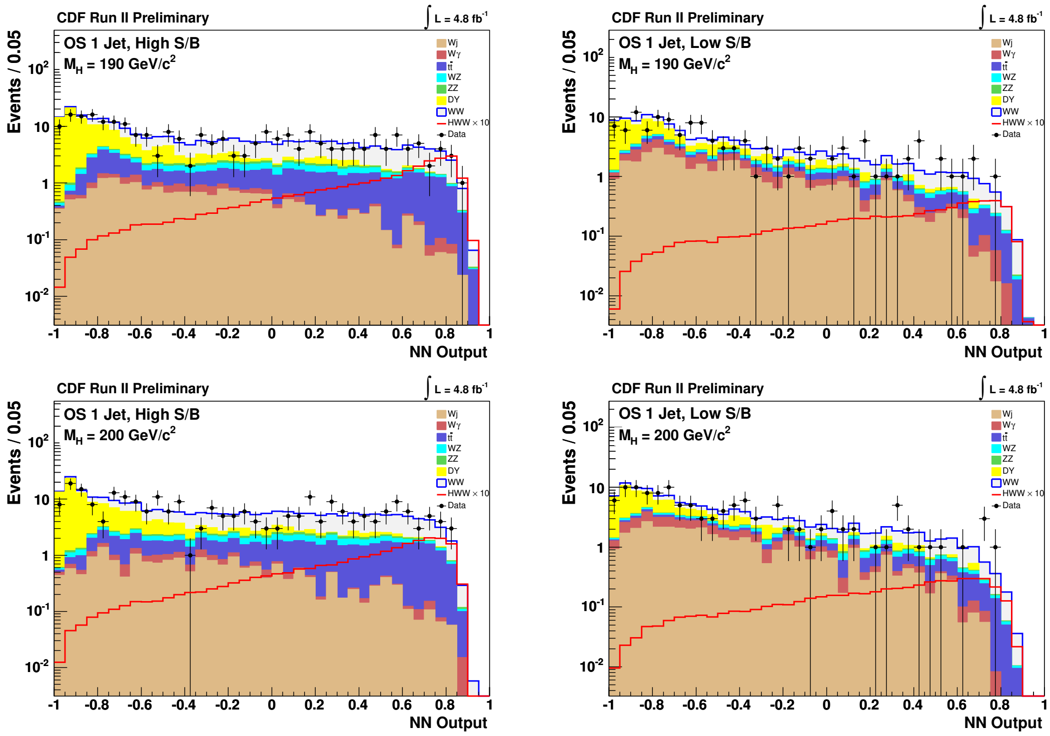

Figure 46: 1J Neural Network output templates for several Higgs masses. On the left for High S/B events and on the right for Low S/B. From the top to bottom: 190 GeV and 200 GeV. **To be updated.**

Uncertainty Source	$gg \to H$	WH	ZH	VBF
Cross Section				
Scale	10.9%			
PDF Model	5.1%			
Total	12.0%	*5.0%*	*5.0%*	10.0%
Acceptance				
Scale (leptons)	2.8%			
Scale (jets)	-5.1%			
PDF Model (leptons)	*1.7%*	*1.2%*	*0.9%*	*2.2%*
PDF Model (jets)	-1.9%			
EWK Higher-order Diagrams		*10.0%*	*10.0%*	*10.0%*
Lepton ID Efficiencies	*1.9%*	*1.9%*	*1.9%*	*1.9%*
Trigger Efficiencies	*3.3%*	*2.1%*	*2.1%*	*3.3%*
Luminosity	*5.9%*	*5.9%*	*5.9%*	*5.9%*

Table 48: Systematics table for 1J analysis signal processes. Cross section systematics are uncorrelated between the signal processes. Higher-order diagrams for the VH and VBF processes, shown in italic font, are correlated among each other but uncorrelated from background processes. The Scale (jets) and PDF Model (jets) systematics for $gg \to H$ are anticorrelated between the 0, 1, and 2+ jet bins, as these systematics cause events to fluctuate between jet bins.

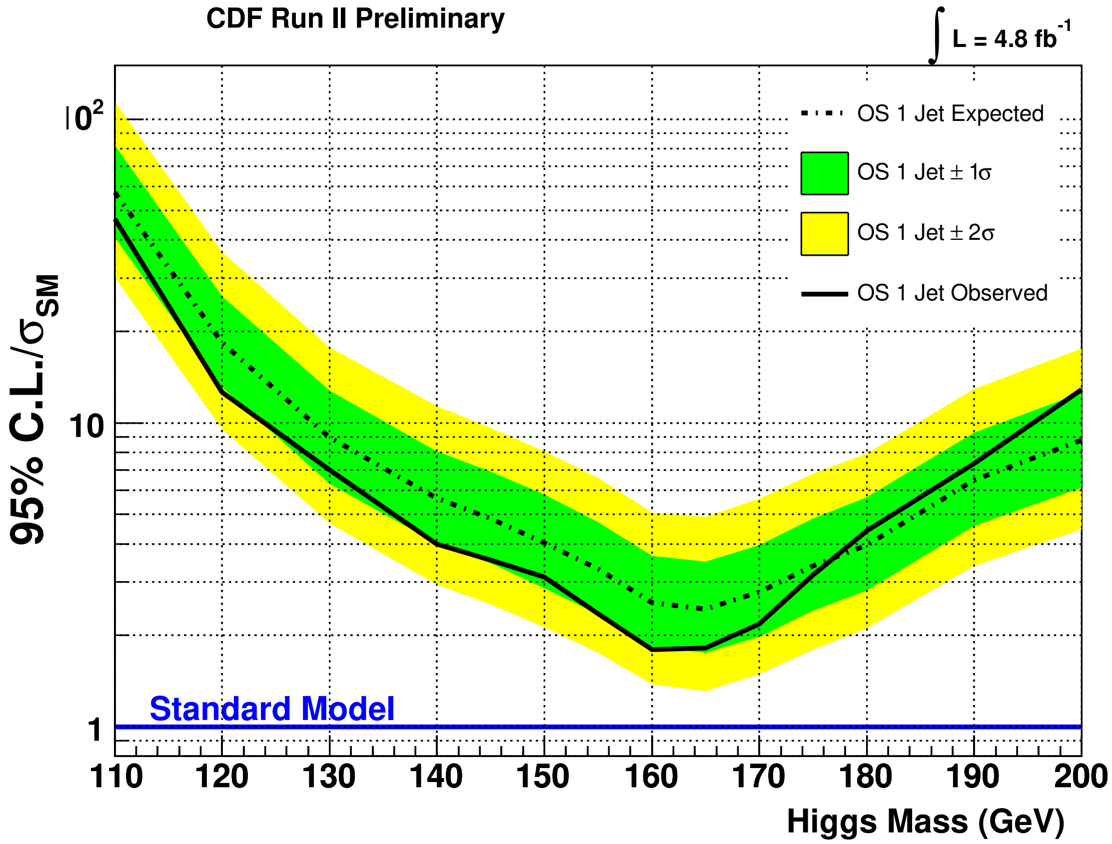

Figure 47: $H \to WW$ sensitivity normalized to NNLL σ_{SM} calculation from the combination of the High S/B and Low S/B channels in the 1J region. In this region we consider potential signal contributions from gluon fusion, vector boson fusion, and associated production with either a W or Z boson. **To be updated.**

OS 1 Jet	110	120	130	140	145	150	155
$-2\sigma/\sigma_{SM}$	30.04	9.54	4.67	2.94	2.53	2.12	1.75
$-1\sigma/\sigma_{SM}$	40.71	13.08	6.31	4.01	3.45	2.86	2.34
Median/$\sigma_{\mathbf{SM}}$	**57.32**	**18.40**	**8.94**	**5.65**	**4.84**	**4.03**	**3.31**
$+1\sigma/\sigma_{SM}$	81.86	26.12	12.76	8.05	6.92	5.82	4.72
$+2\sigma/\sigma_{SM}$	114.07	36.48	17.75	11.36	9.62	8.06	6.59
Observed/$\sigma_{\mathbf{SM}}$	**46.92**	**12.62**	**6.99**	**3.99**	**3.53**	**3.11**	**2.35**
	160	165	170	175	180	190	200
$-2\sigma/\sigma_{SM}$	1.38	1.31	1.49	1.79	2.11	3.38	4.48
$-1\sigma/\sigma_{SM}$	1.83	1.75	1.97	2.41	2.81	4.58	6.13
Median/$\sigma_{\mathbf{SM}}$	**2.56**	**2.44**	**2.78**	**3.38**	**3.97**	**6.49**	**8.77**
$+1\sigma/\sigma_{SM}$	3.66	3.49	3.96	4.85	5.70	9.29	12.59
$+2\sigma/\sigma_{SM}$	5.08	4.91	5.63	6.82	7.92	12.95	17.56
Observed/$\sigma_{\mathbf{SM}}$	**1.80**	**1.81**	**2.18**	**3.16**	**4.41**	**7.36**	**12.86**

Table 49: $H \rightarrow WW$ sensitivity normalized to NNLL σ_{SM} calculation from the combination of the High S/B and Low S/B channels. In this region we consider potential signal contributions from gluon fusion, vector boson fusion, and associated production with either a W or Z boson. **To be updated.**

9 Opposite-sign Dilepton Signal Region with 2+ Jets

The event selection for events with two or more jets in the final state (2J) is nearly identical to that for events with zero or one jets. We require two or more jets with $E_{\mathrm{T}} > 15$ GeV and $|\eta| < 2.5$ using Level 5 jet corrections.

The dominant background in this region is from $t\bar{t}$ production where both top quarks decay via $t \to Wb \to \ell\nu b$. Our requirement of two jets in the final state is satisfied by the presence of the two b-quarks in the final state. In order to reduce the $t\bar{t}$ background, we additionally reject events that contain one or more b-tagged jets. For the b-tag, we use the tight SecVtx information in Stntuple [29]. Since we are apply b-tagging to our $t\bar{t}$ background model, we need to use the standard Data/MC efficiency scale factor correction for b-tagging which we take to be 0.94 ± 0.03[3]. There are no real b-jets in the other sources of background, but we expect to occasionally mistag one of these jets as a b-jet. The mistag matrix for tight SecVtx requirements for the first 2.2 fb^{-1} of data is given in [30] and shows that the rate of mistags is very low. Because our other background sources are small contributions and the mistag rate is also very small, we expect the effect of mistags to be negligible and therefore do not attempt to apply any corrections to our models for these effects. There are two additional scale factors applied to the $t\bar{t}$ sample: one of 0.968 to account for generating the sample with a top quark mass of 175 GeV, and another of 1.037 due to not requiring events to be in the silicon good run list. These scale factors and their contributions to the uncertainty are described in Section 6.4. Even after rejecting events that contain b-tags, $t\bar{t}$ production accounts for more than 50% of the total background in the 2J region.

The background expectation and observed yield for the opposite-sign dilepton signal region for events containing two or more reconstructed jets with $E_T > 15$ GeV are shown in Table 50. The numbers in this table correspond to event totals prior to the removal of events containing b-tags. The expected and observed kinematic distributions for these events are shown in Figures 48-50. We stack the backgrounds on top of each other, and then for comparison we overlay the contribution from a 160 GeV/c^2 Higgs boson with yields scaled up by a factor of 10. In addition, we calculate a confidence level for data versus background expectations on each plot. The confidence levels shown are for Poisson fluctuations and the KS test.

As in the case of 1J events, we do not attempt to calculate Matrix Elements for 2J events. Instead, we rely solely on a neural network (NN) to discriminate signal from background using kinematic variables as inputs to the NN. We do not use jet angular variables, as they are not reliably reproduced by Pythia. Also, we find that using jet angular variables in the NN does not significantly improve the sensitivity. Optimization and training of the neural network are done in the same manner as for the 0J case described in Section 7. For the 2J region our neural network uses 8 inputs, 10 hidden

[3] This is a preliminary value that should fit well with data up to period 23, especially given the large uncertainty we associate with it.

Category	WW	WZ	ZZ	$t\bar{t}$	DY	$W\gamma$	W+jets	Total	Data
$e\ e$	4.9	1.9	0.9	57.0	12.2	1.4	8.3	86.4	61.0
$e\ \mu$	11.9	1.1	0.4	140.2	19.9	1.5	10.8	185.8	175.0
$\mu\ \mu$	3.9	1.2	0.7	48.8	10.4	0.0	2.0	66.9	76.0
e trk	3.4	0.8	0.4	41.5	6.6	0.3	2.4	55.4	44.0
μ trk	2.2	0.4	0.2	26.0	2.9	0.1	2.5	34.2	27.0
Total:	26.2	5.4	2.5	313.5	52.0	3.2	25.9	428.7	383.0

Category	WW	WZ	ZZ	$t\bar{t}$	DY	$W\gamma$	W+jets	Total	Data
LBE LBE	3.0	1.0	0.5	39.4	6.0	0.3	1.2	51.4	38.0
LBE PHX	1.6	0.8	0.3	15.9	5.1	0.8	4.7	29.2	19.0
PHX PHX	0.3	0.1	0.0	1.7	1.0	0.3	2.4	5.8	4.0
LBE CMUP	3.6	0.3	0.1	48.3	5.9	0.3	2.1	60.6	61.0
LBE CMP	0.5	0.0	0.0	6.5	0.9	0.0	0.5	8.5	10.0
LBE CMX	1.6	0.1	0.1	19.2	3.4	0.1	0.7	25.2	18.0
LBE CMXMsKs	0.2	0.0	0.0	3.2	0.0	0.0	0.2	3.6	6.0
LBE BMU	0.3	0.0	0.0	3.8	0.5	0.0	0.0	4.7	9.0
LBE CMIOCES	2.6	0.2	0.1	30.6	2.7	0.0	0.3	36.5	34.0
LBE CMIOPES	0.6	0.1	0.0	6.1	2.1	0.0	0.4	9.3	10.0
PHX CMUP	1.0	0.1	0.0	9.7	1.7	0.5	2.5	15.5	10.0
PHX CMP	0.1	0.0	0.0	1.2	0.1	0.1	0.4	1.8	1.0
PHX CMX	0.4	0.1	0.0	3.9	1.1	0.3	1.4	7.2	3.0
PHX CMXMsKs	0.1	0.0	0.0	0.7	0.1	0.0	0.4	1.2	2.0
PHX BMU	0.1	0.0	0.0	0.7	0.1	0.0	0.0	0.9	2.0
PHX CMIOCES	0.7	0.1	0.0	5.2	0.5	0.1	0.4	7.0	7.0
PHX CMIOPES	0.2	0.0	0.0	1.1	0.8	0.1	0.8	3.0	2.0
CMUP CMUP	0.6	0.2	0.1	9.5	1.7	0.0	0.3	12.3	15.0
CMUP CMP	0.1	0.1	0.0	2.4	0.3	0.0	0.1	3.0	4.0
CMUP CMX	0.7	0.2	0.1	7.7	1.9	0.0	0.2	10.7	10.0
CMUP CMXMsKs	0.1	0.0	0.0	1.3	0.6	0.0	0.1	2.0	2.0
CMUP BMU	0.1	0.0	0.0	1.5	1.1	0.0	0.0	2.8	3.0
CMUP CMIOCES	1.0	0.2	0.2	12.0	1.6	0.0	0.3	15.3	18.0
CMUP CMIOPES	0.3	0.1	0.0	2.4	0.3	0.0	0.3	3.4	5.0
CMX CMP	0.0	0.0	0.0	1.0	0.3	0.0	0.0	1.4	0.0
CMX CMX	0.2	0.0	0.0	1.4	0.0	0.0	0.0	1.7	3.0
CMX CMXMsKs	0.0	0.0	0.0	0.6	0.2	0.0	0.0	0.8	0.0
CMX BMU	0.1	0.0	0.0	0.6	0.3	0.0	0.0	1.0	1.0
CMX CMIOCES	0.3	0.1	0.1	4.6	0.8	0.0	0.1	6.0	7.0
CMX CMIOPES	0.1	0.0	0.0	0.9	0.8	0.0	0.2	2.1	1.0
CMXMsKs CMP	0.0	0.0	0.0	0.3	0.0	0.0	0.0	0.3	1.0
CMXMsKs CMXMsKs	0.0	0.0	0.0	0.1	0.1	0.0	0.0	0.1	0.0
CMXMsKs BMU	0.0	0.0	0.0	0.1	0.0	0.0	0.0	0.1	1.0
CMXMsKs CMIOCES	0.1	0.0	0.0	0.6	0.2	0.0	0.0	1.0	2.0
CMXMsKs CMIOPES	0.0	0.0	0.0	0.1	0.0	0.0	0.0	0.2	1.0
CMP CMP	0.0	0.0	0.0	0.2	0.1	0.0	0.0	0.4	0.0
CMP BMU	0.0	0.0	0.0	0.2	0.1	0.0	0.0	0.3	0.0
CMP CMIOCES	0.1	0.0	0.0	1.1	0.0	0.0	0.0	1.3	1.0
CMP CMIOPES	0.0	0.0	0.0	0.2	0.1	0.0	0.0	0.4	1.0
LBE CrkTrk	2.7	0.6	0.3	35.4	5.5	0.1	1.7	46.3	31.0
PHX CrkTrk	0.7	0.2	0.1	6.1	1.1	0.2	0.4	8.8	13.0
CMUP CrkTrk	1.4	0.2	0.1	16.8	2.0	0.0	1.7	22.2	17.0
CMP CrkTrk	0.2	0.0	0.0	1.6	0.1	0.0	0.1	2.0	4.0
CMX CrkTrk	0.6	0.1	0.1	6.7	0.7	0.0	0.7	8.9	5.0
CMXMsKs CrkTrk	0.1	0.0	0.0	0.9	0.1	0.0	0.0	1.1	1.0
Total:	26.2	5.4	2.5	313.5	52.0	3.2	24.7	427.5	383.0

Table 50: Yields in opposite-sign dilepton signal region for events with two or more jets, before removing those that contain a b-tagged jet.

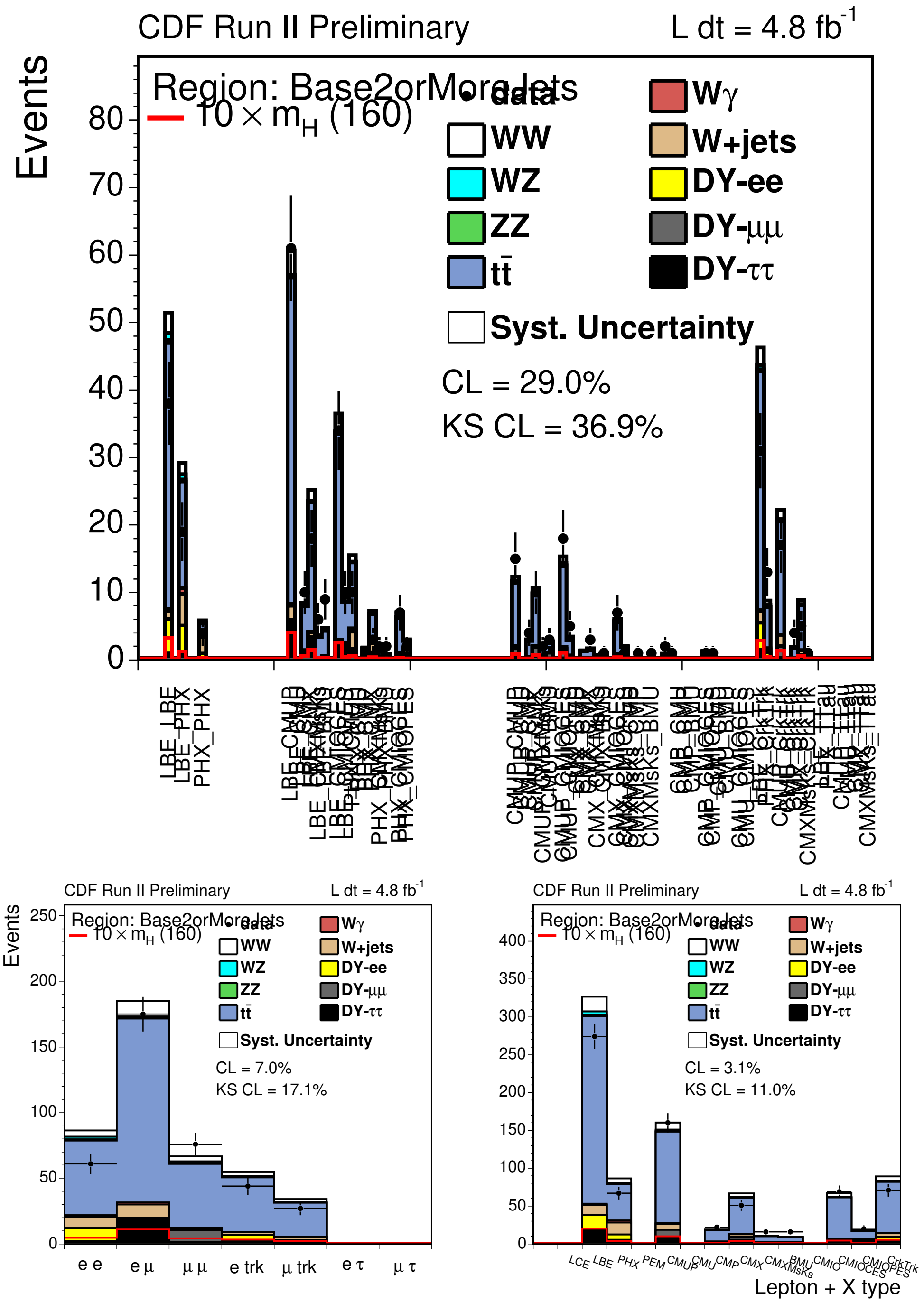

Figure 48: Signal and background in the opposite-sign signal region for events containing two or more reconstructed jets with $E_T > 15$ GeV (prior to removal of events containing a b-tagged jet).

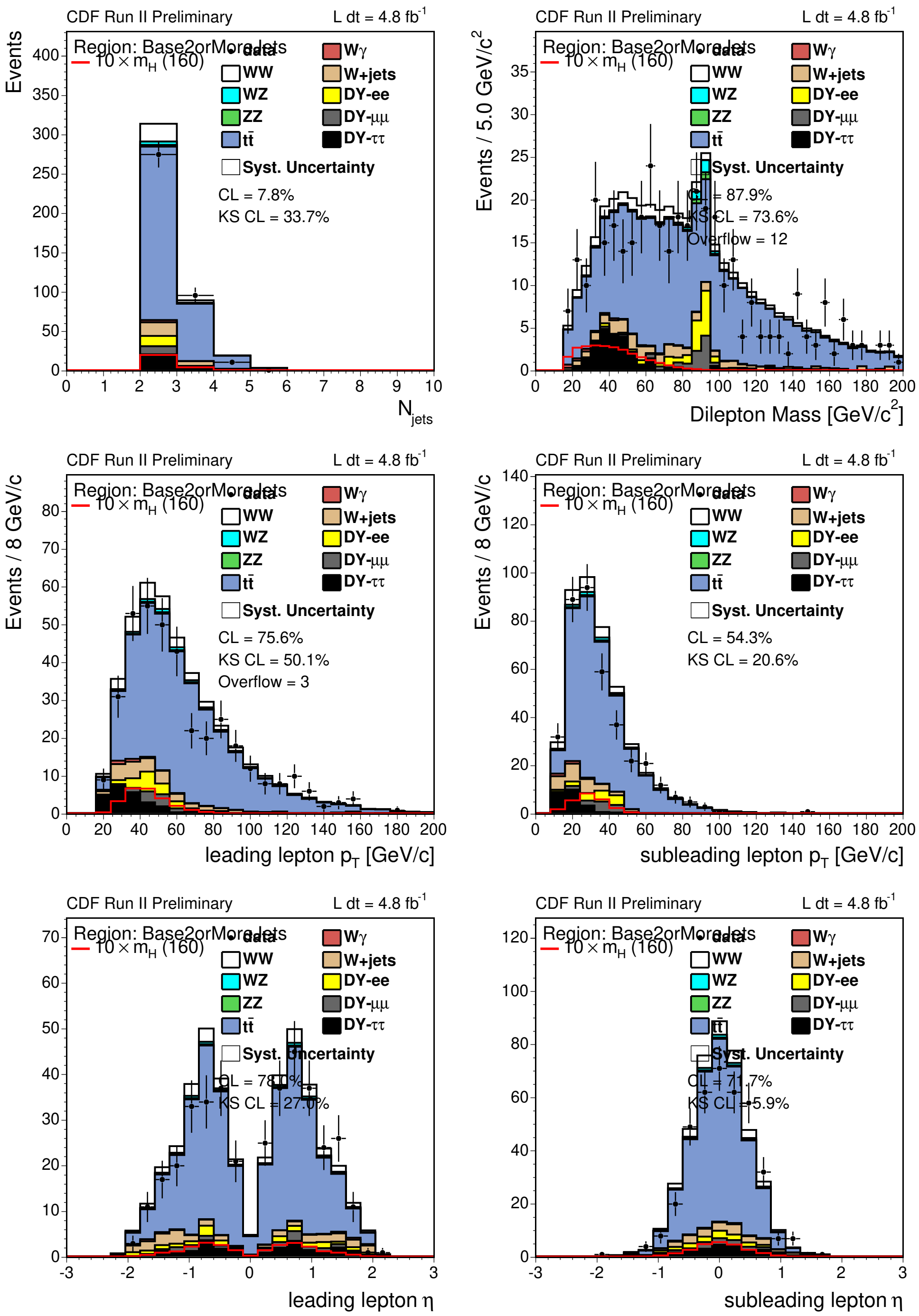

Figure 49: Signal and background in the opposite-sign signal region for events containing two or more reconstructed jets with $E_T > 15$ GeV (prior to removal of events containing a b-tagged jet).

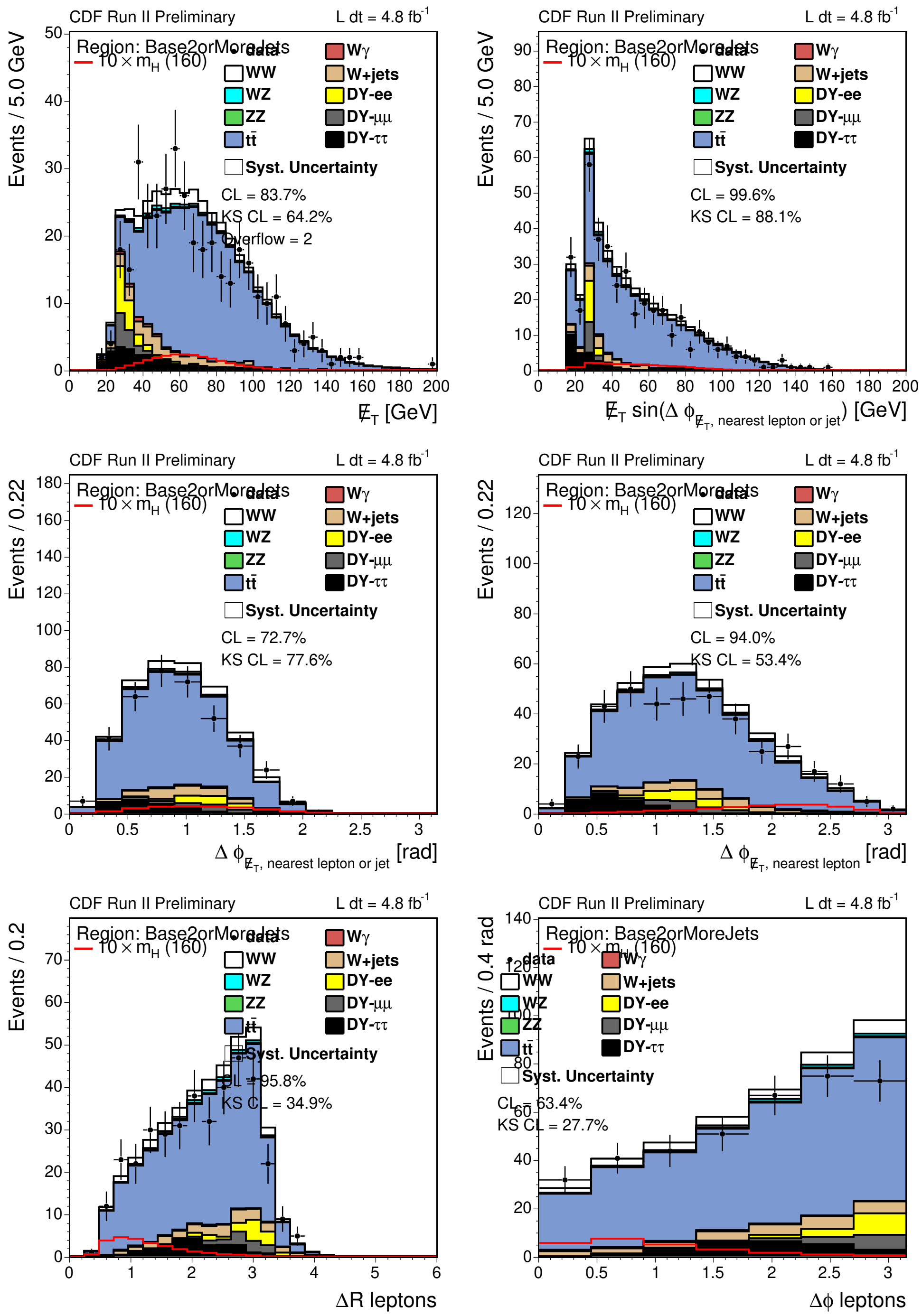

Figure 50: Signal and background in the opposite-sign signal region for events containing two or more reconstructed jets with $E_T > 15$ GeV (prior to removal of events containing a b-tagged jet).

Variable	Meaning
	2J neural networks
dRLeptons	ΔR between the leptons
dPhiLeptons	$\Delta\phi$ between the leptons
dPhiLepSumMet	$\Delta\phi$ between vector sum of first and second lepton momenta and $\not\!\!E_T$
sumJetPt	Vector sum of first and second jet p_{T}
Lep1Et	Transverse energy E_{T} of the first lepton
Lep2Et	Transverse energy E_{T} of the second lepton
Ht	Transverse mass H_{T} (scalar sum of lepton E_{T}'s, jet E_{T}'s, and $\not\!\!E_T$)
Mll	Dilepton invariant mass M_{ll}

Table 51: Summary of inputs to 2J neural networks.

nodes and 1 output node. The input variables used for the 2J NN are shown in Table 51. The observed distributions of each 2J neural network input parameter compared with the distributions predicted by our background model are shown in Figures 51 and 52. Here, events containing a b-tagged jet have been removed in both the observed and predicted distributions. For reference, we also include a hypothetical signal component for a Higgs boson with $m_H = 160$ GeV$/c^2$.

Templates are created for each neural network and used for calculating 95% CL limits with the MCLimit program [28]. Due to the low statistics in the 2J region, we do not divide events into High S/B and Low S/B categories as is done for the 0J and 1J regions. Output templates for the trained 2J neural network are shown in Figures 53 and 54.

In the 2J region we also consider potential signal contributions from all four Higgs production processes that contribute significantly at high masses (gluon fusion ($gg \to H \to WW \to ll\nu\nu$),Vector Boson Fusion (VBF), and associated production VH ($q\bar{q} \to ZH \to ZWW$ and $q\bar{q} \to WH \to WWW$). The additional processes contribute significantly to the event regions with one or more jets and incorporating their contributions is fairly straight-forward since we do not attempt to use neural network inputs based on Matrix Element calculations in these regions. We evaluate the number of events expected from each production process as a function of the mass of the Higgs. These numbers are shown in Table 52.

In calculating the final limits, we take into account systematic uncertainties on both the signal and background models we use to train our neural networks. Systematic uncertainties for the 2J region are summarized in Tables 53 and 54.

Tables 55 and Figure 55 show the expected (based on 10000 pseudo-experiments) and observed limits obtained from the 2J region, incorporating the systematic uncertainties listed in Tables 53 and 54.

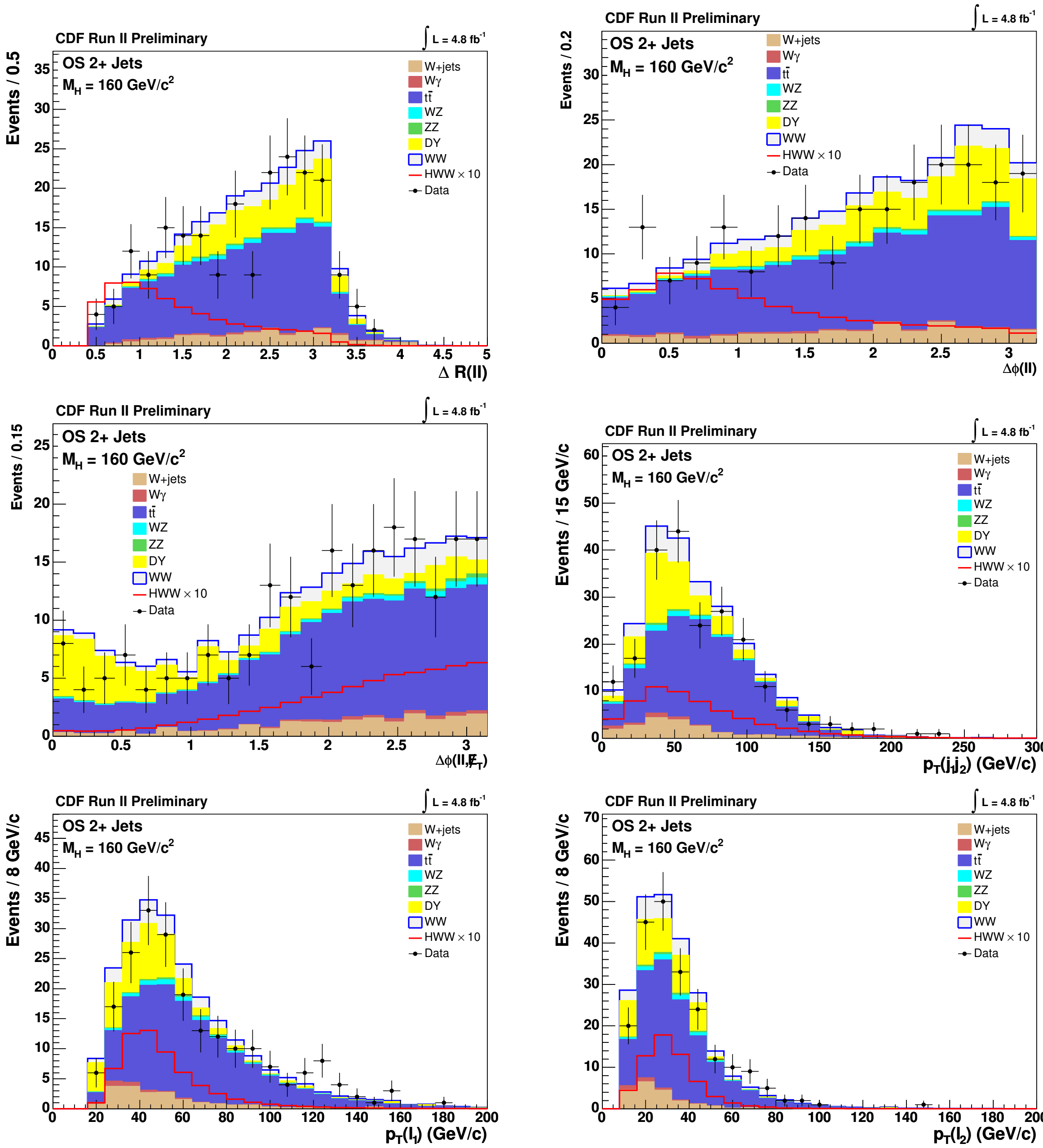

Figure 51: Neural Network input variables for 2J NN (signal for $M_H = 160$ GeV/c^2). **To be updated.**

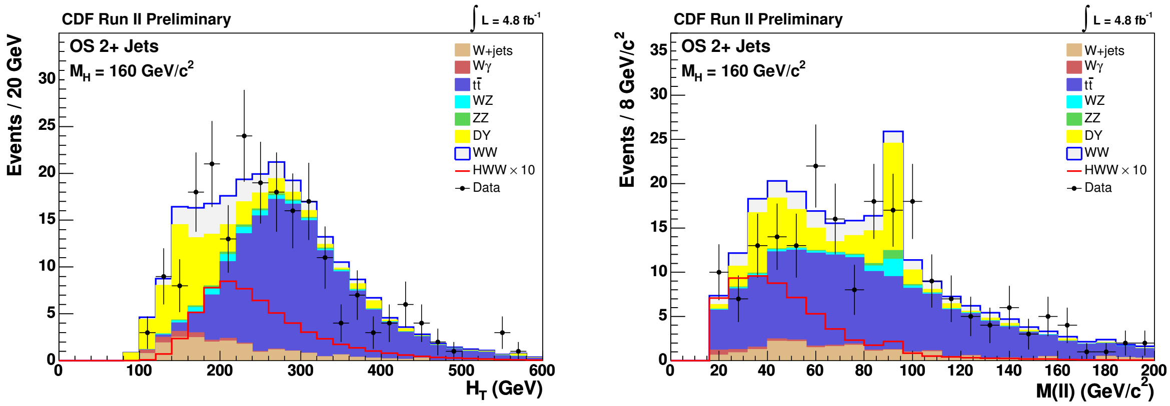

Figure 52: Neural Network input variables for 2J NN (signal for $M_H = 160$ GeV/c^2). **To be updated.**

Mass (GeV/c^2)	gg→H	WH	ZH	VBF
110	0.0865	0.133	0.0669	0.0354
120	0.306	0.404	0.205	0.126
130	0.72	0.828	0.417	0.296
140	1.23	1.28	0.64	0.512
145	1.47	1.42	0.719	0.604
150	1.72	1.57	0.809	0.714
155	2	1.73	0.893	0.834
160	2.24	1.86	0.932	0.941
165	2.29	1.76	0.929	0.972
170	2.16	1.64	0.874	0.939
175	1.98	1.5	0.803	0.88
180	1.85	1.37	0.729	0.822
190	1.33	0.952	0.513	0.609
200	1.1	0.761	0.412	0.505

Table 52: Expected Higgs Signal yields as a function of the Higgs boson mass in the 2J region for each of the contributing production processes. **To be updated.**

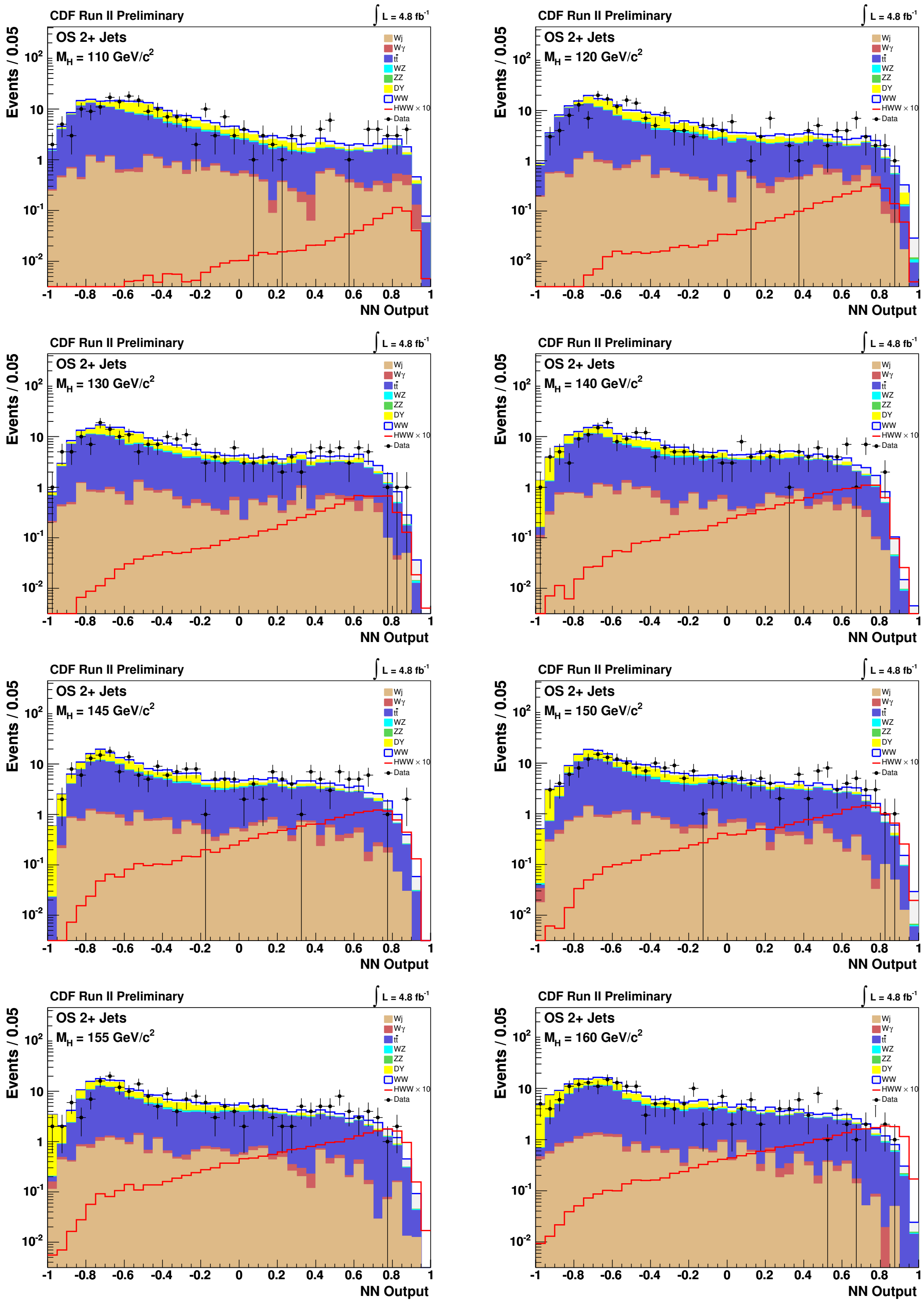

Figure 53: 2J Neural Network output templates for several Higgs masses. From the top left to bottom right: 110 GeV, 120 GeV, 130 GeV, 140 GeV, 145 GeV, 150 GeV, 155 GeV, and 160 GeV. **To be updated.**

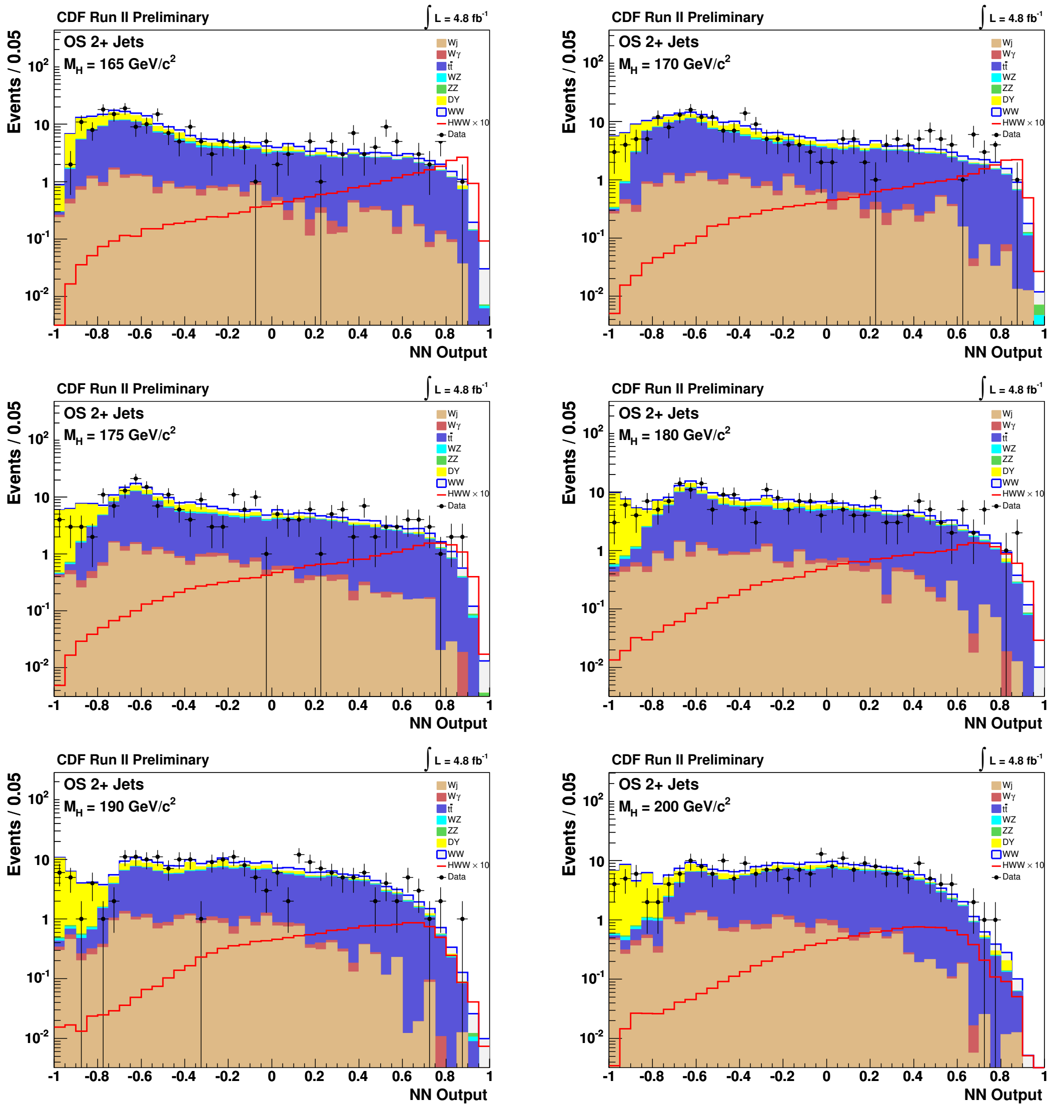

Figure 54: 2J Neural Network output templates for several Higgs masses. From the top left to bottom right : 165 GeV, 170 GeV, 175 GeV, 180 GeV, 190 GeV, and 200 GeV. **To be updated.**

Uncertainty Source	WW	WZ	ZZ	$t\bar{t}$	DY	$W\gamma$	W+jet
Cross Section							
Scale							
PDF Model							
Total	*6.0%*	*6.0%*	*6.0%*	10.0%	5.0%	10.0%	
Acceptance							
Scale							
PDF Model	*1.9%*	*2.7%*	*2.7%*	*2.1%*	*4.1%*	*2.2%*	
Higher-order Diagrams	*5.0%*	*10.0%*	*10.0%*	10.0%		*10.0%*	
Jet Modeling	20.0%				32.0%	20.0%	
Conversion Modeling						20.0%	
b-tag Veto				5.8%			
Jet Fake Rates							27.1%
MC Run Dependence	*1.4%*			*1.5%*		*1.0%*	
Lepton ID Efficiencies	*1.9%*	*2.9%*	*1.9%*	*1.9%*	*1.9%*	*1.9%*	
Trigger Efficiencies	*2.1%*	*2.1%*	*2.1%*	*2.0%*	*3.4%*	*7.0%*	
Luminosity	*5.9%*	*5.9%*	*5.9%*	*5.9%*	*5.9%*	*5.9%*	

Table 53: Systematics table for 2J region background processes. Cross section systematics are correlated for the diboson processes (shown in italic font) but uncorrelated between all other processes. Higher-order diagram systematics shown in bold font are correlated among each other but uncorrelated across the 0, 1, and 2+ jet bins.

Uncertainty Source	$gg \to H$	WH	ZH	VBF
Cross Section				
Scale	10.9%			
PDF Model	5.1%			
Total	12.0%	*5.0%*	*5.0%*	10.0%
Acceptance				
Scale (leptons)	3.1%			
Scale (jets)	-8.7%			
PDF Model (leptons)	*2.0%*	*1.2%*	*0.9%*	*2.2%*
PDF Model (jets)	-2.8%			
EWK Higher-order Diagrams		*10.0%*	*10.0%*	*10.0%*
Lepton ID Efficiencies	*1.9%*	*1.9%*	*1.9%*	*1.9%*
Trigger Efficiencies	*3.3%*	*2.1%*	*2.1%*	*3.3%*
Luminosity	*5.9%*	*5.9%*	*5.9%*	*5.9%*

Table 54: Systematics table for 2J region signal processes. Cross section systematics are uncorrelated between the signal processes. Higher-order diagrams for the VH and VBF processes, shown in italic font, are correlated among each other but uncorrelated from background processes. The Scale (jets) and PDF Model (jets) systematics for $gg \to H$ are anticorrelated between the 0, 1, and 2+ jet bins, as these systematics cause events to fluctuate between jet bins.

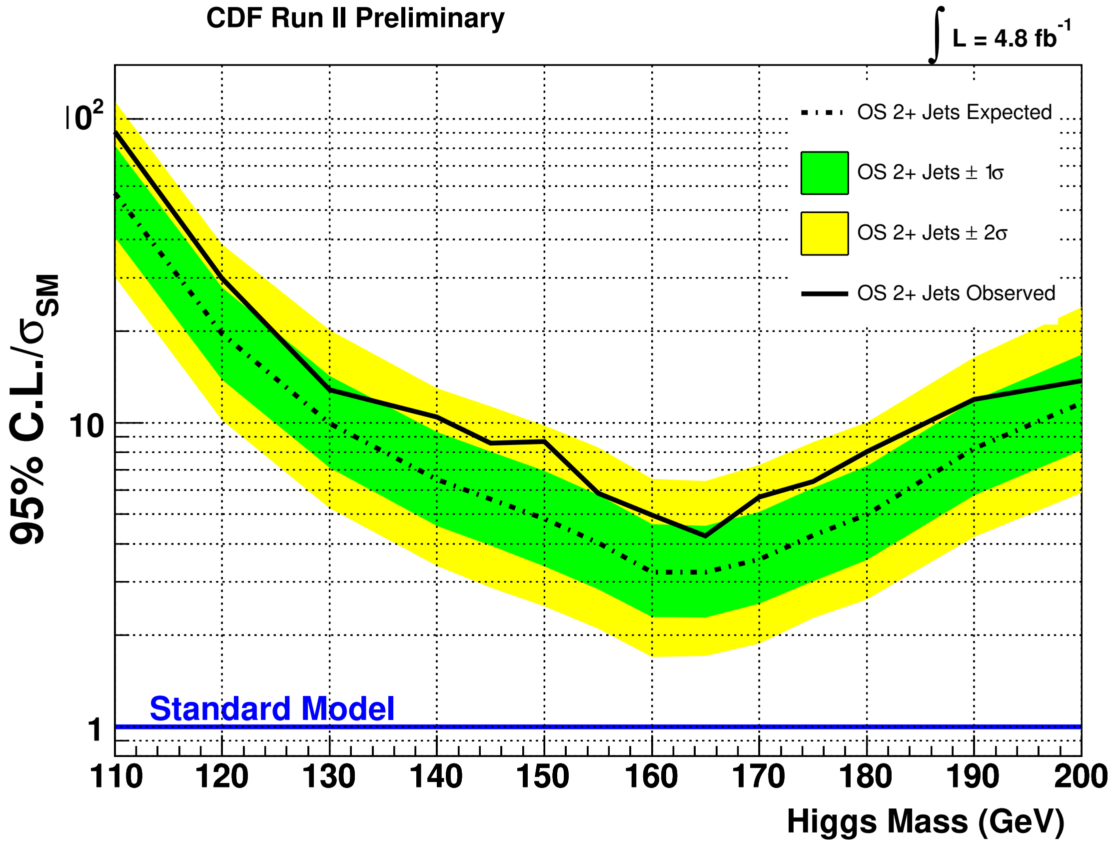

Figure 55: $H \to WW$ sensitivity normalized to NNLL σ_{SM} calculation in the 2J region. In this region we consider potential signal contributions from gluon fusion, vector boson fusion, and associated production with either a W or Z boson. **To be updated.**

OS 2+ Jets	110	120	130	140	145	150	155
$-2\sigma/\sigma_{SM}$	30.25	10.20	5.23	3.38	2.86	2.48	2.10
$-1\sigma/\sigma_{SM}$	40.76	13.86	7.11	4.59	3.94	3.37	2.83
Median/$\sigma_{\mathbf{SM}}$	**56.98**	**19.58**	**9.95**	**6.51**	**5.61**	**4.82**	**4.03**
$+1\sigma/\sigma_{SM}$	81.49	27.88	14.22	9.32	8.03	6.93	5.78
$+2\sigma/\sigma_{SM}$	114.22	38.60	20.16	13.00	11.31	9.79	8.28
Observed/$\sigma_{\mathbf{SM}}$	**90.56**	**29.85**	**12.82**	**10.44**	**8.55**	**8.66**	**5.87**
	160	165	170	175	180	190	200
$-2\sigma/\sigma_{SM}$	1.69	1.71	1.88	2.28	2.62	4.20	5.88
$-1\sigma/\sigma_{SM}$	2.29	2.29	2.54	3.01	3.54	5.78	8.13
Median/$\sigma_{\mathbf{SM}}$	**3.22**	**3.22**	**3.55**	**4.26**	**4.98**	**8.22**	**11.61**
$+1\sigma/\sigma_{SM}$	4.64	4.58	5.09	6.11	7.20	11.83	16.76
$+2\sigma/\sigma_{SM}$	6.53	6.44	7.27	8.63	10.02	16.42	23.94
Observed/$\sigma_{\mathbf{SM}}$	**4.97**	**4.24**	**5.70**	**6.41**	**8.05**	**11.91**	**13.74**

Table 55: $H \to WW$ sensitivity normalized to NNLL σ_{SM} calculation in the 2J region. In this region we consider potential signal contributions from gluon fusion, vector boson fusion, and associated production with either a W or Z boson. **To be updated.**

10 Combination of 0, 1, and 2+ Jets Channels

Because we separate events into High S/B and Low S/B categories in the 0J and 1J regions, there are a total of five channels from which we produce our combined limits. Each channel has its own unique background composition and signal to background ratio, and therefore will contribute different relative sensitivities to the overall cross section limit. As previously mentioned, in the 2J region, we choose to consider all events as a single channel, primarily to maintain sufficient statistics for some of the Monte-Carlo based templates as well as the W+jets (Fakes) templates which lack statistics for the higher jet multiplicities.

A big gain in sensitivity in the 1J and 2J regions comes from including potential signal contributions from the vector boson fusion (VBF) and associated production channels (WH, ZH). As discussed previously, the contributions of these extra production mechanisms are negligible in the 0J regions and so we ignore them in that case. A benefit of this approach is that we can continue to use Matrix Element calculations in the 0J region as additional inputs to the neural network gaining a small amount of additional sensitivity.

As is the case in each of the individual regions, we use Tom Junk's MCLimit [28] to produce a combined limit from all five channels. We have opted to set our own statistical errors on each bin and use the CSM_GAUSSIAN_BINERR option in MCLimit. The bin errors are nothing more then the typical statistical errors calculated by ROOT's Sumw2. The current limits from the combination of all five channels are shown in Table 56 and Figure 56. Using the same integrated luminosity as the previous analyses presented in CDF 9697, the switch to using likelihood-based electrons leads to an increase in overall sensitivity of about XXXX%.

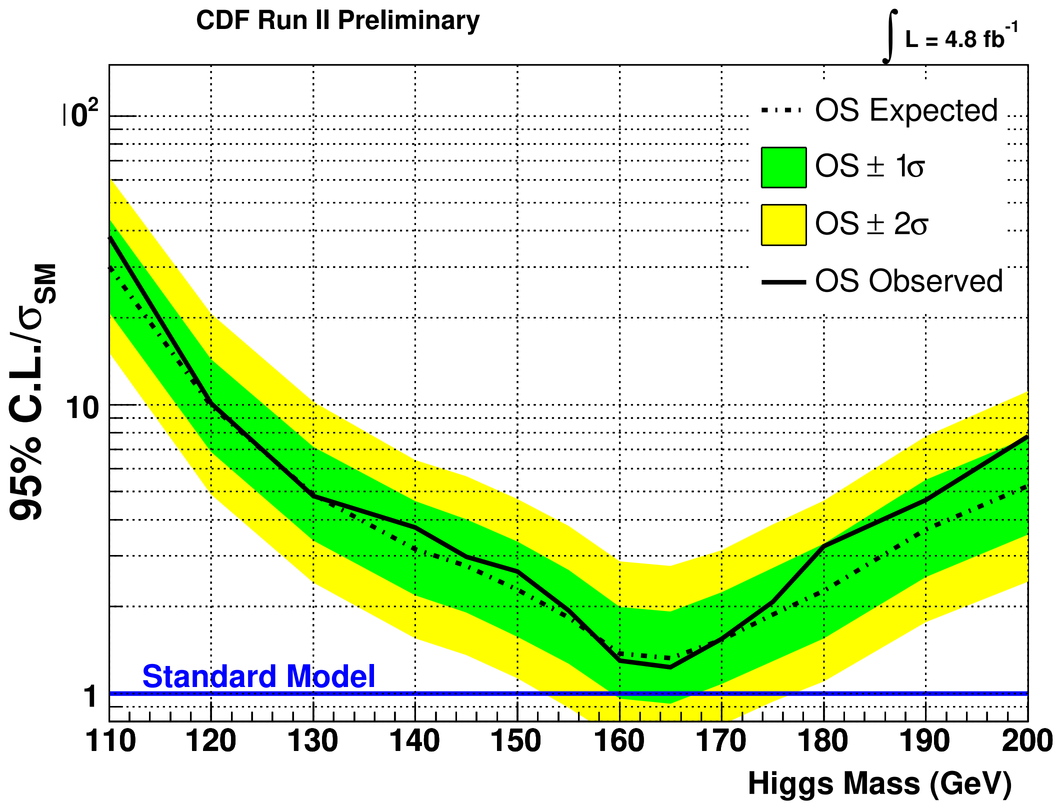

Figure 56: $H \rightarrow WW$ sensitivity normalized to NNLL σ_{SM} calculation for combination of all five channels (0J High S/B, 0J Low S/B, 1J High S/B, 1J Low S/B, and 2J). **To be updated.**

OS	110	120	130	140	145	150	155
$-2\sigma/\sigma_{SM}$	15.13	4.89	2.42	1.55	1.36	1.13	0.89
$-1\sigma/\sigma_{SM}$	20.86	6.85	3.39	2.18	1.91	1.57	1.27
Median/$\sigma_{\mathbf{SM}}$	**30.05**	**9.92**	**4.89**	**3.16**	**2.76**	**2.29**	**1.83**
$+1\sigma/\sigma_{SM}$	43.97	14.39	7.15	4.64	4.00	3.35	2.67
$+2\sigma/\sigma_{SM}$	61.42	20.64	10.25	6.43	5.65	4.72	3.81
Observed/$\sigma_{\mathbf{SM}}$	**38.19**	**10.11**	**4.82**	**3.76**	**2.98**	**2.65**	**1.94**
	160	**165**	**170**	**175**	**180**	**190**	**200**
$-2\sigma/\sigma_{SM}$	0.69	0.67	0.78	0.94	1.10	1.77	2.44
$-1\sigma/\sigma_{SM}$	0.96	0.92	1.08	1.29	1.55	2.53	3.55
Median/$\sigma_{\mathbf{SM}}$	**1.38**	**1.33**	**1.54**	**1.88**	**2.26**	**3.69**	**5.23**
$+1\sigma/\sigma_{SM}$	2.00	1.92	2.24	2.71	3.30	5.49	7.72
$+2\sigma/\sigma_{SM}$	2.86	2.76	3.13	3.86	4.65	7.78	11.14
Observed/$\sigma_{\mathbf{SM}}$	**1.30**	**1.23**	**1.54**	**2.08**	**3.23**	**4.66**	**7.78**

Table 56: Limits on Higgs production using all five channels (0J High S/B, 0J Low S/B, 1J High S/B, 1J Low S/B, and 2J) and 4.8 fb^{-1}. **To be updated.**

11 Same-Sign Dilepton Signal Region with 1+ Jets

To gain extra sensitivity, we also search for Higgs signal in like-sign, or same-sign (SS), dileptons. These occur naturally in $ZH \to ZWW$ production, when the Z and one or both W bosons decay leptonically, and $WH \to WWW$ production, when the associated W and one or both W bosons from the Higgs decay leptonically. It is also possible to search for trilepton signatures from these production modes, but this search will be handled as a separate channel to be added in the future.

11.1 Event Selection

The event selection for same sign dilepton events focues on eliminating background from fake and charge misidentified leptons. Because PHX electrons have a high rate of charge mismeasurement, we do not use PHX electrons in the SS analysis. All other lepton types are included. The WH and ZH events tend to have lower values of missing transverse energy because there are three neutrinos, and the leptons are not necessarily back-to-back. Because Drell-Yan contributes to the same-sign region only when a lepton charge is misidentified, it is not as large a background source in the same-sign region as in the opposite-sign. Therefore we remove all $\not\!\!E_{\mathrm{T}}$ and $\not\!\!E_{\mathrm{T}}^{\mathrm{spec}}$ requirements. To reduce the number of fake leptons in the sample, we increase the p_{T} requirement for the second lepton from 10 GeV/c to 20 Gev/c. To reduce the W+jets and $W\gamma$ contributions, we only use events with one or more jets with $E_{\mathrm{T}} > 15$ GeV and $|\eta| < 2.5$ at L5 correction. Same sign events with zero jets are used as a control sample, as described in Section 11.2.

Even after selection, W+jets accounts for about 50% of the background in the same-sign channel. Drell-Yan contributes about 25% of the total background. Smaller background contributions come from WW, WZ, ZZ, $W\gamma$, and $t\bar{t}$ processes. To estimate the backgrounds, we use the same MC samples as used in the opposite-sign HWW analysis. The W+jets contribution is measured from data, as described in Section 4.3.

Non-triggerable Fake Rates

The primary background to the SS analysis is W+jets; thus, it is important to accurately predict the number of W+jets events. The W+jets contribution measured from data must be corrected for non-triggerable fakes as described in Section 4.3. Due to the low statistics in the same-sign regions, it is difficult to measure the non-triggerable fake contributions directly from these regions. Instead, we use the regions with all SS event selections applied, except with opposite-sign leptons instead of same-sign. Because there is no $\not\!\!E_{\mathrm{T}}$ cut, this region has considerable statistics, primarily due to Drell-Yan events.

The non-triggerable fake rates measured in the opposite-sign regions are then applied to the SS W+jets predictions. The rates, shown in Table 28, cause the total number of W+jets events to increase by about 20% in both SS events with 0 jets and SS events with one or more jets.

Charge Fake Rate

WW is expected to be a very small contribution to the same-sign analysis. Even in 4.8 fb^{-1}, only ~ 0.03 WW events are expected. However, it is expected to look very signal-like, so we still want to include it in the neural network training. To model WW we use the WW MC@NLO sample, which has smaller statistics than many of our other MC samples. Running this MC sample through our same-sign event selection, very few MC events pass the selection. There are not enough events to make a NN template from.

To make a smooth NN template, we instead use events which satisfy all same-sign requirements, except the two leptons have opposite signs instead of the same signs. We then multiply the number of events in this template by a charge fake rate, or the likelihood that the charge of one lepton would be misidentified. We measure this charge fake rate (CFR) in the MC as outlined in the following paragraphs.

To measure a charge fake rate for dilepton types, we use the $Z \to ee$, $Z \to \mu\mu$, and WW Pythia samples. To maximize the statistics, we use only very basic selection cuts: lepton ID, trigger lepton requirements, good run list applied, and a ΔZ cut between the two leptons. Using the MC truth information, we compare the reconstructed charge of both leptons to the generated charge of the two leptons. We then count the number of lepton pairs with both charges correctly measured, and the pairs with the charge of one lepton mismeasured. The ratio of these two numbers is the charge fake rate.

Table 57 shows the charge fake rate for all possible dilepton types. Although we do not use PHX electrons, those CFR are included for completeness. The systematic uncertainty due to the modeling of the CFR in MC is discussed in Section 6.5.

Expectation for Base Region

The background expectation and observed yield for the same-sign dilepton signal region for events containing one or more reconstructed jets with $E_T > 15$ GeV are shown in Table 58. The expected and observed kinematic distributions for these events are shown in Figures 57-59. We stack the backgrounds on top of each other, and then for comparison we overlay the contribution from a 160 GeV/c^2 Higgs boson with yields scaled up by a factor of 10. In addition, we calculate a confidence level for data versus background expectations on each plot. The confidence levels shown are for Poisson fluctuations and the KS test.

11.2 Same-Sign Control Region

The primary background in the same-sign signal region is fakes. The best non-overlapping control region to study the agreement of the fakes prediction is in the region of same-sign dileptons with zero jets. Table 59 and Figures 60 through 62 show the agreement between data and the fakes prediction. The agreement is good within statistics for all variables.

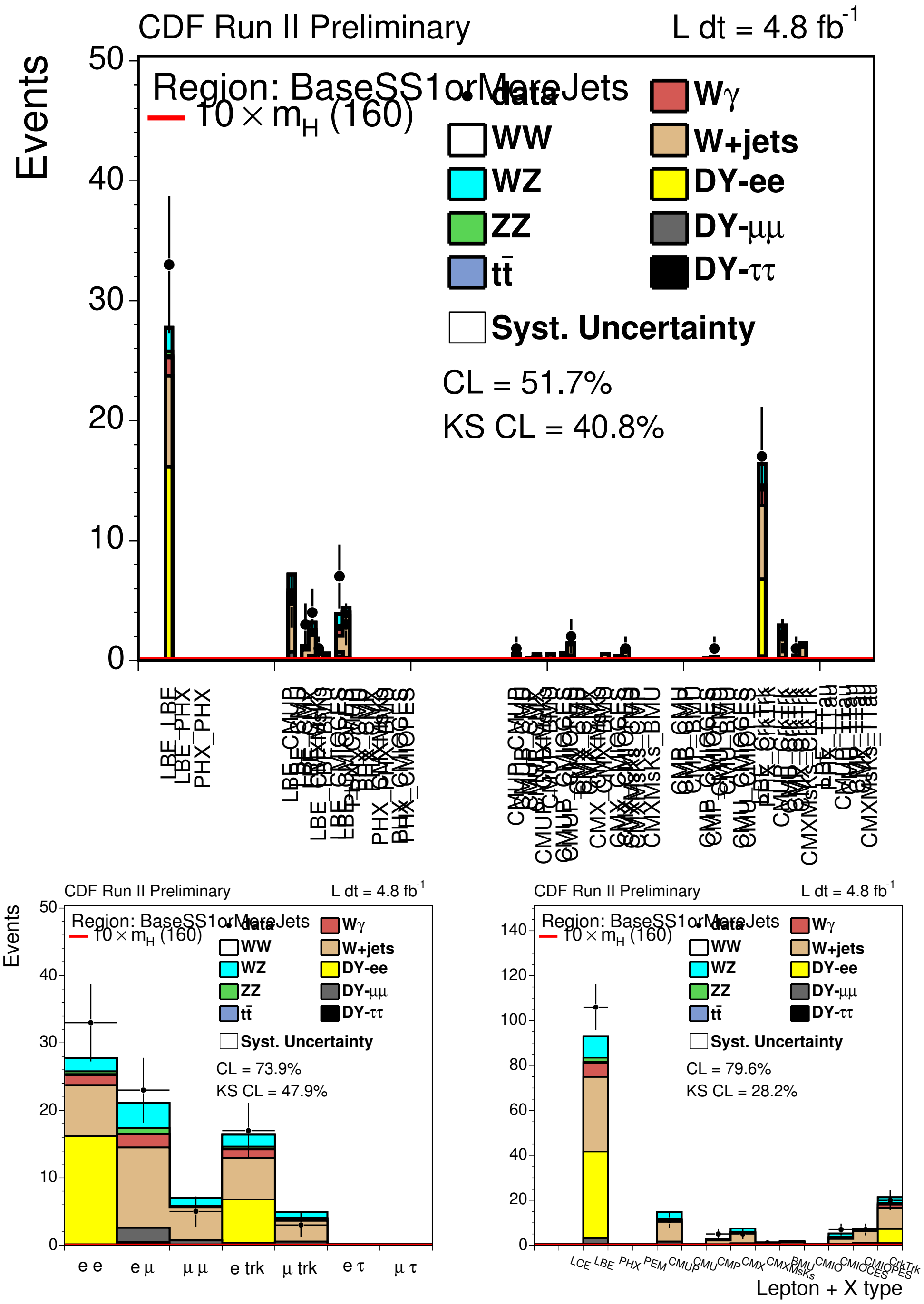

Figure 57: Same-Sign dilepton 1+ jet signal region.

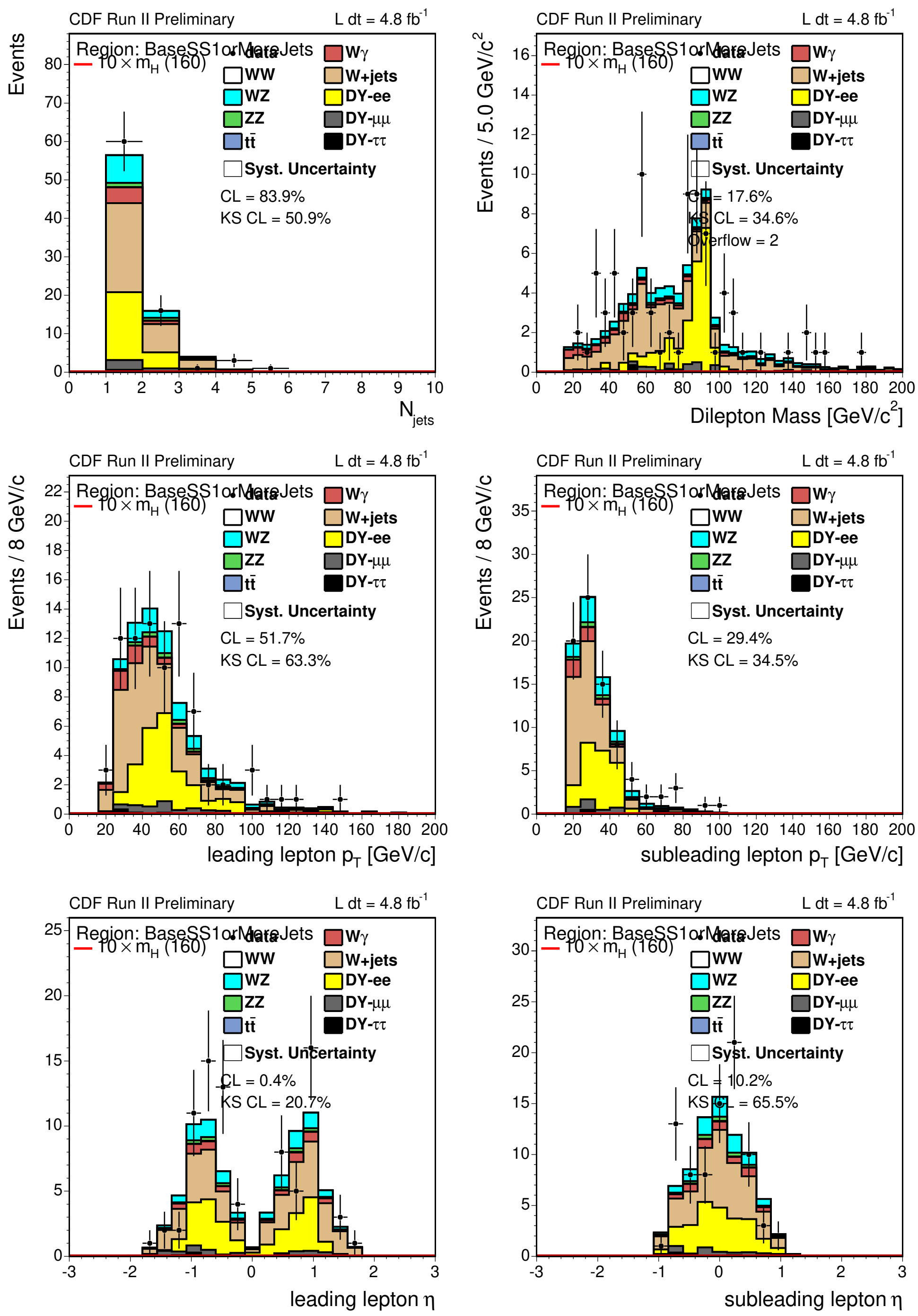

Figure 58: Same-Sign dilepton 1+ jet signal region.

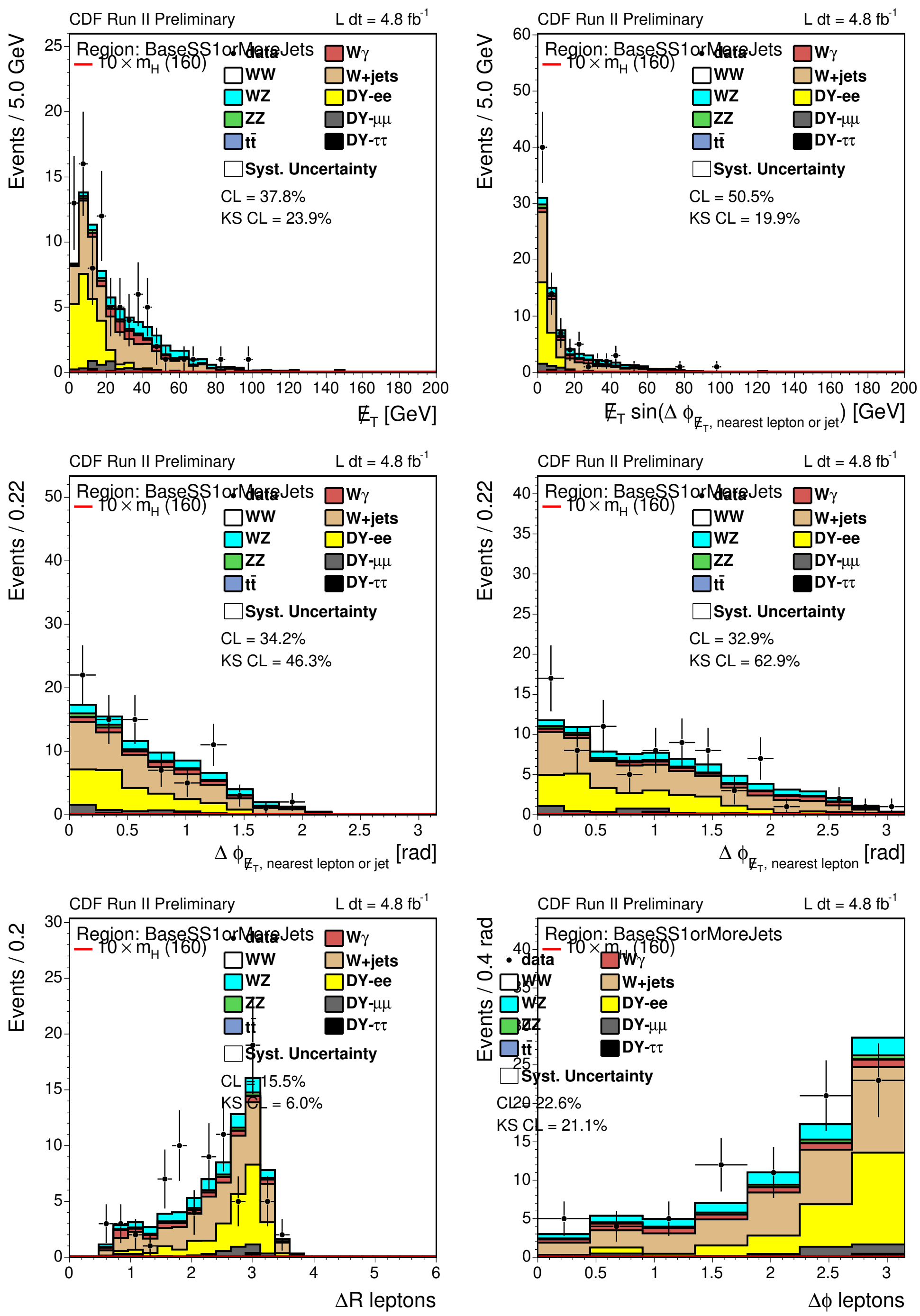

Figure 59: Same-Sign dilepton 1+ jet signal region.

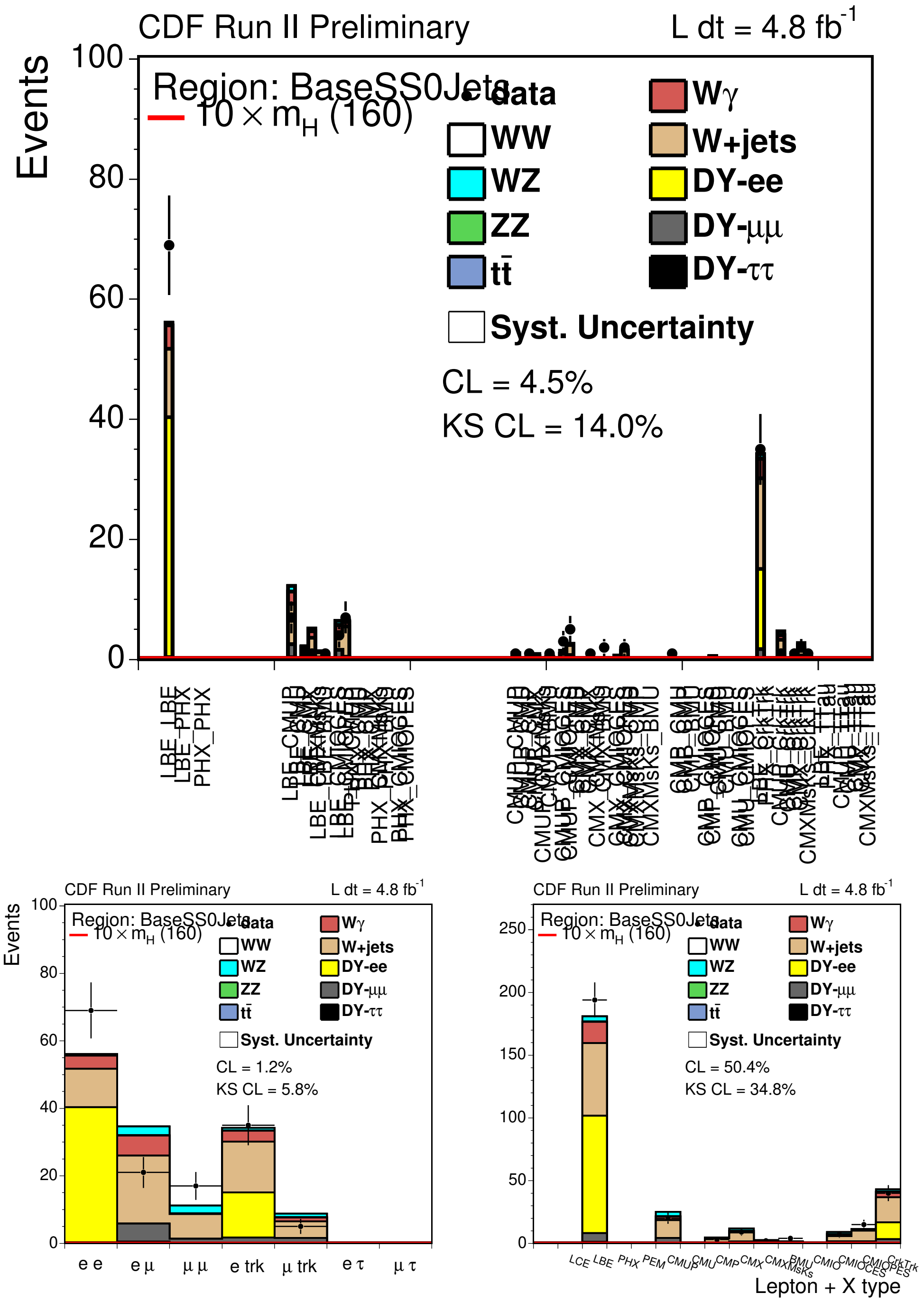

Figure 60: Same-Sign dilepton 0 jet control region.

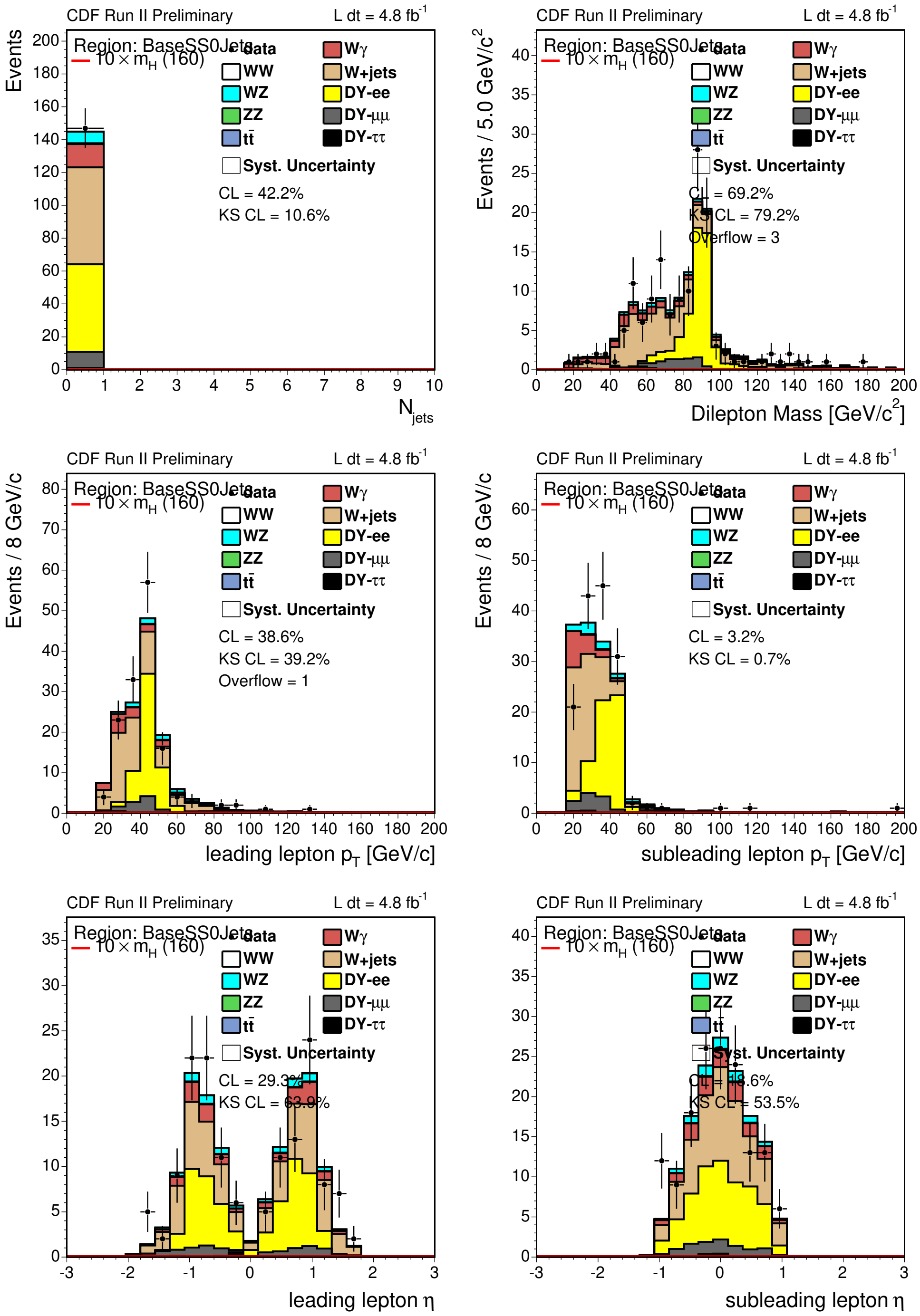

Figure 61: Same-Sign dilepton 0 jet control region.

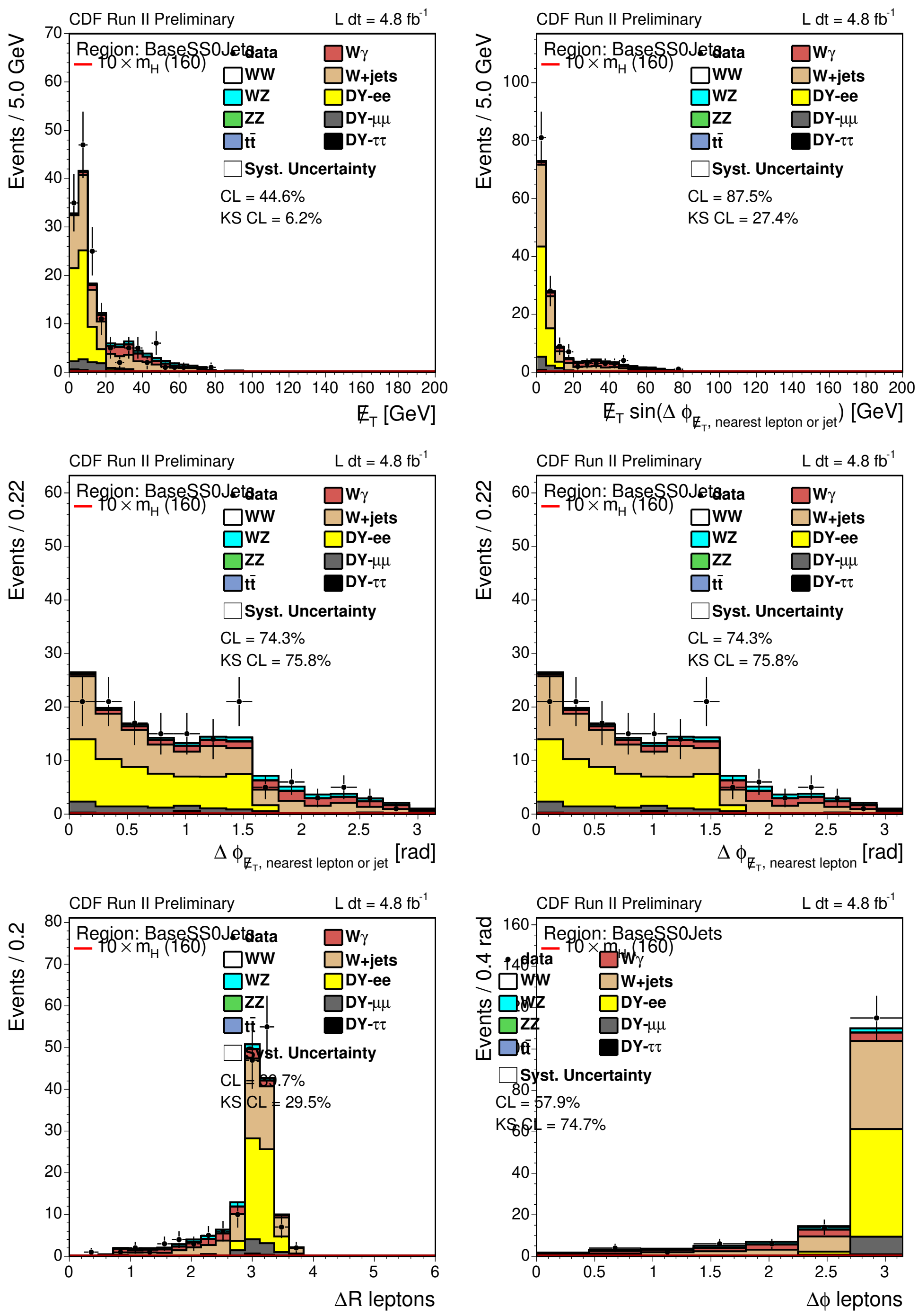

Figure 62: Same-Sign dilepton 0 jet control region.

Dilepton type	Opposite-sign events	Same-sign events	Charge fake rate
LBE-LBE	1804738	914	5.06e-4
LBE-Central μ	793007	270	3.40e-4
LBE-Forward μ	119401	38	3.18e-4
LBE-CrkTrk	1223739	490	4.00e-4
Central μ-Central μ	2350202	1	4.25e-7
Central μ-Forward μ	822095	54	6.57e-5
Central μ-CrkTrk	1109896	35	3.15e-5
PHX-PHX	442445	120832	0.273
PHX-Central μ	266784	34292	0.129
PHX-Forward μ	43481	5922	0.136
PHX-CrkTrk	574412	77449	0.135
LBE-PHX	1781103	228155	0.128

Table 57: Calculated charge fake rates (CFR) for all dilepton types, using WW, $Z \rightarrow ee$, and $Z \rightarrow \mu\mu$ Pythia MC samples. The lepton selection is described in the text. "Central μ" includes CMUP, CMP, CMX, CMXMsKs, CMIOCES, and CMP muons, while "Forward μ" includes CMIOPES and BMU muons.

Category	WW	WZ	ZZ	$t\bar{t}$	DY	$W\gamma$	W+jets	Total	Data
e e	0.0	2.0	0.4	0.1	16.1	1.5	7.6	27.7	33.0
e μ	0.0	3.7	0.8	0.1	2.6	2.0	12.9	22.1	23.0
μ μ	0.0	1.2	0.2	0.0	0.7	0.0	4.2	6.4	5.0
e trk	0.0	1.8	0.4	0.0	6.8	1.3	6.6	16.8	17.0
μ trk	0.0	0.9	0.2	0.0	0.5	0.3	2.6	4.4	3.0
Total:	0.0	9.5	2.0	0.2	26.7	5.0	33.9	77.4	81.0

Category	WW	WZ	ZZ	$t\bar{t}$	DY	$W\gamma$	W+jets	Total	Data
LBE LBE	0.0	2.0	0.4	0.1	16.1	1.5	7.6	27.7	33.0
LBE PHX	0.0	0.0	0.0	0.0	0.0	0.0	0.0	0.0	0.0
PHX PHX	0.0	0.0	0.0	0.0	0.0	0.0	0.0	0.0	0.0
LBE CMUP	0.0	1.3	0.3	0.0	0.7	0.6	4.2	7.2	5.0
LBE CMP	-0.0	0.2	0.0	0.0	0.0	0.1	0.8	1.2	3.0
LBE CMX	0.0	0.6	0.1	0.0	0.4	0.3	1.7	3.1	4.0
LBE CMXMsKs	0.0	0.1	0.0	0.0	0.1	0.1	0.4	0.7	1.0
LBE BMU	0.0	0.2	0.0	0.0	0.3	0.1	0.0	0.6	0.0
LBE CMIOCES	0.0	1.0	0.2	0.0	0.7	0.5	1.6	4.1	7.0
LBE CMIOPES	0.0	0.3	0.1	0.0	0.2	0.3	3.5	4.4	3.0
PHX CMUP	0.0	0.0	0.0	0.0	0.0	0.0	0.0	0.0	0.0
PHX CMP	0.0	0.0	0.0	0.0	0.0	0.0	0.0	0.0	0.0
PHX CMX	0.0	0.0	0.0	0.0	0.0	0.0	0.0	0.0	0.0
PHX CMXMsKs	0.0	0.0	0.0	0.0	0.0	0.0	0.0	0.0	0.0
PHX BMU	0.0	0.0	0.0	0.0	0.0	0.0	0.0	0.0	0.0
PHX CMIOCES	0.0	0.0	0.0	0.0	0.0	0.0	0.0	0.0	0.0
PHX CMIOPES	0.0	0.0	0.0	0.0	0.0	0.0	0.0	0.0	0.0
CMUP CMUP	0.0	0.2	0.0	0.0	0.0	0.0	0.3	0.6	1.0
CMUP CMP	0.0	0.0	0.0	0.0	0.0	0.0	0.2	0.2	0.0
CMUP CMX	0.0	0.2	0.0	0.0	0.0	0.0	0.3	0.5	0.0
CMUP CMXMsKs	0.0	0.0	0.0	0.0	0.0	0.0	0.1	0.1	0.0
CMUP BMU	0.0	0.1	0.0	0.0	0.0	0.0	0.9	1.0	0.0
CMUP CMIOCES	0.0	0.3	0.1	0.0	0.0	0.0	0.3	0.6	0.0
CMUP CMIOPES	0.0	0.1	0.0	0.0	0.4	0.0	0.9	1.4	2.0
CMX CMP	0.0	0.0	0.0	0.0	0.0	0.0	0.1	0.2	0.0
CMX CMX	0.0	0.0	0.0	0.0	0.0	0.0	0.1	0.1	0.0
CMX CMXMsKs	0.0	0.0	0.0	0.0	0.0	0.0	0.0	0.0	0.0
CMX BMU	0.0	0.0	0.0	0.0	0.0	0.0	0.2	0.2	0.0
CMX CMIOCES	0.0	0.1	0.0	0.0	0.0	0.0	0.3	0.5	0.0
CMX CMIOPES	0.0	0.0	0.0	0.0	0.1	0.0	0.8	1.0	1.0
CMXMsKs CMP	0.0	0.0	0.0	0.0	0.0	0.0	0.1	0.1	0.0
CMXMsKs CMXMsKs	0.0	0.0	0.0	0.0	0.0	0.0	0.0	0.0	0.0
CMXMsKs BMU	0.0	0.0	0.0	0.0	0.0	0.0	0.0	0.0	0.0
CMXMsKs CMIOCES	0.0	0.0	0.0	0.0	0.0	0.0	0.1	0.1	0.0
CMXMsKs CMIOPES	0.0	0.0	0.0	0.0	0.0	0.0	0.1	0.1	0.0
CMP CMP	0.0	0.0	0.0	0.0	0.0	0.0	0.0	0.0	0.0
CMP BMU	0.0	0.0	0.0	0.0	0.0	0.0	0.0	0.0	0.0
CMP CMIOCES	0.0	0.0	0.0	0.0	0.0	0.0	0.2	0.2	0.0
CMP CMIOPES	0.0	0.0	0.0	0.0	0.1	0.0	0.1	0.2	1.0
LBE CrkTrk	0.0	1.8	0.4	0.0	6.8	1.3	6.6	16.8	17.0
PHX CrkTrk	0.0	0.0	0.0	0.0	0.0	0.0	0.0	0.0	0.0
CMUP CrkTrk	0.0	0.5	0.1	0.0	0.3	0.2	1.5	2.6	2.0
CMP CrkTrk	0.0	0.1	0.0	0.0	0.0	0.0	0.3	0.4	1.0
CMX CrkTrk	0.0	0.3	0.0	0.0	0.3	0.0	0.7	1.3	0.0
CMXMsKs CrkTrk	0.0	0.0	0.0	0.0	0.0	0.0	0.1	0.2	0.0
Total:	0.0	9.5	2.0	0.2	26.7	5.0	34.1	77.7	81.0

Table 58: Yields in same-sign dilepton signal region for events with one or more jets.

Category	WW	WZ	ZZ	$t\bar{t}$	DY	$W\gamma$	W+jets	Total	Data
$e\ e$	0.0	0.4	0.0	0.0	40.4	3.9	11.4	56.1	69.0
$e\ \mu$	0.0	2.6	0.1	0.0	5.8	5.9	22.3	36.8	21.0
$\mu\ \mu$	0.0	2.2	0.3	0.0	1.3	0.0	7.0	10.9	17.0
e trk	0.0	0.8	0.0	0.0	15.1	3.2	15.8	34.9	35.0
μ trk	0.0	1.0	0.1	0.0	1.6	1.1	4.5	8.3	5.0
Total:	0.1	7.0	0.5	0.0	64.2	14.2	61.0	147.0	147.0

Category	WW	WZ	ZZ	$t\bar{t}$	DY	$W\gamma$	W+jets	Total	Data
LBE LBE	0.0	0.4	0.0	0.0	40.4	3.9	11.4	56.1	69.0
LBE PHX	0.0	0.0	0.0	0.0	0.0	0.0	0.0	0.0	0.0
PHX PHX	0.0	0.0	0.0	0.0	0.0	0.0	0.0	0.0	0.0
LBE CMUP	0.0	0.9	0.0	0.0	2.5	2.0	6.7	12.2	7.0
LBE CMP	0.0	0.1	0.0	0.0	0.2	0.2	1.7	2.2	1.0
LBE CMX	0.0	0.5	0.0	0.0	0.4	1.0	3.2	5.2	1.0
LBE CMXMsKs	0.0	0.1	0.0	0.0	0.3	0.1	0.9	1.4	0.0
LBE BMU	0.0	0.1	0.0	0.0	0.4	0.3	0.0	0.8	1.0
LBE CMIOCES	0.0	0.7	0.0	0.0	1.6	1.5	3.3	7.1	4.0
LBE CMIOPES	0.0	0.2	0.0	0.0	0.5	0.8	5.4	6.9	7.0
PHX CMUP	0.0	0.0	0.0	0.0	0.0	0.0	0.0	0.0	0.0
PHX CMP	0.0	0.0	0.0	0.0	0.0	0.0	0.0	0.0	0.0
PHX CMX	0.0	0.0	0.0	0.0	0.0	0.0	0.0	0.0	0.0
PHX CMXMsKs	0.0	0.0	0.0	0.0	0.0	0.0	0.0	0.0	0.0
PHX BMU	0.0	0.0	0.0	0.0	0.0	0.0	0.0	0.0	0.0
PHX CMIOCES	0.0	0.0	0.0	0.0	0.0	0.0	0.0	0.0	0.0
PHX CMIOPES	0.0	0.0	0.0	0.0	0.0	0.0	0.0	0.0	0.0
CMUP CMUP	0.0	0.3	0.0	0.0	0.0	0.0	0.7	1.0	1.0
CMUP CMP	0.0	0.1	0.0	0.0	0.0	0.0	0.2	0.3	1.0
CMUP CMX	0.0	0.3	0.0	0.0	0.0	0.0	0.6	0.9	0.0
CMUP CMXMsKs	0.0	0.1	0.0	0.0	0.0	0.0	0.2	0.2	0.0
CMUP BMU	0.0	0.1	0.0	0.0	0.1	0.0	0.2	0.4	1.0
CMUP CMIOCES	0.0	0.5	0.1	0.0	0.0	0.0	0.9	1.5	3.0
CMUP CMIOPES	0.0	0.2	0.0	0.0	0.7	0.0	1.5	2.4	5.0
CMX CMP	0.0	0.0	0.0	0.0	0.0	0.0	0.1	0.1	0.0
CMX CMX	0.0	0.1	0.0	0.0	0.0	0.0	0.2	0.2	1.0
CMX CMXMsKs	0.0	0.0	0.0	0.0	0.0	0.0	0.0	0.1	0.0
CMX BMU	0.0	0.0	0.0	0.0	0.0	0.0	0.1	0.2	2.0
CMX CMIOCES	0.0	0.2	0.0	0.0	0.0	0.0	0.4	0.7	0.0
CMX CMIOPES	0.0	0.1	0.0	0.0	0.3	0.0	1.0	1.4	2.0
CMXMsKs CMP	0.0	0.0	0.0	0.0	0.0	0.0	0.0	0.0	0.0
CMXMsKs CMXMsKs	0.0	0.0	0.0	0.0	0.0	0.0	0.0	0.0	0.0
CMXMsKs BMU	0.0	0.0	0.0	0.0	0.0	0.0	0.0	0.0	0.0
CMXMsKs CMIOCES	0.0	0.0	0.0	0.0	0.0	0.0	0.1	0.2	0.0
CMXMsKs CMIOPES	0.0	0.0	0.0	0.0	0.1	0.0	0.3	0.3	1.0
CMP CMP	0.0	0.0	0.0	0.0	0.0	0.0	0.1	0.1	0.0
CMP BMU	0.0	0.0	0.0	0.0	0.0	0.0	0.0	0.0	0.0
CMP CMIOCES	0.0	0.0	0.0	0.0	0.0	0.0	0.2	0.2	0.0
CMP CMIOPES	0.0	0.0	0.0	0.0	0.1	0.0	0.5	0.6	0.0
LBE CrkTrk	0.0	0.8	0.0	0.0	15.1	3.2	15.8	34.9	35.0
PHX CrkTrk	0.0	0.0	0.0	0.0	0.0	0.0	0.0	0.0	0.0
CMUP CrkTrk	0.0	0.6	0.1	0.0	0.9	0.8	2.2	4.6	1.0
CMP CrkTrk	0.0	0.1	0.0	0.0	0.1	0.1	1.4	1.6	1.0
CMX CrkTrk	0.0	0.3	0.0	0.0	0.6	0.3	1.4	2.5	2.0
CMXMsKs CrkTrk	0.0	0.0	0.0	0.0	0.0	0.1	0.3	0.4	1.0
Total:	0.1	7.0	0.5	0.0	64.2	14.2	60.7	146.8	147.0

Table 59: Yields in same-sign dilepton signal region for events with zero jets.

Variable	Meaning
Met	$\not{E}_T$
SumEtJets	Sum E_{T} of all jets
dimass	Dilepton mass M_{ll}
Ht	Transverse mass H_{T}
MetSpec	${\not{E}_T}^{\mathrm{spec}}$
jet1Et	E_{T} of leading jet
lep1E	Energy of leading lepton
MetDelPhi	$\Delta\phi$ between $\not{E}_T$and nearest lepton or jet
LepSumPt	Vector sum of lepton 1 and 2 p_{T}
dPhiLeptons	$\Delta\phi$ between leptons
MetSig	$\not{E}_{T\mathrm{sig}}$
lep2Pt	p_{T} of subleading lepton
lep1Pt	p_{T} of leading lepton

Table 60: Kinematic neural network inputs for the same-sign analysis. Variables are listed in order of decreasing significance to the NN. Plots of the input variables are shown in Figs. 63 through 64.

11.3 Same-Sign Analysis

We do not attempt to calculate Matrix Elements for SS events. Instead, we rely solely on a neural network (NN) to discriminate signal from background using kinematic variables as inputs to the NN. Optimization and training of the neural network are done in the same manner as for the 0J case described in Section 7. For the SS region our neural network uses 13 inputs, 14 hidden nodes and 1 output node. The input variables used for the SS NN are shown in Table 60. The observed distributions of each SS neural network input parameter compared with the distributions predicted by our background model are shown in Figures 63 and 64. For reference, we also include a hypothetical signal component for a Higgs boson with $m_H = 160$ GeV/c^2.

Templates are created for each neural network and used for calculating 95% CL limits with the MCLimit program [28]. Due to the low statistics in the SS region, we do not divide events into High S/B and Low S/B categories as is done for the 0J and 1J regions. Output templates for the trained SS neural network are shown in Figures 65 and 66.

The most significant signal contributions in the SS region are from associated production VH ($q\bar{q} \to ZH \to ZWW$ and $q\bar{q} \to WH \to WWW$). The gluon fusion ($gg \to H \to WW \to ll\nu\nu$) and Vector Boson Fusion (VBF) production methods contribute only when the charge of a lepton is misidentified. Consequently, we only consider WH and ZH production in the SS analysis. We evaluate the number of events expected from each production process as a function of the mass of the Higgs. These numbers are shown in Table 61.

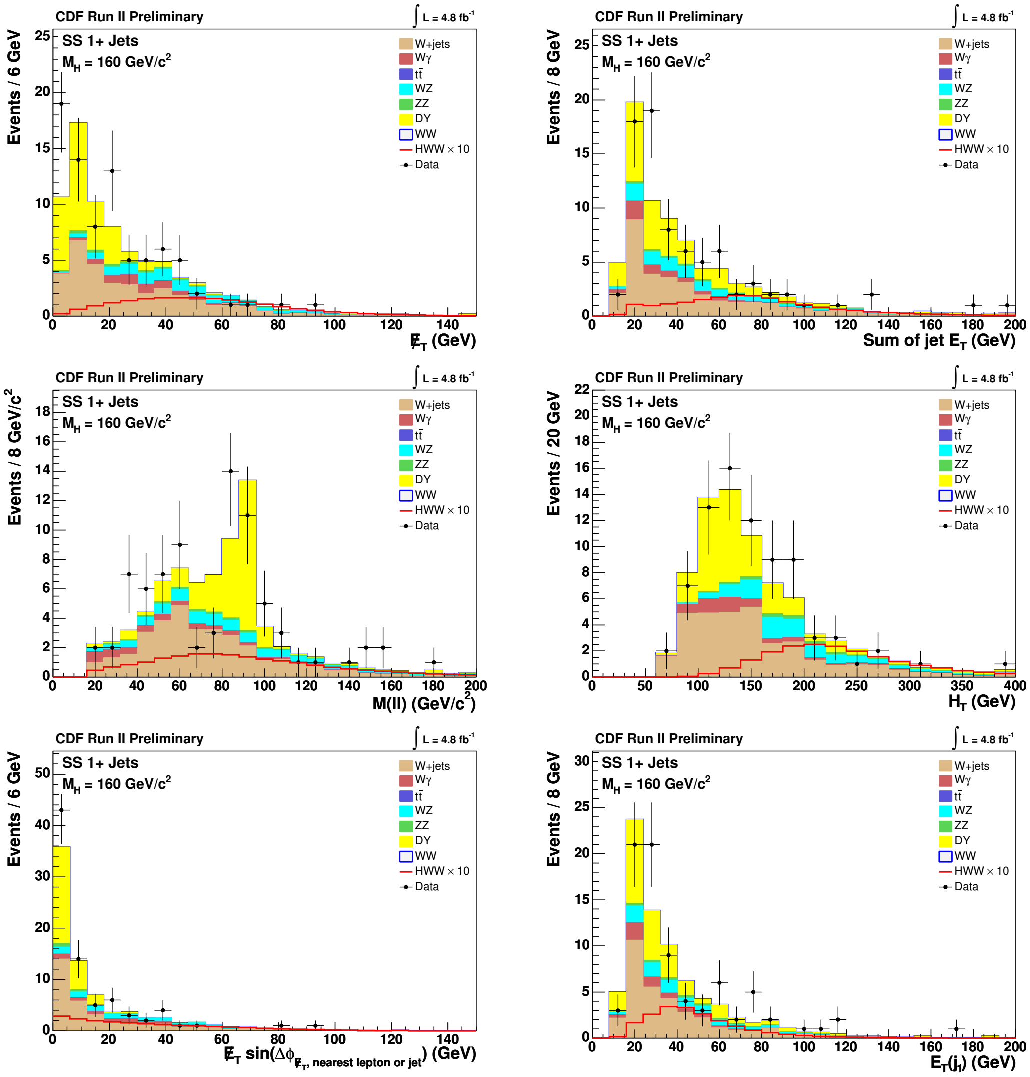

Figure 63: Neural Network input variables for SS NN (signal for $M_H = 160$ GeV$/c^2$).

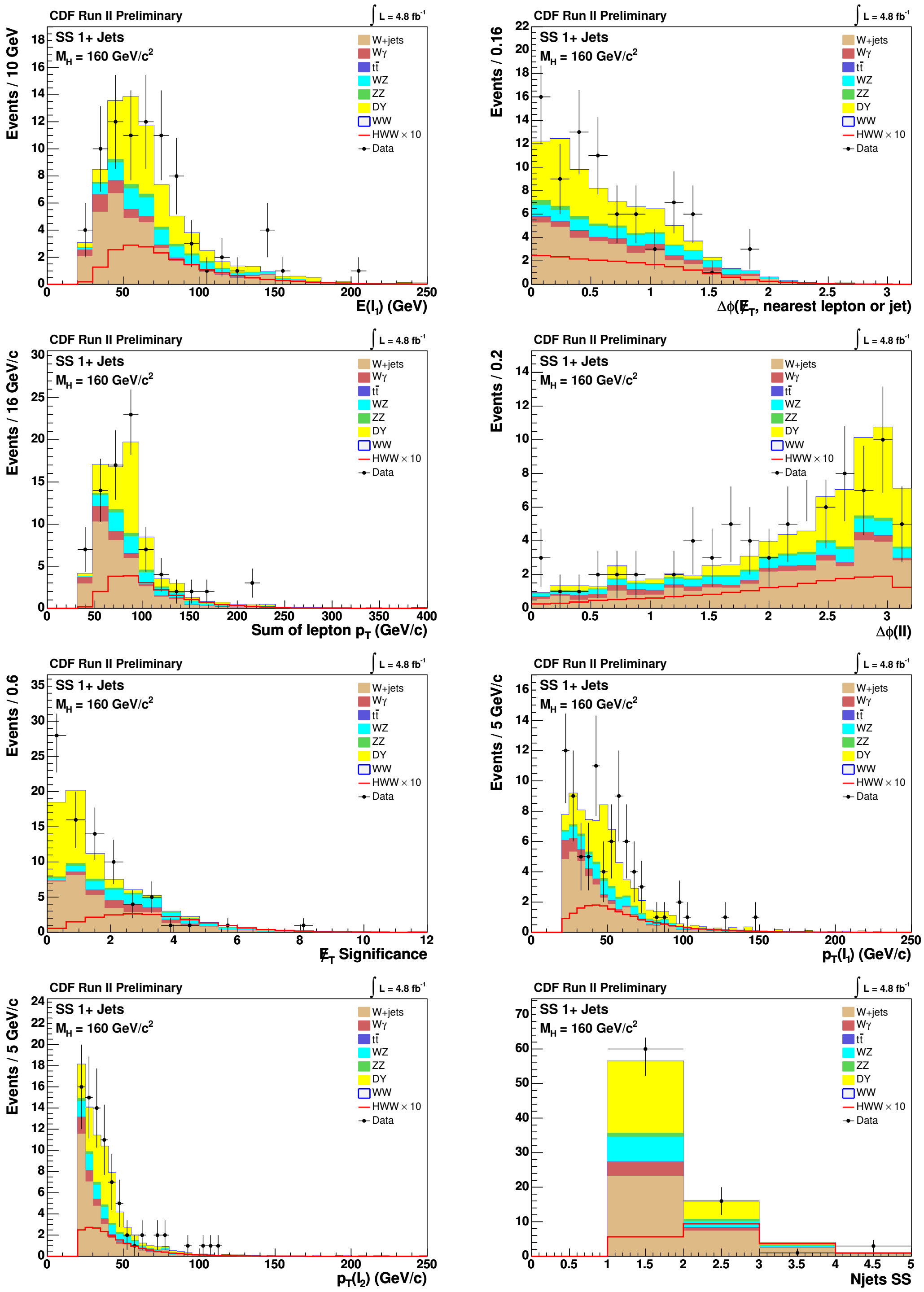

Figure 64: Neural Network input variables for SS NN (signal for $M_H = 160\ \mathrm{GeV}/c^2$). N_{jets} is not actually a NN input variable.

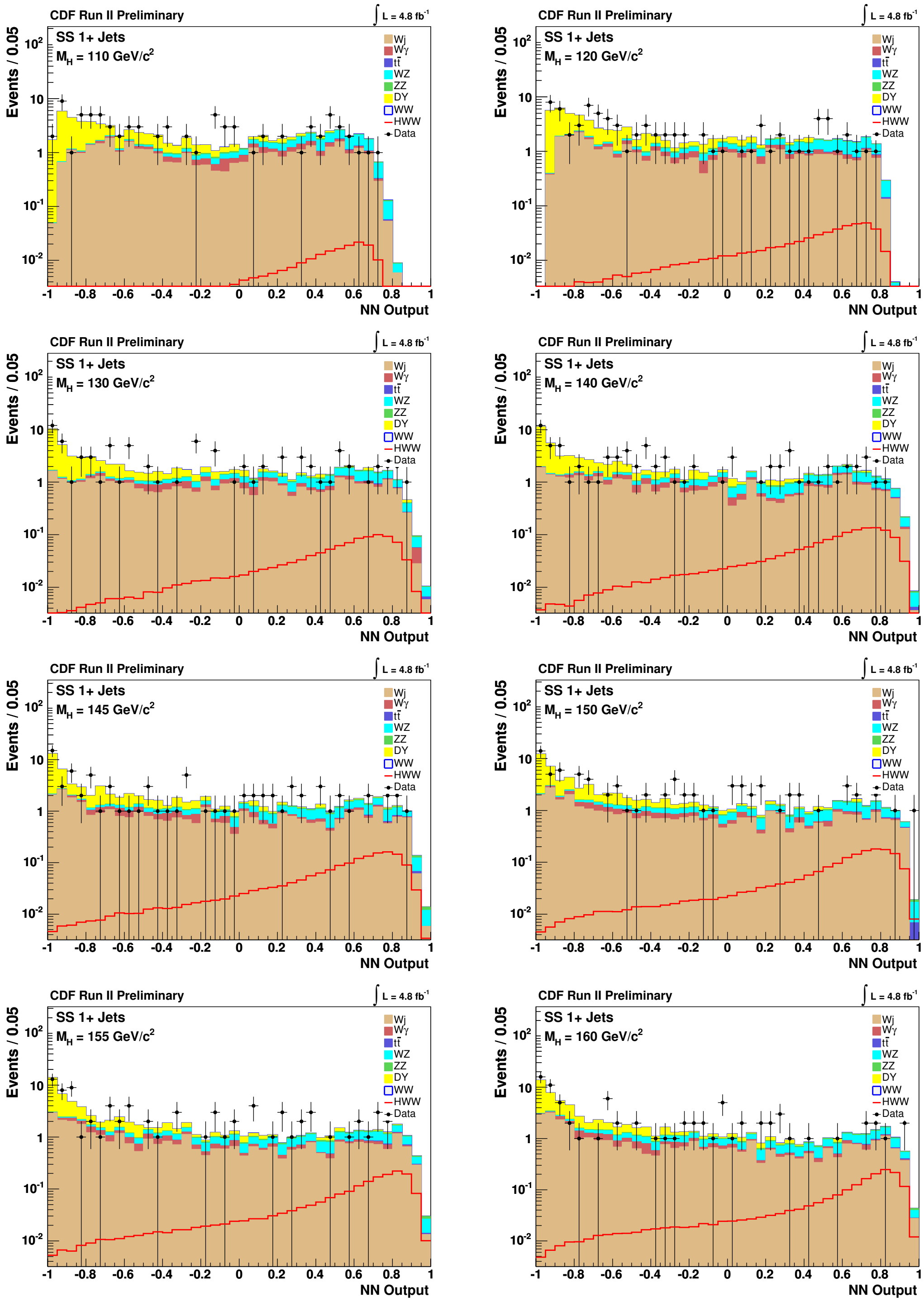

Figure 65: SS Neural Network output templates for several Higgs masses. From the top left to bottom right: 110 GeV, 120 GeV, 130 GeV, 140 GeV, 145 GeV, 150 GeV, 155 GeV, and 160 GeV.

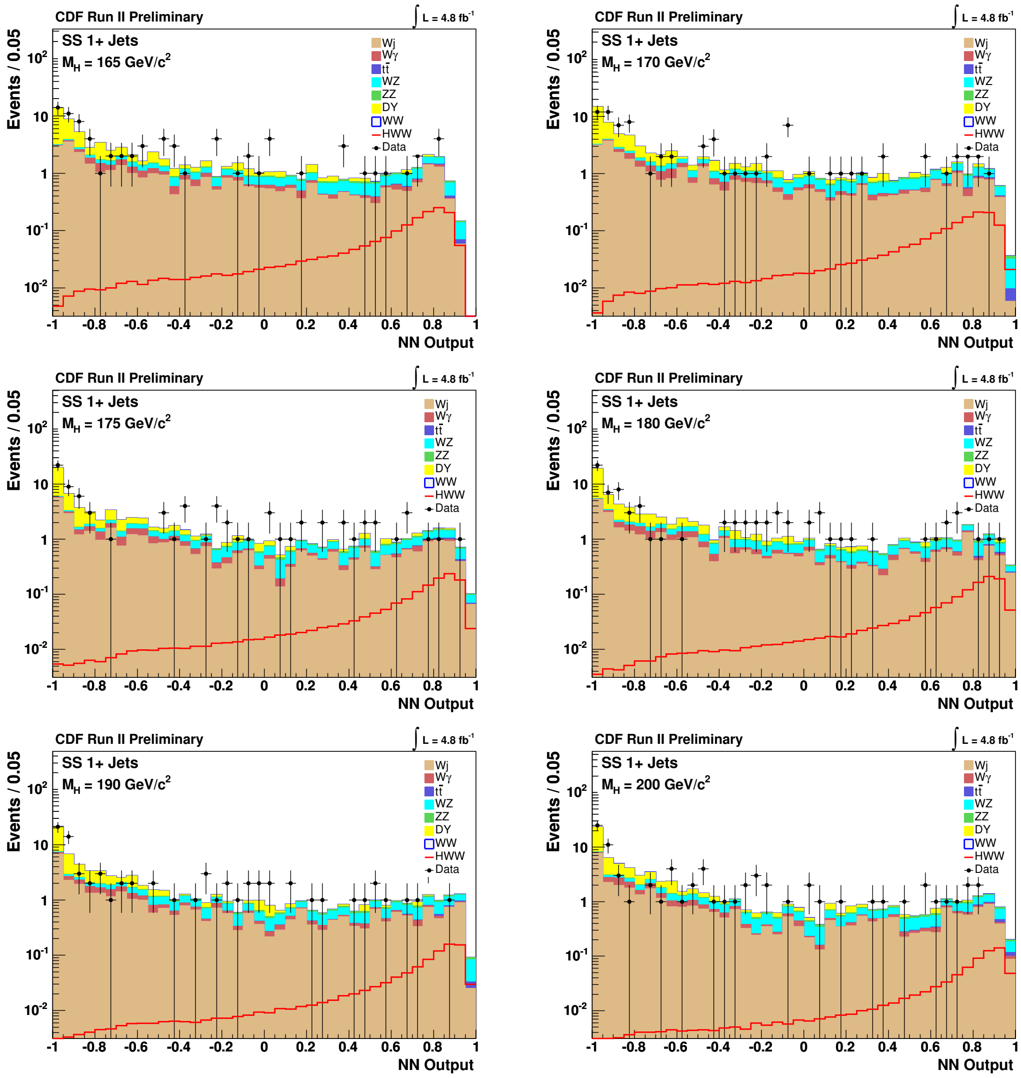

Figure 66: SS Neural Network output templates for several Higgs masses. From the top left to bottom right : 165 GeV, 170 GeV, 175 GeV, 180 GeV, 190 GeV, and 200 GeV.

Mass (GeV/c^2)	gg→H	WH	ZH	VBF
110	-	0.163	0.0284	-
120	-	0.449	0.0747	-
130	-	0.879	0.144	-
140	-	1.26	0.202	-
145	-	1.36	0.222	-
150	-	1.48	0.24	-
155	-	1.57	0.256	-
160	-	1.59	0.256	-
165	-	1.49	0.25	-
170	-	1.39	0.232	-
175	-	1.28	0.209	-
180	-	1.15	0.194	-
190	-	0.82	0.135	-
200	-	0.651	0.108	-

Table 61: Expected Higgs Signal yields as a function of the Higgs boson mass in the SS region for each of the contributing production processes. **To be updated.**

In calculating the final limits, we take into account systematic uncertainties on both the signal and background models we use to train our neural networks. Systematic uncertainties for the SS region are summarized in Tables 62 and 63.

Table 64 and Figure 67 show the expected (based on 10000 pseudo-experiments) and observed limits obtained from the SS region, incorporating the systematic uncertainties listed in Tables 62 and 63.

Uncertainty Source	WW	WZ	ZZ	$t\bar{t}$	DY	$W\gamma$	W+jet
Cross Section							
Scale							
PDF Model							
Total	*6.0%*	*6.0%*	*6.0%*	10.0%	5.0%	10.0%	
Acceptance							
Scale							
PDF Model	*1.9%*	*2.7%*	*2.7%*	*2.1%*	*4.1%*	*2.2%*	
Higher-order Diagrams	*5.0%*	*10.0%*	*10.0%*	10.0%		*10.0%*	
Jet Modeling	3.0%				17.0%	16.0%	
Conversion Modeling						20.0%	
Charge Mismeasurement Rate	16.5%			16.5%	16.5%		
Jet Fake Rates							30.0%
MC Run Dependence	*1.9%*			*1.0%*		*2.4%*	
Lepton ID Efficiencies	*2.0%*	*2.0%*	*2.0%*	*2.0%*	*2.0%*	*2.0%*	
Trigger Efficiencies	*2.1%*	*2.1%*	*2.1%*	*2.0%*	*3.4%*	*7.0%*	
Luminosity	*5.9%*	*5.9%*	*5.9%*	*5.9%*	*5.9%*	*5.9%*	

Table 62: Systematics table for SS region background processes. Cross section systematics are correlated for the diboson processes (shown in italic font) but uncorrelated between all other processes.

Uncertainty Source	$gg \to H$	WH	ZH	VBF
Cross Section				
Scale				
PDF Model				
Total		*5.0%*	*5.0%*	
Acceptance				
PDF Model (leptons)		*1.2%*	*0.9%*	
EWK Higher-order Diagrams		*10.0%*	*10.0%*	
Lepton ID Efficiencies		*2.0%*	*2.0%*	
Trigger Efficiencies		*2.1%*	*2.1%*	
Luminosity		*5.9%*	*5.9%*	

Table 63: Systematics table for SS region signal processes. Cross section systematics are uncorrelated between the signal processes. Higher-order diagrams for the VH, shown in italic font, are correlated among each other but uncorrelated from background processes.

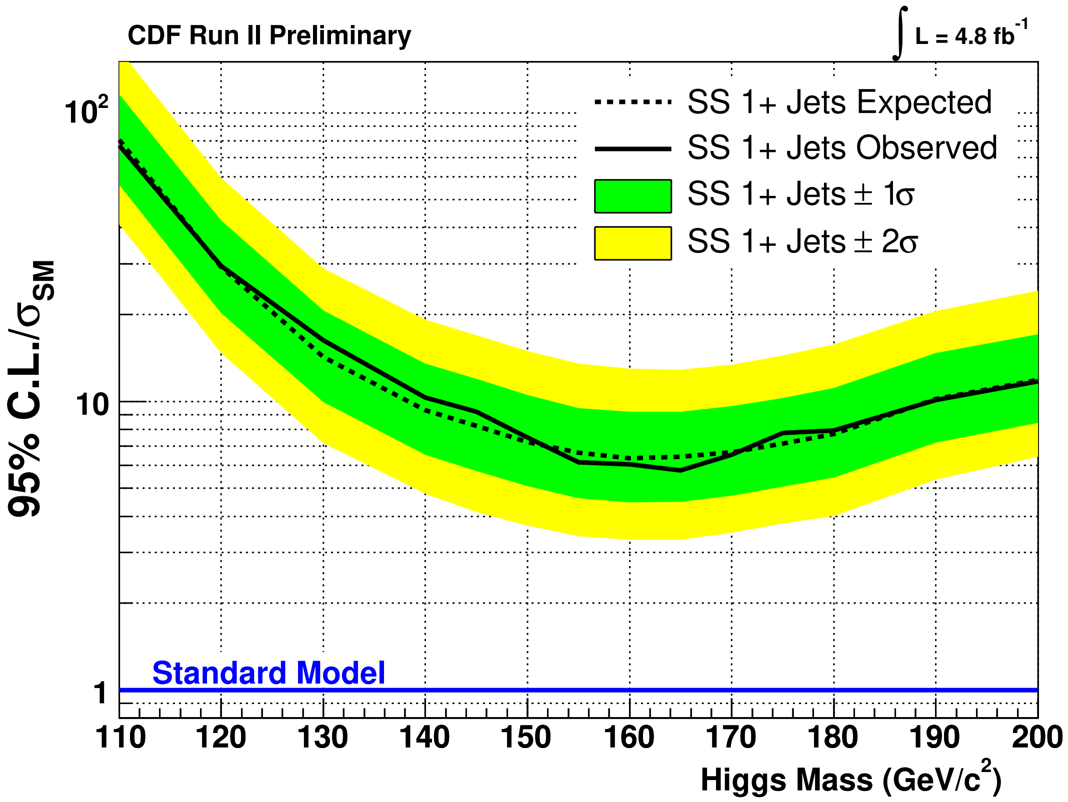

Figure 67: Expected and observed sensitivity for $H \to WW$ events with two same-sign leptons in the final state.

SS 1+ Jets	110	120	130	140	145	150	155
$-2\sigma/\sigma_{SM}$	41.01	14.72	7.16	4.78	4.14	3.71	3.41
$-1\sigma/\sigma_{SM}$	56.23	20.28	9.94	6.52	5.73	5.08	4.61
Median/$\sigma_{\mathbf{SM}}$	**80.43**	**29.23**	**14.24**	**9.31**	**8.23**	**7.23**	**6.63**
$+1\sigma/\sigma_{SM}$	116.08	42.33	20.62	13.49	11.97	10.53	9.45
$+2\sigma/\sigma_{SM}$	165.71	59.61	28.94	19.22	16.95	14.94	13.54
Observed/$\sigma_{\mathbf{SM}}$	**76.96**	**29.47**	**16.26**	**10.32**	**9.22**	**7.51**	**6.15**
	160	165	170	175	180	190	200
$-2\sigma/\sigma_{SM}$	3.30	3.31	3.51	3.77	4.01	5.36	6.42
$-1\sigma/\sigma_{SM}$	4.46	4.48	4.71	5.06	5.45	7.21	8.43
Median/$\sigma_{\mathbf{SM}}$	**6.34**	**6.42**	**6.66**	**7.15**	**7.72**	**10.20**	**11.88**
$+1\sigma/\sigma_{SM}$	9.19	9.20	9.62	10.25	11.12	14.69	17.09
$+2\sigma/\sigma_{SM}$	12.96	12.87	13.41	14.43	15.77	20.59	24.20
Observed/$\sigma_{\mathbf{SM}}$	**6.06**	**5.76**	**6.54**	**7.78**	**7.94**	**10.09**	**11.74**

Table 64: $H \to WW$ sensitivity normalized to NNLL σ_{SM} calculation in the SS region. In this region we consider potential signal contributions only from associated production with either a W or Z boson.

OS+SS	110	120	130	140	145	150	155
$-2\sigma/\sigma_{SM}$	13.70	4.55	2.24	1.42	1.24	1.05	0.86
$-1\sigma/\sigma_{SM}$	19.38	6.41	3.15	2.01	1.76	1.48	1.19
Median/$\sigma_{\mathbf{SM}}$	**28.23**	**9.45**	**4.63**	**2.97**	**2.59**	**2.15**	**1.74**
$+1\sigma/\sigma_{SM}$	41.99	13.85	6.79	4.39	3.81	3.16	2.57
$+2\sigma/\sigma_{SM}$	60.07	19.83	9.61	6.18	5.35	4.44	3.65
Observed/$\sigma_{\mathbf{SM}}$	**36.44**	**9.78**	**5.33**	**3.92**	**2.99**	**2.89**	**1.90**
	160	165	170	175	180	190	200
$-2\sigma/\sigma_{SM}$	0.66	0.64	0.74	0.88	1.04	1.63	2.14
$-1\sigma/\sigma_{SM}$	0.92	0.89	1.03	1.22	1.45	2.31	3.12
Median/$\sigma_{\mathbf{SM}}$	**1.32**	**1.28**	**1.48**	**1.78**	**2.09**	**3.39**	**4.61**
$+1\sigma/\sigma_{SM}$	1.91	1.87	2.16	2.62	3.11	5.01	6.81
$+2\sigma/\sigma_{SM}$	2.68	2.63	3.06	3.70	4.42	7.23	9.68
Observed/$\sigma_{\mathbf{SM}}$	**1.31**	**1.25**	**1.48**	**1.95**	**2.86**	**3.84**	**6.93**

Table 65: Limits on Higgs production using all six channels (0-jet High S/B, 0-jet Low S/B, 1-jet High S/B, 1-jet Low S/B, 2 or more-jets, and same-sign) and 4.8 fb^{-1}. **To be updated.**

12 Combination of Opposite-sign and Same-sign Channels

Incorporating the same-sign region into our previous combination leaves us with a total of six channels from which we produce our combined limits.

As in the case of 2 or more-jets region, events in the same-sign channel are grouped as a single channel, primarily to maintain sufficient statistics for some of the Monte-Carlo based templates as well as the $W+$ jets (Fakes) templates which lack statistics for the higher jet multiplicities. In addition, dilepton categories including a PHX electron are removed in the same-sign, and most categories treated as Low S/B in the 0-jet and 1-jet regions contain at least one PHX electron. The sensitivity in the same-sign region comes almost entirely from the associated production channels (WH, ZH).

As is the case of the five channel combination, we use Tom Junk's MCLimit [28] to produce a combined limit from all six channels. We have opted to set our own statistical errors on each bin and use the CSM_GAUSSIAN_BINERR option in MCLimit. The bin errors are nothing more then the typical statistical errors calculated by ROOT's Sumw2.

Incorporating the same-sign region in the combined limits provide a small but non-negligible gain in the overall sensitivity. The current limits from the combination of all six channels are shown in Table 65 and Figure 68.

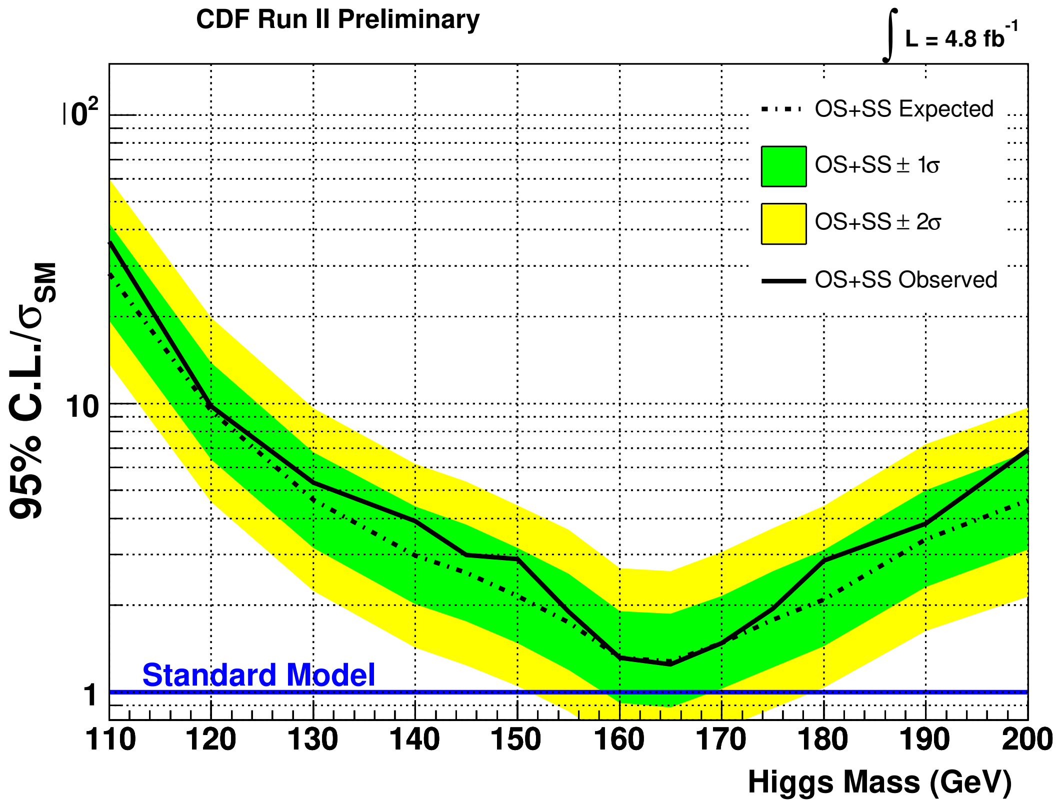

Figure 68: $H \rightarrow WW$ sensitivity normalized to NNLL σ_{SM} calculation for combination of all six channels (0-jet High S/B, 0-jet Low S/B, 1-jet High S/B, 1-jet Low S/B, 2 or more-jets, and same-sign). **To be updated.**

References

[1] D. Benjamin, D. Hidas, M. Kruse, E. James, S. Jindariani, B. Rutherford, R. Lysak, A. Robson, R. St. Denis, P. Bussey, et al., *Updated search for h to ww production using 3.6 fb-1* (2009), CDF/PHYS/EXOTIC/CDFR/9697.

[2] E. Lipeles, M. Neubauer, S.-C. Hsu, and F. Wurthwein, *Lepton id for multilepton diboson analyses* (2007), CDF/PHYS/ELECTROWEAK/CDFR/8538.

[3] C. Cox, D. Cox, R. Erbacher, R. Forrest, A. Ivanov, A. Lister, and A. Soha, *Xftl2 stereo upgrade overview* (2007), CDF/DOC/TRIGGER/CDFR/8975.

[4] *Cdf data processing status, http://www-cdf.fnal.gov/tiki/tiki-index.php?page=ProductionFarm.DataProcessing*.

[5] U. Baur and E. L. Berger, Phys. Rev. **D47**, 4889 (1993).

[6] D. Benjamin, A. Goshaw, M. Kirby, B. Heinemann, H. Hayward, and N. Tanimoto, *Measurement of the wgamma and zgamma production cross sections using 200/pb of run 2 data* (2003), CDF/PHYS/ELECTROWEAK/CDFR/6601.

[7] D. Benjamin, D. Hidas, M. Kruse, V. Necula, S. Burke, E. James, S. Jindariani, R. Lysak, S. Hsu, E. Lipeles, et al., *Search for h to ww production using 3.0 fb-1* (2008), CDF/PHYS/EXOTIC/CDFR/9402.

[8] S. Moch and P. Uwer, Nucl. Phys. Proc. Suppl. **183**, 75 (2008), `arXiv:0807.2794 [hep-ph]`.

[9] J. Campbell and K. Ellis, *Mcfm - monte carlo for femtobarn processes* (2005), http://mcfm.fnal.gov/.

[10] J. M. Campbell and R. K. Ellis, Phys. Rev. **D60**, 113006 (1999), `hep-ph/9905386`.

[11] U. Baur, T. Han, and J. Ohnemus, Phys. Rev. **D57**, 2823 (1998).

[12] *See the* TEV4LHC *working group webpage*, http://maltoni.home.cern.ch/maltoni/TeV4LHC/SM.html.

[13] C. Anastasiou, K. Melnikov, and F. Petriello, Nucl. Phys. **B724**, 197 (2005), `hep-ph/0501130`.

[14] S. Catani and M. Grazzini, Phys. Rev. Lett. **98**, 222002 (2007), `hep-ph/0703012`.

[15] M. Grazzini, JHEP **0802**, 043 (2008), `0801.3232 [hep-ph]`.

[16] HNNLO *program is publically available at*, http://theory.fi.infn.it/grazzini/codes.html.

[17] S. Catani, D. de Florian, M. Grazzini, and P. Nason, JHEP **0307**, 028 (2003), `hep-ph/0306211`.

[18] S. Moch and A. Vogt, Phys. Lett. B **631**, 48 (2005), `hep-ph/0508265`.

[19] F. Petriello, *Talk from* CDF *week june 16-20, 2008, with comparisons between* N^{3}LO *and* FEHIP*, day 3 in webtalks*, http://www-cdf.fnal.gov/internal/WebTalks/Archive/0806/080618_collaboration_meeting_day_3/01_080618_collaboration_meeting_day_3_Frank_Petriello_1_roser_Fermi2008.pdf.

[20] A. D. Martin, R. G. Roberts, W. J. Stirling, and R. S. Thorne, Phys. Lett. B **604**, 61 (2004), `hep-ph/0410230`.

[21] *All* MRST *parton distributions are available from the webpage*, http://durpdg.dur.ac.uk/hepdata/mrs.html.

[22] A. D. Martin, R. G. Roberts, W. J. Stirling, and R. S. Thorne, Eur. Phys. J. C **14**, 133 (2000), `hep-ph/9907231`.

[23] K. Yorita and Y.-K. Kim, *Search for the standard model higgs boson using tau* (2008), CDF/ANAL/EXOTIC/CDFR/9179.

[24] A. Attal and A. Canepa, *Photon conversion removal efficiency* (2006), CDF/ANAL/ELECTRON/CDFR/8073.

[25] W. M. Yao *et al.* (Particle Data Group), J. Phys. G **33**, 1 (2006).

[26] *See the jet energy and resolution group at* CDF *webpage*, http://www-cdf.fnal.gov/internal/physics/top/jets/corrections.html.

[27] M. Feindt, Technical Report IEKP-KA/01-1 (2001).

[28] T. Junk, *Sensitivity, exclusion and discovery with small signals, large backgrounds, and large systematics* (2006), CDF/DOC/STATISTICS/PUBLIC/8128.

[29] C. Rott, H. Bachacou, K. Hoffman, A. Dominguez, W. Yao, D. Glenzinski, D. Bortoletto, and M. Shochet, *Secvtx optimization for the 2003 winter conferences* (2002), CDF/DOC/SEC VTX/CDFR/6242.

[30] J. Freeman, T. Junk, E. Palencia, and S. Grinstein, *Secvtx mistag matrices for 2.2 fb^{-1} of data up to p13* (2008), CDF/DOC/SEC VTX/CDFR/9280.